CHARACTERISATION OF ION EXCHANGE RESINS FOR THE CATALYTIC CONVERSION OF BIOREFINERY STREAMS TO FUELS

Manuela Schirru
Doctor of Philosophy

ASTON UNIVERSITY
December, 2020

Aston University

CHARACTERISATION OF ION EXCHANGE RESINS FOR THE CATALYTIC CONVERSION OF BIOREFINERY STREAMS TO FUELS

Manuela Schirru

Doctor of Philosophy, 2020.

Thesis summary

This thesis describes the work performed to test and characterise various ion exchange resins as heterogeneous catalysts for the transesterification reaction of tributyrin with methanol to produce methyl butyrate as biodiesel. Depleting reserves of fossil fuel and environmental restrictions on the emission of greenhouses gases have been drawing attention to find a renewable resource such as biodiesel. Biodiesel can be produced *via* transesterification reaction of oil using an acid or base as a homogenous catalyst. Due to the disposal problem of these catalysts; a more sustainable alternative such as a heterogeneous catalyst is required. Due to the lack of literature on the use of resins as a catalyst, in particular for anionic resins, a preliminary study of the pre-treatment of ion exchange resins was initially carried out to build the foundations for further experiments. Then, a screening test was performed to detect the most promising catalyst. The strong anion exchange resins showed much higher catalytic activity than the strong cation exchange resins. Among the anion exchange resins, Amberlyst 26OH with high density of functional groups and the ability to swell in the reaction mixture gave rise to the conversion of approximately 88 %. The influence of the reaction parameters such as temperature, molar ratio, catalyst loading and stirring rate was investigated by factorial design.

The pore size and volume of resins can affect activity for triglyceride transesterification. A proper study of the internal mass transfer on the resins was introduced here. Diffusion Ordered Nuclear Magnetic Resonance Spectroscopy (DOSY NMR) has been utilized for the first time to characterize the internal mass transfer using the motion of the reacting species, confined within their pores. The measurements on the resins failed because of heterogeneity of the samples and the presence of moisture. The results of these resins were compared with mesoporous silica SBA-15, which allowed simple characterisation. Tributyrin and methyl butyrate showed reduced diffusion coefficients within the confined pores. At the same time, glycerol exhibited interesting behaviour; it showed enhancement of its diffusion coefficient due to the ability of the silica support to disrupt the intermolecular H-bonding network of glycerol.

Ion exchange resins are high-performance catalysts and catalytically active even at very low temperature. The work reported here enhance the use of ion exchange resins more used in catalysis, and the choice of resin-type could be aided by the comprehensive characterisation provided here.

Keywords: Biodiesel; transesterification; ion exchange resins; NMR diffusometry.

List of publications

- Porcedda, S., Marongiu, B., **Schirru**, **M.**, Falconieri, D. and Piras, A. Excess enthalpy and excess volume for binary systems of two ionic liquids + water. *Journal of thermal analysis and calorimetry*, **2011**, *103*, 29-33.
- Marras, C., Loche, D., Carta, D., Casula, M.F., **Schirru**, **M.**, Cutrufello, M.G. and Corrias, A. Copper-Based Catalysts Supported on Highly Porous Silica for the Water Gas Shift Reaction. *ChemPlusChem*, **2016**, *81*, 421-432.
- Rottreau, T.J., Parkes, G.E., **Schirru**, **M.**, Harries, J.L., Mesa, M.G., Topham, P.D. and Evans, R. NMR cryoporometry of polymers: Cross-linking, porosity and the importance of probe liquid. *Colloids and Surfaces A: Physicochemical and Engineering Aspects*, **2019**, *575*, 256-263.

Dedication

To the memory of my father
To mom
and to Virginia

"E quindi uscimmo a riveder le stelle"
(“and thence we came forth to see again the stars”)
The Divine Comedy. Inferno, XXXIV, I. 139. Dante Aligheri

Acknowledgements

I am deeply indebted to my supervisors, Professor Paul Topham and Dr Rob Evans, for their support and their assistance over the last two years. I express my deepest gratitude to Rob for suggestions concerning the thesis, for revising the language in this thesis and for helping me with the DOSY work.

I am extremely grateful to the School of Chemical Engineering and Applied Science at Aston University for providing the funding for this research project and their facilities.

I must also thank DuPont for providing the ion exchange resins for this research project and pratical suggestions.

Part of the work was carried out in collaboration with the University of Cagliari, Italy. In particular, we acknowledge the CeSAR (Centro Servizi Ricerca d'Ateneo) core facility of the University of Cagliari, Dr Marco Marceddu for the assistance with the generation of the ESEM data, Mr Antonio Sabeddu for the CHN analyses and Professor Maria F. Casula for running and funding CHN analyses, ESEM analyses and nitrogen adsorption-desorption analyses, and her moral support over the last two years.

Special thanks to Dr Khalid Doudin for his indispensable help in the labs. I would also like to extend my gratitude to Dr Christopher M. A. Parlett for providing the silica sample for the NMR study, Dr Lucia Frattini and Dr Anupam Singha Roy for training me to use the porosimeter and the GC equipment.

My thanks are due to other CEAC PhD students and my friends for always being supportive people.

And last but not least, my loving family. I would like thank my parents who made many sacrifices to let me and my sister continue our schooling, and my sister Virginia who is always present for me. You are my lifeline.

Table of contents

Thesis summary 1
List of publications 2
Acknowledgements 4
List of Abbreviations 9
List of Tables 11
List of Figures 13
Chapter 1 24
Sustainable chemistry for biodiesel production 24
1.1. Introduction 24
1.1.1. Transesterification reaction catalysed by acid and base 27
1.2. Ion exchange resins 30
1.2.1. Properties of ion exchange resins 38
1.2.2. Applications of ion-exchange resins 41
1.2.2.1. Water treatment 41
1.2.2.2. Pharmaceutical applications 42
1.2.2.3. Hydrometallurgy: recovery of gold and rare earth metals 43
1.2.2.4. Ion exchange and adsorbent resins for the food market 44
1.2.2.5. Ion exchange resins as catalysts 44
1.3. Literature review of transesterification reaction over ion exchange resins 46
1.3.1 Literature review of transesterification of tributyrin catalysed via solid acid and base catalysts 47
1.4. Novelty of this research 50
1.5. Aim of the thesis 50
1.6. Outline of the chapters 50
Chapter 2 52
Materials and experimental methods 52
2.1. Introduction 52
2.2. Materials 52
2.2.1 Chemicals 52
2.2.2 Catalysts 52
2.3. Investigation of the thermal stability of ion exchange resins 53
2.3.1. Thermogravimetric analysis 54
2.3.2. Differential scanning calorimetry 54
2.4. Investigation of morphological features 57
2.4.1. Nitrogen physisorption 57

2.4.2. Nitrogen physisorption analysis 63
2.4.3. Thermoporometry: DSC as alternative pore size technique 64
2.4.4. Environmental scanning electron microscopy and energy-dispersive X-ray spectroscopy analysis 66
2.5. Determination of total capacity and operating capacity of ion exchange resins.............68
2.5.1. Elemental analysis..69
2.5.2. Determination of the operating capacity by back titration of the resins in OH- and H-form 70
2.5.3. Analytical determination of halide ions...71
2.5.3.1. Calibration curve for the analytical determination of halide ions..............................73
2.5.3.2. Determination of operating capacity for the resins in Cl-form by ion-selective electrode 73
2.5.3.3. Study of the catalyst activation 74
2.6. Study of resin accessibility: swelling tests..75
2.7. Catalytic tests 75
2.7.1. Catalyst activation and preparation..76
2.7.2. Calibration curves...76
2.7.3. Catalytic performance testing 77
2.7.4. A chemometric approach: design of experiment 78
2.7.5. Gas-liquid chromatography..81
Chapter 3 83
Characterisation of ion exchange resins...83
3.1. Introduction 83
3.2. Morphology and thermal analysis of ion exchange resins...85
3.2.1. Thermal study to select the outgassing conditions of ion exchange resins 91
3.2.2. Dry and swollen-state morphology...95
3.3. Determination of total capacity and operating capacity 104
3.4. Study of the accessibility of the active sites in the polymeric resins 107
3.5. Conclusions..110
Chapter 4 112
Catalytic tests for the transesterification of tributyrin with methanol over commercial ion exchange resins...112
4.1. Introduction 112
4.1.1. Chemical and physical properties of the catalysts 113
4.2. Catalyst activation 114
4.2.1. Activation of the chloride resins 116

4.2.1.1. Calibration curve....116
4.2.1.2. Analysis of chloride ions....116
4.3. Transesterification reaction of tributyrin with methanol over ion exchange resins....119
4.3.1. Calculations....119
4.3.2. Calibration curve for the catalytic tests....120
4.3.3. Catalyst pre-treatment....121
4.3.3.1. Effect of water content on the catalytic performance of ion exchange resins....123
4.4. Catalyst screening test....126
4.5. Analysis of the transesterification reaction variables....133
4.6. Conclusion....141
Chapter 5....143
NMR diffusion studies: liquid confined in a porous material....143
5.1. Introduction....143
5.2. Introduction to Nuclear Magnetic Resonance....144
5.2.1. Chemical shift....148
5.2.2. *J*-coupling: spin-spin interactions....149
5.2.3. Relaxation....150
5.2.3.1. Longitudinal relaxation-T_1....150
5.2.3.2. Transverse relaxation-T_2....152
5.3. Diffusion theory....153
5.4. NMR hardware....158
5.5. Calibration of the instrument....159
5.6. Materials....161
5.7. Sample preparation....161
5.8. NMR experiment....161
5.8.1. Diffusion study....162
5.8.2. Results and discussion....162
5.9. Conclusions....167
Chapter 6....169
Conclusions and future work....169
6.1. Limitations of this work....169
6.2. Future work....169
6.2.1. Complementary techniques for characterisation of the ion exchange resins....169
6.4.2. Further improvements of the catalytic performances of ion exchange resins....170
6.2.3. Continuation of NMR diffusion work on SBA-15....170
References....172

APPENDICES 184
Appendix A-Supporting information for Chapter 3 184
Appendix B-Supporting information for Chapter 4 218

List of Abbreviations

BET	Brunauer-Emmett-Teller
BJH	Barrett-Joyner-Halenda
BSE	backscattered electrons
DCM	dichloromethane
DoE	design of experiment
DOSY	diffusion ordered spectroscopy
DSC	differential scanning calorimetry
DSTEBPGP_3S	double stimulated echo bipolar gradient pair sequence
DVB	divinylbenzene
ESEM−EDS	Environmental scanning electron microscopy energy−dispersive X−ray spectroscopy
FFA	free fatty acid
FID (GLC)	flame ionization detector
FID (NMR)	free induction decay
FT	Fourier transform
GC	gas chromatography
GHG	Greenhouse gas
GLC	Gas-liquid chromatography
IEB	incident electron beam
IER	ion exchange resin
ISA	ionic strength adjuster
ISE	ion selective electrode
ISEC	Inverse size−exclusion chromatography
KIT-6	Korean institute of technology
LHP	low hysteresis pressure
MA−DVB	Methylmethacrylic divinylbenzene
MAA	methacrylic acid
MB	methyl butyrate
MCM-41	Mobil composition of matter
NLDFT	non-local density functional theory
NMR	nuclear magnetic resonance
OC	operating capacity
PIM	polymer of intrinsic microporosity
PSD	pore size distribution
R.F.	radiofrequency

SBA	strongly basic anion exchange resin
SBA-15	Santa-Barbara amorphous
SAC	strongly acidic cation exchange resin
SE	secondary electrons
ST	styrene
TB	tributyrin
TC	total capacity
TGA	thermogravimetric analysis
TMS	tetramethylsilane
TOF	turn over frequency
TPM	thermoporosimetry
WAC	weakly acidic cation exchange resin
WAB	weakly basic anion exchange resin

List of Tables

Table 1.1. Comparison of homogeneous and heterogeneous catalytic processes (Reproduced from [21])....27
Table 1.2. Reactions catalysed by IERs....45
Table 1.3. Reaction conditions and TB conversion % for transterification of tributyrin with methanol over solid base and acid catalysts reported in the literature....49
Table 2.1. Chemical and physical properties of the commercial resins used in this work....53
Table 2.2. Nominal millimoles for the individual standard solutions used for tributyrin (TB) and methyl butyrate (MB) to fit the calibration curves....77
Table 2.3. Level 1 and level 2 of four factors for the DoE....81
Table 2.4. Temperature program for the BPX50 capillary column employed in this work....82
Table 3.1. Mass losses (%) of the IERs....92
Table 3.2. Onset and midpoint of the glass transition point for the IERs studied in this work....94
Table 3.3. Morphological properties of the native IERs (as received) outgassed at 313 K 3 h....100
Table 3.4. Morphological properties of the native IERs (as received) outgassed at 313 K 12 h....100
Table 3.5. Morphological properties of the pre-treated IERs at 313 K 3 h followed by outgassing at 313 K 12 h....101
Table 3.6. Comparison of the IERs morphological properties in the dry state using the NLDFT-desorption model and in the swollen state using thermoporosimetry (TMP)....104
Table 3.7. Nominal, operating (OC) and total (TC) capacities of IERs studied in this work. 106
Table 4.1. List of ion exchange resins tested for the transesterification reaction of tributyrin with methanol....114
Table 4.2. Measured potential (***P***) converted into concentration (mg L^{-1}) using the appropriate calibration curves....117
Table 4.3. Comparison of the operating capacities measured by the ion-selective electrode in OH^- form and SO_4^{2-} form expressed as meq of Cl^- released from 1 g of dry resin....119
Table 4.4. Comparison of the catalytic performance of native and pre-treated resin 26OH with the water content (%). Reaction conditions: stirring rate of 500 rpm, tributyrin: methanol molar ratio of 1:30 and 50 mg of catalyst, 333 K....124
Table 4.5. Adsorption test of tributyrin over the anion exchange resin 26OH. Reaction conditions: 10 mmol of tributyrin, 50 mg of catalyst, 500 rpm of stirring rate, a constant temperature of 333 K....125

Table 4.6. Conversion and selectivity towards methyl butyrate after 180 min. Reaction conditions: 10 mmol of tributyrin, 300 mmol of MeOH, 50 mg of catalyst, 500 rpm of stirring rate, a constant temperature of 333 K. 127

Table 4.7. Conversion and selectivity towards methyl butyrate after 180 min. Reaction conditions: 10 mmol of tributyrin, 300 mmol of MeOH, 50 mg of catalyst, 500 rpm of stirring rate, a constant temperature of 313 K. 127

Table 4.8. Comparison of the behaviour of chloride ion percentage within the tested IERs on the conversion of tributyrin at 333 K and 313 K. 133

Table 4.9. Design matrix and the results of the four-factor full factorial design using the codes +1 and −1 for the appropriate levels. 135

Table 4.10. Estimated effects and coefficients for conversion generated by Minitab 1.4. ...136

Table 4.11. Estimated effects and coefficients for selectivity generated by Minitab 1.4. 137

Table 4.12. Size of the effects of each significant factor and their interpretation for conversion. 137

Table 4.13. Size of the effects of each significant factor and their interpretation for selectivity. 137

Table 5.1. NLDFT characterisation of the catalysts investigated in this study. 162

Table 5.2. ^{1}H NMR data for tributyrin (TB) in methanolic solution. 163

Table 5.3. ^{1}H NMR data for methyl butyrate (MB) in methanolic solution. 164

Table 5.4. ^{1}H NMR data for glycerol (GLY) in methanolic solution......................................165

Table 5.5. Diffusion coefficients, $\boldsymbol{D}$ and tortuosity, $\boldsymbol{\xi}$ of tributyrin, methyl butyrate and glycerol confined in SBA-15, 26OH and 402OH. 167

Table A1.1. Elemental analysis of acetanilide as a calibration standard............................216

Table A1.2. Complete elemental analysis of the resins studied in this work. 217

List of Figures

Figure 1.1. Scheme of the biodiesel production process: the oil obtained from non-edible crops is converted by transesterification into glycerol and biodiesel. Biodiesel used as biofuel for transportation and carbon dioxide emitted is taken up by plants during photosynthesis (Reproduced from [7]). 24

Figure 1.2. Generic reaction scheme for transesterification of triglyceride. 25

Figure 1.3. The twelve principles of the Green Chemistry (Reproduced from [17]). 26

Figure 1.4. Acid-catalyzed transesterification reaction (Reproduced from [24]). 28

Figure 1.5. Base-catalyzed transesterification reaction (Reproduced from [24]). 29

Figure 1.6. Illustration of an ion exchange resin. 30

Figure 1.7. Scheme of the polymerisation of (**a**) styrene (ST) and (**b**) methacrylic acid (MA) with divinylbenzene (DVB) for the copolymer reaction (Reproduced from [36]). 31

Figure 1.8. Morphologies of gel and macroreticular resins (Reproduced from [37]). 32

Figure 1.9. Reaction scheme of SAC functionalisation (Reproduced from [33]). 33

Figure 1.10. Introduction of chloromethyl group into the copolymer using chloromethyl methyl ether (Reproduced [48]). 34

Figure 1.11. Amino functionalization of the vinylbenzene chloride divinylbenzene copolymer using (**a**) trimethylamine and (**b**) dimethylethanolamine to yield Type I and Type II SBA exchange resins, respectively (Reproduced from [48, 50]). 34

Figure 1.12. Functionalization reaction of MA-DVB matrix to yield SBA exchange resins. **Step 1:** Amination of the copolymer with dimethylaminopropylamine; **Step 2:** Formation of the salt using methyl chloride [51]. 35

Figure 1.13. Decomposition of the quaternary ammonium Type I (Reproduced [54]). 35

Figure 1.14. Decomposition of the quaternary ammonium (Type I) via Hofmann elimination or β-elimination (Reproduced from [56]). 36

Figure 1.15. Decomposition of the quaternary ammonium Type II (Reproduced from [54]). .36

Figure 1.16. Classification of IERs based on their basic and acidic functional groups. 38

Figure 1.17. Pore classification based upon (**A**) accessibility: closed pores (**a**); (**b**) and (**f**) pores open in one direction; (**c**), (**d**) and (**g**) pores open through different directions; (**e**) open pore at two ends [63]; (**B**) the pore shapes [64] and (**C**) pore diameter [63]. 40

Figure 1.18. Heterogeneous catalytic mechanism (Reproduced from [63]). 41

Figure 1.19. Schematic representation of SAC (strong acidic cation) and SBA (strong basic anion) exchange resin beads before and after the demineralisation process. 42

Figure 1.20. Reaction between the drug resinate and the ions in the gastrointestinal environment (Reproduced from [45]). 42

Figure 1.21. Cyanidation reaction allows converting gold ore into a more soluble complex. 43

Figure 1.22. Schematic drawing of the volatilisation process of cyanuric acid (Reproduced from [73])..........43

Figure 1.23. Transesterification reaction between a higher molecular weight ester and an alcohol to obtain a lower molecular weight ester (R_1 and R_2 are alkyl groups)..........46

Figure 1.24. Mechanism of transesterification over (**a**) a cation exchange resin and (**b**) an anion exchange resin where Y, A, F and D are triglyceride, alcohol, fatty acid alkyl ester and diglyceride, respectively (Reproduced from [84])..........47

Figure 1.25. Transesterification reaction of tributyrin (TB) with methanol (MeOH) to form methyl esters (MB, biodiesel) and glycerol (GLY)..........48

Figure 2.1. Schematic drawing of Perkin Elmer PyrisTM 1 thermogravimetric analyser (TGA)...........54

Figure 2.2. Schematic drawing of a DSC plot displays the endothermic changes glass transition, T_g, and melting point, T_m, and the exothermic transition as crystallisation temperature, T_c. 55

Figure 2.3. Schematic representation of DSC 1 Perkin-Elmer differential scanning calorimeter...........56

Figure 2.4. Gas adsorption (blue arrow) and gas desorption process (red arrow) (Reproduced from [105])..........58

Figure 2.5. A typical BET plot: a linear plot of $1 V\cdot p^\circ p - 1$ versus pp° which for most material using nitrogen as adsorbate is restricted to the p/p° region of 0.05 and 0.35 [103, 106].......59

Figure 2.6. IUPAC classification of physisorption isotherms showing both adsorption and desorption branches. Only Type IV and V isotherms exhibit hysteresis loops (Reproduced from [108])..........60

Figure 2.7. Schematic representation of the capillary condensation process into a pore of a radius, r [103]..........61

Figure 2.8. Representative hysteresis loops and pore shapes (Reproduced from [108, 111])...........62

Figure 2.9. Schematic drawing of Quantachrome Nova 4000e porosimeter..........64

Figure 2.10. Illustration of DSC profile of solid to liquid phase transition showing the peak–difference method for the determination of the melting temperature depression, ΔT. 66

Figure 2.11. Schematic drawing of ESEM FEI Quanta 200 microscope equipped with an EDS and secondary electron detector (Reproduced from [124])..........67

Figure 2.12. An incident electron beam (IEB) hits the specimen producing secondary electrons (SE), backscattered electrons (BSE) and X-ray..........68

Figure 2.13. Schematic representation of Perkin Elmer PE 2400 Series II CHNS/O elemental analyser (Reproduced from [125])..........69

Figure 2.14. Schematic illustration showing the colour transition of the bromothymol blue indicator across the pH range...71
Figure 2.15. Schematic drawing of the ion-selective electrode (ISE)..................................72
Figure 2.16. Flow diagram explains the stages of the IER activation and pre-treatment used in this study for preparing the resins in order to catalyse the transesterification reactions of tributyrin with methanol. 76
Figure 2.17. Schematic representation of the reactor used for running transesterification reaction. 78
Figure 2.18. Illustration of a Pareto chart. 80
Figure 2.19. Schematic representation of a gas-liquid chromatography apparatus used for the catalytic tests...81
Figure 2.20. Typical chromatogram for tributyrin transesterification. 82
Figure 3.1. Schematic illustration of dry and swollen morphology of the IERs. Gel types IERs exhibits a non-permanent porosity in the dry state while macroreticular resins permanent macropores and non-permanent micropores. The thick arrows point out the morphology changes from dry state to swollen state, opening mesopores of both gel-type and macroreticular IERs (Reproduced from [147] [147])..84
Figure 3.2. Schematic representation of the glass transition. The polymer goes through a glassy state to rubbery state when the temperature is continuously increased (Reproduced from [153])...86
Figure 3.3. The adsorption swelling involves the gas molecules which surround the polymer matrix, lowering its rigidity and forming new pores (volume-swelling) (Reproduced from [159, 165])...88
Figure 3.4. Schematic representation of filling and emptying process of (1) open and (2) limited access pores (Reproduced from [159])..88
Figure 3.5. TG (black line) and DTG (blue line) curves (%) under nitrogen (20 cm^3 min^{-1}) of: (**a**) 26OH and (**b**) 402OH*. 92
Figure 3.6. DSC thermograms under nitrogen (50 cm^3 min^{-1}) of (**a**) 26OH and (**b**) 402OH*.93
Figure 3.7. N_2 adsorption-desorption isotherm at 77 K on (**a**) 26OH and (**b**) 402OH* using different outgassing conditions (black circle) 313 K for 3 h on native; (grey circle) 313 K for 12 h on native; (white circle) 313 K for 3 h on pre-treated at 313 K for 12 h. 96
Figure 3.8. Comparison between pore size distributions (PSDs) of (**a**-**c**) the macroreticular IER 26OH and (**d**-**f**) the gel-type resin 402OH* based on (black circle) the BJH method; (grey circle) the NLDFT (adsorption) method; (white circle) NLDFT (desorption) method. The outgassing conditions were: (**a**-**d**) 313 K for 3 h on native; (**b**-**e**) 313 K for 12 h on native; (**c**-**f**) 313 K for 3 h on pre-treated resins at 313 K for 12 h. 99

Figure 3.9. ESEM images of (**a**-**b**) 26OH (M, ST-DVB); (**c**) 458Cl (G, MA-DVB); (**d**) 958Cl (M, MA-DVB); (**e**) 410Cl (G, ST-DVB) and (**f**) 402Cl (G, ST-DVB) at magnification (**a**-**b**) 600x; (**c**) 85x; (**d**-**f**) 100x; (**e**) 72x. (G= gel; M= macroreticular; ST-DVB= styrene divinylbenzene; MA-DVB= methyl methacrylic divinylbenzene). 102

Figure 3.10. The swelling degree of pre-treated IERs at 313 K brought in contact for 60 minutes with (blank) methanol and (dense pattern) 1:30 mixture tributyrin (TB) to methanol. The error bars represent the standard error of two repeated measurements. 108

Figure 3.11. The swelling grade of pre-treated IERs at 313 K brought in contact for 60 minutes with 1:30 mixture tributyrin (TB) and methanol. The bars of each IER has been marked with the type of matrix. ST and MA stand for styrenic and methyl methacrylic matrix while M and G for macroreticular and gel-type IERs, respectively. The error bars represent the standard deviation of two repeated measurements. 109

Figure 4.1. Transesterification reaction of tributyrin (TB) with methanol: TB reacts with three molecules of methanol (MeOH) to form methyl ester (biodiesel) and glycerol (GLY). 113

Figure 4.2. Exchange reaction between chloride quaternary ammonium and hydroxide ion in solution..115

Figure 4.3. Flow diagram of IERs activation of strongly anionic exchange resins in Cl-form. 115

Figure 4.4. Illustration showing seven-point calibration curves (logarithm scale) for the resins 458Cl and 410Cl immersed in 1 M NaOH solution to convert the potential of unknown samples of the exchange process $Cl^- \rightarrow OH^-$ into concentration. Error bars represent the standard deviation of triplicate measurements. 116

Figure 4.5. Affinities of Type I and Type II strong base anion (SBA) resins (Reproduced from [47])...117

Figure 4.6. Calibration curves for (**a**) tributyrin (TB) and (**b**) methyl butyrate (MB). Error bars indicate standard deviation for replicated experiments. 120

Figure 4.7. Reaction mechanism of transesterification of tributyrin over SBA resins occurs in four steps: (**a**) methanol adsorbs over the surface of the resin, forming water and methoxide; (**b**) adsorption of FFA over the surface of the SBA resin; (**c**) hydrolysis of the tributyrin in the presence of water and (**d**) transesterification of tributyrin catalysed by methoxide formed in the first step to yield methyl ester (biodiesel) (Reproduced from [192]). 122

Figure 4.8. Reaction mechanism of transesterification of tributyrin over SCA exchange resins occurs in three steps: (**a**) free fatty acids adsorption over the resin to form carbocations; (**b**) carbocations react with methanol to form ester and water and (**c**) tributyrin reacts with acidic groups onto the resin to yield methyl butyrate (biodiesel) (Reproduced from [31])..............123

Figure 4.9. Transesterification reaction between tributyrin and methanol profile for the tested IERs: conversion (%) and product selectivity (%). Reaction conditions: 10 mmol of tributyrin, 300 mmol of MeOH, 50 mg of catalyst, 500 rpm of stirring rate, 333 K and 313 K. Error bars indicate the standard error for two replicated measurements. Some replications could not be repeated due to time constraints. 128

Figure 4.10. Dependence of the initial MB reaction rate, $\boldsymbol{r}°$on the density of the counter-ions (H^+ or OH^-) in the dry phase volume ($\boldsymbol{V}_p$). Reaction condition: 500 rpm, molar ratio 1:30 (oil: methanol), 50 mg of catalyst, and 333 K (**a**) and 313 K (**b**). 129

Figure 4.11. Dependence of the conversion of tributyrin on the swollen degree of the tested resins using a solution of molar ratio tributyrin to methanol 1:30. The bars indicate the conversion of each resins using the reaction condition: stirring rate of 500 rpm, molar ratio of tributyrin to methanol 1:30, 50 mg of catalyst, and a temperature of (**a**) 333 K and (**b**) 313 K. The triangles represent the swelling degree of each resin in the reaction mixture tributyrin to methanol 1:30. Error bars represent standard error for replicated catalytic experiments and swelling tests. 130

Figure 4.12. Turnover frequency (TOF) determined at 1 h reaction time for the transesterification reaction of tributyrin with methanol over the ion exchange resins tested in this research project. 132

Figure 4.13. Illustration showing the Pareto charts of the magnitude of effects on (**a**) the TB conversion (%) and (**b**) the response MB selectivity (%) 138

Figure 4.14. Response surface plot for of conversion against (**a**) molar ratio and catalyst loading and, (**b**) temperature and molar ratio. The low and high values of the studied factors are coded −1 and +1. 140

Figure 5.1. Schematic illustration of the nuclear magnetic spins in the spin-up (α) and spin-down (β) state, interacting with an external magnetic field $\boldsymbol{B}_0$ (Reproduced from [219]). 145

Figure 5.2. Splitting of the energy levels of the proton nucleus after a magnetic field, $\boldsymbol{B}_0$, is applied (Reproduced from [217]). 146

Figure 5.3. The net magnetisation ($\boldsymbol{M}_z$) is aligned along z-axis when a magnetic field, $\boldsymbol{B}_0$, is applied (Reproduced from [217]). 148

Figure 5.4. The motion of electrons generates the induced magnetic field, $\boldsymbol{B}_{ind}$ to respond to the applied field $\boldsymbol{B}_0$. $\boldsymbol{B}_{ind}$ opposes $\boldsymbol{B}_0$ and reduce the effect of $\boldsymbol{B}_0$ on the nucleus from $\boldsymbol{B}_0$ (Reproduced from [224]). 149

Figure 5.5. T_1 relaxation is a process in which the magnetization $\boldsymbol{M}_z$ turns back to its original maximum value $\boldsymbol{M}_0$ (Reproduced from [227]) 151

Figure 5.6. T_2 relaxation is a process due to loss of coherence of the spins. (Reproduced from [230]). 152

....159
Figure 5.7. Schematic diagram detailing the main components of a modern nuclear magnetic resonance (NMR) spectrometer (Reproduced from [217]). 159
Figure 5.8. The double stimulated echo bipolar pulse pair sequence (DSTEBPGP_3S) used in this work (Reproduced from [210]). 160
Figure 5.9. Chemical structure of tributyrin (TB). 163
Figure 5.10. DOSY spectra for tributyrin (TB) in methanol-d4 in bulk solution (blue), 26OH (red), 402OH* (green) and SBA-15 (purple). 163
Figure 5.11. Chemical structure of methyl butyrate (MB). 164
Figure 5.12. DOSY spectra for methyl butyrate (MB) in methanol-d4 in bulk solution (blue), 26OH (red), 402OH* (green) and SBA-15 (purple). 164
Figure 5.13. Chemical structure of glycerol (GLY). 165
Figure 5.14. DOSY spectra for glycerol (GLY) in methanol-d4 in bulk solution (blue), 26OH (red), 402OH* (green) and SBA-15 (purple). 165
Figure 5.15. Illustration showing the heterogeneity in the sample of the resins. 166
Figure A1.1 a. TGA (black line) and DTG (blue line) curves for the IER 458Cl under nitrogen performed in the temperature range 298 K–878 K with a flow rate of 20 cm^3 min^{-1} and heating rate of 10 K...184
Figure A1.1 b. TGA (black line) and DTG (blue line) curves for the IER 958Cl under nitrogen performed in the temperature range 298 K–878 K with a flow rate of 20 cm^3 min^{-1} and heating rate of 10 K...185
Figure A1.1 c. TGA (black line) and DTG (blue line) curves for the IER 410Cl under nitrogen performed in the temperature range 298 K–878 K with a flow rate of 20 cm^3 min^{-1} and heating rate of 10 K...185
Figure A1.1 d. TGA (black line) and DTG (blue line) curves for the IER 402Cl under nitrogen performed in the temperature range 298 K–878 K with a flow rate of 20 cm^3 min^{-1} and heating rate of 10 K...186
Figure A1.1 e. TGA (black line) and DTG (blue line) curves for the IER 15H under nitrogen performed in the temperature range 298 K–878 K with a flow rate of 20 cm^3 min^{-1} and heating rate of 10 K...186
Figure A1.1 f. TGA (black line) and DTG (blue line) curves for the IER 120H under nitrogen performed in the temperature range 298 K–878 K with a flow rate of 20 cm^3 min^{-1} and heating rate of 10 K...187
Figure A1.2 a. DSC thermograms of the gel resin 458Cl under nitrogen (50 cm^3 min^{-1}). ...187
Figure A1.2 b. DSC thermograms of the macroreticular resin 958Cl under nitrogen (50 cm^3 min^{-1}). 188

Figure A1.2 c. DSC thermograms of gel resin 410Cl under nitrogen (50 cm^3 min^{-1}). 188
Figure A1.2 d. DSC thermograms of gel resin 402Cl under nitrogen (50 cm^3 min^{-1})..........188
Figure A1.2 e. DSC thermograms of the macroreticular 15H under nitrogen (50 cm^3 min^{-1}). 189
Figure A1.2 f. DSC thermograms of the gel resin 120H under nitrogen (50 cm^3 min^{-1})......189
Figures A1.3 a. N_2 adsorption-desorption isotherm at 77 K on 458Cl using different outgassing conditions (black circle) 313 K for 3 h on native; (grey circle) 313 K for 12 h on native; (white circle) 313 K for 3 h on pre-treated at 313 K for 12 h. 190
Figures A1.3 b. N_2 adsorption-desorption isotherm at 77 K on 958Cl using different outgassing conditions (black circle) 313 K for 3 h on native; (grey circle) 313 K for 12 h on native; (white circle) 313 K for 3 h on pre-treated at 313 K for 12 h. 190
Figures A1.3 c. N_2 adsorption-desorption isotherm at 77 K on 410Cl using different outgassing conditions (black circle) 313 K for 3 h on native; (grey circle) 313 K for 12 h on native; (white circle) 313 K for 3 h on pre-treated at 313 K for 12 h. 191
Figures A1.3 d. N_2 adsorption-desorption isotherm at 77 K on 402Cl using different outgassing conditions (grey circle) 313 K for 12 h on native; (white circle) 313 K for 3 h on pre-treated at 313 K for 12 h...191
Figures A1.3 e. N_2 adsorption-desorption isotherm at 77 K on 15H using different outgassing conditions (black circle) 313 K for 3 h on native; (grey circle) 313 K for 12 h on native; (white circle) 313 K for 3 h on pre-treated at 313 K for 12 h. 192
Figures A1.3 f. N_2 adsorption-desorption isotherm at 77 K on 120H using different outgassing conditions (black circle) 313 K for 3 h on native; (grey circle) 313 K for 12 h on native; (white circle) 313 K for 3 h on pre-treated at 313 K for 12 h. 192
Figures A1.4 a. pore size distributions (PSDs) of the gel-type resin 458Cl based on (black circle) the BJH method; (grey circle) the NLDFT (adsorption) method; (white circle) NLDFT (desorption) method. The outgassing conditions were 313 K for 3 h on native. 193
Figures A1.4 b. Pore size distributions (PSDs) of the gel-type resin 458Cl based on (black circle) the BJH method; (grey circle) the NLDFT (adsorption) method; (white circle) NLDFT (desorption) method. The outgassing conditions were 313 K for 12 h on native. 194
Figures A1.4 c. Pore size distributions (PSDs) of the macroreticular resin 958Cl based on (black circle) the BJH method; (grey circle) the NLDFT (adsorption) method; (white circle) NLDFT (desorption) method. The outgassing conditions were 313 K for 3 h on native. 194
Figures A1.4 d. Pore size distributions (PSDs) of the macroreticular resin 958Cl based on (black circle) the BJH method; (grey circle) the NLDFT (adsorption) method; (white circle) NLDFT (desorption) method. The outgassing conditions were 313 K for 12 h on native. 195

Figures A1.4 e. Pore size distributions (PSDs) of the macroreticular resin 958Cl based on (black circle) the BJH method; (grey circle) the NLDFT (adsorption) method; (white circle) NLDFT (desorption) method. The outgassing conditions were 313 K for 3 h on native. 195

Figures A1.4 f. Pore size distributions (PSDs) of the gel-type resin 410Cl based on (black circle) the BJH method; (grey circle) the NLDFT (adsorption) method; (white circle) NLDFT (desorption) method. The outgassing conditions were 313 K for 3 h on native. 196

Figures A1.4 g. Pore size distributions (PSDs) of the gel-type resin 410Cl based on (black circle) the BJH method; (grey circle) the NLDFT (adsorption) method; (white circle) NLDFT (desorption) method. The outgassing conditions were 313 K for 3 h on pre-treated IER. ...196

Figures A1.4 h. Pore size distributions (PSDs) of the gel-type resin 410Cl based on (black circle) the BJH method; (grey circle) the NLDFT (adsorption) method; (white circle) NLDFT (desorption) method. The outgassing conditions were 313 K for 3 h on pre-treated IER. ...197

Figures A1.4 i. Pore size distributions (PSDs) of the gel-type resin 402Cl based on (black circle) the BJH method; (grey circle) the NLDFT (adsorption) method; (white circle) NLDFT (desorption) method. The outgassing conditions were 313 K for 12 h on native. 197

Figures A1.4 j. Pore size distributions (PSDs) of the gel-type resin 402Cl based on (black circle) the BJH method; (grey circle) the NLDFT (adsorption) method; (white circle) NLDFT (desorption) method. The outgassing conditions were 313 K for 3 h on pre-treated IER. ...198

Figures A1.4 k. Pore size distributions (PSDs) of the macroreticular resin 15H based on (black circle) the BJH method; (grey circle) the NLDFT (adsorption) method; (white circle) NLDFT (desorption) method. The outgassing conditions were 313 K for 3 h on native. 198

Figures A1.4 l. Pore size distributions (PSDs) of the macroreticular resin 15H based on (black circle) the BJH method; (grey circle) the NLDFT (adsorption) method; (white circle) NLDFT (desorption) method. The outgassing conditions were 313 K for 12 h on native. 199

Figures A1.4 m. Pore size distributions (PSDs) of the macroreticular resin 15H based on (black circle) the BJH method; (grey circle) the NLDFT (adsorption) method; (white circle) NLDFT (desorption) method. The outgassing conditions were 313 K for 3 h on pre-treated IER. 199

Figures A1.4 n. Pore size distributions (PSDs) of the gel-type resin 120H based on (black circle) the BJH method; (grey circle) the NLDFT (adsorption) method; (white circle) NLDFT (desorption) method. The outgassing conditions were 313 K for 3 h on pre-treated IER. ...200

Figures A1.4 o. Pore size distributions (PSDs) of the gel-type resin 120H based on (black circle) the BJH method; (grey circle) the NLDFT (adsorption) method; (white circle) NLDFT (desorption) method. The outgassing conditions were 313 K for 12 h on native. 200

Figures A1.4 p. Pore size distributions (PSDs) of the gel-type resin 120H based on (black circle) the BJH method; (grey circle) the NLDFT (adsorption) method; (white circle) NLDFT (desorption) method. The outgassing conditions were 313 K for 3 h on pre-treated IER. ...201

Figures A1.5 a. BET surface area plot of the native macroreticular 26OH outgassed at 313 K for 3h. The C constant was obtained from BET equation. 201

Figures A1.5 b. BET surface area plot of the native macroreticular 26OH outgassed at 313 K for 12h. The C constant was obtained from BET equation. 202

Figures A1.5 c. BET surface area plot of the pre-treated macroreticular 26OH outgassed at 313 K for 3h. The C constant was obtained from BET equation..202

Figures A1.5 d. BET surface area plot of the native gel-type 458Cl outgassed at 313 K for 3h. The C constant was obtained from BET equation. 203

Figures A1.5 e. BET surface area plot of the native gel-type 458Cl outgassed at 313 K for 12h. The C constant was obtained from BET equation. 203

Figures A1.5 f. BET surface area plot of the native gel-type 958Cl outgassed at 313 K for 3h. The C constant was obtained from BET equation. 204

Figures A1.5 h. BET surface area plot of the pre-treated gel-type 958Cl outgassed at 313 K for 3h. The C constant was obtained from BET equation. 205

Figures A1.5 i. BET surface area plot of the native gel-type 410Cl outgassed at 313 K for 3h. The C constant was obtained from BET equation. 205

Figures A1.5 j. BET surface area plot of the native gel-type 410Cl outgassed at 313 K for 3h. The C constant was obtained from BET equation. 206

Figures A1.5 k. BET surface area plot of the pre-treated gel-type 410Cl outgassed at 313 K for 3h. The C constant was obtained from BET equation. 206

Figures A1.5 l. BET surface area plot of the native gel-type 402Cl outgassed at 313 K for 12h. The C constant was obtained from BET equation. 207

Figures A1.5 m. BET surface area plot of the pre-treated gel-type 402Cl outgassed at 313 K for 3h. The C constant was obtained from BET equation. 207

Figures A1.5 n. BET surface area plot of the native gel-type 402OH outgassed at 313 K for 3h. The C constant was obtained from BET equation. 208

Figures A1.5 o. BET surface area plot of the native gel-type 402OH outgassed at 313 K for 12 h. The C constant was obtained from BET equation. 208

Figures A1.5 p. BET surface area plot of the pre-treated gel-type 402OH outgassed at 313 K for 3h. The C constant was obtained from BET equation. 209

Figures A1.5 q. BET surface area plot of the native macroreticular 15H outgassed at 313 K for 3h. The C constant was obtained from BET equation. 209

Figures A1.5 r. BET surface area plot of the native macroreticular 15H outgassed at 313 K for 12h. The C constant was obtained from BET equation. 210

Figures A1.5 s. BET surface area plot of the pre-treated macroreticular 15H outgassed at 313 K for 3h. The C constant was obtained from BET equation. 210

Figures A1.5 t. BET surface area plot of the native gel-type 120H outgassed at 313 K for 3h. The C constant was obtained from BET equation. 211

Figure A1.5 u. BET surface area plot of the native gel-type 120H outgassed at 313 K for 12h. The C constant was obtained from BET equation. 211

Figure A1.5 v. BET surface area plot of the pre-treated gel-type 120H outgassed at 313 K for 3h. The C constant was obtained from BET equation. 212

Figures A1.6 a. Melting thermogram of water in the porous network of the macroreticular resin 26OH using a heating rate of 0.5 K min^{-1}. 212

Figures A1.6 b. Melting thermogram of water in the porous network of the gel resin 458Cl using a heating rate of 0.5 K min^{-1}. 213

Figures A1.6 c. Melting thermogram of water in the porous network of the gel resin 958Cl using a heating rate of 0.5 K min^{-1}. 213

Figures A1.6 d. Melting thermogram of water in the porous network of the gel resin 410Cl using a heating rate of 0.5 K min^{-1}. 214

Figures A1.6 e. Melting thermogram of water in the porous network of the gel resin 402Cl using a heating rate of 0.5 K min^{-1}. 214

Figures A1.6 f. Melting thermogram of water in the porous network of the gel resin 402OH using a heating rate of 0.5 K min^{-1}. 215

Figures A1.6 g. Melting thermogram of water in the porous network of the macroreticular resin 15H using a heating rate of 0.5 K min^{-1}. 215

Figures A1.6 h. Melting thermogram of water in the porous network of the gel resin 120H using a heating rate of 0.5 K/min. 216

Figure A1.7. Calibration curve (logarithm scale) for the determination of total capacity of the Cl-resins (458Cl, 958Cl, 402Cl and 410Cl). Error bars represent the standard deviation for two repeated experiments. 217

Figure B1.1 a. Calibration curve of the macroreticular resin 958Cl in 1M NaOH solution. Error bars represent the standard deviation for two repeated experiments. 218

Figure B1.1 b. Calibration curve of the gel resin 402Cl in 1M NaOH solution. Error bars represent the standard deviation for two repeated experiments. 219

Figure B1.1 c. Calibration curve of the resins 458Cl, 958Cl, 410Cl and 402Cl in 0.1M NaOH solution. Error bars represent the standard deviation for two repeated experiments. 219

Figure B1.2. Catalytic performance on native and pre-treated 26OH. Reaction conditions: 10 mmol of tributyrin, 300 mmol of methanol, 500 rpm, 50 mg of catalyst, 333 K. Error bars represent the standard deviation for two repeated experiments..220

Chapter 1

Sustainable chemistry for biodiesel production

1.1. Introduction

Energy and environmental crises such as the depletion of petroleum reserves and the increase in greenhouses gases and air pollutants into the atmosphere are leading a historic transition to sustainable energy [1-3]. Both crises have increased clean energy demand and environmental policies contributing to replace fossil fuel with renewable resources such as biodiesel [1-3].

Biodiesel is not a novel concept. The use of vegetable oil as a fuel dates back to the 1900s when Rudolf Diesel designed a diesel engine capable of running on vegetable oil. He claimed *"The use of vegetable oils for engine fuels may seem insignificant today. But such oils may become over time as important as petroleum and the coal tar products of the present time"* [4]. Diesel's prediction is now becoming a reality. Biodiesel can be consumed as fuel in a modified engine or as a blend (ranging from 1 % to 20 % with the petroleum fuel) in a standard engine, reducing the carbon dioxide emissions produced [1-3, 5]. Biodiesel is considered to be carbon-neutral (zero carbon dioxide (CO_2) emissions) because feedstocks used for making it, such as soybean plants absorb as much carbon dioxide during the growth as they produce, as illustrated in **Figure 1.1** [6,7].

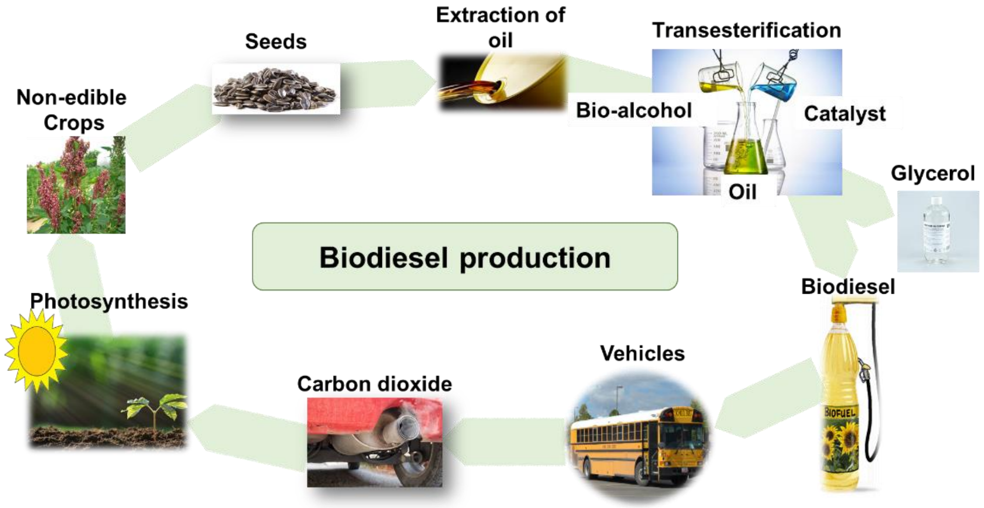

Figure 1.1. Scheme of the biodiesel production process: the oil obtained from non-edible crops is converted by transesterification into glycerol and biodiesel. Biodiesel used as biofuel for transportation and carbon dioxide emitted is taken up by plants during photosynthesis (Reproduced from [7]).

First-generation biodiesel, obtained from edible feedstocks (such as vegetable oil, sugar and corn), has shown three critical disadvantages: limited feedstock, high costs and only partial miscibility with petroleum fuel. Second-generation biodiesel is produced from sustainable non-edible feedstocks which are more economically competitive than edible ones [8, 9].

In general, vegetable oil contains 90-98 % triglycerides of its mass, a small portion of mono- and diglycerides and 1-5 % of free fatty acids (FFA) [10]. FFA are carboxylic acids of various chain length and number of double bonds while triglycerides, which are high molecular weight esters, are derived from the reaction between three fatty acids and glycerol. The oil cannot be used directly as fuel. Its high viscosity may damage the engine by producing coke deposits as a result of partial oil combustion [11]. Transesterification is a common approach to reduce the viscosity of the oil. It is noteworthy that FFA can be converted into biodiesel or fatty acid methyl esters via esterification using acid catalysts. Transesterification is a reversible reaction used to obtain a lower molecular weight ester from the reaction between a higher molecular weight ester and an alcohol. The stoichiometric reaction involves 1 mol of triglyceride and 3 mol of alcohol to give 3 mol of fatty acid esters (biodiesel) and 1 mol of glycerol, as illustrated in **Figure 1.2**.

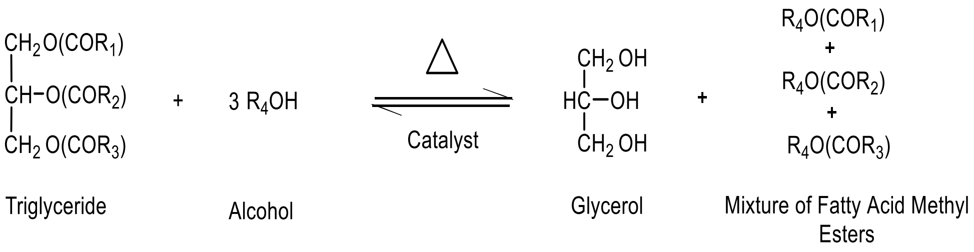

Figure 1.2. Generic reaction scheme for transesterification of triglyceride.

This reaction does not proceed spontaneously, and an excess of alcohol is used to drive the reaction to completion. Primary and secondary alcohols such as methanol, ethanol, propanol and butanol have been employed [12]. The solubility of triglycerides in alcohol is typically low, so sufficient stirring is required to ensure an excellent blend of the phases [5]. Adding solvents such as tetrahydrofuran and n-hexane improves the miscibility of the two phases [5, 13]. The reaction is conducted at the boiling temperature of the alcohol [14]. Thus, the methanolysis of oil is generally performed at 338 K, while ethanolysis and butanolysis are wider taken at higher temperatures; at 351 K and 390 K, respectively [15]. The molar ratio of alcohol: oil depends on the type of catalyst used in the reaction and varies between 30:1 and 6:1 [14].

A catalyst is a supplementary substance that, when added to a reaction, accelerates the reaction rate by reducing the activation energy barrier without consuming the catalyst itself and without modifying the reaction equilibrium position, which is under thermodynamic conditions

[16]. Catalyst recyclability and reduction of energy and waste fit most principles of Green Chemistry. In 1998, Paul Anastas developed the twelve principles of Green Chemistry, these principles are “design rules” to ensure chemical processes achieve a goal of sustainability in a chemical process. The twelve principles are illustrated in **Figure 1.3** [17].

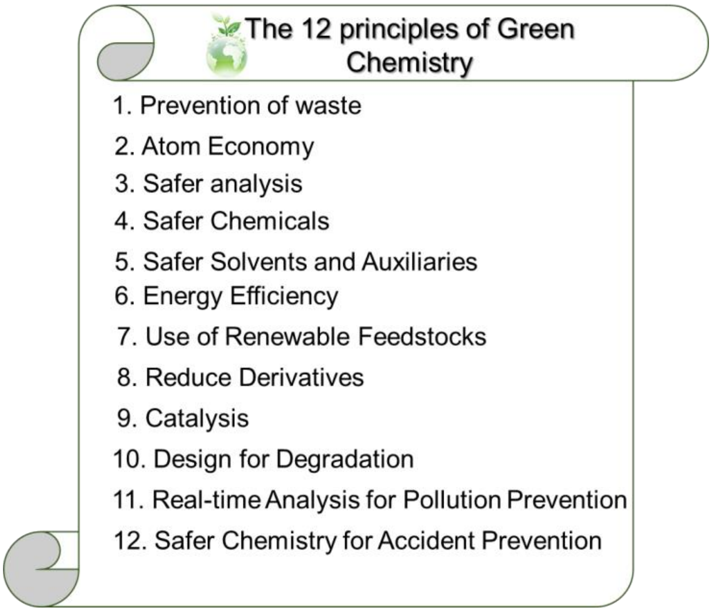

The 12 principles of Green Chemistry

1. Prevention of waste
2. Atom Economy
3. Safer analysis
4. Safer Chemicals
5. Safer Solvents and Auxiliaries
6. Energy Efficiency
7. Use of Renewable Feedstocks
8. Reduce Derivatives
9. Catalysis
10. Design for Degradation
11. Real-time Analysis for Pollution Prevention
12. Safer Chemistry for Accident Prevention

Figure 1.3. The twelve principles of the Green Chemistry (Reproduced from [17]).

The most common and useful homogeneous catalysts for biodiesel production are mineral acids and bases. In a homogeneous process, where catalyst and reactants are in the same phase, the active species and the mechanism are well-known, and the miscibility of the system improves with the stirring rate. Despite these advantages, the separation of reactants and catalyst, and catalyst recovery is challenging and expensive. A further concern is the environmental impact of handling and disposing of these catalysts, encouraging the use of safer, heterogeneous catalysts [18]. These catalysts are in a different phase to the reactants so that they can be readily separated, recovered and reused [19, 20]. However, they are sensitive to both poisoning and active site leaching, while the reaction mechanism is little understood. **Table 1.1** summarises the advantages and disadvantages of homogeneous and heterogeneous catalytic processes.

Table 1.1. Comparison of homogeneous and heterogeneous catalytic processes (Reproduced from [21]).

Homogeneous	Heterogeneous
Same phases	Different solid phase
Arduous separation	Easily separated
High-priced recycling	Easily regenerated and recycled
Frequently high rates	No as fast rates as homogeneous
Free diffusion	Limited diffusion
Resistance to poisons	Sensitivity to poisons
Elevated selectivity	Low selectivity
Short-lasting	Long-lasting
Mild conditions	Frequently high energy conditions
Well understood mechanism	Poorly understood mechanism

Heterogeneous catalysts are composed of porous inorganic or polymeric supports, which can be designed with either functional groups or metals. Catalyst pores can be considered as microscopic flow reactors [22]. The dispersion and density of active sites rely upon the total surface area of the material, which is higher than the external area because of the contribution from the surface of internal pores. The surface area can span between 1 and > 1000 $m^2 g^{-1}$ [23]. As the molecules go through the pores, the reaction takes place because of the interactions with the pore walls. Pore architecture of the catalyst plays an essential role in controlling diffusion, adsorption and selectivity of the reagents. Therefore, the pore size of the catalyst is crucial when a specific target product is desired. A given reaction depends on the pore structure and the size of products and reagents. Thus, catalyst pore architecture is named "shape selectivity". The concepts of porosity and surface area are described in **Chapter 2**.

1.1.1. Transesterification reaction catalysed by acid and base

Acids and bases can catalyze the transesterification reaction. The transesterification reaction catalysed by mineral acids such as sulfonic and sulfuric acids, achieve high yields in alkyl esters. However, the reaction rate is slow, and long experimental times, high temperatures (typically above 373 K) and alcohol-to-oil molar ratios of 30:1 or more are required [11, 14]. The mechanism of the acid-catalyzed reaction is illustrated in **Figure 1.4**.

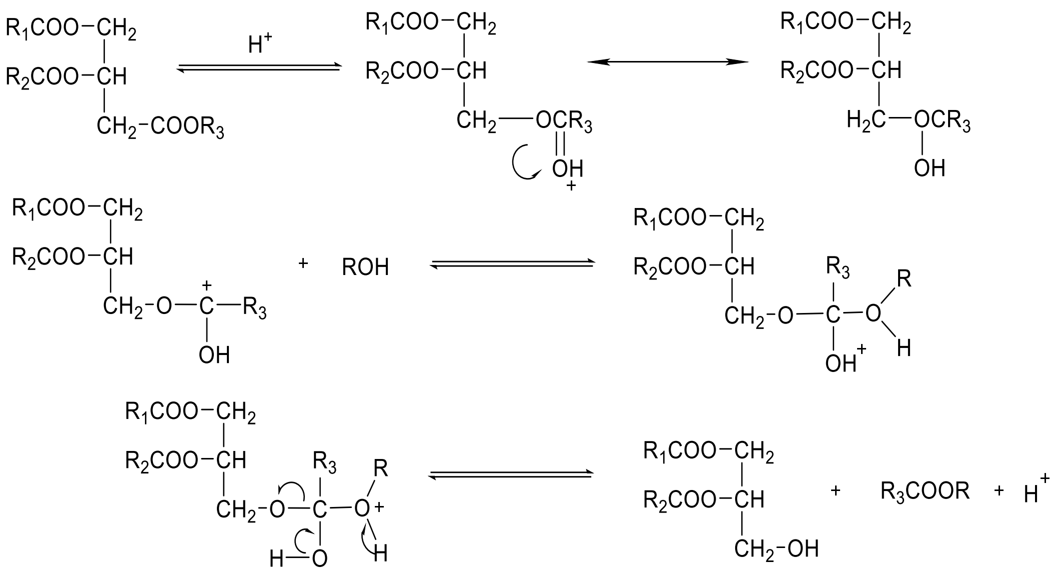

Figure 1.4. Acid-catalyzed transesterification reaction (Reproduced from [24]).

When the same reaction is base-catalyzed, it is faster, and an alcohol-to-oil molar ratio of only 6:1 is required [11, 14]. The mechanism of the base-catalyzed reaction is illustrated in **Figure 1.5**. However, side reactions may take place [11]. As aforementioned, vegetable oil consists of triglycerides and free fatty acids (FFA). In a base-catalyzed reaction, FFA are neutralized by alkali, forming the respective salts (soap) and water. This reaction is called saponification. The formation of FFA consumes and poisons the catalyst, reducing fatty acid methyl ester conversion and increasing the solution viscosity with chain length of acids [5, 14]. Two useful alternatives used to overcome this problem are the use of an oil with a lower FFA content (< 0.5 %) and a heterogeneous catalyst [25]. The heterogeneous catalyst may ensure salt-and methanol-free glycerol and allow quick catalyst recovery from the reaction system [26].

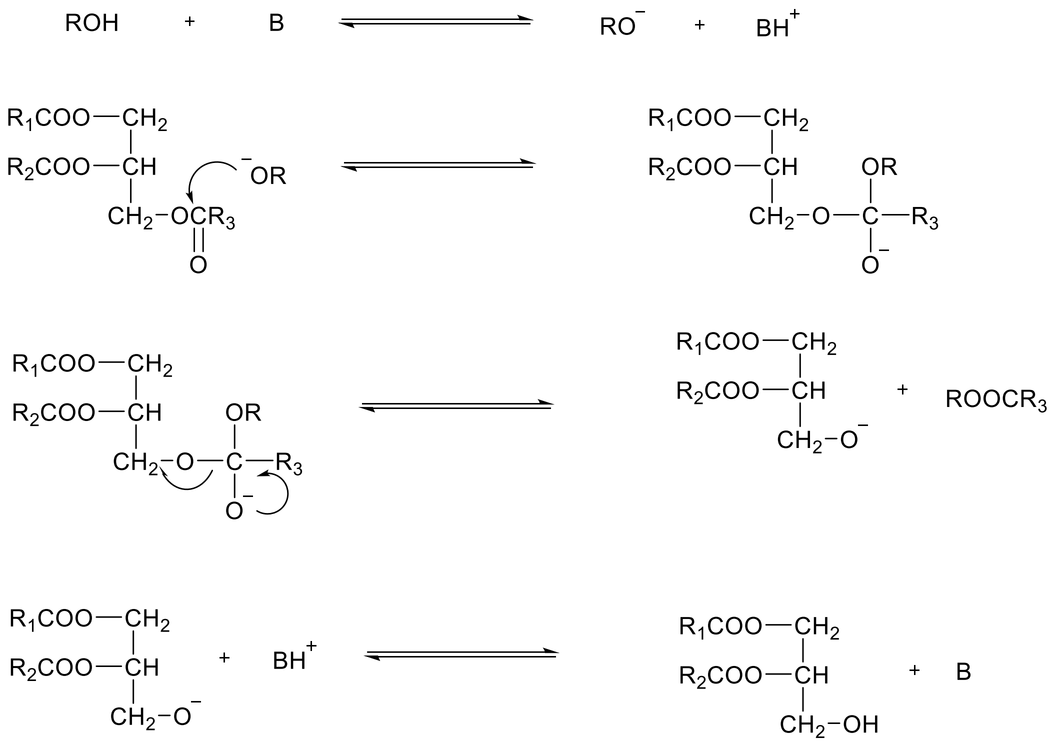

Figure 1.5. Base-catalyzed transesterification reaction (Reproduced from [24]).

The environmental impacts of handling and disposing of mineral acids and bases have encouraged the use of safer and reusable alternative heterogeneous catalysts. Several solid acidic and basic catalysts have been designed over the last fifty years [27]. Both basic and acidic groups have been incorporated into a diverse range of different solid materials such as silica-based materials (e.g. SBA-15 and MCM-41) and polymers (e.g. ion exchange resins (IERs)) by covalent and non-covalent binding [28]. Thus, the catalyst performance relies on the density and nature of the functional groups and supporting solid material.

Biodiesel production can be promoted by heterogeneous catalysts, such as ion exchange resins, heteropolyacid supported on silica, CaO and lipase [29, 30]. Heteropolyacid supported on silica, CaO and lipase require laborious preparation and expensive activity [31]. In contrast to these catalysts, ion exchange resins are compatible with many reactors types such as tubular packed-bed and batch reactors, and quickly recovered from the reactor by filtration due to their millimetre-sized beads [28]. Moreover, the functionalization of the resin is achieved by using different functional groups. Given the potential of ion exchange resins for catalytic applications, the next section of this thesis further explores these materials, their properties and the applications they have found use in.

1.2. Ion exchange resins

"*Corpora non agunt nisi fluida seu solute*", a popular Latin quotation of the Greek philosopher Aristotle (384-322 BC), can be translated into English as "solid compounds do not react unless in solution or if dissolved". This statement is not universally true; one exception of this rule is in ion exchange resins (IERs) [31]. Ion exchange resins consist of solid organic cross-linked polymer with uniform distributions of charged groups onto the surface, which can exchange their counter ions with the ions in solution. The exchange process is not permanent, and does not alter the structure of the material [32]. The ion exchange resins are synthesized as hard beads, as shown in **Figure 1.6** [33].

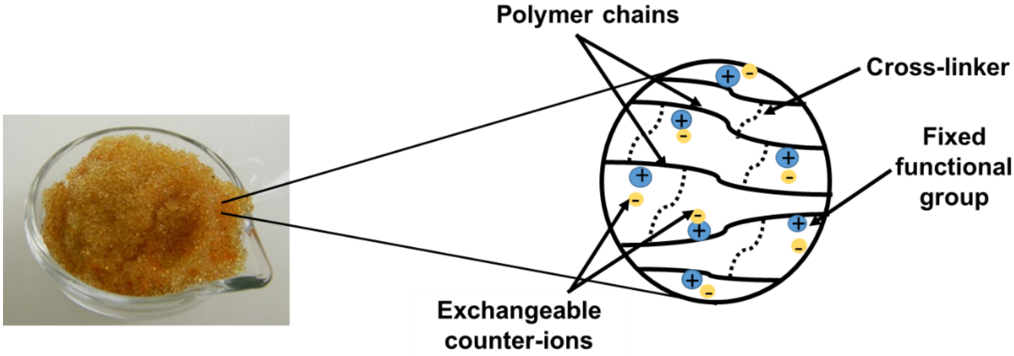

Figure 1.6. Illustration of an ion exchange resin.

The concept of ion exchange has been known and used since ancient times. The earliest reference comes from Exodus 15 (verses 23-25), where Moses "transforms" bitter water into drinkable water [34]. There are a number of naturally occurring ion exchange materials, such as woods, clays and zeolite [35].

In 1935, the first resin backbone was synthesised using phenolic condensation and then subsequently functionalised with both sulfonic acid or amines groups, giving rise to two classes of the exchanger; cationic and anionic [32, 33]. These polycondensation resins have been partially replaced in chemical processes by radical polymerisation resins [32]. The polymer resin synthesis involves two steps: manufacture of the cross-linked polymer followed by functionalisation. In short, the copolymerisation reaction takes place between a monomer (styrene (ST) or/and methacrylic acid (MAA)) and a crosslinking co-monomer (divinyl benzene (DVB)) in the presence of an initiator and a porogenic agent. Thus, matrices made of styrene-divinyl benzene and methacrylic acid-divinyl benzene copolymer beads are termed ST-DVB and MA-DVB, respectively. **Figures 1.7 a** and **b** illustrate the copolymerisation reaction. In commercial IERs, the DVB content tends to vary between 8 % and 12 % [27].

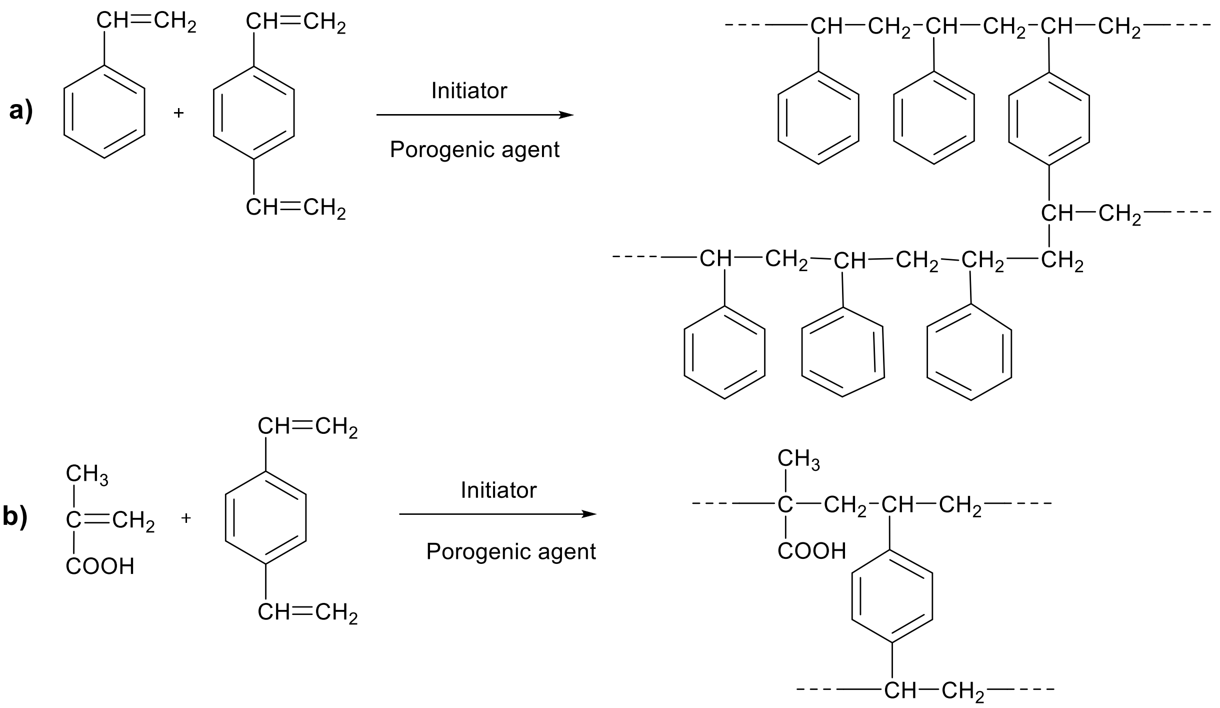

Figure 1.7. Scheme of the polymerisation of (**a**) styrene (ST) and (**b**) methacrylic acid (MA) with divinylbenzene (DVB) for the copolymer reaction (Reproduced from [36]).

The morphologies of IERs are generally classified as either gel or macroreticular. Gel resins have a low degree of crosslinking, and the porosity is visible only in a suitable swelling medium. Resins swell when in contact with a solvent, generating temporary voids [37]. As a result of this permanent porosity, the molecules have free accessibility to the resin network, and their catalytic performance relies on the type of solvent used in reaction [27, 37]. This is known as latent porosity [32]. When dry, gel-types exhibit very low surface area <10 $m^2 g^{-1}$ [37].
However, macroreticular resins have higher degree of crosslinking, and exhibit macropores, ensuring ready accessibility to the molecules without swelling [32, 33, 37]. This permanent porosity is introduced by using a porogenic agent during the copolymerisation stage [38]. The macroreticular resin consists of macropores and embedded microgel particles, as illustrated in **Figure 1.8** [18, 37]. The microgel particles swell moderately with a polar solvent, while the size of the macropores do not vary significantly in the medium (**Figure 1.8**) [37]. Thus, macroreticular resins exhibit limited swelling behaviour compared to gel resins, and therefore their catalytic performance is independent of the type of solvent [27].

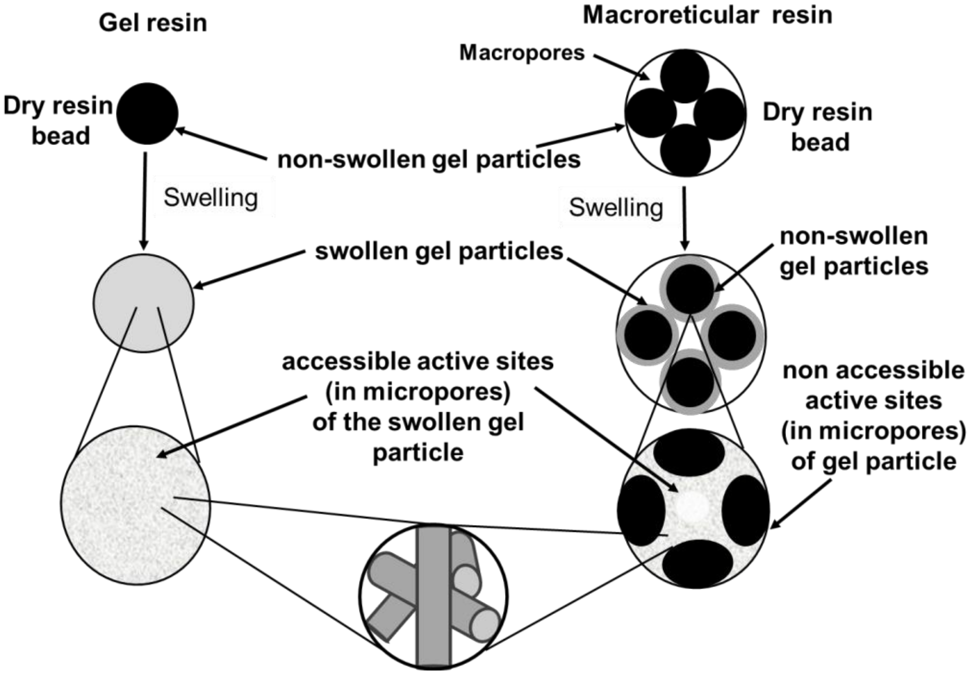

Figure 1.8. Morphologies of gel and macroreticular resins (Reproduced from [37]).

The textural properties of resins in the dry state can be measured using mercury intrusion porosimetry [39] and nitrogen porosimetry [40]. Alternatively, when the porous material is in a wet state, Inverse Size Exclusion Chromatography (ISEC) [39, 41, 42], Nuclear magnetic resonance (NMR) cryoporometry [43] and thermoporometry [42] can be used. In this work, the porosity and the specific surface area have been measuring using nitrogen porosimetry and thermoporometry, which are described in detail in **Chapter 2**.

The polymeric backbone can be functionalised with different groups to give [33]:

Strong acid cation (SAC) exchange resins: their structure is based on a ST-DVB matrix with negatively charged sulfonic groups fixed onto its surface, which can exchange the counter-ions, such as hydrogen ions (H^+). The incorporation of the sulfonic groups is conducted by using sulfuric acid, sulfuric trioxide and chlorosulfonic acid as sulfonating acids, as shown in **Figure 1.9** [32].

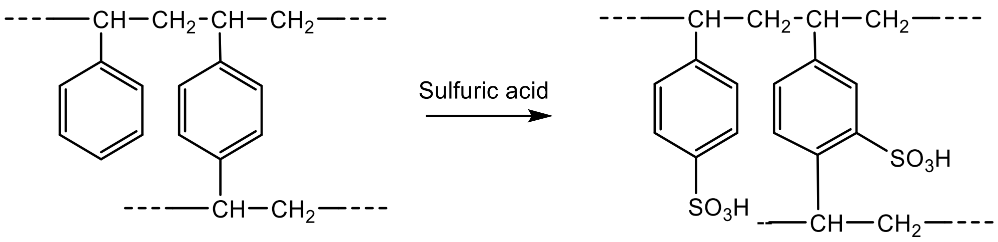

Figure 1.9. Reaction scheme of SAC functionalisation (Reproduced from [33]).

SAC exchange resins are highly ionised and show Brönsted acidity in the protonic form (H^+) and Lewis acidity in the metallic form (Na^+) [44, 45]. These resins, in their hydrogen form, can undergo the hydrolysis of sulfonic groups at temperatures above 473 K [44]. The sulfoalkylated resins show superior thermal stability because of the introduction of the electron withdrawing group of the phenyl but lower acidity when the sulfonic group is directly bound to the phenyl ring [44]. SAC affinity of the sulfonic groups for ions shows the following trend [46]:

$$Pb^{2+} > Ca^{2+} > Mg^{2+} > Na^+ > H^+$$

The chemical resemblance of these exchangers with strong acids, such as sulfonic acid, makes them valid alternatives for the same catalytic processes [8].

Weak acid cation (WAC) exchange resins: exhibit negatively charged carboxylic groups COO^- with exchangeable counterions such as the hydrogen ion (H^+). The incorporation of carboxylic groups occurs using the polymerisation between divinylbenzene and acrylic acid or methacrylic acid, respectively [33].
The WAC exchange resin dissociation constant (pK_a) is between 4 and 6 [47]. Thus, their functional groups are weakly ionised in solution and have restricted capacity in basic pH [45]. Hence, separation processes have mainly exploited these resins [8]. For this work, further details of WBA resins are omitted.

Strong base anion (SBA) exchange resins: are typically based on either ST-DVB or MA-DVB matrices. These copolymers are functionalised using two different routes. On the one hand, ST-DVB copolymer can be successfully functionalised via chloromethylation, followed by amination to introduce positively charged groups. The introduction of the chloromethyl groups occurs by using chloromethyl methyl ether or bis chloromethyl ether as alkylating reagents and a Friedel-Crafts catalyst, such as stannic chloride ($SnCl_4$), as illustrated in **Figure 1.10** [48].

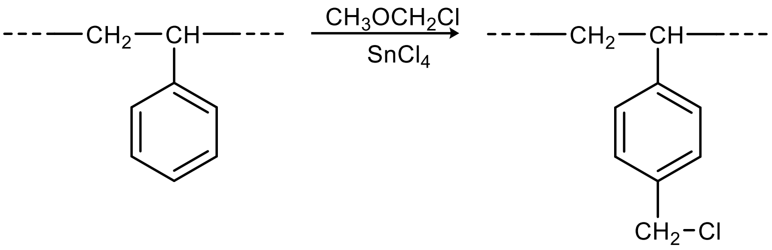

Figure 1.10. Introduction of chloromethyl group into the copolymer using chloromethyl methyl ether (Reproduced [48]).

However, these alkylating reagents are carcinogenic substances and their use has been regulated since 1967 [49]. However, Ezzeldin *et al.* reported an alternative synthesis [48]. In this route, vinyl benzyl chloride is used as starting monomer to generate the vinylbenzene chloride divinylbenzene copolymer [48]. Amination with precursors, trimethylamine and dimethylethanolamine gives SBA type I and SBA type II, respectively (**Figure 1.11**) [33].

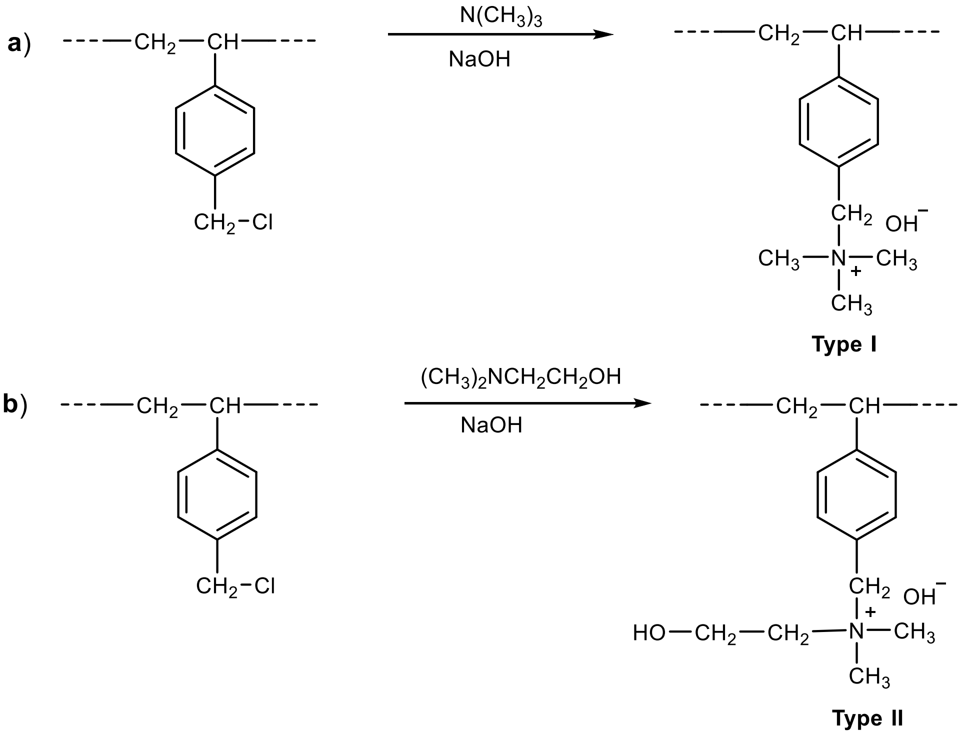

Figure 1.11. Amino functionalization of the vinylbenzene chloride divinylbenzene copolymer using (**a**) trimethylamine and (**b**) dimethylethanolamine to yield Type I and Type II SBA exchange resins, respectively (Reproduced from [48, 50]).

On the other hand, the MA-DVB copolymer reacts with dimethylaminopropylamine to generate a basic exchanger. Then, this reacts with methyl chloride to yield the quaternary salt (**Figure 1.12**) [51].

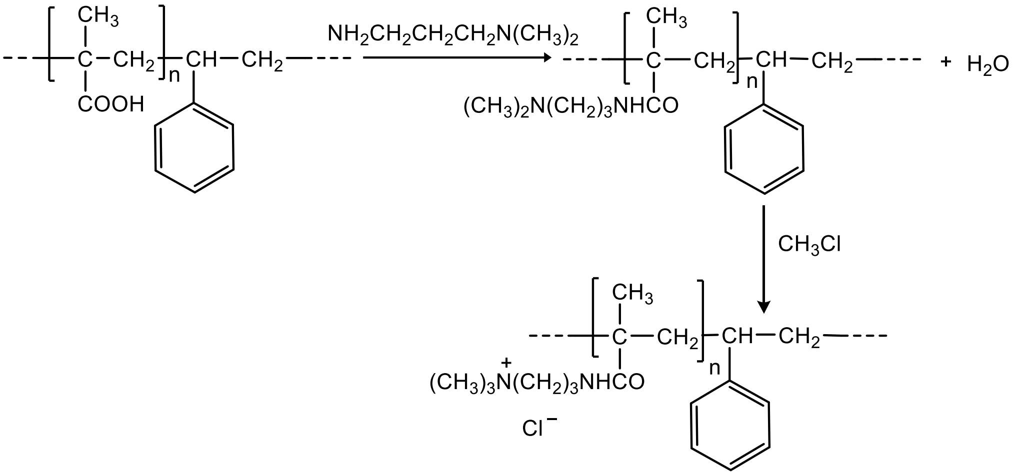

Figure 1.12. Functionalization reaction of MA-DVB matrix to yield SBA exchange resins. **Step 1:** Amination of the copolymer with dimethylaminopropylamine; **Step 2:** Formation of the salt using methyl chloride [51].

SBA type II shows a lower base strength and higher chemical stability than SBA type I functionality [32, 33]. SBA exchange resins are mostly provided in Cl-form because of their high stability [51, 52]. They can be converted into another ionic form by soaking the resin in a solution of the salt precursor [52]. In the catalytic field, SBA exchange resins are used mostly in OH ionic form [53]. However, the quaternary salt of SBA resins in OH ionic form can be prone to thermal decomposition. Depending on the type of functionality, the decomposition occurs through different pathways [54]. This decomposition is catalysed by OH^- and occurs at temperatures above 333 K [55, 56]. The decomposition of the type I SBA resins is illustrated in **Figure 1.13**.

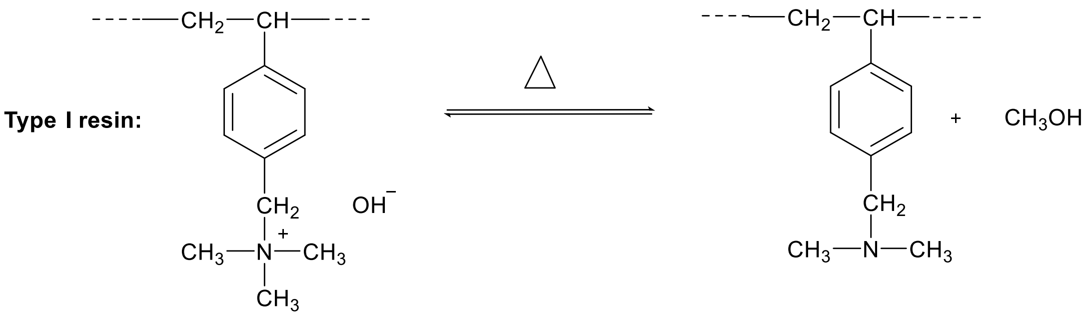

Figure 1.13. Decomposition of the quaternary ammonium Type I (Reproduced [54]).

Another decomposition of the Type I quaternary ammonium reported in the literature is thermal decomposition via Hofmann elimination [54]. The Hofmann elimination destroys resin functionality, forming a trialkyl amine and an olefin, as illustrated in **Figure 1.14** [56].

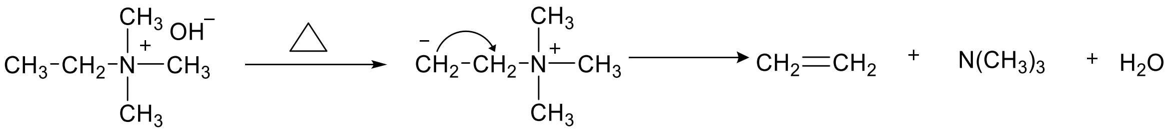

Figure 1.14. Decomposition of the quaternary ammonium (Type I) via Hofmann elimination or *β*-elimination (Reproduced from [56]).

The decomposition of the quaternary ammonium hydroxide via Hofmann elimination has been reported as E2 elimination and depends on the base strength and the substrate (quaternary ammonium), where the rate-determining step is *bimolecular* [57].

Type II SBA resins can overgo three decompositions of the quaternary ammonium, forming tertiary amine and alcohols [54]. These decompositions are illustrated in **Figure 1.15** [54].

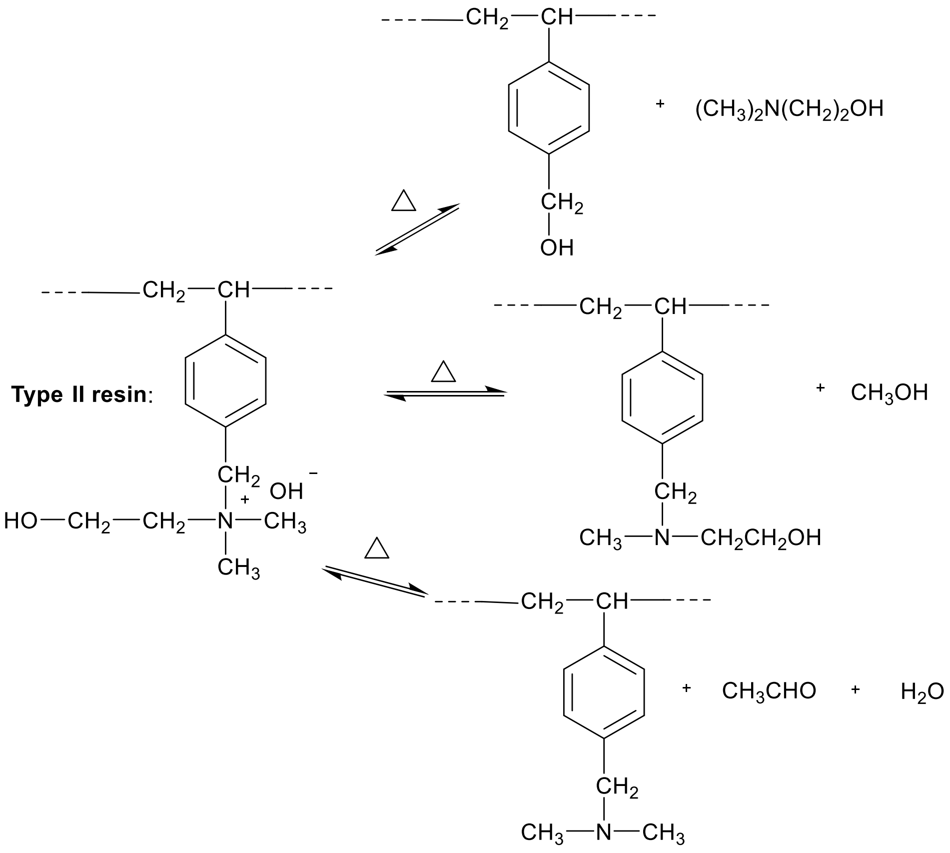

Figure 1.15. Decomposition of the quaternary ammonium Type II (Reproduced from [54]).

To overcome the degradation of the functional group, spacer alkene chains such as butylene or heptylene groups can be designed between the benzene ring and the quaternary ammonium to increase the thermal stability of the exchanger [55]. SBA exchange resins can perform at temperatures up to 333 K [33, 55]. The use of different counter-ions can help to circumvent these thermal limitations. The SBA affinity towards counter-ions shows the following trend [46]:

$$SO_4^{2-} > NO_3^- > Cl^- > HCO_3^- > OH^- > F^-$$

Another aspect that affects the decomposition of the quaternary ammonium is the stirring rate. Decomposition was shown to increase as the stirring rate increased until a plateau was reached [58]. As with SCA exchange resins, the chemical properties of SBA exchangers closely resemble those of a strong base, such as NaOH. This makes them good substitutes for base-catalysed processes [8].

Weak base anion (WBA) exchange resins: can be functionalised with primary ($-NH_2$), secondary (=NH) and tertiary (≡N) amines, which are non-exchangeable groups [59]. The dissociation degree of the weak base is strongly affected by the pH range because the groups will only partially ionize in solution [33]. Similar to WAC exchange resins, the working capacity of WBA exchange resins relies on the pH. As a consequence, these resins exhibit a reduced role in acidic solution ($pH < 7$) [45]. Owing to their weak strength, these resins have found applications in separation processes [27]. Further details of WBA resins are beyond the scope of this thesis.

The choice of using strong and acid resins relies on the capacity of these to emulate the homogeneous catalysts in the same reaction and replace their use where feasible. For the sake of clarity, a summary of IERs and their functional groups is provided in **Figure 1.16**.

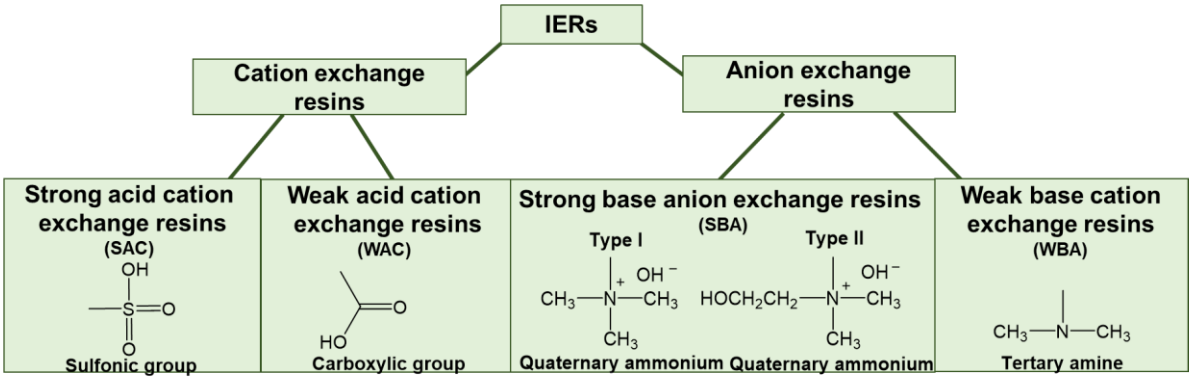

Figure 1.16. Classification of IERs based on their basic and acidic functional groups.

1.2.1. Properties of ion exchange resins

The different chemical and physical features of IERs affect their performance and use in the real world. Their primary features are discussed here.

Appearance: Most IERs are synthesized as hard beads with a narrow particle size distribution between 0.3 mm and 1.2 mm (50-16 mesh) [33].

Total capacity: This is the total number of functional sites grafted onto the polymeric backbone, which depends on the degree of functionalization of the final copolymer [50]. The total capacity (TC) is expressed as milliequivalents per gram of dry resin (**Equation 1.1**) [33]. The capacity can be measured microcalorimetrically by titration using appropriate gases [60]. However, in this work, it has been measured by elemental analysis.

Operating capacity: This is the exchangeable groups attached onto the polymeric resin. In general, it is defined as the number of milliequivalents over either weight or volume of dry resin (**Equation 1.1**) [33]. The operating capacity (OC) can be measured by back titration of acid or base.

$$\text{Capacity / meq g}^{-1} = \frac{\text{milliequivalents}}{\text{mass of dry resin}} \qquad \textbf{Equation 1.1}$$

Chemical stability: Stability is a limiting factor when polymeric catalysts are used in experimental applications [44]. Most polymers undergo significant degradation when exposed to strong oxidizing agents, such as nitric acid and chromic acid. These agents can attack resins, causing deterioration of the polymers.

Thermal stability: Thermal stability is a critical factor when considering the operation at temperature of chemical reactions. Resins are subject to thermal degradation when overheated above their limit temperatures, resulting in the loss of functional groups and, therefore, loss of capacity. Anion exchange resins can be operated up to 333 K while cation exchange resins up to 423 K [33, 54]. Thermal stability has been studied in this work by thermal gravimetric and differential scanning analysis, as described in **Chapter 2**.

Swelling: It occurs when a dry resin is in contact with a medium. Resins absorb liquids until they reach equilibrium. Thus, it induces a rise of beads volume. This phenomenon occurs at a macro-scale and can be measured using equation (**Equation 1.2**) [37].

$$\text{Swelling degree / \%} = \frac{V - V_0}{V_0} \qquad \textbf{Equation 1.2}$$

where V and V_0 are the volume of the beads after swelling and the volume of the desiccant beads, respectively.

When the polymeric resin is in contact with a mixture of different components it tends to absorb each component to a different extent. Therefore, the swelling is the total result of the partition of the components in the polymeric resin and the liquid phase [61]. The adsorption causes the resin volume to increase the flexible and dynamic structure of the resin. The swelling extent depends on the total content of DVB monomer or crosslinking degree (expressed in %), the nature and charge of counter-ions, the liquid polarity, temperature and polymer matrix (polystyrene or polyacrylic) [32, 37]. An exhaustive study of the swelling behaviour has been reported [37]. There are some general rules based on empirical observations. For example, such as the lower the crosslinking degree, the more flexible the matrix. Also, a highly concentrated solution decreases the swelling capacity of the resin because of the decrease in osmotic pressure gradient [27, 32].

Morphological properties: The applications of porous materials depend on the pore characteristics, so it is crucial to have complete characterisation of these systems, such as pore size and volume, specific surface area and how these affect the diffusion of reagents through the pores [62]. The porosity plays a crucial role in the exchange and diffusion process. Pores can be classified based on size, geometry and accessibility, as shown in **Figure 1.17**. These are discussed in detail in **Chapter 2**.

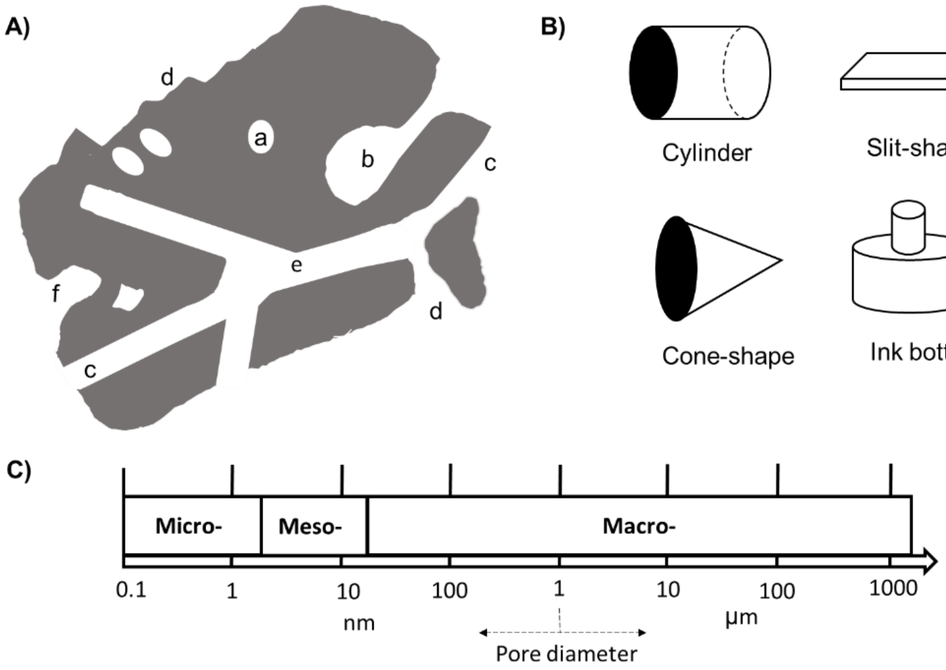

Figure 1.17. Pore classification based upon (**A**) accessibility: closed pores (**a**); (**b**) and (**f**) pores open in one direction; (**c**), (**d**) and (**g**) pores open through different directions; (**e**) open pore at two ends [63]; (**B**) the pore shapes [64] and (**C**) pore diameter [63].

Chemical reactions, which occur within the pores of solid catalysts, depend on the pore size and intraparticle diffusion [27]. The overall rate of the reaction is the sum of individual rates of the molecules travelling through the pores and the rate of chemical reaction [27]. Mechanisms of heterogeneous catalytic reactions for a given reaction R→P has seven steps as illustrated in **Figure 1.18**. Mechanisms for most heterogeneous catalysts, including IERs, are still unclear [8]. Solving this issue requires the development of more advanced tailor-made catalysts for application in specific reactions to achieve high conversion, selectivity and high rates.

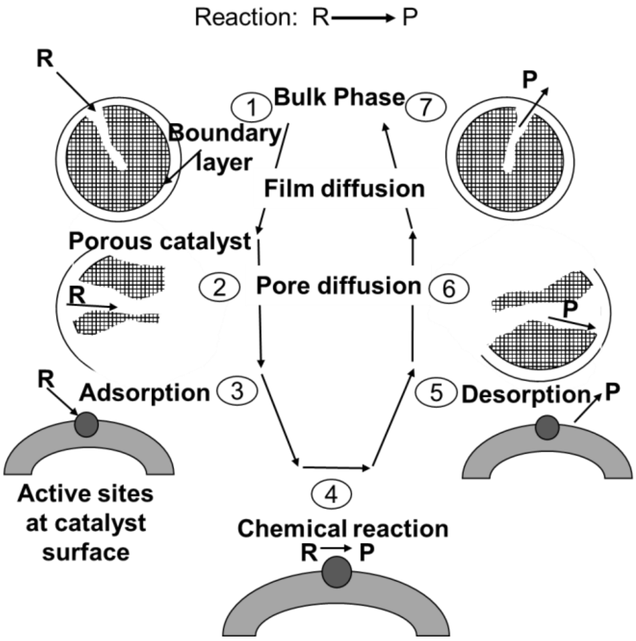

Figure 1.18. Heterogeneous catalytic mechanism (Reproduced from [63]).

Diffusion of molecules from bulk to surface and within the pores of porous catalysts are termed external diffusion and internal diffusion, respectively. These aspects are described in detail in **Chapter 4** and **Chapter 5**, respectively.

Another remarkable feature of porous material is their enhanced surface area, which allows the active sites to be dispersed into the porous material [27]. Hence, the porosity and the dispersion of the active sites affect the overall rate of reactions. Moreover, its surface area in the dry state varies between 50 and 1000 $m^2\ g^{-1}$ [37].

1.2.2. Applications of ion-exchange resins

IERs which are considered good candidates for their properties are widely involved in numerous fields such as water treatment [33, 48, 65], medicine (e.g. drug delivery) [32, 45], hydro-metallurgy [13, 32, 33], food processing [32, 33] and catalysis [13, 66].

1.2.2.1. Water treatment

The water hardness associated with the presence of calcium (Ca^{2+}) and magnesium ions (Mg^{2+}) in water, is the leading cause of obstruction in pipes. To overcome this problem, the less soluble ions, divalent calcium and magnesium ions present must be exchanged with more soluble sodium ions. This process is called softening. Softening uses cation exchange resins with monovalent sodium ions, which are termed as Na-form resins [33]. Another vital process, which involves the use of IERs, is demineralisation.

All cations and anions in solution are replaced by hydrogen (H^+) and hydroxide ions (OH^-) from an H-form cation exchange resins and OH-form anion exchange resins , respectively, as illustrated in **Figure 1.19**.

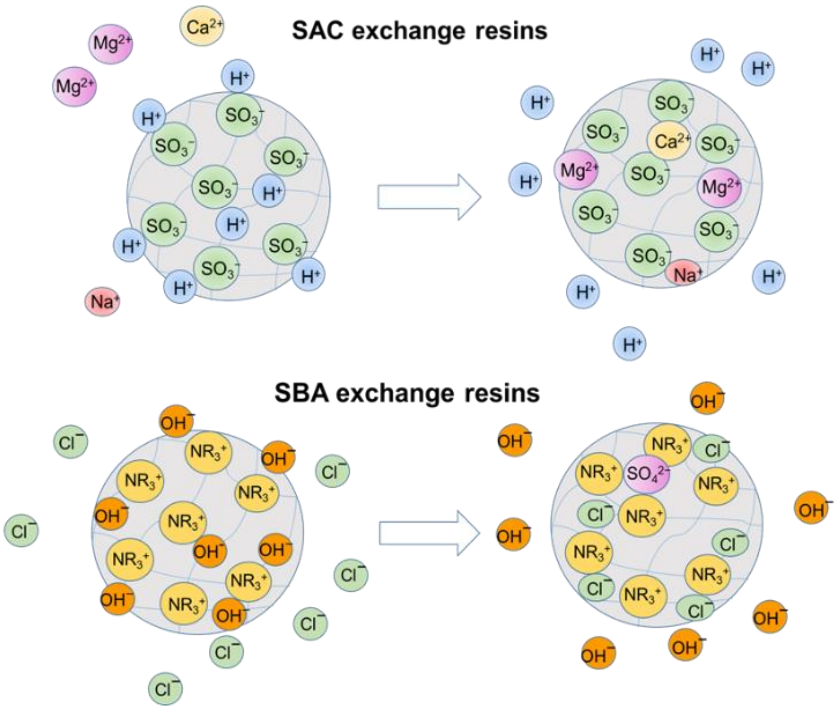

Figure 1.19. Schematic representation of SAC (strong acidic cation) and SBA (strong basic anion) exchange resin beads before and after the demineralisation process.

1.2.2.2. Pharmaceutical applications

IERs are well-established as drug delivery systems, and the numerous patents are proof of the ability of these materials to release pharmaceutical compounds into the human body [67-69]. The release of drug resinate from the resin occurs by exchanging ions with the gastrointestinal fluid, as illustrated in **Figure 1.20** [45].

$$\text{Resin}^{-}\ \text{Drug}^{+} + X^{+} \rightarrow \text{Resin}^{-}\cdots X^{+} + \text{Drug}^{+}$$
$$\text{Resin}^{+}\ \text{Drug}^{-} + X^{-} \rightarrow \text{Resin}^{+}\cdots X^{-} + \text{Drug}^{-}$$

Figure 1.20. Reaction between the drug resinate and the ions in the gastrointestinal environment (Reproduced from [45]).

The use of drug resinate allows medicine to be released gradually, avoiding dose dumping. The drug amount on IERs depends on selectivity of IER functional groups, the drug concentration of the loading solution and the competing ions present in the same solution, the type of solvent and the drug size [70].

1.2.2.3. Hydrometallurgy: recovery of gold and rare earth metals

An unrestrained expansion of the mining market has been foreseen for the next thirty years [71]. In 2006, gold extraction involving the use of chemicals such as cyanide, which accounted for 18 % of the total cyanide production, was one of the most used processes for gold recovery [72]. **Figure 1.21** shows how gold reacts with cyanide ions to form a water soluble complex, which can be extracted [73].

$$4Au + O_2 + 2H_2O + 8NaCN \rightarrow 4Na[Au(CN)_2] + 4NaOH$$

Figure 1.21. Cyanidation reaction allows converting gold ore into a more soluble complex.

However, the selectivity of the process depends on other metals present in the system, by restrictive pH range (pH > 7). Also, its storage process, as $HCN_{(l)}$ is not easy because of its high volatility, as depicted in **Figure 1.22** [73].

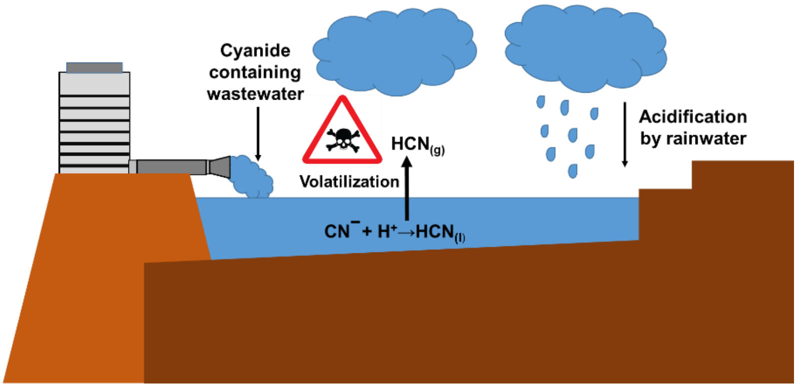

Figure 1.22. Schematic drawing of the volatilisation process of cyanuric acid (Reproduced from [73]).

Environmental protection agency (EPA) claimed some restrictions that must be taken to deal with the volatilisation process of cyanuric acid and therefore alternative routes have been investigated [74]. Due to the lack of pH dependency, SBA exchange resins seem to be promising adsorbents for gold across the entire pH range, avoiding the use of the dangerous cyanuric acid (HCN) [75]. Moreover, IERs acting as chelating agents for the recovery of rare earth elements (REE) have attracted the interest of researchers and the industry for their applicability in high technological-manufacturing products (e.g. television, smartphone, fluorescent and light emitted diode (LED), cameras and computers) [75-77].

1.2.2.4. Ion exchange and adsorbent resins for the food market

A wide variety of resins are used in the food industry to obtain performance-improvement of products. Resolution ResAP (2004) defined the requirements for IERs to be used in food processing [78]. Hence, IERs must be prepared according to the certified Quality Assurance System using substances and conditions listed in "Technical document Nº1- List of substances to avoid release of dangerous substances to foodstuffs, which may have an impact on the human food chain [78]. For instance, the SBA exchange resin, DOWEX^{TM}, and the SAC exchange resin, DOWEX 88, have been involved in the fructose Corn Syrup process [79]. DOWEX MONOSPHERE^{TM} 99 K in potassium form has been used in chromatography to achieve sugar separation from salts and colour in the beet sugar softening process which are forwarded to the animal feedstock, reducing operating costs [79].

The resins also play a vital role as an adsorbent in juice decolourisation and protein haze stabilisation. For example, DOWEX OPTIPORE^{TM} SD-2 is used as adsorbent of undesirable flavours, colours, and it is highly efficient in the removal of 5-(hydroxymethyl)furfural (HMF) [79].

1.2.2.5. Ion exchange resins as catalysts

The use of IERs as catalysts consists of approximately 10-15 % of the total industrial processes [27]. Strong anion and cation exchange resins are functionalised with strong basic, and acidic group, respectively. These resins emulated homogeneous catalysts, bases and acids, promoting the same types of reaction [27]. As described in **Section 1.2**, IERs are available on the market as beads, which are easy to handle, regenerate, are separated from the reagents readily and easily disposed [27]. As with other heterogeneous catalysts, it is possible to tailor physical and chemical properties for target reactions [27].

IERs exhibit higher production costs than homogeneous catalysts [27]. Compared to other heterogeneous catalysts that are designed as a fine powder, IERs are made as cheap hard beads [27, 28]. The other heterogeneous catalysts require laborious preparation, costly activation and catalyst separation may block the reactor [27, 31]. The benefits of using bead-shaped materials in catalysis are multiple, but the most important one is that the beads can be easily recovered. IER porosity consists of macroporous and micropores. The former are large channels which allow reactant diffusion while the latter are small channels with a high density of attached active sites [27]. In catalysis, coexistence of macro- and micropores in the resin is a preferable choice to facilitate the reactant diffusion through the pores and their accessibility of the active sites into micropores [27]. Consequently, the rates of molecules passing through the polymer pores affect the overall rate of the chemical process [27]. The IER reaction rates for aqueous reactions are similar to their homogeneous counterparts, pursuing the Langmuir-Hinshelwood (L-H) or Rideal-Eley (R-E) mechanisms [27]. The resins, like other catalysts such as nanocarbon tubes, need to be carefully handled during pre-treatment [80]. In the case of IERs, pre-treatment involves water removal or IER activation from one ionic form to another.

Their widespread use has been limited by three key factors: scarcity of characterisation in the catalysis field, low thermal stability and deactivation of the functional groups [28]. The understanding of the reaction mechanism for a heterogeneous process is challenging and requires further investigation on the characterisation of these materials for understanding their behaviour in the liquid phase. Both strong base (OH-form) and acid (H-form) exchangers exhibit considerable degradation of their attached functional groups at temperatures above 333 K and 393 K, respectively. As a result, these exchangers, in those forms, can only be used in a limited number of reactions. The use of different counterions can help to circumvent these thermal limitations. Barbaro and Liguori have recently reported a complete review, which enlists the reactions catalysed by IERs [28]. These reactions are reported in **Table 1.2**.

Table 1.2. Reactions catalysed by IERs.

Cation resin catalysed reaction	Anion resin catalysed reaction
Alkylation [18]	Transesterification [18]
Olefin isomerization and oligomerization [18]	Aldolization and ketalization [80]
Acylation [18]	Esterification [27]
Hydration and dehydration of olefins [18]	Hydrolysis [27]
Aldolization and ketalization [80]	Condensation [27]
Esterification [18]	Cyclization [27]
Transesterification [18]	Acylation [27]
Amidation [27]	
Cyclization [27]	
Carbonylation [27]	

As can be seen in **Table 1.2**, the existing literature of the catalytic performance over acid exchangers has been extensively investigated. At the same time, it presents a gap concerning the role of base exchangers in catalysis. This thesis reports on the use of ion exchange resins in the base-catalysed transesterification reactions.

1.3. Literature review of transesterification reaction over ion exchange resins

As pointed out by Harmer *et al.*, IERs have been successfully used as catalysts for esterification and transesterification reactions since 1995, minimising the environmental impact of the wastes [18]. Transesterification reactions produce a lower molecular weight ester from the reaction of a higher molecular weight ester with an alcohol, as illustrated in **Figure 1.23**.

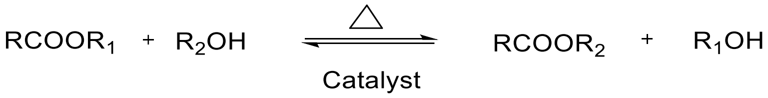

Figure 1.23. Transesterification reaction between a higher molecular weight ester and an alcohol to obtain a lower molecular weight ester (R_1 and R_2 are alkyl groups).

The transesterification reaction can be catalysed by either acid or base ion exchange resins [81-85]. He *et al.* have investigated both SAC exchange resins (NKC-9) and SBA exchange resins (D261) used in the production of biodiesel from soybean oil and methanol [13]. The use of these catalysts resulted in more easily separable products and less corrosion of the reactor used [13]. Shibasaki-Kitakawa *et al.* used anion and cation exchange resins for the transesterification of triolein [84]. They have found that anion exchange resins with low cross-linking and smaller particle size obtained higher reaction rates and conversion [84]. The conversion was comparable with homogeneous counterparts without promoting the saponification reaction of FFA [84]. Van de Steene *et al.* have investigated macroreticular and gel resins (Lewatit K2640, Lewatit K2629, Amberlyst 15H and Lewatit K1221) for the transesterification of ethyl acetate with methanol and have found that the swelling of the resins controlled the accessibility of the reacting species to active sites [37]. Hence, gel resins brought in contact with a swelling medium such as methanol seem to be more productive than the macroreticular counterpart [37]. Despite the positive results reported earlier, Vicente *et al.* have reported low conversion (< 1 %) for the transesterification of sunflower oil with methanol catalysed by SBA (Amberlyst A26OH and Amberlyst A27) and SAC (Amberlyst 15H) exchange resins [13]. Shibasaki-Kitakawa *et al.* have also reported two different mechanisms for the transesterification catalysed by an SAC ($R(H^+)$) and an SBA ($R(OH^-)$) exchange resin, as illustrated in **Figures 1.24 a** and **b**, respectively [84].

Y, A, F and D represent triglyceride, alcohol, fatty acid alkyl ester and diglyceride, respectively.

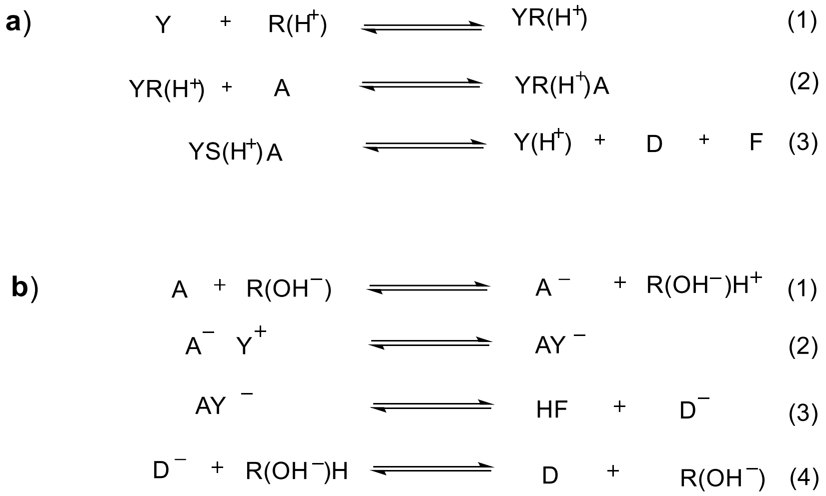

Figure 1.24. Mechanism of transesterification over (**a**) a cation exchange resin and (**b**) an anion exchange resin where Y, A, F and D are triglyceride, alcohol, fatty acid alkyl ester and diglyceride, respectively (Reproduced from [84]).

The first step of transesterification catalysed by the solid acid catalyst SAC ($R(H^+)$) involves the adsorption of triglyceride (Y) onto the active sites of the catalyst (**Figure 1.24 a**) [84]. Monoglyceride is obtained from the conversion of diglyceride following step (3).

However, anion exchange resins show a different mechanism in which the adsorption of the alcohol over the resin is the first step of the mechanism, as shown in **Figure 1.24 b** [84]. This mechanism occurs because of the higher adsorption energy for alcohol than the ester [60].

Polymeric resins brought into contact with a mixture of different components tend to absorb each component to a different extent. The different affinities of the polymeric resins for the reagents and products may damage the catalytic performance of the resins in terms of selectivity and conversion [60].

1.3.1 Literature review of transesterification of tributyrin catalysed via solid acid and base catalysts

Vegetable oils contain a distribution of triglycerides ranging from C_4 to C_{24} with different degrees of saturation and branching, and in varying proportion [86, 87]. The evaluation of the catalytic activity for their final products and intermediates of long chain fatty acids requires an on-column injector gas-chromatography (GC) equipment [86]. However, the transesterification reaction of small triglycerides, such as tributyrin ($C_{15}H_{26}O_6$) forms di- and mono- intermediates and target products, which can be detected by conventional GC equipment. Tributyrin has generally been used to test the performance of a catalyst for the transterification reaction with an alcohol, such as methanol [81, 84]. The reaction of tributyrin (TB) with methanol (MeOH,

CH_3OH) involves the formation of intermediates, dibutyrin and monobutyrin, in the first and second steps, respectively. In the final step, MB reacts with an alcohol to form methyl butyrate (MB, $C_5H_{10}O_2$) or biodiesel and, glycerol (GLY, $C_3H_8O_3$), as shown in **Figure 1.25**.

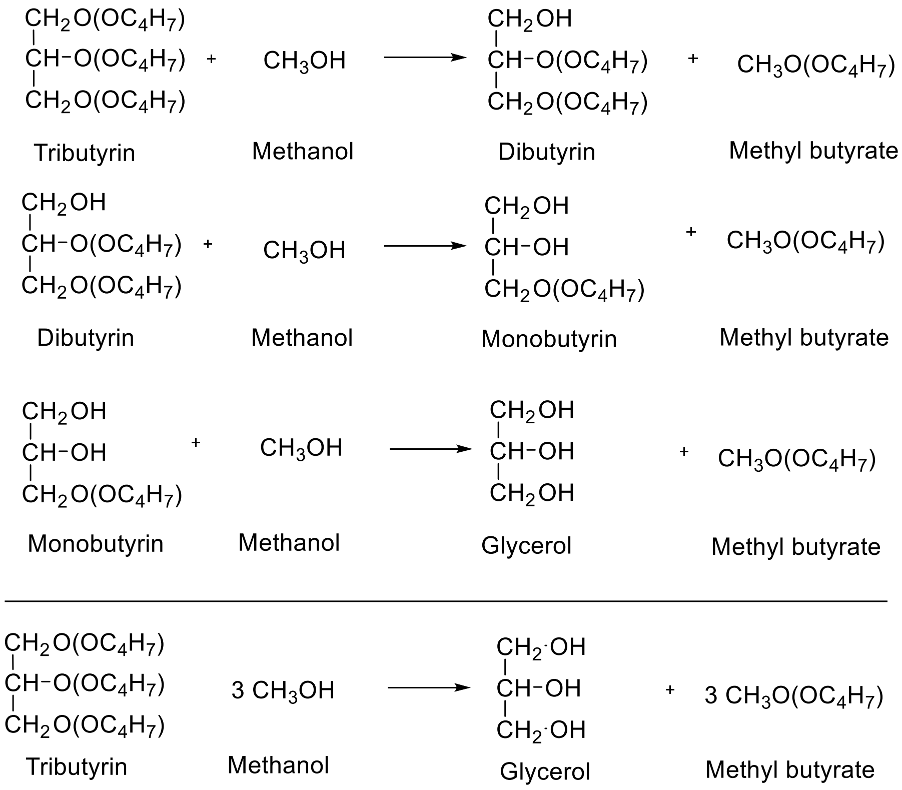

Figure 1.25. Transesterification reaction of tributyrin (TB) with methanol (MeOH) to form methyl esters (MB, biodiesel) and glycerol (GLY).

A solid catalyst for the transesterification should exhibit strong Brönsted or Lewis sites immobilised onto the surface of the supports. An appreciable amount of literature has been published on transesterification of tributyrin over different solid catalysts. Wang *et al.* have investigated the catalytic performance of carbon-based sulfonated acid as a catalyst [88]. The reaction was performed in a batch reactor equipped with a condenser using a molar ratio (TB: MeOH) of 1:20 at 353 K. 99.4 % conversion was achieved within 8 hours [88]. Basic catalysts are more active at a lower temperature for transesterification reactions [88]. Xi *et al.* have used decomposed and rehydrated magnesium-aluminium hydrotalcite with Mg/Al molar ratio of 4 as a catalyst [89]. The reaction was conducted in a batch reactor equipped with a condenser with a molar ratio TB: MeOH 1:30 at 333 K using a stirring rate of 800 rpm under inert atmosphere (N_2, 40 cm^3 min^{-1}) [89]. Montero *et al.* have investigated the catalytic properties of Cs over MgO nanoparticles using two different methodologies for the incorporation of Cs [90] [90]. They have used the co-precipitation method ($Cs_2Mg(CO_3)_2$-C) and the impregnation method ($Cs_2Mg(CO_3)_2$-I) [90]. The reaction was carried out in a batch reactor at 333 K with a molar ratio TB: MeOH 1:30 monitored for 24 hours, 100 % conversion was reached within 3 hours for $Cs_2Mg(CO_3)_2$-C [90]. Jiang *et al.* have reported the preparation of KF supported on $La_2O_2CO_3$ and its catalytic activities for the transesterification reaction of TB [91].

The reaction was performed in a batch reactor with a condenser using a molar ratio TB: MeOH of 1:30 and 30 mg of catalyst [91]. The reaction has been investigated over a limited temperature range, 298 to 338 K, and 98.5 % was achieved within 1 hour [91]. The performances and reaction conditions of each catalyst mentioned earlier are summarised in **Table 1.3**.

Table 1.3. Reaction conditions and TB conversion % for transterification of tributyrin with methanol over solid base and acid catalysts reported in the literature.

Ref.	**Active site for TB transesterification**	**Catalyst loading** / mg	**Molar ratio** (TB:MeOH)	**TB conversion** / %	**T** / K	**Reaction time** / h
[88]	Sulfonic group	20	1:20	99.4	353	8
[89]	Mg/Al hydrotalcite	250	1:30	80	333	7
[90]	Cs-doped-MgO-C	50	1:30	100	333	3
[90]	Cs-doped-MgO-I	50	1:30	40	333	24
[91]	KF supported on $La_2O_2CO_3$	30	1:30	98.5	308	1

The reaction conditions outlined in **Table 1.3** have been used as starting points to study the catalytic performance of eight ion exchange resins, which have been characterised by different functional groups, type of matrices, capacities of the resins and textural properties.

1.4. Novelty of this research

A successful production of biodiesel is dictated by the need of repleacing petroleum fuel via transesterification reaction of tryglycerides using a catalyst that can be easily recovered from the reactors and regenerated. This type of reaction can be a perfect niche for functionalised polymers such as ion exchange resins. The concept beyond using these resins as catalysts stems from the easy regeneration of the functional groups, and adaptability to any reactor because of the physical appearance. These resins are acquiring a prominent role as catalysts for their performances [28]. Anionic resins are much less investigated than cationic resins, their effectiveness as catalysts and their characterisation would provide insight into their behaviour in the working state have not been widely studied [92]. Thus, the research gaps in the existing literature concerns the role of base exchangers in catalysis.

This thesis serves an overview of the catalytic performance of commercial anion exchange resins for biodiesel production and addresses some methodologies questions for the characterisation study.

1.5. Aim of the thesis

The purpose of this study is to advance the knowledge of exchanger materials and their potential applications.

- To characterise the IERs with quantitative and qualitative techniques to better understand their physical and chemical properties.
- To investigate the catalytic activities of both anion and cation exchange resins, as heterogeneous catalysts for biodiesel production.
- To plan an experimental design for the resin that has shown the best catalytic performance.
- To study the diffusion of molecules into the IER pores.

1.6. Outline of the chapters

Chapter 1 provides an introduction to porous materials and background information into ion exchange resins, their classification and applications, and the catalytic processes employed for biodiesel production.

Chapter 2 describes the equipment and analytical methods used for this work.

Chapter 3 concerns the characterisation of polymeric materials employing the equipment and analytical methods described earlier in **Chapter 2**.

Chapter 4 focuses on the catalyst activation, the catalytic performance for the transesterification reaction catalysed by eight ion exchange resins and the experimental design performed for the catalyst with the best performance.

Chapter 5 describes the use of Diffusion Ordered Nuclear Magnetic Resonance Spectroscopy (DOSY NMR) as a tool to investigate the diffusion of molecules into the resin pores.

Chapter 6 concludes the thesis and highlights potential research areas for future work.

Chapter 2

Materials and experimental methods

2.1. Introduction

Characterisation is a process, covering a comprehensive investigation of the chemical and physical features of material (including defects) and also the satisfactory reproducibility of material in operation [93, 94]. **Chapter 2** brings together the experimental techniques used for characterisation of ion exchange resins: their thermal stability, their morphological properties, their swelling degree and capacity. It then states the method for performing the catalytic tests. It also describes the apparatus and the method employed for the catalytic tests. This chapter ends by outlining the criteria used for selecting the appropriate design of experiments.

2.2. Materials

2.2.1 Chemicals

Bromothymol blue, buffer solution pH 4.01 ± 0.01 at 293 K, buffer solution pH 10.00 ± 0.01 at 298 K, dichloromethane and sodium chloride, supplied by Thermo Fisher Scientific; hydrochloric acid (37 %), nitric acid (70 %), methanol (≥ 99.9 %) and toluene supplied by VWR Chemicals; mesitylene (98 %), potassium hydrogen phthalate, sodium hydroxide (> 97 %) and sodium nitrate (> 99 %) supplied by Acros Organics; tributyrin (97 %), acetanilide, deionised water (13.6 Ω) supplied by Sigma Aldrich, Carlo Erba and Purolite, respectively; were used in this work.

2.2.2 Catalysts

Eight commercial ion exchange resins were used as catalyst that were supplied by DuPont: These ion exchange resins were Amberlyst A26OH, Amberlite IRA402Cl, Amberlite IRA958Cl, Amberlite IRA458Cl, Amberlite IRA402OH, Amberlite IRA410Cl, Amberlyst 15H wet and Amberlite IR120H. The resins are termed with their short names that consists of numbers and letters, throughout this work. The numbers and the letters indicate the commercial resin name and their counter-ion, respectively. **Table 2.1** reports the resin properties.

Table 2.1. Chemical and physical properties of the commercial resins used in this work.

Ref.	**Commercial name**	**Counter-ions**	**Short name**	**Matrix**	**Type**	**Capacity** /meq mL^{-1}	**Functional group**	**Max T** / K
[95]	Amberlyst A26OH	OH^-	26OH	ST	M	≥ 0.80	QA (Type I)	333
[96]	Amberlite IRA458Cl	Cl^-	458Cl	MA	G	≥ 1.25	QA (Type I)	333
[97]	Amberlite IRA958Cl	Cl^-	958Cl	MA	M	≥ 0.80	QA (Type I)	333
[98]	Amberlite IRA410Cl	Cl^-	410Cl	ST	G	1.25	QA (Type II)	333
[99]	Amberlite IRA402Cl	Cl^-	402Cl	ST	G	≥ 1.20	QA (Type I)	333
[100]	Amberlite IRA402OH	OH^-	402OH*	ST	G	≥ 0.95	QA (Type I)	333
[101]	Amberlyst 15Hwet	H^+	15H	ST	M	≥ 1.7	S	393
[102]	Amberlite IR120H	H^+	120H	ST	G	1.8	S	408

ST= styrenic; MA= methylmethacrylic; M= macroreticular; G= gel; S= sulfonic acid; QA (Type I)= trimethyl ammonium and QA (Type II)= dimethylethanol ammonium.

2.3. Investigation of the thermal stability of ion exchange resins

The thermal stability of IERs can be characterised by using both thermogravimetric analysis and differential scanning calorimetry. These techniques provide an insight into the behaviour of the resins as a function of temperature.

2.3.1. Thermogravimetric analysis

Thermogravimetric analysis (TGA) is a technique in which the mass of a specimen is recorded as a function of temperature or time as the sample is monitored by temperature ramp under an inert atmosphere such as nitrogen. In TGA, approximately 8 mg of sample is placed into a ceramic crucible. This crucible is put into a sample pan supported by a microbalance with sensitivity of ± 0.001 g. **Figure 2.1** shows a schematic drawing of the Perkin Elmer Pyris^{TM} 1 TGA instrument used in this work.

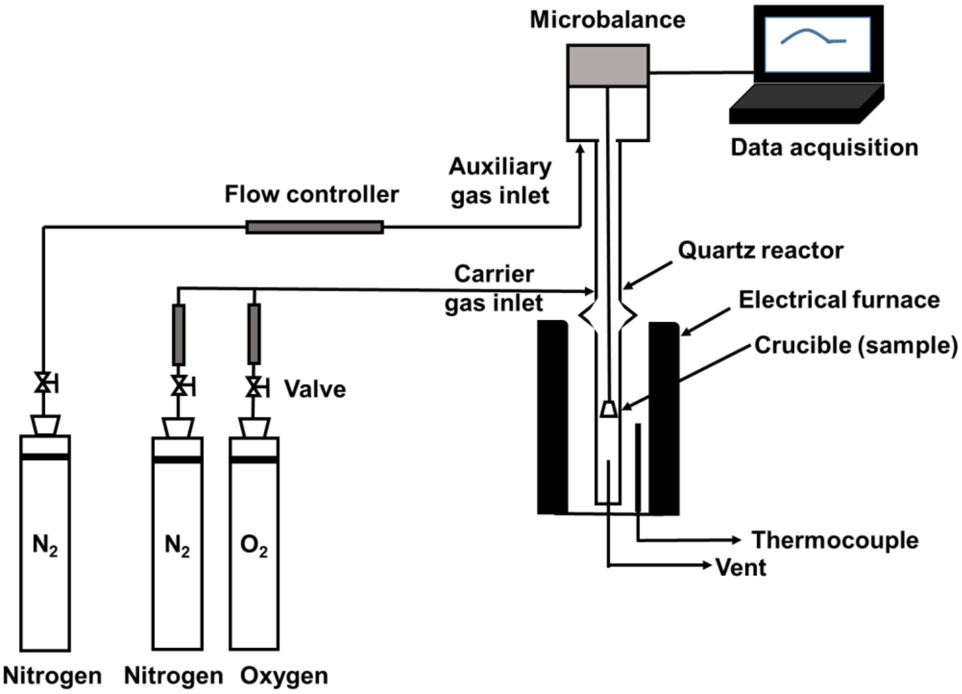

Figure 2.1. Schematic drawing of Perkin Elmer PyrisTM 1 thermogravimetric analyser (TGA).

The microbalance apparatus is located in a furnace that heats the sample during the analysis. In the microbalance, nitrogen is purged to prevent the gases from the back-streaming into the balance chamber. In the furnace, carrier gas, nitrogen, is used to control the sample environment and vent out the exhausting gas through the appropriate vent system. Before the analysis, the balance was calibrated using metallic standards, such as indium and zinc. For all samples, a temperature ramp from room temperature to 973 K was employed, with a ramp rate of 10 K min^{-1} and a nitrogen flow rate of 20 cm^3 min^{-1}.

2.3.2. Differential scanning calorimetry

Differential scanning calorimetry (DSC) is a thermal analysis technique that investigates how the heat capacity of a material varies with temperature.

The heat capacity, $\boldsymbol{c_p}$ is defined as the amount of heat, $\boldsymbol{Q}$ required to raise its temperature, $\boldsymbol{T}$, by one degree, expressed as J K^{-1}, as shown in **Equation 2.1** [103].

$$\frac{\mathrm{d}\boldsymbol{Q}}{\mathrm{d}\boldsymbol{T}} = \boldsymbol{c_p} \qquad \textbf{Equation 2.1}$$

A known sample, such as a polymer, is heated and cooled down, and the variations of heat capacity are recorded as variations of heat flow using a heating rate, $\mathrm{d}\boldsymbol{T}/\mathrm{d}\boldsymbol{t}$. The relationship between the three variables, $\boldsymbol{Q}$, $\boldsymbol{T}$ and $\boldsymbol{t}$, is summarised in **Equation 2.** [103].

$$\frac{\frac{\mathrm{d}\boldsymbol{Q}}{\mathrm{d}\boldsymbol{T}}}{\frac{\mathrm{d}\boldsymbol{T}}{\mathrm{d}\boldsymbol{t}}} = \frac{\mathrm{d}\boldsymbol{Q}}{\mathrm{d}\boldsymbol{t}} \qquad \textbf{Equation 2.2}$$

Tracking the heat flow, $\mathrm{d}\boldsymbol{Q}/\mathrm{d}\boldsymbol{t}$, using a heating rate, $\mathrm{d}\boldsymbol{T}/\mathrm{d}\boldsymbol{t}$ as the function of temperature allows phase transitions to be detected. These are typically the most important thermodynamic parameters, such as melting point, glass transition point, and other changes in phase. Polymers may contain amorphous and crystalline phases, showing both glass transition and melting temperatures. Materials with a significant crystalline phase show small differences and a defined melting peak. When crystalline polymers melt, they absorb latent heat and they undergo heat exchange. This is described as a first-order transition. Melting temperatures of a material, $\boldsymbol{T_m}$, are associated with endothermic events. Phase changes of a sample such as polymorphism, re-crystallisation, solvent loss and chemical reactions are associated with heat flow changes, occurring at $\boldsymbol{T_c}$. This event is exothermic. These events are illustrated in **Figure 2.2**.

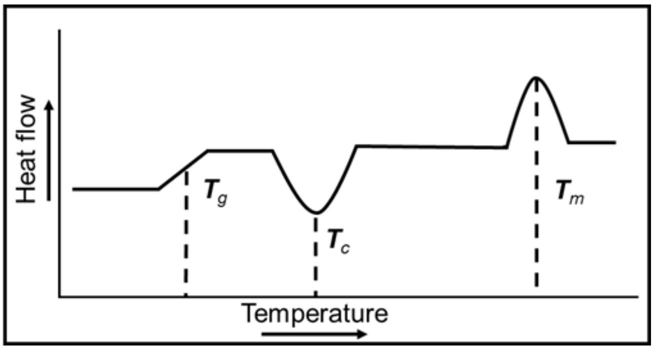

Figure 2.2. Schematic drawing of a DSC plot displays the endothermic changes glass transition, $\boldsymbol{T_g}$, and melting point, $\boldsymbol{T_m}$, and the exothermic transition as crystallisation temperature, $\boldsymbol{T_c}$.

Amorphous materials exhibit only a glass transition temperature, T_g, which is a thermal event associated with an amorphous domain. Amorphous polymers are heated at their glass transition, T_g, the temperature does not stop rising because T_g does not involve latent heat. T_g is an endothermic change and shows up as a shift in the baseline, as depicted in **Figure 2.3**. This is described as second-order transition.

All samples in this thesis were characterised using a DSC 1 Perkin-Elmer differential scanning calorimeter interfaced with Mettler STAR^e V12.0 software, which can operate in the temperature range between 123 K to 773 K using a cryogenic system, as illustrated in **Figure 2.3**.

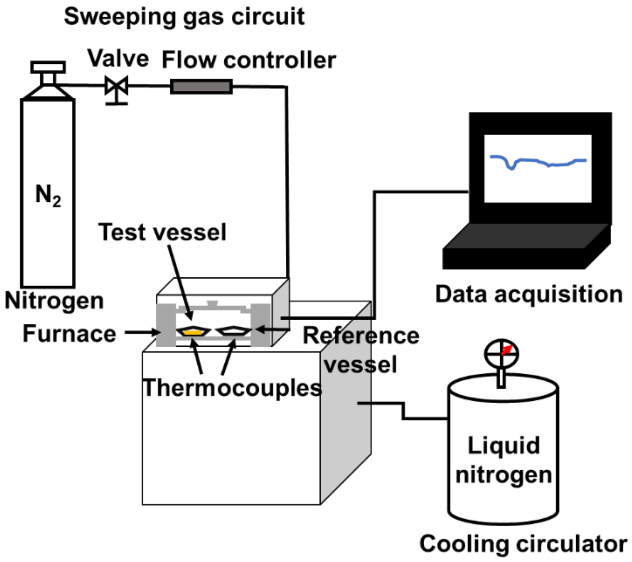

Figure 2.3. Schematic representation of DSC 1 Perkin-Elmer differential scanning calorimeter.

The equipment is calibrated using indium and zinc as high-quality reference standards. A temperature ramp from 273 K to 473 K and a heating rate of 10 K min^{-1} is set up through the software. The sample specimen is weighted out into aluminium pans and sealed with their appropriate pre-perforated lid using a crucible sealing press. Then, the sample vessel and the reference vessel are placed on the proper sensor position in the furnace chamber, as shown in **Figure 2.4**. Nitrogen flushes through the apparatus with a flow of 50 cm^{3}min^{-1}. During the analysis, the thermocouples, located in the furnace chamber, measure the differential heat flow using Ohm's Law (**Equation 2.3**) [103].

$$\frac{\mathrm{d}\boldsymbol{Q}}{\mathrm{d}\boldsymbol{t}} = \frac{\mathrm{d}\boldsymbol{T}}{R} \qquad \textbf{Equation 2.3}$$

Ohm's law reflects the linear relationship between the change in heat flow, $\mathrm{d}\boldsymbol{Q}/\mathrm{d}\boldsymbol{t}$, the shift in temperature ($\Delta\boldsymbol{T}$) of the reference and the sample and the resistance of the cell, R.

2.4. Investigation of morphological features

The morphological parameters of the resins, key to their applications as catalysts were characterised by three different techniques: nitrogen physisorption, thermoporometry, and Environmental Scanning Electron Microscopy (ESEM). The most important parameters investigated in this section are surface area, pore diameter and volume of polymers. Nitrogen physisorption provides pore size and distribution, and surface area of the resins in the dry state. In contrast, thermoporometry estimates pore size in the wet state by using water as a solvent. Imaging methods, such as ESEM gives an image of the material surface, from which estimates of pore size can be made. As will be seen, complementary methods need to be used to validate the estimated pore sizes and structures.

2.4.1. Nitrogen physisorption

Nitrogen porosimetry is the most common technique used for the direct measurement of textural properties such as porosity and surface area. It can be used to successfully measure pore sizes from 0.3 to 300 nm [104]. Adsorption is a surface process. It relies on the accumulation of adsorbate gas, typically nitrogen, on a solid surface (adsorbent) by either chemical or physical adsorption [103]. Chemical adsorption or chemisorption is an irreversible process between the adsorbent and the adsorbate. Heats of adsorption are similar to chemical bond energy in the range of -837 kJ mol^{-1} [103]. As the surface interactions involved in most catalytic reactions are reversible, this thesis concentrates on reversible, physi-sorption, processes. Unlike, chemisorption, physical adsorption (physisorption) is a reversible process at isothermal conditions. The interaction between adsorbate and adsorbent occurs by Van der Waals forces. Heats of adsorption are in the range of -84 KJ mol^{-1} [103]. In physisorption, the variation of the volume of gas adsorbed ($\boldsymbol{V}$) onto the surface of a porous solid as a function of the relative pressure ($\boldsymbol{p}/\boldsymbol{p}°$) at liquid nitrogen temperature $\boldsymbol{T}$ (77 K) is called adsorption isotherm (**Equation 2.4**) [103].

$$V = \mathrm{f}\left(\frac{p}{p^{\circ}}\right)_T \qquad \textbf{Equation 2.4}$$

The relative pressure, ***p/p***°, is the ratio of the equilibrium pressure to saturated pressure. Conversely, desorption isotherms can be measured by detecting the adsorbed gas released from the porous material. During the analysis, the adsorbate gas fills micropores and then forms a monolayer on the surface at relatively low pressures, which is termed Point B, as shown in **Figure 2.4**. Then, it continues to fill larger sized pores and to form multilayers at increasing ***p/p***°. The point at which a monolayer forms, incanted by Point B, on a surface allows the estimation of the surface area of a material.

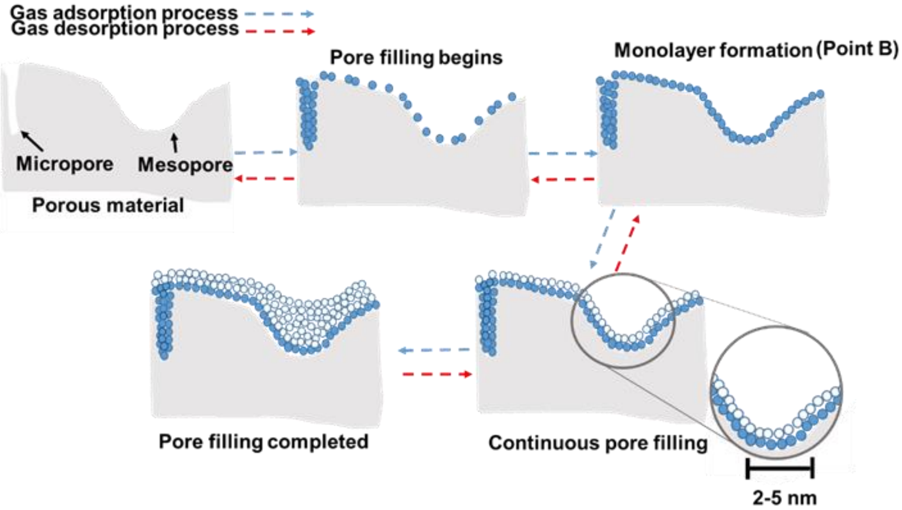

Figure 2.4. Gas adsorption (blue arrow) and gas desorption process (red arrow) (Reproduced from [105]).

The most commonly used method for calculation of the surface area is the Brunauer, Emmet, and Teller (BET) method and it is detailed in **Equation 2.5** [40].

$$\frac{1}{V\cdot\left(\left(\frac{p}{p^{\circ}}\right) - 1\right)} = \frac{1}{V_m \cdot C} + \frac{C-1}{V_m \cdot C}\cdot\left(\frac{p}{p^{\circ}}\right) \qquad \textbf{Equation 2.5}$$

In this expression, ***p*** and ***p***° are the equilibrium and the saturated pressures of adsorbate gas at 77 K (Pa), ***V*** and V_m are the adsorbed volumes at relative pressure ***p/p***° and the monolayer coverage (mL), and ***C*** is a dimensionless constant representing the difference in energetics between desorption and vaporisation. It is expressed in **Equation 2.6** [103].

$$\boldsymbol{C} = \mathrm{e}^{\left[\frac{(\Delta \boldsymbol{H}_{\mathrm{desorption}} - \Delta \boldsymbol{H}_{\mathrm{vaporisation}})}{\mathrm{RT}}\right]} \qquad \textbf{Equation 2.6}$$

The ***C*** constant is significant when the enthalpy of desorption ($\Delta \boldsymbol{H}_{\mathrm{desorption}}$) from a monolayer is larger than the vaporisation enthalpy of the adsorbate ($\Delta \boldsymbol{H}_{\mathrm{vaporisation}}$) [103]. For nitrogen, interacting with both porous and non-porous adsorbents, ***C*** ranges between 80 and 150 [106]. The specific surface area and ***C*** constant of porous materials are calculated by plotting $1/[\boldsymbol{V}\cdot(\boldsymbol{p}^{\circ}/\boldsymbol{p}) - 1]$ against $\boldsymbol{p}/\boldsymbol{p}^{\circ}$, as shown in **Figure 2.5**.

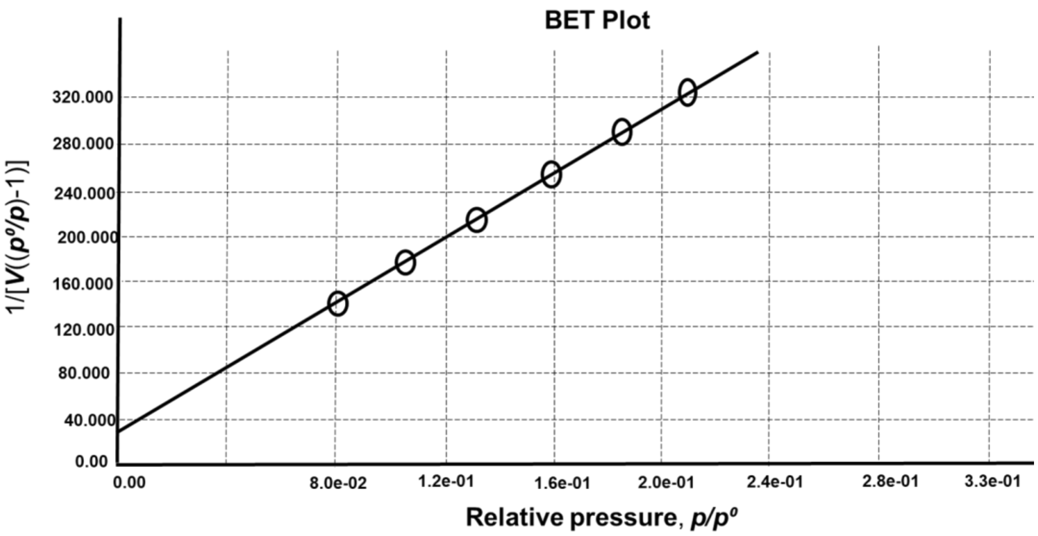

Figure 2.5. A typical BET plot: a linear plot of $1/[\boldsymbol{V}\cdot(\boldsymbol{p}^{\circ}/\boldsymbol{p}) - 1]$ versus $\boldsymbol{p}/\boldsymbol{p}^{\circ}$ which for most material using nitrogen as adsorbate is restricted to the $\boldsymbol{p}/\boldsymbol{p}^{\circ}$ region of 0.05 and 0.35 [103, 106].

BET plot requires a minimum of three points (measurements of volume) in the relative pressure range $0.05 < \boldsymbol{p}/\boldsymbol{p}^{\circ} < 0.35$ in which the linearity of the correlation coefficient is applicable for most solids. From the monolayer volume ($\boldsymbol{V}_{\boldsymbol{m}}$), the specific surface area (***S***) is determined by **Equation 2.7** [107]:

$$\boldsymbol{S}_{BET} = \boldsymbol{V}_{m}\cdot N_{\mathrm{A}}\cdot \frac{\boldsymbol{\sigma}_{m}}{\text{sample mass}} \qquad \textbf{Equation 2.7}$$

The specific surface area of an adsorbent is proportional to monolayer capacity ($\boldsymbol{V}_{m}$), nitrogen cross-sectional area (0.162 nm^2), $\boldsymbol{\sigma}_{m}$, and Avogadro's number N_{A} (6.023×10^{23} mol^{-1}) and inversely proportional to the adsorbent mass.

Pore architecture can be classified in line with the origin of the porosity into three materials: microporous, mesoporous and macroporous with pore diameters of less than 2 nm, between 2 nm and 50 nm, and greater than 50 nm, respectively. These pore structures give different sorption/desorption isotherm features. IUPAC has classified six types of isotherms for physisorption, depicted in **Figure 2.6** [107].

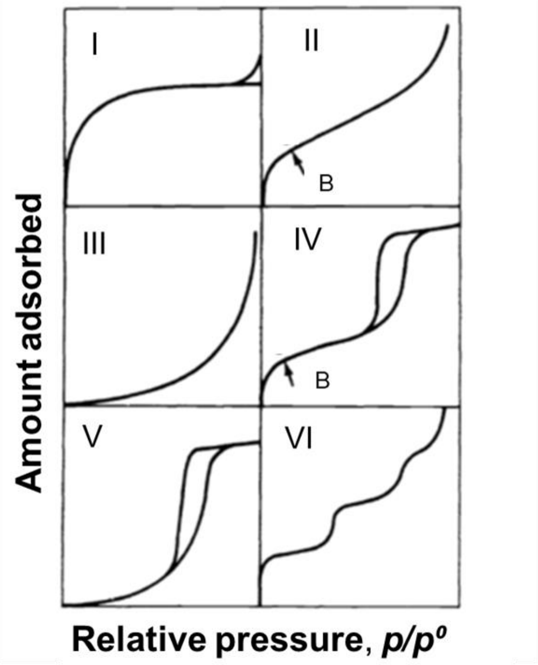

Figure 2.6. IUPAC classification of physisorption isotherms showing both adsorption and desorption branches. Only Type IV and V isotherms exhibit hysteresis loops (Reproduced from [108]).

Type I isotherms are detected for microporous materials with pore size less than 2 nm. At low relative pressure, the amount of adsorbed gas rises, corresponding to the micropores filling. Once the micropores are completely filled, the isotherm levels off. Activated carbons, zeolite and some porous oxides show this isotherm [23, 108].

Type II isotherms are obtained for a non-porous or macroporous adsorbents with pore size greater than 50 nm. At low relative pressure, the molecules form a monolayer (point B); as the relative pressure increases, forms a multilayer [23, 108]. The position of point B in **Figure 2.6** allows for the estimation of the specific surface area of materials.

Type III isotherms are associated with non-porous adsorbents. These isotherms show a convex curvature over the entire range of relative pressure. These types are uncommon and occur when weak interactions adsorbate-adsorbate are involved. Nitrogen on polyethylene exhibits this isotherm [108].

Type IV isotherms are typical for mesoporous material with pores of diameter between 2 and 50 nm. These isotherms show a multilayer and nearly analogous to Type II isotherms. The monolayer follows a continuous mesopore filling and a multilayer formation. Besides, mesopore filling and emptying correspond to the capillary condensation process, which gives rise to a hysteresis loop. This isotherm has been well-documented in porous materials such as SBA-15 and aerogel [109, 110].

Type V isotherms are similar to Type III isotherms, and indicate weak interactions between adsorbent and adsorbate [108].

Type VI isotherms display multilayer adsorption on a uniform nonporous surface [23, 108]. *Type IV* isotherms are characterised by a hysteresis loop, a phenomenon that can be satisfactorily explained by a capillary condensation process. In capillary condensation process, a gas condenses to a liquid-like phase into a pore at a pressure $\boldsymbol{p}$, which is smaller than the saturation pressure $\boldsymbol{p}°$ of bulk liquid, as illustrated in **Figure 2.7**.

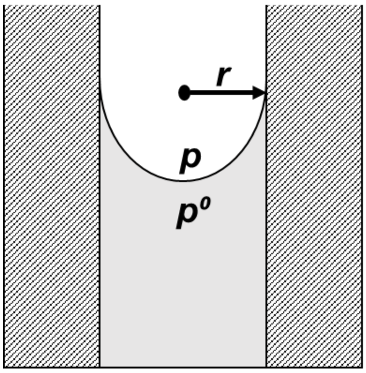

Figure 2.7. Schematic representation of the capillary condensation process into a pore of a radius, $\boldsymbol{r}$ [103].

The capillary condensation phenomenon occurs at a relative pressure $\boldsymbol{p/p°}$, which depends on the pore radius $\boldsymbol{r}$ according to Kelvin's equation (**Equation 2.8**) [103].

$$\ln\frac{\boldsymbol{p}}{\boldsymbol{p}°} = -\frac{2\boldsymbol{\gamma V_m}\cos\boldsymbol{\theta}}{\boldsymbol{rRT}} \qquad \textbf{Equation 2.8}$$

where $\boldsymbol{p}$, $\boldsymbol{p}°$, $\boldsymbol{\gamma}$, $\boldsymbol{V_m}$, R, $\boldsymbol{T}$ and $\boldsymbol{\theta}$ are the equilibrium and saturated gas pressure, solid-liquid interfacial (surface) tension, molar volume, universal gas constant, temperature and contact angle between adsorbate and adsorbent, respectively. $\boldsymbol{\theta}$ is assumed to be 0 throughout, as the systems studied here can be assumed to where the liquid wets the adsorbent walls thoroughly.

The capillary condensation into different morphology pores gives rise to four hysteresis loops, as illustrated in **Figure 2.8**, further classified by IUPAC as

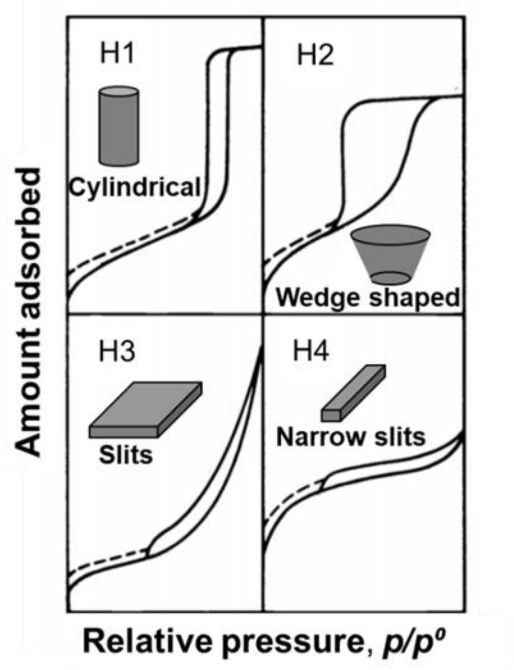

Figure 2.8. Representative hysteresis loops and pore shapes (Reproduced from [108, 111]).

Type H1 hysteresis is associated with materials arranged in a regular array, giving rise to independent cylindrical pores. The desorption branch of the hysteresis emulates the equilibrium phase transition occurring in the pores, which can be described by applying different approaches. One of the most used is Barett-Joyner-Halenda (BJH) method, which is described in detail further below [107]. This hysteresis characterised porous materials such as SBA-15 and aerogel [109, 110].

Type H2 hysteresis are associated with pores have narrow pore mouths and wide bodies, hence, they are called “ink-bottle” pores [112]. Condensation and evaporation occurs with different mechanisms-evaporation does not occur via equilibrium from these pores but it is slowed down. The large pore bodies are still filled when low ***p/p***° is reached and empty through smaller pore necks [113]. In Type *H2*, the pore blocking is correlated with the desorption process, and the analysis of the adsorption branch is required [107, 112].

Both *Type H1* and *Type H2 hystereses* are characterised by a well-defined plateau at high $\boldsymbol{p/p°}$, which allows for calculation of the mesopore volume [112].

Type H3 hysteresis is typical for aggregates of a plate-like and non-rigid adsorbents. As the loop displays no limit at high $\boldsymbol{p/p°}$, this hysteresis should not be attributed to Type IV isotherm [112].

Type H4 hysteresis is associated with high-density microporous materials such as some activated carbon [112].

Nitrogen sorption analysis determines pore size and pore size distribution (PSD) of a material. The PSD is the first derivative of the volume ($\boldsymbol{V}$) with respect to the pore radius $\boldsymbol{r}$, ($\mathrm{d}\boldsymbol{V}/\mathrm{d}\boldsymbol{r}$). Macroscopic approaches for the determination of $\boldsymbol{r}$ and PSD are algorithms based on the Kelvin equation and assumptions on the basis of pore shape. The BJH method remains one of the most used methods for the determination of mesopores. This method predicts the pressure at which adsorptive condenses and evaporates in a cylindrical pore. However, it is worth noticing that it fails for the prediction of micropores and underestimates the mesopores, particularly those with pore diameters smaller than 20 nm [114].

Both the BET and BJH methods can be described as macroscopic methods. Rival microscopic methods, such as non-local density functional theory (NLDFT) describe the adsorbate at the molecular level [113]. This method uses the fluid density functional theory to build the adsorption isotherm using a specific pore morphology (e.g. N_2 adsorption in a cylindrical model at 77 K) [115].

2.4.2. Nitrogen physisorption analysis

Nitrogen porosimetry experiments were all performed on a Quantachrome Nova 4000e porosimeter equipped with Novawin v11.0 software for the data analysis, as illustrated in **Figure 2.9**.

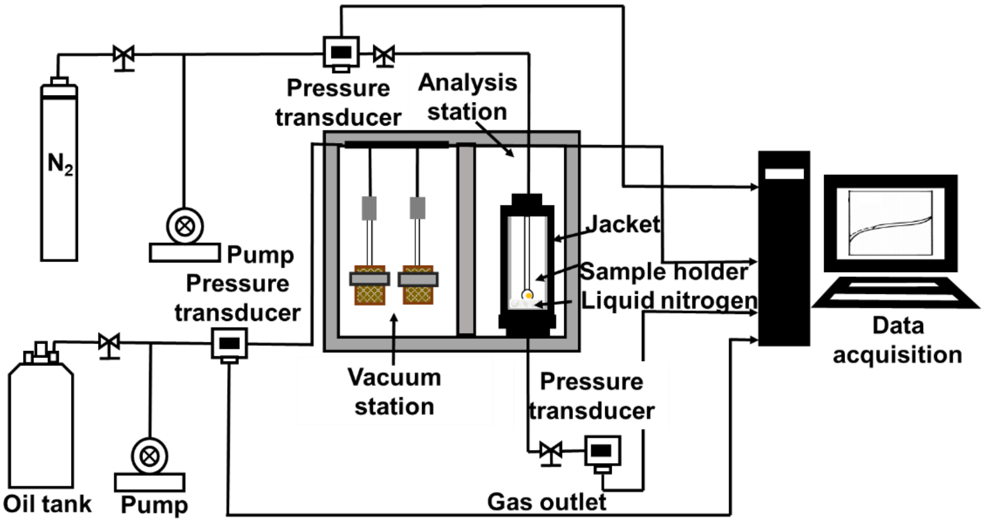

Figure 2.9. Schematic drawing of Quantachrome Nova 4000e porosimeter.

A sample of approximately 200 mg was weighed out into a sample tube and loaded into the degassing port equipped with a heating mantle located in the vacuum station. It was heated at 313 K for 3 hours or 12 hours under vacuum to drive off any water from the material and to leave the sample morphology unchanged. The degassing time has been varied to investigate whether the results were sensitive to time or water content. The sample was re-weighed and uploaded to the analysis port situated in the analysis station, and then the sample was immersed in liquid nitrogen at 77 K.

The isotherm branches were analysed using both BJH and NLDFT approaches to determine both pore sizes and their pore size distributions. Badia *et al.* have assumed a cylindrical geometry for macroreticular and gel resins that allows the gauging of the average pore width $<\boldsymbol{d}_p>$ as shown in **Equation 2.9** [116].

$$<\boldsymbol{d}_p> / \text{nm} = \frac{4000 \cdot \boldsymbol{V}_{\boldsymbol{p/p^o} = 0.99}}{\boldsymbol{S}_{BET}} \qquad \textbf{Equation 2.9}$$

where $\boldsymbol{V}$ is the volume of nitrogen adsorbed at $\boldsymbol{p/p}$°= 0.99, and $\boldsymbol{S}_{BET}$ is the specific surface area calculated employing the BET method. The specific surface area was calculated using a five-point method in the relative pressure range 0.05-0.35 [106].

2.4.3. Thermoporometry: DSC as alternative pore size technique

Thermoporometry is a calorimetric technique for the pore size determination. It is usually performed on either materials that cannot undergo a drying process because the water removal would modify their porosity or materials that show a change in porosity in their wet state. It operates on the principle that the melting point of liquid trapped in pores experiences a shift of the bulk melting point according to the Gibbs-Thomson equation (**Equation 2.10**) [43].

$$\Delta T\,(r) = T_{mB} - T_m(r) = T_{mB}\frac{4\sigma_{SL}\cos\theta}{\Delta H_f \rho_S r} \qquad \textbf{Equation 2.10}$$

ΔT, T_{mB}, T_m, σ_{SL}, ρ_S, ΔH_f and r are the observed melting point depression, the bulk melting temperature, the temperature of the cluster, the solid-liquid interface energy, the density of the solid, the enthalpy of fusion and the pore radius, respectively.

Different probe liquids have been used to study porous materials, such as water, n-heptane and NaCl solution [117-119]. However, water remains the most common probe liquid for the determination of porosity in polymers [120]. The advantage of using water as a probe lies in its high value for enthalpy of fusion ($\Delta H_f = 334$ J g^{-1}), enhancing the sensitivity of the DSC technique[120].

Brun *et al.* evaluated **Equation 2.11** for the measurements of porous non and swellable materials [121]. It relates the depression temperature ΔT as a function of the pore radius, r_p, of the recorded DSC signal in heating mode[121]. **Equation 2.11** is valid only for cylindrical pores [121].

$$r_p \,/\, \text{nm} = -\frac{32.33}{\Delta T} + 0.68 \qquad \textbf{Equation 2.11}$$

where ΔT is the melting temperature depression which is the difference of temperatures of bulk and cluster.

The temperatures of bulk and cluster were determined applying the peak−difference method on the DSC heating curves, as depicted in **Figure 2.10**.

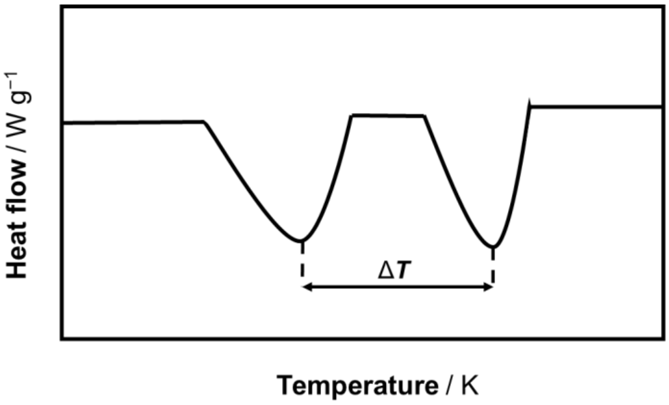

Figure 2.10. Illustration of DSC profile of solid to liquid phase transition showing the peak–difference method for the determination of the melting temperature depression, Δ***T***.

The experiment was conducted as follows: a sample of 3 mg and 5 mg of water were weighed out into an aluminium pan. Then, the pan was sealed with the pre-perforated lid using a crucible sealing press. The experiment was recorded in a temperature range between 233 K and 283 K with a heating rate of 0.5 K min^{-1} as described earlier in **Section 2.3.2**.

2.4.4. Environmental scanning electron microscopy and energy-dispersive X-ray spectroscopy analysis

Environmental scanning electron microscopy and energy-dispersive X-ray spectroscopy (ESEM-EDS) is an elemental analysis technique for the detection and quantification of all elements within a solid (except light elements such as hydrogen, helium, and lithium), crystalline structure, and crystal orientation [122, 123].

Samples were dried at 313 K overnight and deposited on sticky carbon tape mounted on a 15 mm aluminium stub. Then, ESEM images were performed on an ESEM FEI Quanta 200 microscope equipped with a tungsten (W) filament at 25 kV and, EDS and secondary electron detectors, as illustrated in **Figure 2.11**.

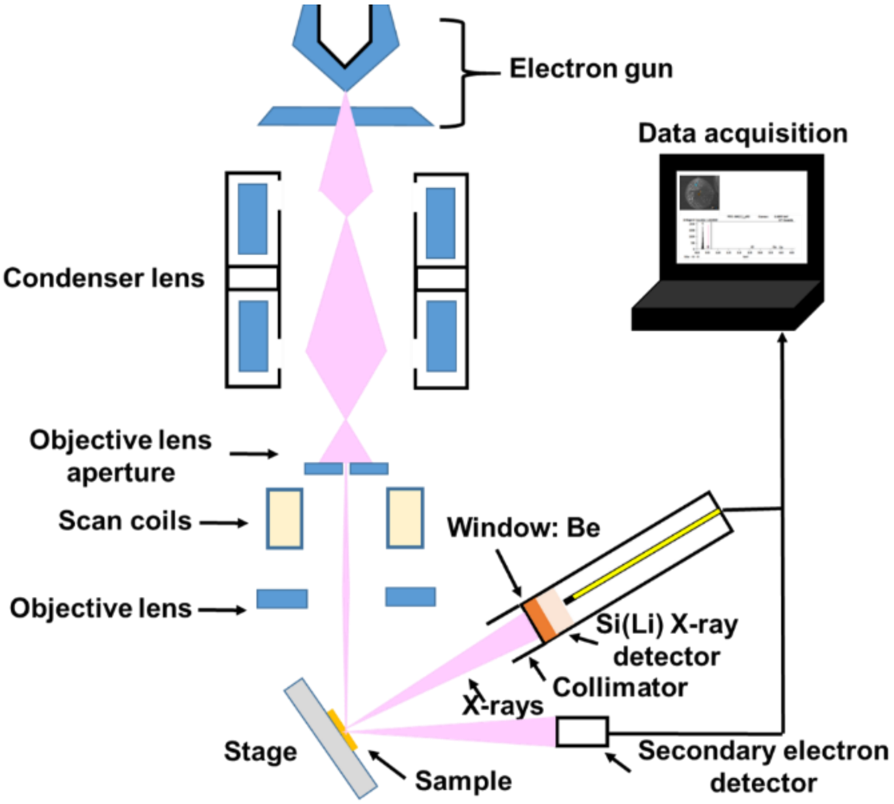

Figure 2.11. Schematic drawing of ESEM FEI Quanta 200 microscope equipped with an EDS and secondary electron detector (Reproduced from [124]).

The ESEM-EDS consists of a conical electron beam focussed through the specimen by a series of the lens. The apparatus is stabilised under vacuum to facilitate the beam pathway. Accelerated electron beam hits the sample to produce these signals: secondary electrons, backscattered electrons, and X-rays, as shown in **Figure 2.12**.

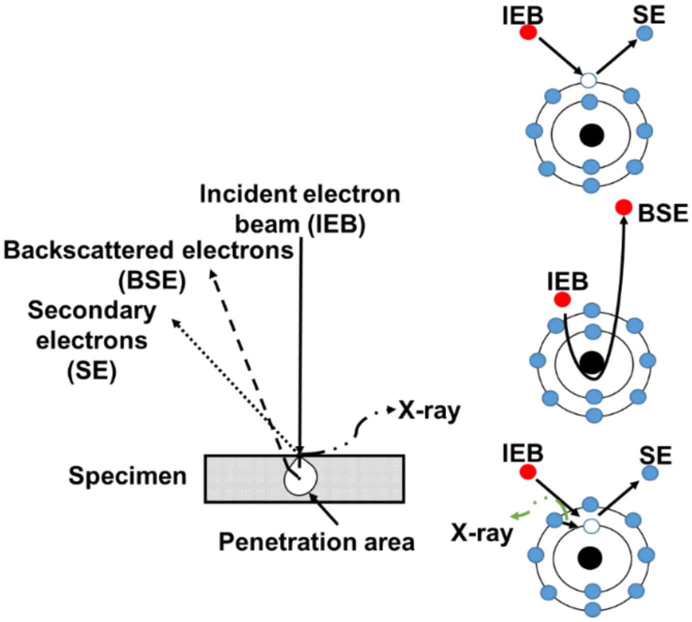

Figure 2.12. An incident electron beam (IEB) hits the specimen producing secondary electrons (SE), backscattered electrons (BSE) and X-ray.

Secondary electrons (SE) are generated by inelastic interaction between the sample and the primary beam. These are detected by a secondary electron detector, providing sample morphology (ESEM image). However, X-rays are produced by inelastic collisions of an electron in discrete orbitals and detected by lithium-drifted silicon (Si(Li)) EDS detector. These collisions are assembled as a map of the chemical elements contained in the sample. The detection of backscattered electrons is also feasible when the SEM apparatus is supplied with a diffracted backscattered electron detector. This detector allows investigating the composition and orientation of phases in crystalline compounds.

2.5. Determination of total capacity and operating capacity of ion exchange resins

Also important to the use of IERs as catalysts is the number of potentially active sites per gram of resin, also known as the capacity of the material. The quantity is important for understanding the potential of the resin to act as a catalyst. The total capacity of an IERs is the total number of functional groups in the material. This can be measured by, for example, elemental analysis to calculate the percentage of nitrogen present. Not all sites are capable of exchanging, so back-titration is required to determine the number of ions that can exchange.

2.5.1. Elemental analysis

Elemental analysis quantifies the amount of elements such as carbon, hydrogen, nitrogen, sulfur and oxygen in an unknown organic sample. The elemental analysis based on the Dumas method, which allows the determination of nitrogen in a matrix. This process involves the complete combustion of the sample under oxygen with the addition of a catalyst to promote the product reduction reaction. Before measurement, the calibration for each element is performed using acetanilide as a high-purity analytical standard. Elemental analyses were performed on dry polymers by a Perkin Elmer PE 2400 Series II CHNS/O elemental analyser, as depicted in **Figure 2.13**.

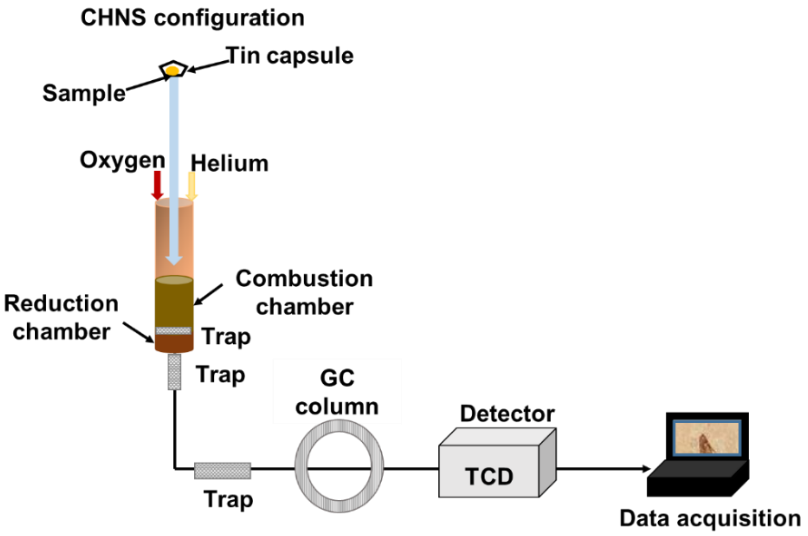

Figure 2.13. Schematic representation of Perkin Elmer PE 2400 Series II CHNS/O elemental analyser (Reproduced from [125]).

A sample of approximately 3 mg was weighed out into a tin capsule in which copper was added as a catalyst to aid the combustion reaction. Then, the sample was transferred into the pre-combustion port using the appropriate tweezers. The combustion occurred in an oxidative atmosphere using high purity oxygen (99.9995 %) to eliminate the blank nitrogen level while helium is purged as carrier gas [126]. As illustrated in **Figure 2.13**, the combustion occurred in a quartz tube reactor at 1273 K where carbon was converted in carbon dioxide, hydrogen in water, nitrogen to nitrogen gas or nitrogen oxide and the additional products formed are removed by an absorbent trap. After the gases were vented out of the combustion chamber by helium, they went through the reduction chamber where copper heated at 873 K is located to reduce any nitrogen oxide into nitrogen gas. Then, the gases were passed through an adsorbent trap to remove the unwanted gases. Finally, the separation and the element quantification occurred utilising the gas chromatography (GC) column and a thermal conductivity detection (TCD), respectively. In short, this detector compared the heat loss rate of the column effluent with reference gas. The signal detected was proportional to the element concentrations.

2.5.2. Determination of the operating capacity by back titration of the resins in OH- and H-form

Back titration is a two-step analytical method. The concentration of an analyte can be determined by reacting it with an excess volume of reactant of a known concentration. Then, the remaining excess is titrated with a known concentration. The relation between the equivalent entity and mass molar is straightforward for strong acid or base, which has a single exchangeable hydrogen or hydroxide ion. For instance, the equivalent entity of sodium hydroxide and hydrochloric acid are equal to their molar masses. However, when acid (base) with more than hydrogen (hydroxide) ions are involved in the reaction, the normality is expressed as the product between molarity and the number of hydrogen (hydroxide) ions released from the acid (the base), as shown in **Equation 2.12** [127].

$$\text{Normality / N = Molarity} \times \text{number of } H^+ \text{ (or } OH^-\text{)} \qquad \textbf{Equation 2.12}$$

The capacity can be expressed as either equivalent per litre, which is also called normality (***N***) or milliequivalents per gram of resin.

For the determination of capacity, the resins were dried in the oven at 313 K for 24 h to drive off the physisorbed water. This experiment demonstrates the most common method for obtaining the operating capacity (OC) of the resins. It involves the preparation of a solution of sodium hydroxide 0.1 M, and the exact concentration of the base solution is performed by direct titration against a primary standard. Potassium hydrogen phthalate (KHP) was used as the acidimetric standard. In contrast, the HCl solution was provided with an accurate concentration of 0.1 M. The bromothymol blue was chosen as an indicator because of the colour transition over a pH range from 6.00 (yellow) to 7.5 (blue), as illustrated in **Figure 2.14**. The indicator solution was prepared using 0.1 g of bromothymol blue, and a solution of 50 % (v/v %) of ethanol and deionised water.

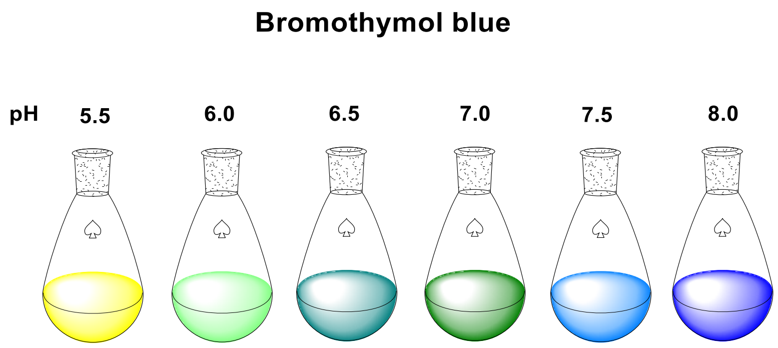

Figure 2.14. Schematic illustration showing the colour transition of the bromothymol blue indicator across the pH range.

The titrations were conducted employing a Class A burette (25.00 ± 0.05 cm^3), a glass pipette class A (10.00 ± 0.01 cm^3) and volumetric flasks (10.00 ± 0.03 dm^3).

A volume of 1 cm^3 of resin in their catalytic form (H or OH) was weighed out in analytical balance (± 0.0001 g) and soaked in 20 cm^3 of sodium hydroxide or hydrochloric acid 0.1 M for 24 hours. Two aliquots of 10 cm^3 were titrated over hydrochloric acid or sodium hydroxide 0.1 M. Fisher and Kunin have proposed the **Equations 2.13 a** and **b** to gauge the operating capacity [128]. However, the operating capacity (OC) of the resins in chloride form was performed using an ion-selective electrode.

$$\text{SAC Capacity/ meq g}^{-1} = \frac{(\boldsymbol{V}_{\mathrm{NaOH}} \cdot \boldsymbol{C}_{\mathrm{NaOH}}) - 2(\boldsymbol{V}_{\mathrm{HCl}} \cdot \boldsymbol{C}_{\mathrm{HCl}})}{\text{sample mass}} \qquad \textbf{Equation 2.13a}$$

$$\text{SBA Capacity/ meq g}^{-1} = \frac{(\boldsymbol{V}_{\mathrm{HCl}} \cdot \boldsymbol{C}_{\mathrm{HCl}}) - 2(\boldsymbol{V}_{\mathrm{NaOH}} \cdot \boldsymbol{C}_{\mathrm{NaOH}})}{\text{sample mass}} \qquad \textbf{Equation 2.13b}$$

$$\text{water / \%} = \frac{\text{mass of native IER} - \text{mass of dried IER}}{\text{mass of native IER}} \cdot 100 \qquad \textbf{Equation 2.13c}$$

where ***V*** and ***C*** are the volumes and the concentrations of HCl or NaOH.

2.5.3. Analytical determination of halide ions

The exchangeable sites present in the Cl-form resin were determined by either ion-selective electrode [126]. A Jenway pH/mV meter 3510 (in mV mode) equipped with the Fisher Bioclock combination chloride electrode (ISE) with a reference electrode. ISE was filled with a solution of 10 %. potassium chloride. An epoxy body and a silver chloride/silver sulfide membrane for the detection of halide ions have been used to investigate the operating capacity of Cl-resins, as depicted in **Figure 2.15**.

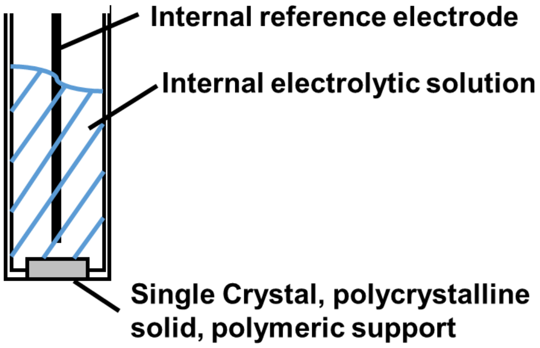

Figure 2.15. Schematic drawing of the ion-selective electrode (ISE).

When ISE is placed in a solution containing the target ions, the diffusion of these across the membrane generates a potential difference. At the equilibrium, the measured membrane potential depends on the activity of ions (effective concentration) in the solution according to the Nernst equation (**Equation 2.14**) [127].

$$\boldsymbol{E} = \boldsymbol{E_0} - \boldsymbol{S} \cdot \log \boldsymbol{a} \qquad \textbf{Equation 2.14}$$

The Nernst equation relates the standard potential, $\boldsymbol{E_0}$ which depends only on the concentration of ions of the filling solution contained in the reference electrode, and the electrode slope $\boldsymbol{S}$ (56 ± 2 mV at 298 K), and the “effective concentration” of the halide ions in solution ($\boldsymbol{a}$). The electrode slop, $\boldsymbol{S}$, expresses the sensitivity of the electrode in mV per decade of activity or concentration (**Equation 2.15**) [127].

$$\boldsymbol{S} = \boldsymbol{P}\,(1000\text{ ppm}) - \boldsymbol{P}\,(100\text{ ppm}) \qquad \textbf{Equation 2.15}$$

where $\boldsymbol{P}$ is the measured differential potential of the solutions (in mV).

The activity, $\boldsymbol{a}$ is the “effective concentration” of a species in solution, and it can be expressed as [127].

$$\boldsymbol{a} = \boldsymbol{\gamma} \cdot \boldsymbol{C} \qquad \textbf{Equation 2.16}$$

where $\boldsymbol{\gamma}$ is the activity coefficient, this coefficient can be derived by Debye and Hückel equation and depends on the total ionic strength, $\boldsymbol{I}$ (**Equation 2.17**) [127].

$$\boldsymbol{I} = \frac{1}{2} \sum \boldsymbol{C}_x \boldsymbol{Z}_x^2 \qquad \textbf{Equation 2.17}$$

In this expression, ***C*** and ***Z*** are the concentration and charge of ion X, respectively.

The accuracy of the potentiometric measurements relies on the ionic strength of the solution. At low ionic strength ($\boldsymbol{C}$ < 0.1 M) the activity coefficient $\boldsymbol{\gamma}$ approaches 1; therefore, the activity is equal to the concentration ($\boldsymbol{a} = \boldsymbol{C}$). However, at high ionic strength ($\boldsymbol{C}$ > 0.1 M), the activity coefficient can increase ($\boldsymbol{\gamma} > 1$); as a consequence, $\boldsymbol{a} \neq \boldsymbol{C}$ [127]. An ionic strength adjuster (ISA) provides constant ionic strength in standards and samples, allowing the gauging of activity of a species rather than concentration.

The operating pH range of the electrode is between 4 and 7 and neutralisation of the solutions with acid and base is necessary to bring the pH in that range. In addition, there is a wide range of ions including, but not limited to, OH^-, NH_3, $S_2O_3^{2-}$, Br^-, S^{2-}, I^-, CN^-, which may interfere with the measurement, so caution should be taken in order to not compromise the analysis.

2.5.3.1. Calibration curve for the analytical determination of halide ions

Before running unknown samples, the electrode was calibrated under the same conditions of temperature (298 K) and ionic strength by using 100 cm^3 of seven standard solutions (1, 2, 4, 6, 10, 100, 1000 ppm Cl^-) prepared by dilution from 1000 ppm stock solution of sodium chloride (NaCl). The salt was dried into the oven at 393 K to drive off the moisture. The electrode slope was recorded from the mV difference of 100 ppm and 1000 ppm solutions as described in **Section 2.5.3**.

2.5.3.2. Determination of operating capacity for the resins in Cl-form by ion-selective electrode

Cl-form resins were dried at 313 K for 24 h and then placed into a desiccator. The experiment was conducted by placing 2 cm^3 of resin (approximately 1.2 g) into a separating funnel and then adding 100 cm^3 of sodium sulfate 0.1 M for 24 hours. Later, the supernatant liquid was recovered into a 250 cm^3 beaker, and 2 cm^3 of ISA was added to the solution. After that, the beaker was placed in a water bath at 298 K to let the solution reach equilibrium and prevent fluctuation of the electrode slope (56 ± 2 mV). The amount of chloride released from the resin was calculated by comparing the unknown potential to a set of standards of known potential. Then, Cl concentration was replaced in **Equation 2.18**.

$$\text{Capacity / meq g}^{-1} = \frac{\boldsymbol{C}\cdot\boldsymbol{V}\cdot(\frac{1}{MM})}{mass_{dry\ resin}} \qquad \textbf{Equation 2.18}$$

where ***C*, *V*,** MM, ***mass*** are the concentration (ppm) and the volume of the Cl^- solution (L), the molar mass of Cl^- (mg/mmol) and the mass of the dry IER (g), respectively.

2.5.3.3. Study of the catalyst activation

In heterogeneous catalysis, an activation process allows conversion of the “unreactive” sites back into active ones. This activation process can involve either gas, chemical or heating, relying on the nature of the sites. DuPont has supplied several resins in their catalytically active forms such as the strong cation exchange resins 15H and 120H in hydrogen form (H^+) and the strong anion exchange resins 26OH and 402OH* in the hydroxide form. Other resins have been supplied in their most stable ionic form, which may not be catalytically active. The process of converting IERs to their desired ionic form occurs by using a regenerant, which is a salt precursor of the counter ion. When IERs are rinsed with a solution of electrolytes, they reach the equilibrium between the ions in solutions and the counter-ions of the polymer.

Selectivity constants define the affinity of a resin for one specific ion over another ion. For instance, Gregor et al. have studied the selectivity coefficients for SBA resins with different cross-linking degrees in different reaction conditions, such as ionic strength and temperature [128]. Their selectivity trend depends on the atomic number, ion valence, concentration of the electrolytic solution, temperature, crosslinking degree and pH solution [129].

The polymers were dried at 313 K for 12 h to drive off any physisorbed water from the sample and leave the sample morphology unchanged. This process involves the use of caustic soda (NaOH) as a regenerator. Before running the unknown sample measurements, a seven-point calibration was conducted as described earlier under the same conditions of temperature, ionic strength, solvent, and pH. A volume of 100 cm^3 of 1 M or 0.1 M sodium hydroxide (NaOH) was poured in a 500 cm^3 vessel. Then 2 cm^3 of chloride resins (approximately 1.2 g) was added to the solution. The reaction was conducted without stirring at 298 K. Aliquot of 100 cm^3 was withdrawn from the reactor to a 250 mL beaker and acidify carefully with HNO_3 70 % until pH 4 by using a pH-meter equipped with a pH electrode. The pH meter has been previously calibrated at 298 K with two buffer solutions (pH= 4.01 ± 0.01 and 10.01 ± 0.01). Then, the beaker was placed in a water bath at 298 K to let the solution reach the thermal equilibrium. After that, 2 cm^3 of ISA was added to the beaker, which was finally analysed immersing the electrode in the solution for at least 15 minutes to allow the electrode in reaching the equilibrium. The concentration of aliquot withdrawn was calculated by comparing its measured potential value to the seven-point calibration curve. Finally, the capacity was determined by **Equation 2.18**.

Furthermore, ESEM-EDS has been used as a complementary technique to estimate the endeavour in the exchanging process and the chloride content. The importance of this investigation was based on the fact that the residual amount of Cl^- onto the polymeric surface can reduce their catalytic performances [80].

2.6. Study of resin accessibility: swelling tests

IUPAC defines swelling as the increase in the volume of a solid because of the uptake process of liquid or gas [130]. The solvent molecules surround the functional groups of the resin and solvate the polymer without dissolving it. The swelling extent relies on the degree of cross-linking, the salt form of resin and the concentration of counter ions [130]. In this work, the swelling tests give insight into the accessibility of reagents into the resin voids and making predictions on their catalytic performances before running the reactions. The swelling degree is expressed in **Equation 1.2** [37].

$$\text{Swelling degree / \%} = \frac{\boldsymbol{V - V_0}}{\boldsymbol{V_0}} \qquad \textbf{Equation 1.2}$$

Equation 1.2 relates the resin volume V_0 in the dry state and the increased resin volume V in the wet state.

For this experiment, the IERs were dried at 313 K for 12h to drive off any physisorbed water within the polymers. The experiment was performed by measuring the resin volume before and after soaking as follows: an amount of 1 cm^3 of pre-treated resins were weighed in a 5 cm^3 cylinder, and 4 cm^3 of solvent was carefully added. The cylinder was thoroughly shaken with a spatula to remove the air bubble. The volume change was recorded after 1 hour. The experiment was conducted using methanol and a mixture of tributyrin and methanol (1:30).

2.7. Catalytic tests

Catalyst testing is the evaluation of the catalyst performance in a chemical process [131]. Testing to find high-performance catalysts involves a range of experiments varying the experimental parameters such as temperature, stirring rate, molar ratio and amount of catalyst.

2.7.1. Catalyst activation and preparation

Ion exchange resins can store a significant amount of polar liquids, such as water and alcohol [132]. IER pre-treatment is highly recommended to remove excess liquid that could affect their performance [132, 133]. The polymer resins in this study were all pre-treated using the following method. The catalysts in OH and H forms as received from the supplier were pre-treated in the atmospheric oven at 313 K for 12 h. This drying process should drive off any physisorbed water from the resin sample, leaving the sample morphology unchanged. The resins received from the supplier in Cl-form were dried at 313 K overnight to drive off the physisorbed water for promoting the activation process. Then, they were converted into the hydroxide form using a 0.1 M NaOH solution. For the preparation, 1 g of polymer was weighed out and transferred into a 150 cm^3 beaker. After that, 25 cm^3 of 0.1 M NaOH was added. The solution was shaken, sealed with a lid, and immersed in a water bath at 298 K for 24 h. Afterwards, the resins were washed with deionised water until the pH of the solution reached neutrality. The pH was measured by pH strips. Finally, a paper filter was used to remove excess of water from the resins. To aid the reader, the catalyst activation of the IERs is summarized in the flow diagram shown in **Figure 2.16**.

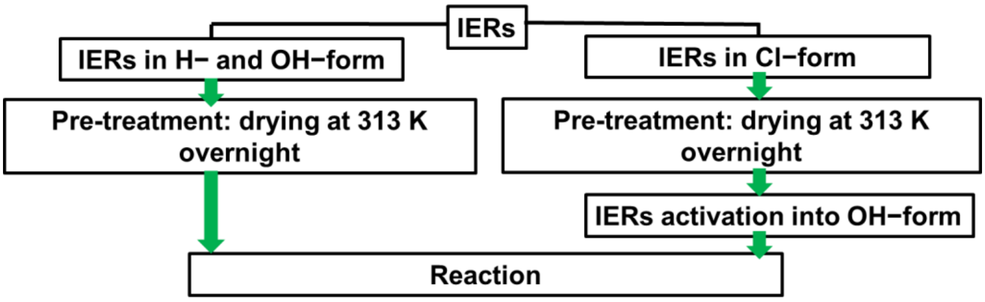

Figure 2.16. Flow diagram explains the stages of the IER activation and pre-treatment used in this study for preparing the resins in order to catalyse the transesterification reactions of tributyrin with methanol.

2.7.2. Calibration curves

Calibration is essential for determining the unknown concentration of analyte. The instrumental response, the ratio between the peak areas of analyte and its internal standard, is plotted against the concentration of analyte. The comparison of the unknown response to a set of standards of known responses of known concentrations determines the unknown concentration of analyte.

The most concentrated standards of tributyrin (TB) and methyl butyrate (MB) were prepared with methanol as follows: 26 mmol of TB and 70 mmol of MB were weighed out into a 10 cm^3 volumetric flask and then filled with methanol. These solutions were diluted by 50% using a 5 cm^3 pipette to prepare the next solution, as shown in **Table 2.2**.

Table 2.2. Nominal millimoles for the individual standard solutions used for tributyrin (TB) and methyl butyrate (MB) to fit the calibration curves.

Solution number	**Nominal mmol** (TB)	**Nominal mmol** (MB)
1	13.0	35.0
2	6.5	17.5
3	3.2	8.8
4	1.6	4.4
5	0.8	2.2
6	0.4	1.1

After that, 2.5 mmol of mesitylene as internal standard for GC was added to each solution. Then, 0.2 cm^3 of each solution was transferred into a 5 cm^3 GC vial and diluted with dimethyl chloromethane (DCM). Finally, each solution was analysed by a Shimadzu AOC-2oi with auto-injector fitted with a BPX50 capillary column and equipped with a flame ionisation detector (FID). This technique is described in **Section 2.7.5**. The analysis for each vial was repeated three times.

2.7.3. Catalytic performance testing

The transesterification reaction was done in a three-neck round-bottom flask (25 cm^3), mixing the solution with a magnetic stirrer, under atmospheric pressure at 313 K and 333 K (**Figure 2.17**).

The solution was prepared by mixing 2.5 mmol of internal standard, mesitylene, 10 mmol of tributyrin (TB) and 300 mmol of methanol (MeOH) in the flask (molar ratio MeOH and TB 30:1). A stirring rate of 500 rpm was used to provide a homogeneous mixture, and the reaction was heated for 10 minutes to reach thermal equilibrium. Then, 50 mg of active resin was added to the homogeneous solution. Aliquots of 0.2 cm^3 were sampled over three hours, filtered with a plugged Pasteur pipette, diluted with DCM in 5 cm^3 vials and analysed by using a Shimadzu AOC-2oi with auto-injector fitted with a BPX50 capillary column and equipped with a flame ionisation detector (FID). This technique is described in details in **Section 2.7.5**.

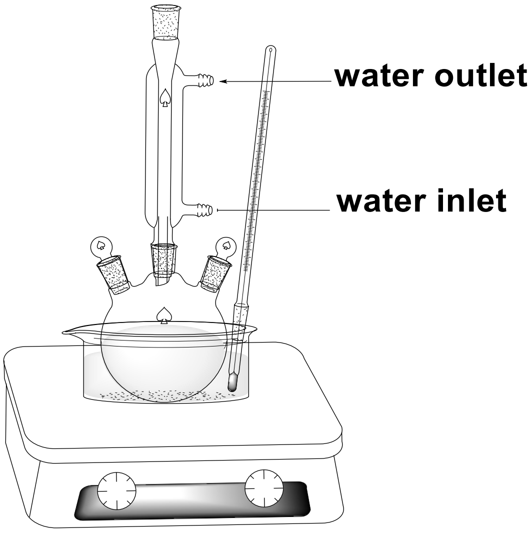

Figure 2.17. Schematic representation of the reactor used for running transesterification reaction.

The measurement for each vial was repeated three times. The average of that measurement was replaced in the calibration curves. Their concentrations were calculated by replacing area value in the appropriate calibration curve. The gauging of conversion (%) and product selectivity (%) was obtained from **Equation 2.19 a** and **b** [134].

$$\text{Conversion / \%} = \frac{n_{TB(0)} - n_{TB\,(t)}}{n_{TB(0)}} \cdot 100 \qquad \textbf{Equation 2.19 a}$$

$$\text{Product selectivity / \%} = \frac{n_{MB(t)}}{n_{TB(0)} - n_{TB(t)}} \cdot \frac{1}{3} \cdot 100 \qquad \textbf{Equation 2.19 b}$$

where $n_{TB(0)}$ is the mmoles of tributyrin at time 0 while $n_{TB(t)}$, and $n_{MB(t)}$ are the mmoles of tributyrin and methyl butyrate at time ***t*,** respectively.

This study was limited by the access to laboratories and research support facilities. Due to these practical constraints, replicates for the catalytic tests could not be undertaken.

2.7.4. A chemometric approach: design of experiment

Chemometrics is a branch of chemistry that employs statistical and mathematical methods to explain data and to find the most significant chemical information [135]. In this work, a design of experiment (DoE) has been conducted to study the performance of the most active catalyst by doing a set of tests in which temperature, stirring rate, molar ratio and amount of catalyst have been varied. Studying these variables at the same time can be more productive than traditional one-at-a-time designs, which study one variable at a time keeping the other variables constant. The one-at-a-time design can be easily analysed and performed.

However, the large number of experiments involved makes it expensive, environmentally unfriendly and time-consuming. A DoE protocol needs to be carefully planned, in three stages. The first stage is to decide the goal and to evaluate the range of interest for all the variables. The reliability of the result of the experiment depends on the selection of the variables [136]. Then, the second stage is to plan and perform the tests. Finally, the third stage is a model validation, which verifies the reliability of the information obtained from DoE with the experiments.

The choice of DoE is a compromise between the number of experiments needed and the detail of the information in the output. To run a factorial model, the experimenters need to select an established number of levels for each factor or variable and then run the tests with all variable combinations. If the experiment involves l levels for each factor k, the design will be a combination of l^K runs. These levels are coded as +1 and −1 for the higher values and lower values, respectively and the sign of interaction among two variables, variable 1 and variable 2, is their product. The DoE responses are the outcome of the experiment performed.

In our case, 2^4 factorial experimental design was designed for studying four factors (temperature, molar ratio tributyrin to methanol, catalyst load, and stirring rate) which can be expressed using two levels. The responses are tributyrin conversion and methyl butyrate selectivity. The responses can be described as function of the experimental variables x_{ij} and the residual. In this work, the responses were conversion and selectivity and the interaction model adopted is represented in **Equation 2.20** [136].

$$\mathbf{Y} = \boldsymbol{b_0} + \sum_{i=1}^{k} \boldsymbol{b}_i x_i + \sum\sum_{i<j} \boldsymbol{b}_{ij} x_i x_j + residual \qquad \textbf{Equation 2.20}$$

Y is the response, $\boldsymbol{b_0}$ is a model constant; $\boldsymbol{b_i}$ are linear coefficients; $\boldsymbol{b_{ij}}$ are cross product coefficients and residual which corresponds to difference between the estimated by the model and the experimental results, so called experimental error.

This model estimated the coefficients by establishing relationship between the responses ***Y***, x_i and x_j and to determine the magnitude of variables.

The statistical investigation is based on a hyphothesis test [137]. This test involves two hyphothesis: the null hypothesis, $\boldsymbol{H_0}$ which is a statement to be tested and the alternative hyphothesis is an alternative statement, $\boldsymbol{H_A}$, to the null hypothesis. $\boldsymbol{H_0}$ is a hypothesis that assumes no relationship between the studied variables [137]. In our case, the null hypothesis is the term's effects of the reaction parameters are equal to zero, so there is no relationship between terms and responses [137]. The criterion selected to reject H_0 is called test statistic. The test statistic is a numerical value computed from data set [138]. Two statistical approaches, such as p-value and critical value are used to validate the rejection of the null hypothesis [138]. For the p-value approach, the probability of the test statistic (p-value), is compared with the significance level, alpha (α) [138]. Alpha is set at 0.05, which indicates there is a 5 % risk of rejecting the null hypothesis when this hypothesis is true [139]. This measures the probability of the investigated significant effects occurring by chance. P-value is an index of α to valuate evidences against null hypothesis. P-value < 0.05 points out that there is less than a 5 % probability null hypothesis is correct and, the result is statistically significant. While p-value > 0.05 indicates evidence of null hypothesis and the result is not statistically significant [139]. The p-values are calculated by the software and reported in the table of the estimated coefficients for the interaction model equation (**Equation 2.20**). The critical value is calculated based on the significance level, α and the probability distribution model and the test statistic is compared with the critical value. The critical value is represented as line in a Pareto chart. This chart is a graphical representation of the tables of the main and interaction effects. It consists of a histogram plot where the bars representing the variables and their interactions show the effect magnitude of each factor in descending order, as illustrated **Figure 2.18**.

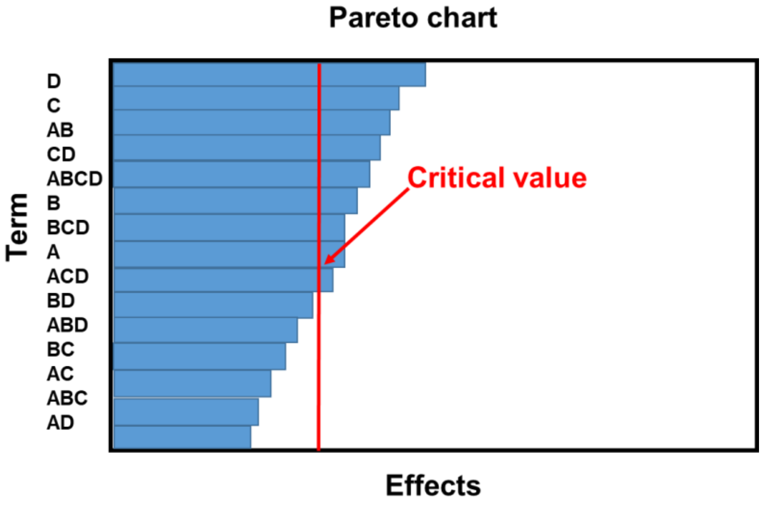

Figure 2.18. Illustration of a Pareto chart.

When the variables show a normal distribution, the critical value defines the region of rejection at α level [139]. The effects reaching beyond the critical value are statistically significance [139].

Minitab 1.4 was used as a statistical and graphical software package to interpret data. Sixteen experiments were performed and the data collected from the testing runs were used to construct the model having conversion and selectivity as responses to the variables and the levels of the four factors are represented in **Table 2.3**.

Table 2.3. Level 1 and level 2 of four factors for the DoE.

Factor	**Code**	**Temperature** / K	**Molar ratio** TB:MeOH	**Catalyst loading** / mg	**Stirring rate** / rpm
Level 1	−1	313	1/4	10	100
Level 2	+1	333	1/30	50	500

2.7.5. Gas-liquid chromatography

Gas-liquid chromatography (GLC) is an analytical separation technique for qualitative and quantitative analysis to analyse volatile substances in the gas phase by using a column. The sample components are dissolved in a solvent and vaporised by separating the sample throughout repartition in the two phases: a stationary phase and a mobile phase. The stationary phase is a liquid, which is held on the surface of an inert solid by adsorption or chemical bond. In contrast, the mobile phase is a gas, which has the only function of transporting the molecules of the analyte throughout the column and must be chemically inert such as helium. **Figure 2.19** illustrates the gas chromatography apparatus used in this work.

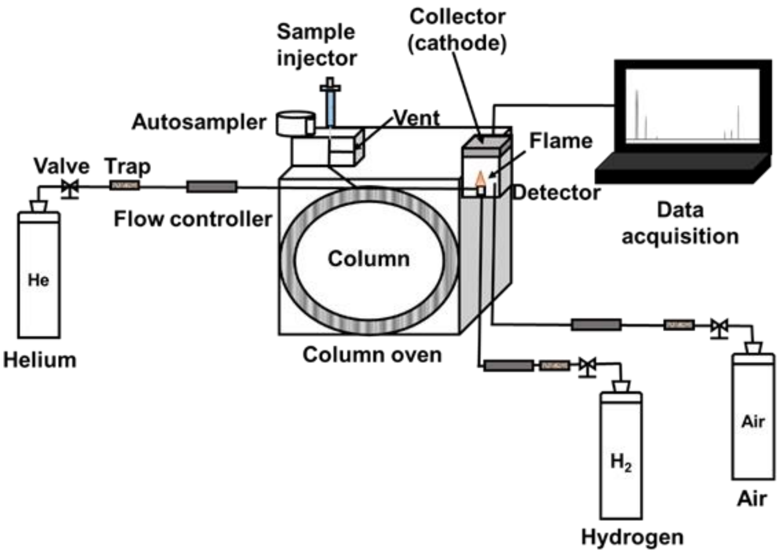

Figure 2.19. Schematic representation of a gas-liquid chromatography apparatus used for the catalytic tests.

Helium is purged from a cylinder and passed through a water trap, and a flow valve controlled the flow rate. The sample was injected using a graduated microsyringe through the sample port, which was kept at 323 K over the boiling point of the less volatile component. The sample was vaporised and carried by helium. Then, the split inlet diluted it with a ratio of 1:20.

As a result, a small fraction entered the capillary column, and the rest portion vented out. The capillary column fitted in the GC was a BPX50 (30.0 m×0.32 mm×0.25 µm; max T: 623 K).

As the components of the sample had a wide boiling point range, a two-step temperature program has been used, as shown in **Table 2.4**.

Table 2.4. Temperature program for the BPX50 capillary column employed in this work.

Rate / K min^{-1}	Temperature / K	Hold time / min
-	323	1.00
15	553	4.00

The column flow velocity is monitored by a flow controller to insure a flow velocity of 2.54 cm^3 min^{-1}. The output of the column is directed and analysed by a flame ionisation detector (FID). The detector works on the principle that most organics generate electrons and ions from their combustion in a hydrogen flame, and this process produces an electric current that is detected by a collector. The signal is translated into a chromatogram, as shown in **Figure 2.20**. The FID is widely used for the analysis of oil, alcohols, antioxidants, and biodiesel [140].

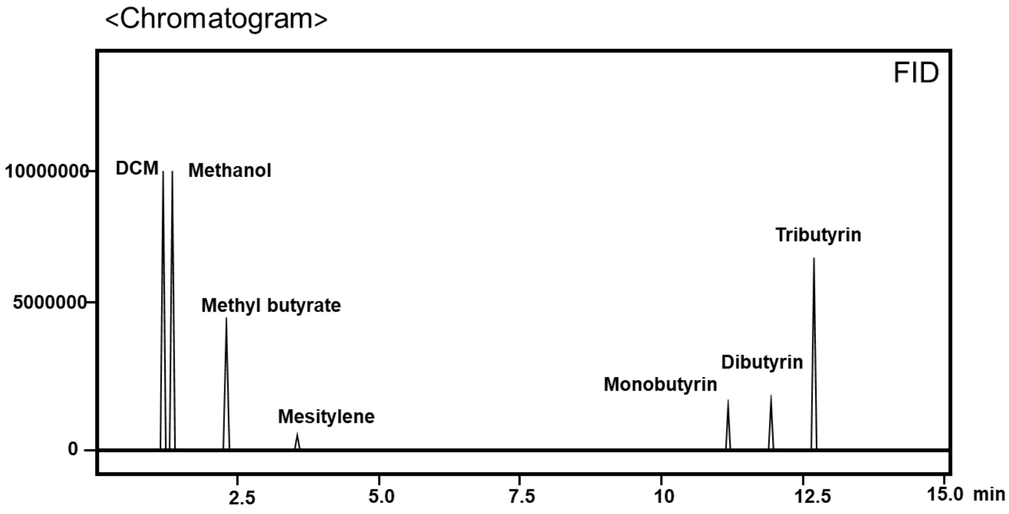

Figure 2.20. Typical chromatogram for tributyrin transesterification.

Chapter 3
Characterisation of ion exchange resins

3.1. Introduction

Heterogeneous catalysts are indispensable materials for industrial processes [27]. Approximately 85-90 % of chemical products are produced by catalytic processes [27]. The catalysts can modify reaction pathways in such a way that higher selectivity towards the desired product is achieved [27]. To better understand and correlate the catalyst properties with its structure, characterisation is a crucial research stage.

Among the heterogeneous catalysts available in the market, ion exchange resins have been widely used as catalysts in industry over the last decade [27]. Despite their industrial use such as ion exchange water softeners, the resins characterisation has mostly addressed the transport model of solutes within resin in chromatography [141]. The use of IERs as catalysts requires that the resins be fully characterised in terms of morphology, capacity and swelling in a reproducible way. Several papers have investigated IER morphology in the dry and wet state by nitrogen porosimetry and Inverse Size Exclusion Chromatography (ISEC) and the operating capacity using direct titration [141-144]. A methodology for characterisation of the tested IERs in catalytic field is still to be addressed.

The characterisation of IERs is complicated by a number of issues including the thermal decomposition of acidic and basic functional groups in aqueous solution even at low temperature, the presence of a large amount of water within the material that makes the results of standard techniques, such porosimetry, challenging to interpret, and the solvent-responsive behaviour of the resins, which induces a rearrangement of the polymeric morphology in both the dry state and the swollen state [144]. The term dry state indicates the water within the polymer is removed by drying while the swollen state is used when the polymer has been placed in a solvent. In this case, the polymer swells and increases in volume by spontaneous absorption of fluids [145]. The polymer matrix swells in the presence of a medium that can be liquid or gas by solvating the polymeric chains. Macroreticular resins consist of micro-gel particles interdispersed within macropores [18, 37]. The macroporosity is permanent in the dry state [146]. The opening of the non-permanent micro and mesopores of the micro-gel phase occurs only when in an aqueous medium [144]. In the swollen state, macroreticular resins exhibit three types of pores: macropores from the permanent porosity, mesopores formed by the swelling of the matrix and, micropores of non-swelling part of the matrix [146]. Gel-type IERs are characterized by a non-permanent porosity in the dry state [144]. Similarly, the opening of the mesopores occurs using a medium [144]. In the swollen state, gel-types consist of two types of pores: micropores of the unattainable part of the matrix and new mesopores formed by the swelling [146]. **Figure 3.1** illustrates the morphology of the macroreticular and gel-type resins in the dry and swollen state.

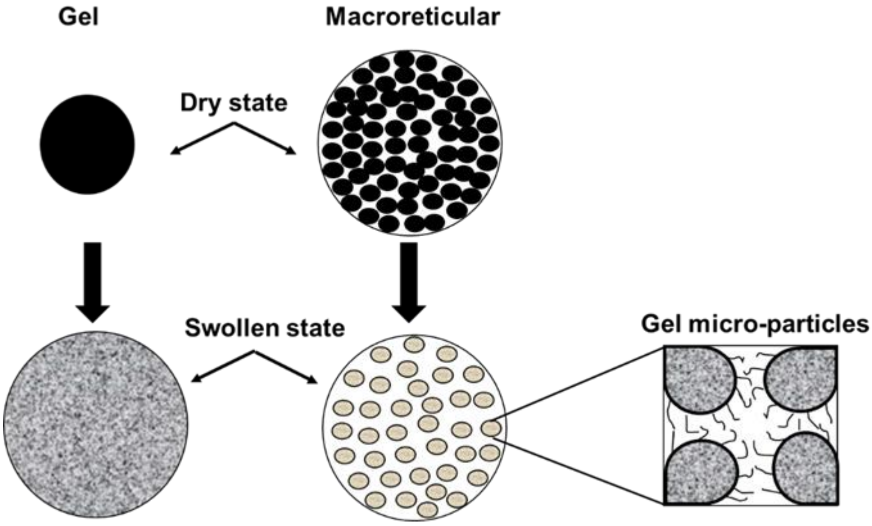

Figure 3.1. Schematic illustration of dry and swollen morphology of the IERs. Gel types IERs exhibits a non-permanent porosity in the dry state while macroreticular resins permanent macropores and non-permanent micropores. The thick arrows point out the morphology changes from dry state to swollen state, opening mesopores of both gel-type and macroreticular IERs (Reproduced from [147] [147]).

IERs possess highly uniform functional groups (1-4 mmol g^{-1}) distributed through the matrix [148]. By opening the mesopores of both gel and macroreticular IERs, swelling enhances the accessibility of the molecules towards their inner part [148]. In the inner parts reside the majority of functional groups immobilized onto the resins [148]. Morphology, accessibility, swelling and capacity are the main characteristics of IERs that are associated with their catalytic activity [142]. Several works have demonstrated that the solvent-responsive morphology of IERs affects the accessibility of uniform functional groups, influencing catalyst activity [142, 143, 148, 149]. In recent work, Soto et al. have studied the etherification reaction of 2-ethoxy-2-methylpropane and 2-ethoxy-2-methyl butane over fifteen-macroreticular acidic resins [143]. They found that the production of 2-ethoxy-2-methylpropane and 2-ethoxy-2-methyl butane were correlated with the highest acidic capacity and the lowest swelling volume [143].

In this chapter, a comprehensive characterisation of the IERs used in this study was conducted by the use of various techniques and analytical methods, such as back titration and swelling tests to describe IER behaviour under operating conditions and to provide guidelines for selecting the most suitable IERs for promoting the transesterification reaction. The macroreticular 26OH and gel-type 402OH* have been selected as representatives of the investigated resins. For a full comparison, the data acquired for all IERs used in this study can be found in **Appendix A**.

3.2. Morphology and thermal analysis of ion exchange resins

The morphology of polymers such as specific surface area, pore size and pore size distribution (PSD) can be studied using nitrogen physisorption at the boiling point of the liquid nitrogen. Nitrogen physisorption is a standard experimental technique, which allows a comparative study of the IER textural properties with benchmark values available in the literature [150]. However, this analysis requires a dry sample, which is obtained by outgassing processes [150]. Outgassing is a cleaning process for clearing away adsorbed gases from the surface sample by a combination of vacuum, heat and purging with inert gases [151]. In the case of a dried polymer, measurement of specific surface area and morphology can be unrealistic because the drying process may induce a dramatic modification of the polymeric structure, leading to an inaccurate structure interpretation [150]. Thus, when samples are prepared for analysis, the first thing to be checked is the temperature at which the material may decompose. Caution is needed when outgassing any polymer sample. It is crucial to keep the temperature low enough to avoid any change of the material. Too high a temperature may cause irreversible damage to the sample by one of several mechanisms: melting, decomposition, sintering and annealing [152]. Melting is a physical process by which materials change state from solid to liquid. Decomposition is a process that involves the physical breakdown of molecules of the material into smaller species. Sintering is a heat treatment, which occurs *via* diffusion of atoms and involves the formation of particles into an agglomerate. This process can occur on both the surface and inside the pores. It is associated with materials with either low glass transition point, $\boldsymbol{T}_g$ or melting point, $\boldsymbol{T}_m$ [152]. A glass transition is a thermal event that changes the polymer state, defining the operational state of the polymer [153]. As $\boldsymbol{T}_g$ increases, the polymer chains change from a disordered glassy state to a slow-moving rubbery, as illustrated in **Figure 3.2** [153, 154].

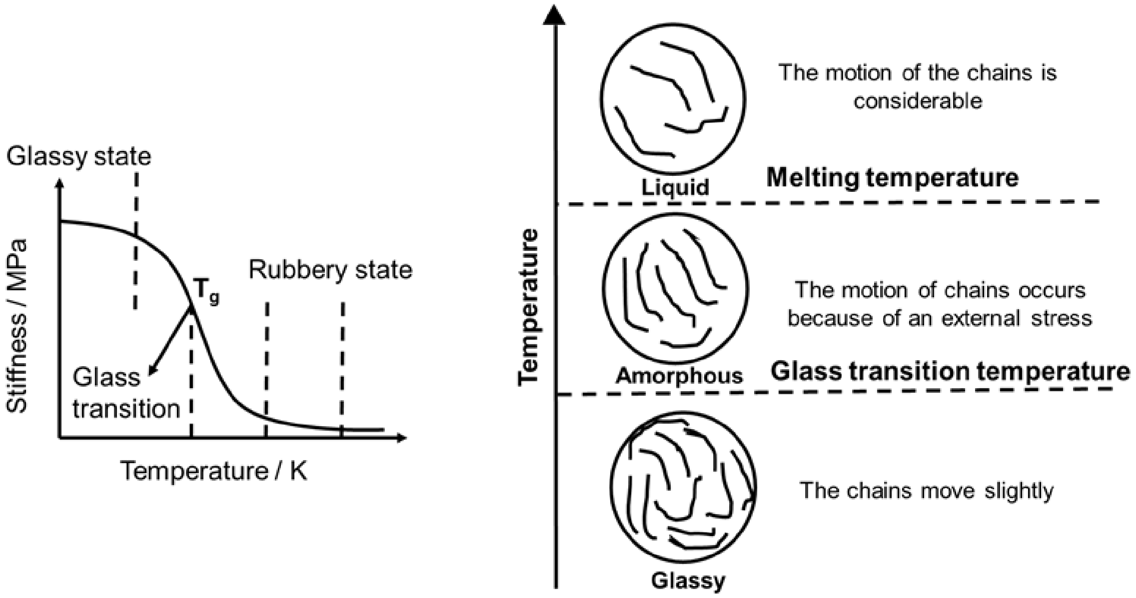

Figure 3.2. Schematic representation of the glass transition. The polymer goes through a glassy state to rubbery state when the temperature is continuously increased (Reproduced from [153]).

Annealing, on the other hand, drives a surface arrangement, lowering both surface energy and tension of the material [152]. This mechanism smooths the roughness of the surface and decreases the specific surface area [152].

However, too low an outgassing temperature may also affect the analysis of the specific surface area and underestimate the porosity because of water molecules trapped in the micro-pores, rendering these pores inaccessible for measurements [155]. As the nitrogen approaches the surface of the sample, water can either hamper its pathway or freeze during the measurement, giving rise to artefacts, such as reduced specific surface area [156, 157]. Water removal is a low energy process, requiring ca. 10-20 kcal mol^{-1}, but the material tortuosity can obstruct the removal rate of water [152]. Ideally, the outgassing temperature should be low enough to remove the physisorbed compounds such as water from the surface of the solid without altering its properties. However, too low an outgassing temperature will prove incapable of removing physisorbed molecules from the sample, and equilibrium time can generate large hystereses named low-pressure hysteresis (LHP) in both hard and soft materials [158, 159]. Hard materials, such as zeolites, highly ordered mesoporous silica materials and activated carbons, are resistant to shape change when a force is applied [160]. However, soft materials, such as gel and polymers, are easily deformed by thermal stress and fluctuations [160, 161]. LHP appears when the desorption branch lies parallel to the adsorption branch, meeting the adsorption branch at relative pressure ***p/p***° below 0.4. The closure point of the hysteresis depends on the gas probe and the nature of adsorbent [106].

In the case of nitrogen, the closure point of the hysteresis is never below ***p/p***° of 0.4 [106]. Traditionally, hysteresis occurs in multilayer range of the isotherm, and it is correlated to the filling and emptying of the mesopores [106]. The isotherm braches are important for the measurement of pore size and PSD of a porous material.

As aforementioned, the lack of thermodynamic equilibrium physisorption can also generate LHP in a nitrogen adsorption-desorption analysis [162]. This is verified by using long equilibration time. The nitrogen adsorption-desorption analysis is a discontinuous, point-by-point measurement of the volume of nitrogen adsorbed against ***p/p***° [106]. During the analysis of each point, the equilibration time is the interval of time in which the pressure in the cell must be constant and lower than the pressure tolerance within equilibration timeout so that the point measured is validated [156]. Prior to the analysis, the equilibration time and equilibration timeout are set, depending on the nature of material [156].

Another origin of LHP was proposed six decades ago; it was hypothesized that the swelling of the material could cause the opening of the inner area during the analysis [163]. Four decades later, Reichenauer and Scherer have found that this type of hysteresis was likely due to the deformation of the adsorbent caused by its bulk modulus [164]. Some very recent studies developed by Jeromenok *et al.* and Hart *et al.* have confirmed this hypothesis based on atomistic simulation and experimental results; the source of the LHP hysteresis is the expansion of the matrix with nitrogen molecules (swelling-volume) and the opening of non-permanent pores [159, 165]. Moreover, in a recent work, Weber *et al.* have attributed the large hysteresis to the swelling of the polymeric matrix due to the dual-mode sorption [166]. The dual-mode sorption was observed on non-porous polymeric films and membranes; this model supposes that free volume pores in the polymer are filled quickly by the gas molecules while further sorption occurs within the framework (swelling), and it is known as Henry sorption [166]. This sorption is associated with the formation of new pores (volume-swelling) and linearly dependent on the pressure, as illustrated **Figure 3.3** [167].

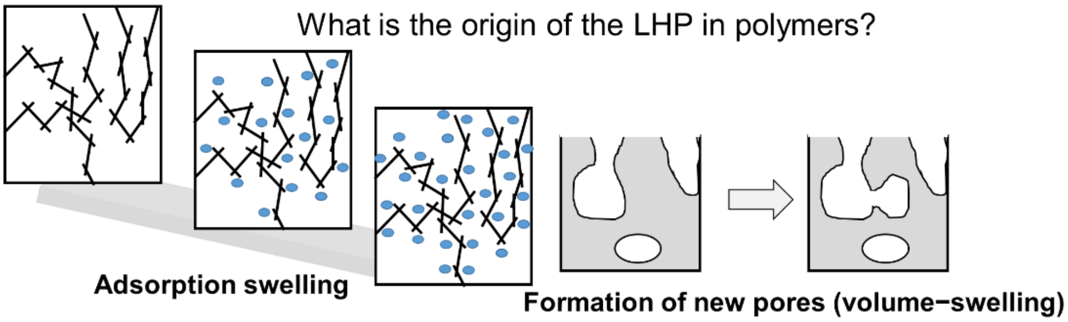

Figure 3.3. The adsorption swelling involves the gas molecules which surround the polymer matrix, lowering its rigidity and forming new pores (volume-swelling) (Reproduced from [159, 165]).

The increasing permeability of the gas molecules changes the polymer properties such as reduced stiffness [166]. This process is named plasticization. In addition, atomistic simulations on linear and cross-linked PIMs have confirmed that the large hysteresis is the result of the swelling of the polymer in a cryogenic environment [166, 168].

Another explanation for these gas sorption hystereses was proposed by Jeromenok *et al.* [159]. This investigation used N_2, Ar and CO_2 as gas probes, obtaining comparable hysteresis-types. Jeromenok and Weber believed that the LHP could be associated primarily with a diffusion due to open and limited-access pore rather than volume-swelling [159]. **Figure 3.4** illustrates their explanation for low-pressure hysteresis.

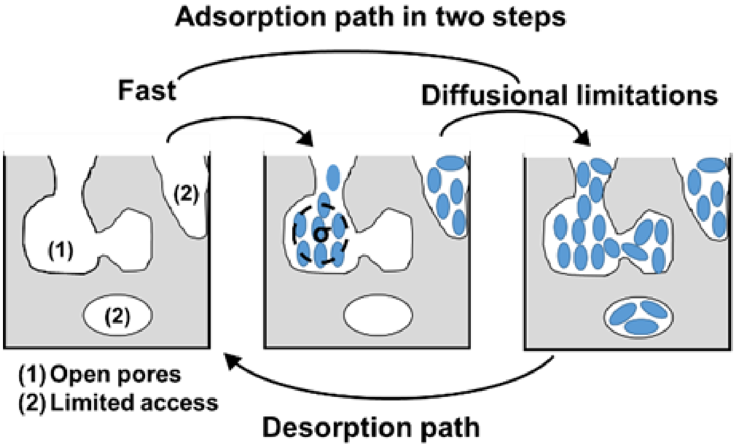

Figure 3.4. Schematic representation of filling and emptying process of (1) open and (2) limited access pores (Reproduced from [159]).

The well-connected pore would be readily filled with gas molecules while closed pores, characterized by their narrow entrance, would not be loaded as quickly due to limited access.

Condensation of the fluid into narrow pores occurs according to the solvation pressure $\boldsymbol{\sigma}$, which is correlated to the pore topology. Thus, this process leads to open hysteresis. It was also found that a longer equilibrium time for an acquired point does not alter the gas uptake [159].
In the case of an LHP isotherm, the condensation-evaporation process is complex and reliable parameters such as pore size and surface area can be derived unless some conditions are met. Prior to applying any method for the measurement of the pore size, the shape of the loop should be classified, and its reproducibility verified [106, 164]. This allows applying the appropriate kernel of the selected method, e.g. NLDFT-cylindrical pores. Traditionally, the porosity of macroreticular IERs is described using cylindrical pores model [144]. Barrett, Joyner, and Halenda (BJH) method derives the pore size distribution of the mesopore region from the desorption branch and is based on the assumption that pores are cylindrical. This model underestimates mesopores smaller than 10 nm ca. 20-30 % [169].
The average pore diameter, $<\boldsymbol{d}_p>$, was gauged using **Equation 2.9** introduced in **Chapter 2** [116]. To aid the reader, the equation is reproduced here.

$$<\boldsymbol{d}_p> / \text{ nm} = \frac{4000 \cdot \boldsymbol{V}_{p/p^o=0.99}}{\boldsymbol{S}_{BET}} \qquad \textbf{Equation 2.9}$$

where $\boldsymbol{V}$ is the pore volume at $\boldsymbol{p/p}°$ 0.99 and $\boldsymbol{S}_{BET}$ is the specific surface area.

In contrast to the BJH method that can be applied to mesopores, the non-local density functional theory (NLDFT) method estimates PSD of micro- and mesopores [114]. The main pitfall of this method is that the PSD depends on NLDFT kernels used. NovaWin 11.0 provides several DFT kernels for treating nitrogen adsorption measurements on porous materials, such as silica and carbons. To the best of our knowledge, no NLDFT kernels are available commercially for studying polymers such as IERs. Any application of the NLDFT method on a material depends on the kernel used. To the best of our knowledge, no NLDFT kernels are available commercially for studying polymers such as IERs. The NLDFT kernel selected for this study was nitrogen adsorption at 77 K on silica with cylindrical pores, which resembles mostly the polymeric network. Enviromental scanning electron microscope (ESEM) imaging gives information on the surface morphology of materials. ESEM imaging can support the results of porosimetry and thermoporosimetry.
As pointed out above, N_2 sorption measurements require the catalyst to be completely dry. Thus, the determination of the IERs morphology with N_2 adsorption-desorption can be inappropriate, and it will not reflect their morphology under operating condition. In the past, the IERs parameters obtained from this technique, such as pore size, pore size distribution, pore

volume were simply listed, with no explanation of the large hysteresis. To gain a better understanding of the solvent-responsive morphology of IERs, measurements can be made based on swollen polymers which preserve their polymer morphology [150].

The characterisation of swollen polymers was addressed by means of several approaches, such as thermoporosimetry (TPM) [120]. Iza et al. have evaluated the pore diameter of hydrogel using TPM and water as a probe [120]. The radius of cylindrical pores was measured using **Equation 2.11** introduced in **Chapter 2** [120]. To aid the reader, that equation is reproduced here:

$$\boldsymbol{r_p} \,/\, \mathrm{nm} = -\frac{32.33}{\Delta \boldsymbol{T}} + 0.68$$ **Equation 2.11**

where $\boldsymbol{r_p}$ is the pore radius, and $\Delta\boldsymbol{T}$ is the melting point depression which is the difference between the bulk melting temperature and the cluster temperature $\Delta\boldsymbol{T} = \boldsymbol{T_{mB}} - \boldsymbol{T}_m(\boldsymbol{r})$.

The BET method estimates the specific surface area. It is based on the simplified physisorption model in which no interactions occur between nitrogen molecules [106]. Surface area, $\boldsymbol{S_{BET}}$, was measured using **Equation 2.5** introduced in **Chapter 2** [106]. To aid the reader, that equation is reproduced here:

$$\frac{1}{\boldsymbol{V}\cdot\left(\left(\frac{\boldsymbol{p}}{\boldsymbol{p°}}\right)-1\right)} = \frac{1}{\boldsymbol{V_m}\cdot\boldsymbol{C}} + \frac{\boldsymbol{C}-1}{\boldsymbol{V_m}\cdot\boldsymbol{C}}\cdot\left(\frac{\boldsymbol{p}}{\boldsymbol{p°}}\right)$$ **Equation 2.5**

By plotting $1/[\boldsymbol{V}(\boldsymbol{p}°/\boldsymbol{p}) - 1]$ against $\boldsymbol{p}/\boldsymbol{p}°$ the value of monolayer capacity, $\boldsymbol{V}_m$, is extrapolated and substituted in **Equation 2.7** to obtain the specific surface area, $\boldsymbol{S_{BET}}$ [107].

$$\boldsymbol{S_{BET}} = \boldsymbol{V_m}\cdot N_{\mathrm{A}}\cdot\frac{\boldsymbol{\sigma_m}}{adsorbent\ mass}$$ **Equation 2.7**

where $\boldsymbol{\sigma_m}$ is nitrogen cross-sectional area (0.162 nm^2), Avogadro's number N_{A} (6.023×10^{23} mol^{-1}) and inversely proportional to the adsorbent mass.

The values of specific surface area may be unrepresentative, even when the BET plot can be successful from a mathematical point of view. The data is considered acceptable if the correlation coefficient, R^2, is greater than or equal to 0.99.

3.2.1. Thermal study to select the outgassing conditions of ion exchange resins

The functional groups on copolymers undergo thermal decomposition at elevated temperature in water [55, 170, 171]. As pointed out in **Chapter 1**, the benzylic trimethylammonium groups attached to the polymeric backbone of strong anion exchange resins undergo thermal degradation, promoted by its counterion OH^- [55, 172]. This degradation makes these resins unstable at a temperature above 333 K [172]. Similarly, at high temperature, the sulfonic groups attached to the copolymer of strong acidic resins can undergo deactivation due to the loss of these groups [173]. These resins are unstable at temperatures above 393 K [173]. The degradation of the IER functional groups can affect their catalytic performances when the transterification reaction is performed with the higher reaction temperatures of 333 K and 393 K for anionic and cationic resins, respectively.

Previous work focussed only on the decomposition of the functional groups in water operation; little is known about thermal behaviour of the dried IERs. Several authors have investigated the thermal degradation of these resins by using thermogravimetric analysis (TGA) [49, 171]. To the best of our knowledge, there is no study that uses differential scanning calorimetric (DSC) analysis to investigate the thermal degradation process and the glass transition point ($\boldsymbol{T_g}$) for the resins. DSC can unravel the role of the water in the polymer [174]. Moreover, it appears that the chemistry of these resins is linked to the availability of their ionic groups, quaternary ammonium hydroxide or sulfonic acids, and the interactions that these species can establish with water molecules [144].

Thermogravimetric and differential scanning calorimetric analyses obtain a comprehensive behaviour of the resins at different temperatures and estimate the required outgassing conditions for the study of the morphological properties to avoid any modification of the material [106].

Throughout this section, the terms TG and DTG are used to refer to thermogravimetric analysis and the first derivative of TG, respectively. TG analysis gives the mass losses during the heating analysis, while the first derivative TG or rate mass change (DTG) profile indicates the reactivity of materials [175]. TG and DTG curves are represented by black and blue lines, respectively. TG and DTG curves of the 26OH and 402OH are displayed in **Figures 3.5 a** and **b**. TG and DTG profiles have shown three significant mass losses in **Figures 3.5 a** and **b**. These losses are termed as mass loss 1, mass loss 2 and mass loss 3 in **Table 3.1**. These masses are related to the dehydratation process, the decomposition of the functional groups and the decomposition of the matrix, respectively.

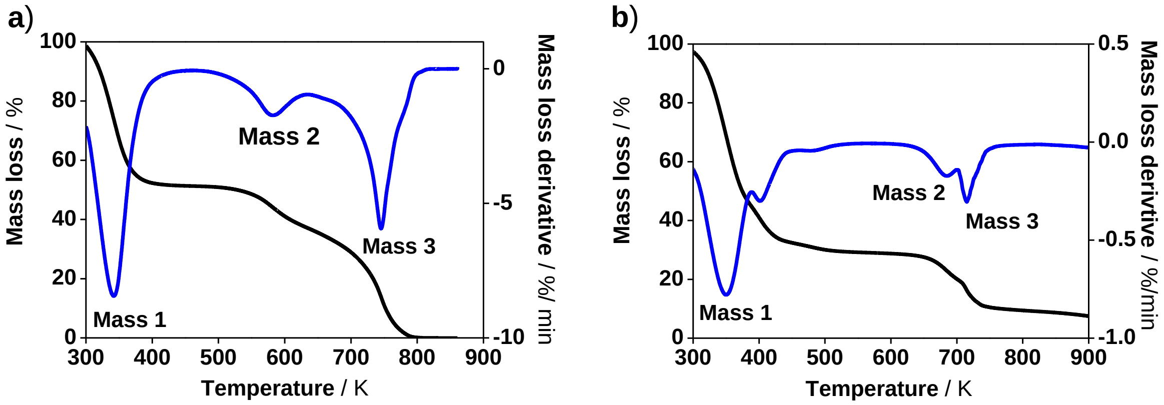

Figure 3.5. TG (black line) and DTG (blue line) curves (%) under nitrogen (20 cm^3 min^{-1}) of: (**a**) 26OH and (**b**) 402OH*.

Table 3.1. Mass losses (%) of the IERs.

IERs	Mass loss 1	Mass loss 2	Mass loss 3
	Water	Functional group	Polymeric backbone
	300-500 K	500-680 K	680-800 K
	/ %	/ %	/ %
26OH	49	19	32
458Cl	54	31	7
958Cl	70	18	6
410Cl	41	24	20
402Cl	64	17	11
402OH*	68	6	14
15H	43	20	12
120H	48	20	4

Figures 3.5 a and **b** show that thermal decomposition occurs through three steps, consistent with previous findings in the literature [58]. The first mass loss, typically occurring between 300 and 500 K, is related to the dehydration process.

The DTG peaks of dehydration indicates the same magnitude of the dehydration rate for the majority of the polymers (-10 % min^{-1}), suggesting a strong interaction between water and polymer. Gel-type IERs 402OH* and 120H showed lower dehydration rate of -1 and -5 % min^{-1}, respectively. These lower rates suggest a weaker polymer-water interaction or no critical role of water in the structure for this pair of IERs. The degradation of the functionality follows, occurring in the temperature range of 500-680 K. By comparing the gel-type IERs, 402Cl and 402OH*, in the latter the DTG peak is shifted to the left at lower temperatures, as quaternary ammonium hydroxide begins to degrade earlier than quaternary ammonium chloride.

Nevertheless, the macroreticular 26OH did not experience this degradation of its functional group at low temperature caused by hydroxide in the quaternary ammonium groups because of structural properties, such as stiffness, that make it more stable to thermal stress. At higher temperature, the polymer underwent further degradation, which occurred within a temperature range of 680 K-800 K in several steps due to the decomposition of the polymeric backbone. Polymer degradation did not occur until the temperature was high enough to contribute to its destruction (approximately 700 K). The dehydration stage indicates the amount of water within the polymers and the temperature at which the process occurred. These parameters are vital to set up suitable pre-treatments and outgassing protocols for the N_2 adsorption-desorption analysis, without altering their structure.

Turning to the differential scanning calorimetric (DSC) analyses, these are used to estimate the glass transition point, $\boldsymbol{T}_g$, of IERs. The glass transition point is an important parameter for understanding the mechanical behaviour of the polymers. $\boldsymbol{T}_g$ is a property of the amorphous region within the polymer and depends on the mobility of the polymeric chains. At temperatures below $\boldsymbol{T}_g$, the polymer chains are stiff, and this state is known as the glassy state. However, above $\boldsymbol{T}_g$, the polymer chain is flexible and the physical and mechanical properties of the polymer change. This state is known as the rubbery state. Polymers absorb water depending on the temperature and the relative humidity. Thus, new hydrogen bonding is generated with water molecules, lowering $\boldsymbol{T}_g$. This process is called plasticization.

The DSC thermograms of 26OH and 402OH* provide a more detailed study of types of water present in the polymers and the glass transition, as shown in **Figures 3.6 a** and **b**. Both of them are essential parameters for setting up the outgassing protocol in the next section. The data at the onset and the midpoint of glass transition are summarised in **Table 3.2**.

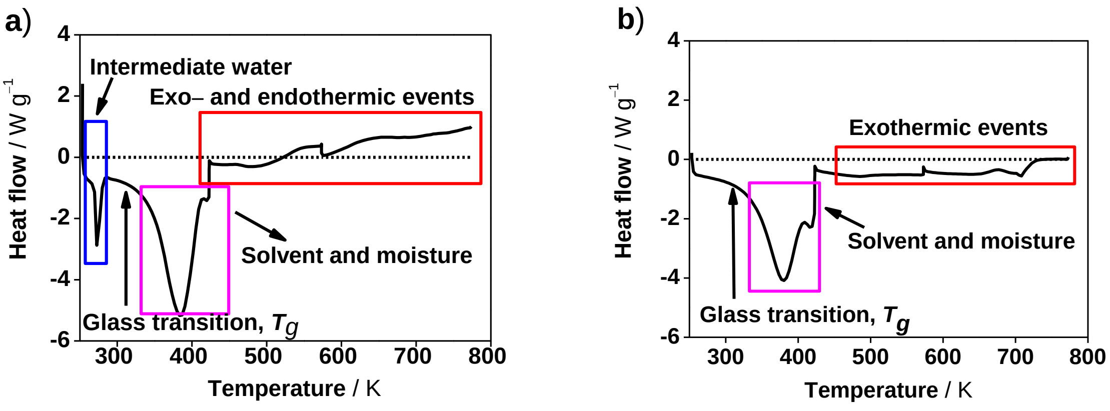

Figure 3.6. DSC thermograms under nitrogen (50 cm^3 min^{-1}) of (**a**) 26OH and (**b**) 402OH*.

Table 3.2. Onset and midpoint of the glass transition point for the IERs studied in this work.

IERs	**Glass transition point, T_g** (Onset) / K	(Midpoint) / K
26OH	365	378
458Cl	344	347
958Cl	365	377
410Cl	363	365
402Cl	339	344
402OH*	345	347
15H	335	338
120H	336	346

Generally, in polymers, three types of water have been detected: free water, intermediate water, and unfrozen water [174]. **Figures 3.6 a** and **b** shows two typical DSC curves, which exhibit either two exothermic peaks, at 273 K and 300 K, or just the one at 350 K. Free and intermediate water freeze at 273 K and below 273 K, respectively [174, 176]. These water-types can be released from the polymer at a temperature under 373 K [177]. However, the unfrozen water cannot freeze at the normal freezing temperature. This water interacts with the polar group through hydrogen bonding and occupies polymer nanocavities, making its removal difficult during heating [177]. The magnitude of the peak associated with the intermediate water varies from polymer to polymer, relying on their tendency to store water. This water can be bound by hydrogen bonding to either the hydrophilic polymeric matrices (i.e. methyl methacrylic) or their functional groups.

At higher temperatures, the polymers undergo further thermal events. All DSC profiles exhibited an endothermic step followed by two broad endo- and exothermic peaks, which indicate glass transition point, T_g, crystallization and melting events, respectively. Crystallization and melting peaks can be seen if the polymers are semi-crystalline or crystalline. This transition is a crucial factor of resin behaviour, showing the changes in physical properties such as rigidity [153]. Our results revealed T_g onsets and midpoints of the tested IERs ranging from 335 K to 365, and from 338 to 378 K, respectively. For the sake of clarity, only the onsets are included in the discussion herein. Depending on the matrix stiffness, T_g of macroreticular is greater than T_g of gel-type IERs. The precursors of the IERs are linear polystyrene and poly(methyl methacrylate), which have T_g at 373 K and 374 K, respectively [178, 179]. The crosslinking and the functionalization should contribute to increasing its T_g [178]. Thus, the T_g should appear at a higher temperature. This discrepancy may be due to the water content within the tested IERs that was approximately 50 %. The water acts as a plasticizer, shifting T_g to a lower temperature (T < 373 K) [152]. Moreover, the data also revealed that T_g is affected by the presence of counter ions present in the resin, which is in good agreement with Tiihonen *et al.* [178]. The gel-type 402 in OH-form has T_g of 345 K while in Cl-form 339 K. The remaining exo and endothermic events in the DSC thermogram supported the reactivity of the functional groups and the decomposition of the backbone observed in the TGA analysis.

Together TGA and DSC analyses allowed measurements of the amount of moisture released by the IERs when exposed to a selected heating schedule, confirming the presence of three types of water. The water volatilization begins above approximately 310 K, and its completion occurs at 400-423 K. Water has been shown to act as a plasticizer in polymers, affecting the T_g of IERs studied in this work. T_g plays a crucial role in setting up the outgassing protocols and understanding the operational state of the polymer.

3.2.2. Dry and swollen-state morphology

The study of the morphology of the IERs in their dry and swollen state was carried out by N_2 adsorption-desorption analysis and thermoporometry, respectively. The outgassing was carried out by heating the sample and purging inert gas under vacuum [180]. The outgassing of organic compounds should be carried out at a lower temperature than the glass transition points, T_g [156]. Thus, a general rule for the choice of the outgassing temperature is generally *ca.* 20 K lower than the onset of its T_g. For the majority of porous materials, such as activated carbons and porous silica, the outgassing procedure is available in the literature [181, 182]. To the best of our knowledge, no previous research has studied an outgassing procedure for IERs failing to draw a distintion based on the different type of polymers.

Temperature, time and T_g have been carefully considered as crucial factors to drive off any physisorbed water from the samples and to leave their morphologies unchanged [106]. The temperature of outgassing and pre-treatment was set at 313 K, far away from the T_g, avoiding, therefore, any thermal event. However, the duration of the outgassing was varied with short and long periods of 3 and 12 h, respectively. These outgassing conditions were carried out on the native and pre-treated, or dry, IERs. The term dry state for IERs is hard to pin down. As pointed out above, the removal of non-freezing bound water requires temperature above the boiling point of water. Thus, throughout this work, the term pre-treated is used for the resinous beads that underwent an oven treatment at a temperature of 313 K for 3h or 12h while those with no pre-treatment are termed as native; none of these represents a resin that is completely free of sorbed water molecules. **Figures 3.7 a** and **b** depict N_2 adsorption-desorption isotherms of the IERs, 26OH and 402OH*. However, for a full comparison, the data acquired of all IERs used can be found in **Appendix A**. Black and grey circles represent the outgassing at 313 K for 3 h and 12 h on native IERs, while white circles, the outgassing at 313 K for 3 h on pre-treated IERs at 313 K for 12 h.

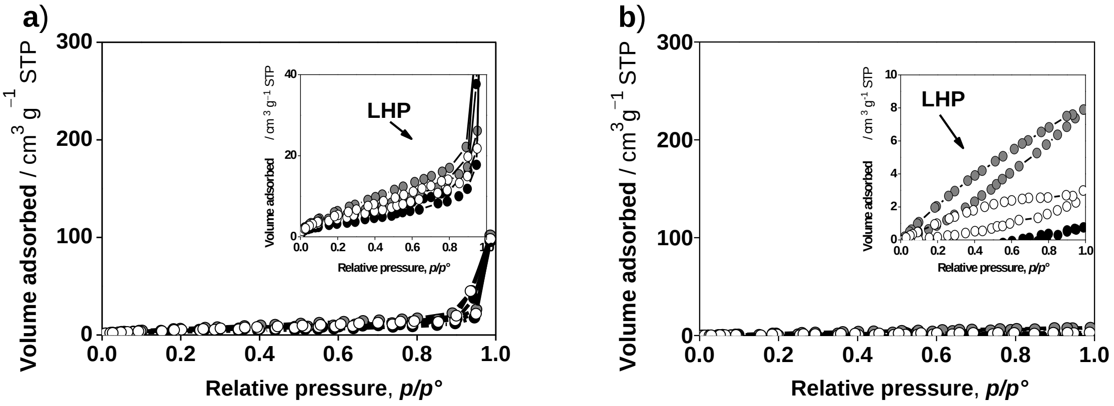

Figure 3.7. N_2 adsorption-desorption isotherm at 77 K on (**a**) 26OH and (**b**) 402OH* using different outgassing conditions (black circle) 313 K for 3 h on native; (grey circle) 313 K for 12 h on native; (white circle) 313 K for 3 h on pre-treated at 313 K for 12 h.

These polymers exhibit either Type III (non-porous material) or Type V (meso-/macroporous network) profiles characterized by a low-pressure hysteresis (LHP). The LHP occurs when the desorption branch lies parallel to the adsorption branch, meeting the adsorption branch at p/p°< 0.4. The rigid macro-exchangers (26OH and 15H) display an H3 hysteresis loop with their desorption branches lying parallel to the adsorption branch until the closure point (**Figure 3.7 a**). This hysteresis is similar to that of some hard materials such as zeolite ZSM-5 and silicalite-1 [183]. On the other hand, both gel-types and acrylic macroreticular polymers show a combination of H3 and H4 loops characterized by a large hysteresis with closure at very low ***p/p***° (**Figure 3.7 b**). These classes of hysteresis were associated with soft materials, such as microporous polymers (e.g. linear polymers of intrinsic microporosity (PIMs)) [159].

Despite this, the hysteresis loops did not close at low pressure, confirming that the gel-type and macroreticular IERs exhibited low-pressure hystereses. Gel-types rely on the pre-treatment and outgassing; the volume of gas adsorbed by native IERs was smaller than that of samples outgassed for a long time and pre-treated. However, the macroreticular IERs were not affected by the outgassing and pre-treatment, showing no dramatic changes in the isotherms.

Several years ago, the LHP pattern was related to swelling of the adsorbent due to N_2 uptake [163]. This hypothesis has been successfully validated by experimental and computational experiments [154, 164]. The isotherm shape of the adsorbent was strictly correlated to their nature and pore geometry [159]. The polymer stiffness was reduced by the permeability increase of the gas molecules, which was referred to as plasticization [164, 168]. The diffusion of molecules through the polymer may cause a rearrangement change of itself into a novel conformation, causing the swelling of the polymer in a cryogenic environment and the large LHP [165, 168, 184].

Gel-type and macroreticular resins exhibited two different isotherm shapes, depending on the resin stiffness. Neither gel-types nor macroreticular resins showed steep uptake isotherms. It indicated that micropores were inaccessible to the gas molecules. The gel-type IERs showed poor polymer dilatation associated with very little N_2 uptake at very low ***p/p*°**, followed by the slight upturn of the isotherm, which was likely correlated to the non-linearity of the matrix. The desorption branch failed at recovering the matrix entirely, preventing volume recovery during this process. This phenomenon was more pronounced in the matrix of gel-types than that of the macroreticular IERs. However, the acrylic macroreticular 958Cl acted more like the gel-type IERs. The functionality of the resin 958Cl has weakened the polymeric framework, enhancing the interaction with the gas molecules. This process occurs because of hydrogen bond donor/acceptor functionalities such as the acrylic groups, which reduced the effect of plasticization of nitrogen [165].

The morphological parameters such as pore size, pore size distribution (PSD) and surface area were extrapolated from the branches of the isotherms by using appropriate models. The choice of the branch, desorption or adsorption, can show limitations describing the morphology [159]. On the one hand, the desorption branch was described as the closest representation of the equilibrium state [159]. The limit of this branch is that it may be affected by pore blocking due to the nature of the elastic polymer, which may entrap the gas molecule through the pore emptying [159].

On the other hand, the adsorption branch allows for an estimation of the specific surface area yet can scarcely differentiate between micro and meso-sized pores, giving an improper PSD representation [159]. The limit of this branch is mostly related to an inability to detect either limited-access pores or meso and macro-sized pores [159]. The pore shape of the IERs is hard to classify because of the large hysteresis loop. It is assumed that the pores are cylindrical and independent, which are only approximations [144]. Thus, a comparison of the BJH method and NLDFT method of IERs, both based on cylindrical pore model, can help understand the nature of the adsorbent structure. The BJH method is based on the desorption branch of isotherm. In contrast, the NLDFT kernel is based on adsorption of nitrogen over silica at 77 K and applicable to both adsorption and desorption branches.

The textural properties, average $\boldsymbol{d_p}$, $\boldsymbol{V_p}$ and PSD, were obtained using both BJH and NLDFT methods with the software NovaWin 11.0 (Quantachrome). For the BJH method, the average mesopore diameter was calculated as shown in **Equation 2.9** [116].

$$\langle \boldsymbol{d_p} \rangle \text{ / nm} = \frac{4000 \cdot \boldsymbol{V_{p/p^{o}=0.99}}}{\boldsymbol{S_{BET}}} \qquad \textbf{Equation 2.9}$$

The specific surface area, $\boldsymbol{S_{BET}}$, was calculated using the software NovaWin 11.0. The data was considered acceptable only if the correlation coefficient, R^2, was not less than 0.99.

A comparison of PSDs acquired for macroreticular 26OH and gel-type 402OH* are illustrated in **Figures 3.8 a** and **b**, and the other IER PSDs associated with each outgassing protocol are reported in **Appendix A**. The results for BJH, NLDFT-adsorption and NLDFT-desorption models are represented as black, grey and white circles, respectively. The morphological properties of all IERs studied in this work associated with each outgassing protocol are reported in **Table 3.3**, **Table 3.4** and **Table 3.5**.

As can be seen, all models exhibited broad and asymmetrical pore size distributions because of the bimodal porosity of the IERs. This is in line with Zhu's findings [185]. The BJH model (black circle) and NLDFT-desorption branch (white circle) displayed similar patterns while NLDFT-adsorption (grey circle) consisted of broader PSDs. The comparison highlights that the NLDFT-adsorption has overestimated the pore size, validating the theory of limited access pores proposed by Jeromenok [159]. Outgassing and pre-treatment did not affect the PSDs of the macroreticular but did significantly affect those of gel resins, including the macroreticular 958Cl acting more like gel-type IERs.

The specific surface area, $\boldsymbol{S_{BET}}$, was calculated only for the macroreticular exchangers, 26OH and 15H, that showed a coefficient correlation, R^2, greater than 0.99. It is worth noting that $\boldsymbol{S_{BET}}$ relies on outgassing and pre-treatment protocol. The $\boldsymbol{S_{BET}}$ values of the tested IERs ranged from 2 to 50 $m^2\ g^{-1}$. These findings were in line with the $\boldsymbol{S_{BET}}$ of other resins reported by Badia and co-workers [142]. They have found values of up to *ca.* 60 $m^2\ g^{-1}$ for the resins tested in the dry state [142]. These surface areas are small compared with the majority of the other heterogeneous catalysts such as SBA-15 with $\boldsymbol{S_{BET}}$ greater than 900 $m^2\ g^{-1}$ [118]. Although the BET method applied for the gel-types and the methyl methacrylic macroreticular 958Cl IERs displayed small $\boldsymbol{S_{BET}}$ were successful from the mathematical point of view, the values were unrepresentative because the correlation coefficient, R^2 was less than 0.99.

Consequently, neither the specific surface area, $\boldsymbol{S_{BET}}$, nor the mesopore size, $\boldsymbol{d_p}$, could be determined with accuracy. These results reinforce the ineffectiveness of the BET theory at describing the $\boldsymbol{S_{BET}}$ of soft materials [165]. The data obtained from the NLDFT-desorption are used in the next chapter and help to explain the catalytic tests.

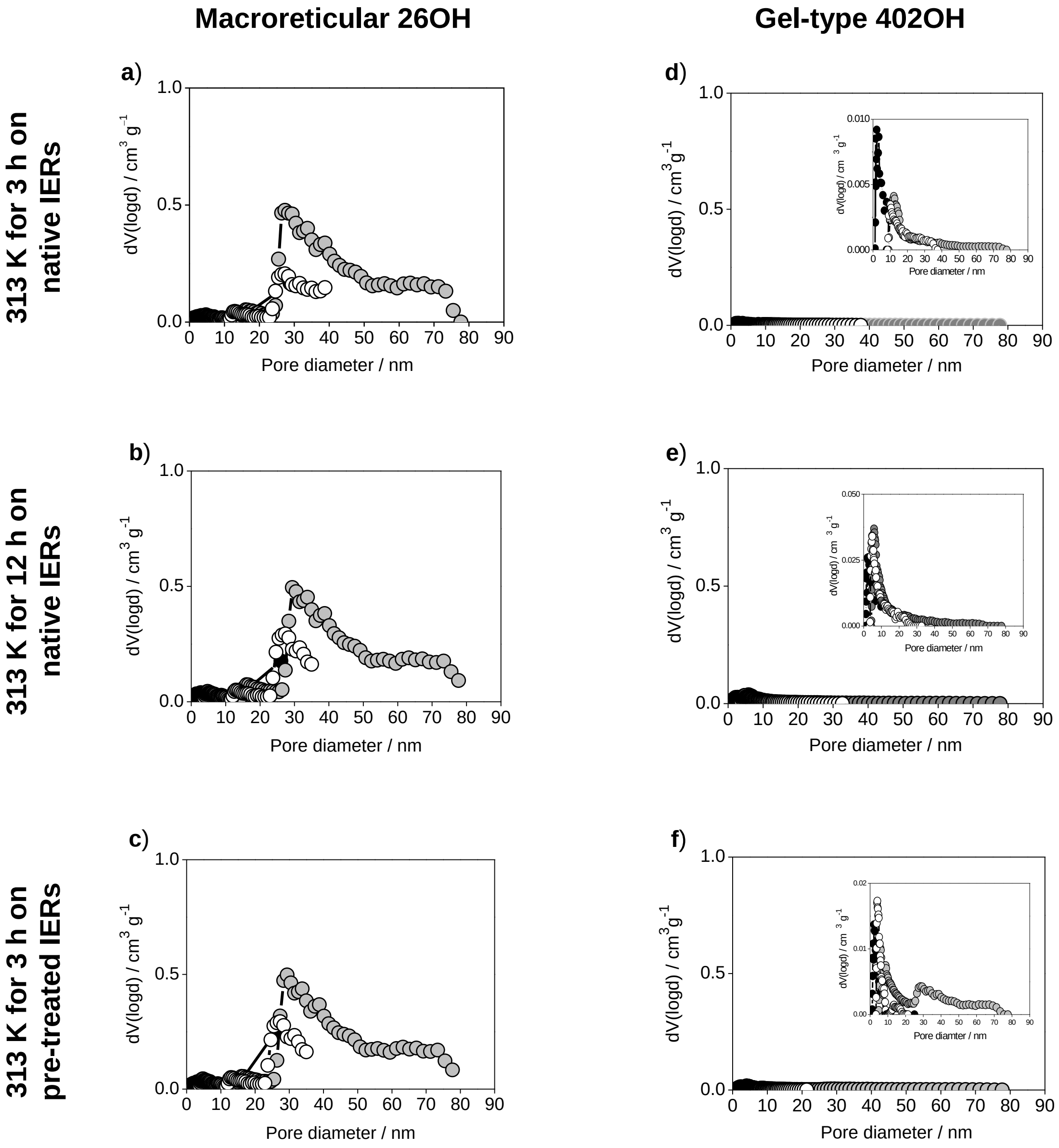

Figure 3.8. Comparison between pore size distributions (PSDs) of (**a**-**c**) the macroreticular IER 26OH and (**d**-**f**) the gel-type resin 402OH* based on (black circle) the BJH method; (grey circle) the NLDFT (adsorption) method; (white circle) NLDFT (desorption) method. The outgassing conditions were: (**a**-**d**) 313 K for 3 h on native; (**b**-**e**) 313 K for 12 h on native; (**c**-**f**) 313 K for 3 h on pre-treated resins at 313 K for 12 h.

Table 3.3. Morphological properties of the native IERs (as received) outgassed at 313 K 3 h.

IERs	***S_{BET}*** / m^2 g^{-1}	***$V_{p\ (p/p°=0.99)}$*** / cm^3 g^{-1}	**Average BJH *d_p*** (desorption) / nm	**Average NLDFT *d_p*** (adsorption) / nm	**Average NLDFT *d_p*** (equilibrium) / nm
26OH	12.1	0.153	50.6	27.4	27.8
458Cl	4.1	0.024	23.4	6.1	4.7
958Cl	n.d.	0.013	n.d.	8.1	5.5
410Cl	n.d.	0.016	n.d.	5.5	4.7
402Cl	n.d.	n.d.	n.d.	n.d.	n.d.
402OH*	n.d.	0.005	n.d.	9.4	19.9
15H	n.d.	0.163	n.d.	29.4	23.4
120H	n.d.	n.d.	n.d.	9.1	n.d.

n.d. = not determined

Table 3.4. Morphological properties of the native IERs (as received) outgassed at 313 K 12 h

IERs	***S_{BET}*** / m^2 g^{-1}	***$V_{p(p/p°=0.99)}$*** / cm^3 g^{-1}	**Average BJH *d_p*** (desorption) / nm	**Average NLDFT *d_p*** (adsorption) / nm	**Average NLDFT *d_p*** (equilibrium) / nm
26OH	18.7	0.159	34.1	29.4	27.4
458Cl	n.d.	0.024	n.d.	5.9	4.7
958Cl	2.3	0.026	45.2	4.7	5.5
410Cl	n.d.	0.014	n.d.	5.7	4.7
402Cl	n.d.	0.015	n.d.	5.3	n.d.
402OH*	n.d.	0.017	n.d.	5.9	19.9
15H	40.9	0.359	35.1	26.4	23.4
120H	n.d.	0.012	n.d.	5.9	4.9

n.d. = not determined

Table 3.5. Morphological properties of the pre-treated IERs at 313 K 3 h followed by outgassing at 313 K 12 h.

IERs	S_{BET} / $m^2 g^{-1}$	$V_{p\ (p/p°=0.99)}$ / $cm^3 g^{-1}$	**Average BJH** d_p (desorption) / nm	**Average NLDFT** d_p (adsorption) / nm	**Average NLDFT** d_p (equilibrium) / nm
26OH	21.5	0.120	22.3	29.4	27.4
458Cl	n.d.	n.d.	n.d.	n.d.	n.d.
958Cl	n.d.	0.024	n.d.	4.9	4.1
410Cl	n.d.	0.020	n.d.	6.1	4.7
402Cl	n.d.	0.163	n.d.	8.1	4.7
402OH*	n.d.	0.007	n.d.	5.9	4.1
15H	40.5	0.398	39.3	27.4	27.4
120H	n.d.	n.d.	n.d.	5.9	4.7

n.d. = not determined

The ESEM images provided a qualitative analysis on the irregular pore distribution of open and close pores on the IERs surface in the dry state. The micrographs of the SBA resins have been collected using scales of 50 µm and 500 µm and magnifications of 100x, 600x and 59x. **Figures 3.9 a-e** depict the ESEM images recorded.

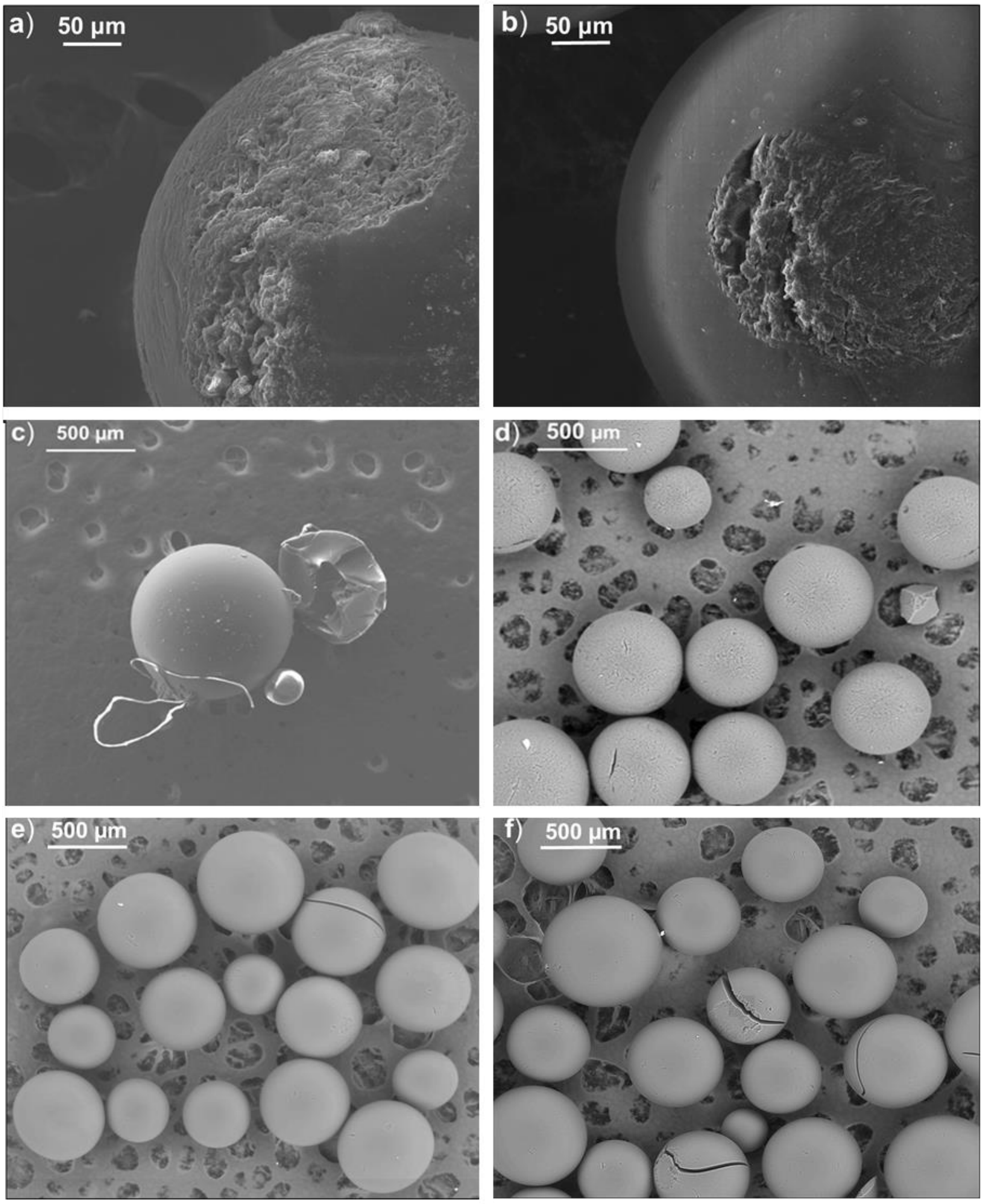

Figure 3.9. ESEM images of (**a**-**b**) 26OH (M, ST-DVB); (**c**) 458Cl (G, MA-DVB); (**d**) 958Cl (M, MA-DVB); (**e**) 410Cl (G, ST-DVB) and (**f**) 402Cl (G, ST-DVB) at magnification (**a**-**b**) 600x; (**c**) 85x; (**d**-**f**) 100x; (**e**) 72x. (G= gel; M= macroreticular; ST-DVB= styrene divinylbenzene; MA-DVB= methyl methacrylic divinylbenzene).

On the one hand, the macroreticular 26OH based on ST-DVB was representative of remarkable surface porosity characterized by a cauliflower-like microsphere (**Figures 3.9 a** and **b**).

On the other hand, the gel-types and the MA-DVB macroreticular 958Cl were both characterized by a mixed surface with scattered visible micro-voids throughout in the smooth surface (**Figures 3.9 c**-**f**). No ESEM images were acquired for the SCA 15H and 120H due to time restrictions. However, ESEM images of macroreticular ST-DVB 15H and gel-type 120H have been reported elsewhere [186, 187]. These IERs exhibited porous cauliflower-like microspheres and smooth microspheres, respectively. These findings were in good agreement with those of the SBA resins [186, 187].

As pointed out in **Section 3.1**, N_2 adsorption-desorption analysis provides morphological properties of the IERs in the dry state, without explaining their dynamic structure in operation. Thus, further comparison of the IER morphology in the dry state and the swollen state was necessary. One of the features, which distinguish IERs, is their ability to swell in a medium. Thermoporosimetry (TMP) provided the IER morphology in the swollen state. The graphs of TMP analyses were reported in **Appendix A**. The analysis of IERs in their swollen state was achieved only for two macroreticular IERs based on ST-DVB matrix (26OH and 15H), which are characterized by two distinct melting peaks, as illustrated in **Appendix A**. Both resins have shown an increase of volume when brought in contact with the swollen medium. However, the partial overlapping of peaks attributed to the other exchangers did not allow measuring the $\boldsymbol{r_p}$ (wet) applying the peak-difference method on the DSC heating curves.

The determination of the pore radius, $\boldsymbol{r_p}$ (wet), in the wet state was calculated using **Equation 2.11** [121].

$$\boldsymbol{r_p}\ /\ \mathrm{nm} = -\frac{32.33}{\Delta \boldsymbol{T}} + 0.68 \qquad \textbf{Equation 2.11}$$

where $\Delta \boldsymbol{T}$ is the difference of temperatures of bulk and cluster. The temperatures of bulk and cluster were determined applying the peak-difference method on the DSC heating curves.

Equation 2.11 shows a comparison between the pore diameters, $\boldsymbol{d_p}$, measured in the wet state using water as a probe and the pore diameters measured with N_2 adsorption-desorption analysis in the dry state by applying the NLDFT-desorption at 77 K on silica with cylindrical pores.

Table 3.6. Comparison of the IERs morphological properties in the dry state using the NLDFT-desorption model and in the swollen state using thermoporosimetry (TMP).

IERs	**NLDFT**-desorption d_p (dry) / nm	**TMP** d_p (wet) / nm
26OH	27.4	53.7
458Cl	n.d.	n.d.
958Cl	4.1	n.d.
410Cl	4.7	n.d.
402Cl	4.7	n.d.
402OH*	4.1	n.d.
15H	27.4	32.2
120H	4.7	n.d.

n.d.= not determined.

As can be seen, the macroreticular resins, 26OH and 15H, exhibited pore diameters of 53.7 and 32.2 nm, respectively. A larger diameter of 26OH in the water-swollen state was found than reported by Rottreau *et al.* [188]. In their work, Rottreau *et al.* estimated the PSD of the macroreticular resin by conducting NMR cryoporometry measurements of the resins in swollen probe media such as *t*-butanol and menthol. The polarity of the solvents allowed the resin to expand, obtaining a pore size of 29 nm in *t*-butanol and 47 nm in menthol [188]. These results were in agreement with the value estimated from porosimetry measurement by applying the NLDFT-adsorption but exhibited discrepancy with the thermoporometry results. This discrepancy may rely on either the swelling medium used or the methodology selected to analyze the peak from the DSC thermogram.

Both the dry and swollen states provided data that were subject to limitations of the models used to measure these morphological parameters, so care is needed when comparing results generated from one technique with those generated by another.

3.3. Determination of total capacity and operating capacity

The IERs studied in this work are based on either ST-DVB or methyl methacrylic-DVB matrices with functional groups, which can dissociate in an aqueous medium. The IERs contain polar groups, either positively charged, strong anion base (SBA) exchange resins, or negatively charged, strong cation acid (SCA) exchange resins [189]. These fixed polar groups are associated with ions of opposite charge by electrostatic forces [189]. SBA exchange resins are immobilized with quaternary ammonium counterbalanced by either hydroxide or chloride ions while SCA resins with sulfonic groups and protons as counter-ions. In a non-aqueous environment or low water content, the IERs functional groups immobilized to the polymeric network remain undissociated. In contrast, in an aqueous environment, the catalytic activity species are dissociated and move freely in the vicinity of the bulky ionic group attached to the copolymer [144, 190].

The catalytic activity of the IERs depends on the distribution of the active sites within the micro-particles [149]. As stated above, the macroreticular resin consists of micro-gel particles interdispersed within macropores [18, 37]. These IERs have two types of active sites: one resides on the surface, and the other one is located within the inner part of the gel micro-particles [149]. However, the gel-type consists of only a single gel phase where all sites reside [37].

The resin capacity establishes the number of sites attached to the polymeric network. In general, this can be expressed as either equivalent per litre or per gram of dry resin. The capacity and the water contain within the resins after the drying process (% water) were measured using **Equations 2.13 a-c** introduced in **Chapter 2** [128]. To aid the reader, these equations are represented again.

$$\text{SAC Capacity / meq g}^{-1} = \frac{(\boldsymbol{V}_{\text{NaOH}}\cdot\boldsymbol{C}_{\text{NaOH}}) - 2(\boldsymbol{V}_{\text{HCl}}\cdot\mathbf{C}_{\text{HCl}})}{\text{sample mass}} \qquad \textbf{Equation 2.13a}$$

$$\text{SBA Capacity / meq g}^{-1} = \frac{(\boldsymbol{V}_{\text{HCl}}\cdot\boldsymbol{C}_{\text{HCl}}) - 2(\boldsymbol{V}_{\text{NaOH}}\cdot\boldsymbol{C}_{\text{NaOH}})}{\text{sample mass}} \qquad \textbf{Equation 2.13b}$$

$$\text{water / \%} = \frac{\text{mass of native IER} - \text{mass of dried IER}}{\text{mass of native IER}}\cdot 100 \qquad \textbf{Equation 2.13c}$$

where ***V*** and ***C*** are the volumes and the concentrations of HCl or NaOH.

The total number of sites on each catalyst, i.e. total capacity (TC), was estimated by an elemental analyzer to quantify concentrations of nitrogen, present on the anionic resins as quaternary ammonium groups. However, for the acidic resins, concentrations of sulfur attached to the acidic resins as sulfonic acid were available in the literature. For the sake of clarity, only the mass percentage of nitrogen and sulfur are reported in **Table 3.7**. These are supported by complete C, H, N, S and O measurements, tabulated in **Appendix A**.

However, the number of functional groups attached to the resin in the liquid phase is defined as operating capacity (OC). The OC of IERs in OH-form and H-form was estimated using back-titration. In contrast, the OC of exchangers in Cl-form was measured using an ion-selective electrode. The measurements were converted into concentration by an appropriate calibration curve built with 1, 2, 4, 6, 10, 100 and 1000 ppm NaCl standard solutions. The calibration curves and the comparison of capacities were reported in **Appendix A** and **Table 3.7**, respectively. As stated above, a different methodology for Cl-resins was selected since a comparison was needed with the results obtained for the catalyst activation in **Section 4.2.1**. **Table 3.7** compares the operating and total capacities with the nominal capacity reported in the IERs datasheets. The table also lists the % solid which quantifies the water present in the IERs after drying.

Table 3.7. Nominal, operating (OC) and total (TC) capacities of IERs studied in this work.

IERs	**% water**	**Nominal capacity**	**Operating capacity**				**Total capacity**	
					N sites	**S sites**	**N sites**	**S sites**
		/ eq L^{-1}	/ eq L^{-1}	/ meqg^{-1}	/ %	/ %	/ %	/ %
26OH	43	≥ 0.80	0.8	1.7	2.4	n.d.	n.d.	n.d.
458Cl	51	≥ 1.25	n.d.	1.3	3.6	n.d.	11.24	11.24
958Cl	38	≥ 0.80	1.3	1.0	3.7	n.d.	10.83	10.83
410Cl	59	≥ 1.25	1.0	1.4	3.4	n.d.	5.06	5.06
402Cl	59	≥ 1.20	1.8	1.6	3.9	n.d.	5.36	5.36
402OH	51	≥ 0.95	0.8	1.8	2.5	n.d.	4.93	4.93
15H	53	≥ 1.70	n.d.	1.6	n.d.	5.4	0.05[186]	16.17[186]
120H	53	≥ 1.80	1.0	1.0	n.d.	5.9	n.d.	18.38[187]

n.d. = not determined

On average, the majority of the tested IERs showed an operating capacity equal to the minimum nominal capacity provided in IER datasheets, confirming the validity of the methodology used. However, many research works have found values of OC between 3 and 5 meq g^{-1}, albeit only for a limited number of acidic resins pre-treated at 373 K [116]. Low exchange rates and diffusion can delay reaching the active groups, complicating the determination of capacity [128]. Sometimes the resinous beads need to be crumbled to achieve OPs close to their nominal capacity [128]. Thus, our conclusion of OC ranging from 1.0 to 1.8 meq g^{-1} would seem to be acceptable. The most remarkable observation to emerge from the data comparison was the discrepancy between OC and TC. The total capacities displayed a high functionality density onto the copolymer ranging from *ca.* 5 to 18 %. The acidic resins exhibited the highest density of functional groups onto their matrices.

In contrast, the operating capacities in terms of nitrogen-containing groups spanned from *ca.* 2 to 4 %. Thus, not all sites were operating in the liquid-phase. It is worth noting that the operating capacities reported here mainly indicated the effect of our drying protocol. In this work, a pre-treatment temperature of 313 K was selected to preserve the IER morphology, resembling the IERs in operation.

What is important is that these resins have slightly higher capacity than their heterogeneous counterparts, such as a catalyst on inorganic supports, and on the basis of this enhanced capacity, have potential as catalysts [148]. In this work, the OC will be correlated to the catalytic performance of the individual resin. Moreover, the study of converting the catalysts from the Cl-form resins into the OH-form was carried out to find the conditions to maximize the mobile ions onto the polymeric matrices and to reach optimal conversion and selectivity in the catalytic tests.

3.4. Study of the accessibility of the active sites in the polymeric resins

A characteristic of IERs is their solvent-responsive behaviour [147]. Essentially, the swelling of the gel phase spreads the polymeric chains, enhancing the accessibility of the molecules to the functional groups [147]. Thus, in a resin, *ca.* 5 % of the functional groups reside in the pore walls while the remaining 95 % of groups are only accessible after the swelling of the polymeric resin, which allows the opening of non-permanent pores in the gel-phase [144]. The reaction occurs in the gel-phase of the resins.

The accessibility of gel phase depends on more parameters than just the polarity of the matrix, such as the reaction medium, the content of cross-linking agent (% DVB), the number and the nature of functional groups, and ionic form of the resins [37, 143].

The swelling degree of the polymers was investigated as a probe of accessibility of the pores to liquids by employing volumetric tests. The swelling degree was measured using **Equation 1.2** introduced in **Chapter 2** [37]. To aid the reader, that equation is shown here.

$$\text{Swelling degree / \%} = \frac{\boldsymbol{V - V_0}}{\boldsymbol{V_0}} \qquad \textbf{Equation 1.2}$$

where $\boldsymbol{V_0}$ is the initial volume and $\boldsymbol{V}$ is the final volume of the polymeric material after 60 minutes of contact time with the solvent.

The resins were tested in the OH-form and H-form, which are the ionic form used for the catalytic tests for resembling most their behaviour in reactions. The activation of the Cl-resins into the OH-ionic form is discussed in **Chapter 4**. The swelling tests were carried out by bringing the IERs in the OH-form in contact with methanol and the reaction mixture. The reaction mixture used had a composition of 1:30 tributyrin (TB) to methanol.

This study aims to quantify the accessibility of the resins in the mixture used for the transesterification reaction. **Figure 3.10** shows the results of the swelling tests conducted with methanol and the reaction mixture.

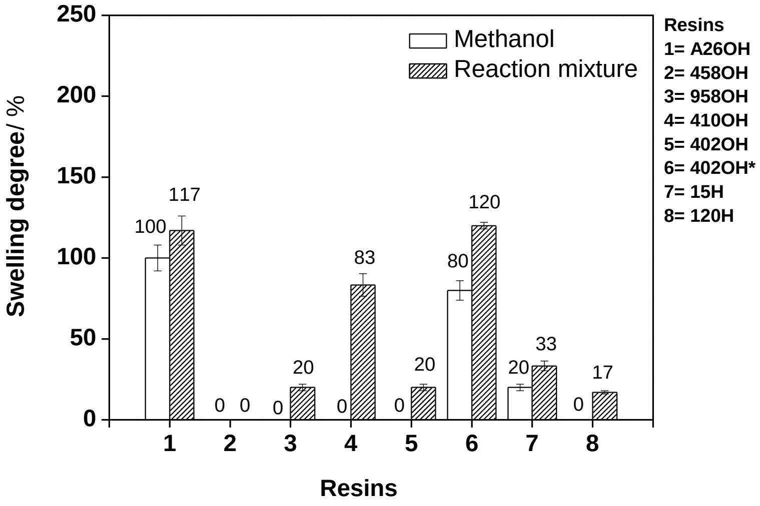

Figure 3.10. The swelling degree of pre-treated IERs at 313 K brought in contact for 60 minutes with (blank) methanol and (dense pattern) 1:30 mixture tributyrin (TB) to methanol. The error bars represent the standard error of two repeated measurements.

Based on the data collected in **Figure 3.10**, the volumetric tests of the homemade activated resins (958OH (type I), 410OH (type II) and 402OH (type I)) displayed no swelling in methanol but a significantly more pronounced swelling ratio in the reaction medium methanol than those brought in contact with methanol. This is likely due to the activation of the resins and the nature of copolymers. The resins provided by the supplier in the active form, 26OH and 402OH*, swelled more in the mixture, reaching 120% and 125%, respectively. However, the acidic resins swelled only a little in both liquids. The swelling degrees of 26OH and 15H have been studied by Oliveira and co-workers [193] [193]. They found swelling degrees in methanol of 126% and 42%, for 26OH and 15H, respectively [193]. There only was a small discrepancy in the swelling degrees of those resins between our results and Oliveira’s. This discrepancy was likely related to the grade of the alcohol used.

Figure 3.11 illustrates the relationship between the swelling ratio trend of the IERs in the reaction mixture and type of matrix. The bars of each IER has been marked with the type of matrix: ST and MA stand for styrenic and methyl methacrylic matrix while M and G for macroreticular and gel-type IERs, respectively. The error bars represent the standard deviation of two repeated measurements.

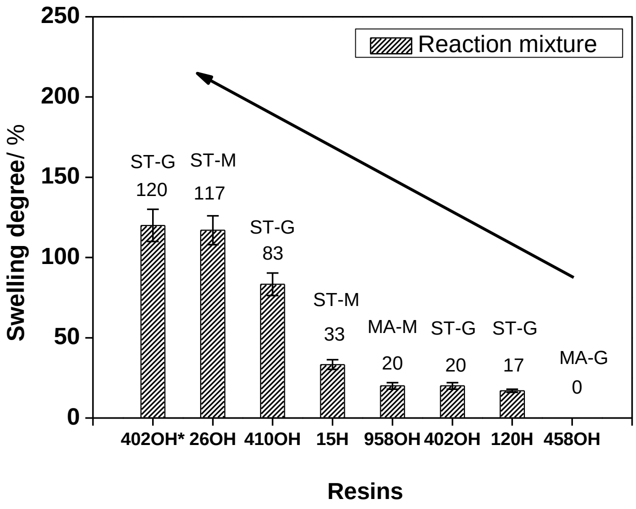

Figure 3.11. The swelling grade of pre-treated IERs at 313 K brought in contact for 60 minutes with 1:30 mixture tributyrin (TB) and methanol. The bars of each IER has been marked with the type of matrix. ST and MA stand for styrenic and methyl methacrylic matrix while M and G for macroreticular and gel-type IERs, respectively. The error bars represent the standard deviation of two repeated measurements.

As can be seen in **Figure 3.11**, it appears that the anionic resins based on the ST-DVB copolymer swelled more in the mixture than MA-DVB anionic and ST-DVB cationic resins. The hydrophilic character of acrylic IERs such as 458OH and the sulfonic groups of the SBA resins are scarcely compatible with the reaction mixture. Note that these findings were in agreement with previous results reported in the literature. Sienkiewicz *et al.* noted that the exchanger Amberlite XAD7, with moderate hydrophilic matrix, swelled more in the polar solvent than the apolar medium because of the solvent-polymeric matrix interactions [191]. This study revealed that the anionic resins 26OH and the commercial 402OH* were promising catalysts for the transesterification reaction since they exhibited enhancement of accessibility in the reaction mixture.

3.5. Conclusions

Chapter 3 has introduced the reader to the experimental techniques used for IER characterisation and challenges in the data interpretation. Although ion exchange resins have been used in catalysis over the last decades, their behaviour is still poorly-understood and their use is limited by the thermal stability of their functional groups. Thus, the thermal stability was investigated to measure both water content and glass transition temperature of the IERs. The glass transition temperature, in turn, was shown to be vital for the choice of the outgassing procedure used for the N_2 sorption analysis to determine the IER porosity in the dry state. TGA results showed a mass loss of *ca.* 50 % due to moisture content and thermal degradation of the functionality and polymer matrix at a higher temperature. DSC analysis revealed a glass transition temperature at *ca.* 343 K, which pointed out that the IERs may undergo physical transitions above that temperature. Both TGA and DSC analyses established the methodology of outgassing and pre-treatment for the IERs. A temperature of 333 K was therefore selected to remove moisture content, preserving the resins. The N_2 sorption analysis demonstrated that low-pressure hysteresis (LHP) was not an artefact associated with outgassing and pre-treatment protocols but instead a reproducible characteristic of the IER isotherms. The similarity with Polymers of Intrinsic Microporosity (PIMs) validated the conclusion that LHP was due to both matrix swelling and, open and limited-access pores. The LHP reflects the elastic behaviour of a non-recoverable polymeric structure. The choice of the isotherm branch for the pore size and PSD has also been addressed. The desorption branch was selected as the more realistic results based on the theory of swelling and limited access of the pores in the cryogenic sorption. The most suitable method for the IERs was NLDFT-desorption; which quantified the porosity of both gel-types and macroreticular resins. The tested resins exhibited average pore diameter ranging over a broad scale, from *ca.* 5 to 27 nm for gel and macroreticular resins, respectively. The validity of specific surface area has been evaluated by the correlation coefficient, R^2. It was found that long pre-treatments enabled large correlation coefficients. It was possible to measure only for the macroreticular resins, 26OH and 15H, which exhibited specific surface areas of 22 and 41 $m^2\ g^{-1}$, respectively.

SEM images supported the morphology in the dry state found for the two types of IERs: macroreticular and gel-type. The macroreticular ones have a cauliflower-like structure with well-defined voids across the structure but the acrylic IER, 958Cl, that seemed more like a gel resin. Their structure is related to the permanent porosity of the macroreticular matrix. The gel-type resins have a smooth surface with micro-voids because of the non-permanent porosity, which can be only measured in the presence of a medium.

Another challenge to the success of the characterisation was the fact that the use of traditional techniques, such as N_2 adsorption-desorption analysis, require dry materials. Since the resin porosity change in a medium, an alternative technique used to measure the porosity of the IERs based on the Gibbs-Thompson equation was identified as thermoporosimetry. This technique evaluated the IER pore size in the swollen state using water as a probe. This technique characterized the pore size of only two macroreticular IERs, 26OH and 15H. The use of different probes for the investigation of ion exchange resins in thermoporosimetry should be further investigated. Moreover, cryporometry could help to validate the results of the thermoporosimetry analysis.

The determination of the operating and total capacities was also investigated, showing a reduced availability of the sites. Among the tested IERs, the macroreticular 26OH and the gel-type 402OH* both showed an operating capacity of *ca.* 2 meq g^{-1}. The remaining resins exhibited a low operating capacity similar to the methyl methacrylic macroreticular 958Cl and the ST-DVB gel-type resin 12H. The anionic methyl methacrylic and the acidic IERs exhibited a significant number of sites on the polymeric backbone, but only a low number of functional groups could take part in the exchange process. In the ion exchange resins, the reaction occurs on the active sites of the swollen gel. Thus, a study of IER swelling and accessibility of the active groups was performed in the reaction mixture, demonstrating good accessibility for the commercial activated IERs based on the ST-DVB copolymer. The best performances in terms of swelling were achieved by the macroreticular 26OH and the commercial activated gel-type 402OH*.

Chapter 4 provides the experimental evidence that an accurate characterisation of the material has allowed the prediction of the IERs catalytic activity in the transesterification reaction.

Chapter 4

Catalytic tests for the transesterification of tributyrin with methanol over commercial ion exchange resins

4.1. Introduction

IERs are tailor-made materials designed by selecting polymerization parameters and immobilizing functional groups [92]. It is possible to prepare resins with different morphologies, different functional groups and different counter-ions, different degrees of cross-linking and particle size [92]. IERs are available in various bead sizes, making them compatible with many reactors such as fluised beds and tubular fix bed reactors and insuring an uniform gradient temperature and a good mixing [28, 31]. IERs with millimetre-sized beads are easy to recover from the reactor by filtration [28, 31]. IERs have found widespread use in industrial processes [27]. Several papers have investigated transesterification reactions promoted by ion exchange resins [31, 84, 85, 133, 192]. In these papers, a comparison of the catalytic performance of cationic and anionic resins was reported. They found that the efficiency of anionic resins was greater than that of cation resins in the transesterification reaction [31, 84]. Anion exchange resins have been much less studied than cation exchange resins [92]. Thus, the existing literature presents gaps concerning the role of base exchangers in catalysis.

Since IERs can retain polar liquids such as water in their structures, their use as catalysts requires pre-treatment to remove excess water, which can in turn detrimentally affect their catalytic performances [132]. Interactions of sulfonic acid and quaternary ammonium hydroxide groups of the resins with water molecules can reduce the dissociation of these ionic groups, and, therefore, their availability to react with reactant molecules. The best catalytic activity of the resins is achieved when the water content is low and functionalities are consequently completely dissociated [173].

In this research project, eight commercial IERs were tested for the transesterification of a small triglyceride, tributyrin, with methanol. Tributyrin is short chain fatty acid, which is naturally present in butter and vegetable oils [193]. Small triglycerides such as tributyrin are commonly used to test the catalytic activity of catalysts because the formation of di- and monodiglyceride intermediates and final products are dectable by conventional GC analysis [194]. The transesterification reaction of tributyrin and methanol is illustrated in **Figure 4.1**.

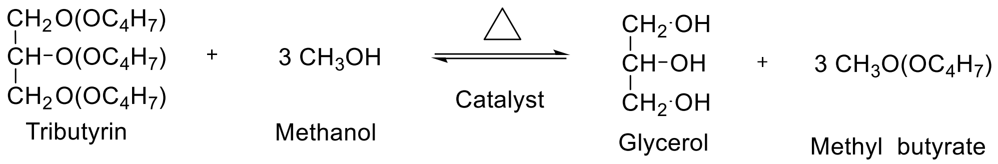

Figure 4.1. Transesterification reaction of tributyrin (TB) with methanol: TB reacts with three molecules of methanol (MeOH) to form methyl ester (biodiesel) and glycerol (GLY).

First, a study on the activation of the Cl-resins into the OH-form was conducted. Second, the effect of pre-treatment on the IER catalytic performance was investigated. With the development of an appropriate pre-treatment protocol, catalytic screening was carried out to detect the most promising catalyst for the transesterification of tributyrin with methanol. Finally, the effects of the reaction parameters, such as temperature, molar ratio, stirring speed and catalyst loading, on the conversion and selectivity of the most promising catalyst were analyzed by factorial design.

4.1.1. Chemical and physical properties of the catalysts

Eight commercial ion exchange resins supplied by DuPont were used as catalysts. Their physical and chemical properties are listed in **Table 4.1**. The temperature limit of each IER and their crosslinkings were provided by their data sheets and the literature [95-102]. While the remaining properties such as total capacity and swelling degree were measured and discussed in **Chapter 3**.

Table 4.1. List of ion exchange resins tested for the transesterification reaction of tributyrin with methanol.

Catalyst properties	**26OH**	**458Cl**	**958Cl**	**410Cl**	**402Cl**	**402OH***	**15H**	**120H**
Counter-ion of IER as received	OH^-	Cl^-	Cl^-	Cl^-	Cl^-	OH^-	H^+	H^+
Porosity-Matrix	M-ST	G-MA	M-MA	G-ST	G-ST	G-ST	M-ST	G-ST
T limit /K	333	308	353	308	350	333	393	408
OC /meq g^{-1}	1.7	1.3	1.0	1.4	1.6	1.8	1.6	1.0
S_{BET} /m^2 g^{-1}	21.5	n.d.	n.d.	n.d.	n.d.	n.d.	40.5	n.d.
V_p /cm^3 g^{-1}	0.120	n.d	0.024	0.020	0.163	0.007	0.398	n.d.
$<d_p>$ / nm	27.4	n.d.	4.1	4.7	4.7	4.1	27.4	4.7
Degree of cross-linking / %	n.d.	11[195]	n.d.	n.d.	n.d.	n.d.	20[196]	8[197]

n.d.= not determined.; M= macroreticular and G= gel; ST = styrene divinylbenzene; MA = methyl methacrylic divinylbenzene.

4.2. Catalyst activation

IERs can be prepared in different ionic forms, which is one of the key strengths of these materials. Catalyst activation is a process in which resins exchange their original counter-ions with ions available in solution. DuPont has provided several IERs in their catalytic forms such as 15H, 120H, 26OH and 402OH*. The remaining strong basic anion exchange resins, 458Cl, 958Cl, 410Cl and 402Cl, were supplied in the standard shipping form, which is the Cl-form. These resins, with chloride counter-ions, must be replaced with hydroxyl ions using sodium hydroxide as precursor. This is an activation or exchange process because the hydroxyl counter-ions are the active catalytic species used for promoting the studied reaction. As resinous beads are in contact with a solution, the ion migration in and out occurs through their semipermeable membranes, allowing the quaternary ammonium of the strong anion exchange resins to replace their counter-ions, chloride ions, with the hydroxyl ions in solution, preserving electrical neutrality. This process is illustrated in **Figure 4.2**.

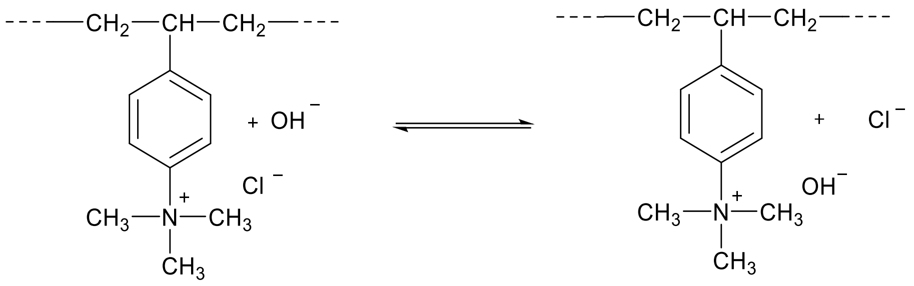

Figure 4.2. Exchange reaction between chloride quaternary ammonium and hydroxide ion in solution.

To ensure a successful activation process of IERs from one ionic form to another, a minimum contact time of 1 hour with a solution of sodium hydroxide is required. In the case of the exchange process Cl^-→OH^- it is recommended the use of high-grade caustic soda containing low concentrations of impurities such as sodium chloride [198]. A saline solution of 1 % NaCl can potentially reduce 10 % of the resin performance [198]. Liberti *et al.*, have found that factors such as capacity, DVB degree, bead size, $p\boldsymbol{K_b}$ of the functional groups and moisture content may not affect the rate of the exchange process [195]. To the best of the author's knowledge, there are no previous studies on the exchange process of these commercial resins to hydroxide form. Thus, an activation study was carried out to evaluate the hydroxyl uptake of each IER in Cl-form. Since the stoichiometric ratio Cl^- to OH^- in the exchange reaction is 1:1, the chloride ions released are equal to hydroxyl ion uptake in the IERs. The evaluation of the hydroxyl uptake was conducted by measuring the concentration of chloride ions released from the IERs.

The activation process with 0.1 M NaOH and 1 M NaOH solutions were also investigated to optimize their capacities. To aid the reader, the catalyst activation of the IERs is summarized in the flow diagram shown in **Figure 4.3**.

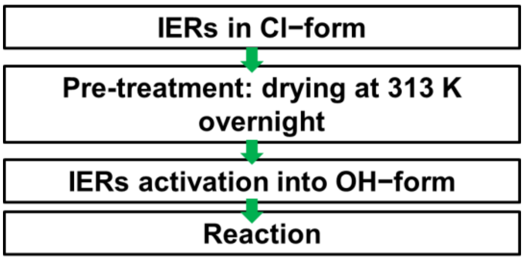

Figure 4.3. Flow diagram of IERs activation of strongly anionic exchange resins in Cl-form.

4.2.1. Activation of the chloride resins

4.2.1.1. Calibration curve

Prior to the measurement of unknown samples, a seven-point calibration curve has been prepared by preparing a set of standard solutions of 1, 2, 4, 6, 10, 100 and 1000 ppm Cl^- from a solution of 1000 ppm Cl^-. The measured potential of each solution recorded within 15 minutes of stabilization of the electrode. These potentials were plotted against the concentration of the standard solutions. The calibration curve for the resins 458Cl and 410Cl to convert the measured potential (***P***) of unknown solutions into concentration of chloride is illustrated in **Figure 4.4**.

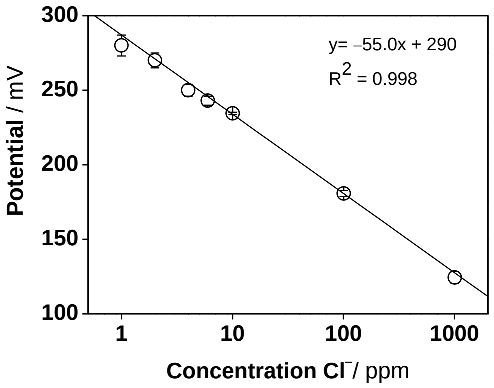

Figure 4.4. Illustration showing seven-point calibration curves (logarithm scale) for the resins 458Cl and 410Cl immersed in 1 M NaOH solution to convert the potential of unknown samples of the exchange process $Cl^- \to OH^-$ into concentration. Error bars represent the standard deviation of triplicate measurements.

The calibration curves for the remaining resins exchanged in 0.1 M NaOH solution and 1 M solution are reported in **Appendix B**.

The concentrations of the unknown samples were calculated by replacing the measured potential values into the appropriate calibration curve equation. The error bars represent the standard deviation of triplicate measurements.

4.2.1.2. Analysis of chloride ions

The catalyst activation is a stoichiometric and reversible process where the counter-ions of the resin are replaced with the ions in solution.

The IERs were dried at 313 K overnight to drive off the physisorbed water to promote the activation process. The experiments were conducted at 298 K with 0.1 M (1700 ppm OH^-) and 1 M (17000 ppm OH^-) NaOH solutions. A temperature of 298 K was selected because of the low limit temperature of several tested IERs such as 410Cl as illustrated in **Table 4.1**.

Table 4.2 summarises the measured potential, and the concentration of Cl^- released within 24 h using 0.1 M and 1 M NaOH solutions. The Cl^- released was detected by the ion-selective electrode. Deionized water was used as a blank and its value was subtracted from the sample values. The measurements were conducted in duplicate and the averaged value of ***P*** was substituted into the appropriate calibration curves reported in **Appendix B**.

Table 4.2. Measured potential (***P***) converted into concentration (mg L^{-1}) using the appropriate calibration curves.

IERs	**Time** / min	**[OH^-]** / ppm	***P*** / mV	**[Cl^-]** / ppm	**[OH^-]** / ppm	***P*** / mV	**[Cl^-]** / ppm
410Cl	0(blank)	1700	263.5	1.3	17000	295.2	0.8
	1440		130 ± 1	712 ± 6		165 ± 1	188 ± 1
402Cl	0(blank)	1700	263.5	1.3	17000	298.5	0.8
	1440		138 ± 2	484 ± 14		174 ± 2	149 ± 16
458Cl	0(blank)	1700	263.5	1.3	17000	295.2	0.8
	1440		139 ± 1	466 ± 8		179 ± 1	106 ± 7
958Cl	0(blank)	1700	263.5	1.3	17000	297.8	0.8
	1440		143 ± 1	392 ± 7		184 ± 2	93 ± 6

These data revealed a number of important points: the dilute solution promotes the replacement of Cl^- over OH^- ions. The IERs based on a polystyrene matrix exhibited higher exchange affinity towards hydroxyl ions than those with an acrylic matrix. The IERs exchanged chloride ions for hydroxyl ions in this preferential order: 410Cl (Type II) > 402Cl (Type I) > 458Cl (Type I) > 958Cl (Type I). This trend is in good agreement with the sequences of selectivity for the resinous anionic exchangers reported by Harland [47]. **Figure 4.5** reproduces Harland's affinities for Type I and Type II anionic resins.

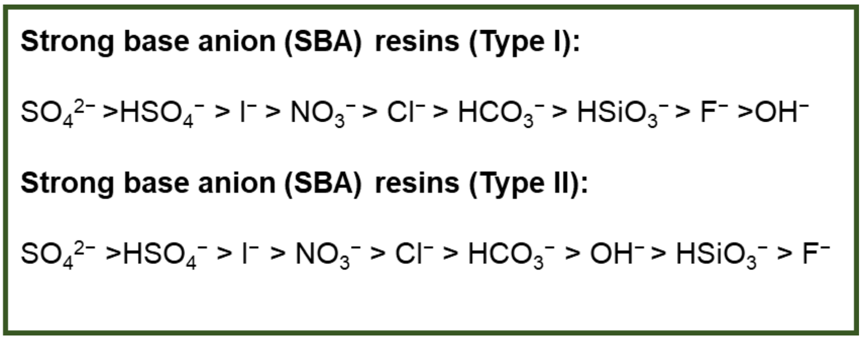

Strong base anion (SBA) resins (Type I):

$SO_4^{2-} > HSO_4^- > I^- > NO_3^- > Cl^- > HCO_3^- > HSiO_3^- > F^- > OH^-$

Strong base anion (SBA) resins (Type II):

$SO_4^{2-} > HSO_4^- > I^- > NO_3^- > Cl^- > HCO_3^- > OH^- > HSiO_3^- > F^-$

Figure 4.5. Affinities of Type I and Type II strong base anion (SBA) resins (Reproduced from [47]).

The type II resin 410Cl released more chloride ions than the other gel-type resins, which released a chloride concentration of 712 ppm, 402Cl and 458Cl. This result is due to the slightly higher affinity towards hydroxyl ions of the Type II SBA resins, which provides slightly higher hydroxyl uptakes [47]. The resin affinity towards hydroxyl ions over chloride ions controls the exchange process. Although the polyacrylic types, 458Cl and 958Cl, were associated with the highest total capacity, they released less Cl^- ions than their polystyrene counterparts. These results are in line with Liberti's work [195].

Lokhande and co-workers have investigated IER equilibrium for uni-univalent Cl^-/I^-, Cl^-/Br^-, and uni-divalent Cl^-/SO_4^{2-}, $Cl^-/C_2O_4^{2-}$ exchange systems using anionic IER Duolite A-102 D at a constant temperature of 303 K [199]. In the exchange process of univalent systems, the concentration of the electrolytic solution was varied from 0.02 to 0.08 M. The results showed increased uptake of target ions with the more concentrated electrolyte solution [199]. Our findings do not support previous research in this area. In fact, the 0.1 M NaOH solution promoted more hydroxyl uptake in the resins than the concentrated solution did.

Cl^- concentrations exchanged were determined using the appropriate calibration curves reported in **Appendix B** and substituted into **Equation 2.18**, for the determination of operating capacities. **Equation 2.18** was described in **Chapter 2** [128]. However, to aid the reader here is shown again.

$$\text{Capacity / meq g}^{-1} = \frac{\boldsymbol{C}\cdot\boldsymbol{V}\cdot\left(\frac{1}{MM}\right)}{mass_{\text{dry resin}}} \qquad \textbf{Equation 2.18}$$

where ***C, V***, *MM*, mass are the concentration Cl^- (mg L^{-1}), the volume of the Cl^- solution (L), the molar mass of Cl^- (mg/mmol) and the mass of the dry IER (g), respectively.

Since the operating capacity, measured using sulfate ions as exchangeable counter-ions because of their higher affinity of the SBA resins for those ions, indicates the maximum capacity that resins can exchange. **Table 4.3** compares operating capacities of the Cl-form resins after replacement of chloride ions with the hydroxyl and sulfate ions, evaluating, therefore, the affinity of the resins towards hydroxyl ions.

Table 4.3. Comparison of the operating capacities measured by the ion-selective electrode in OH^- form and SO_4^{2-} form expressed as meq of Cl^- released from 1 g of dry resin.

IERs	**OC** (in term of Cl^-) $Cl^- \rightarrow OH^-$ / meq g^{-1}	**TC** (in term of Cl^-) $2Cl^- \rightarrow SO_4^{2-}$ / meq g^{-1}
458Cl	1.3	1.3
958Cl	1.1	1.0
410Cl	1.4	1.4
402Cl	1.0	1.6

The operating capacities in the table are in good agreement with the total capacities measured in **Chapter 3**, and indicate that all the available sites to exchange had been exchanged. Note that 458Cl, 958Cl and 410Cl exhibited similar operating capacities in two different systems. However, 402Cl displayed a higher affinity for sulfate ions than hydroxyl ions, showing, therefore, a partial exchange process. Thus, the IERs used for the catalytic tests were activated using a NaOH concentration of 0.1 M. After activation, the IERs were washed with deionized water until the pH of the elute was 7 to remove unreacted hydroxyl anions. Excess water was removed with a paper filter. In this project work, the resins converted into OH-form were termed homemade active resins to distinguish them from the other hydroxyl-IERs supplied by DuPont. Moreover, to differentiate between the graphs of the homemade activate resin 402OH and the commercial activate 402OH, the latter is named 402OH* throughout this work.

4.3. Transesterification reaction of tributyrin with methanol over ion exchange resins

4.3.1. Calculations

The equations for the determination of conversion and product selectivity were described in **Chapter 2** [116]. However, to aid the reader, are shown again here.

$$\text{Conversion / \%} = \frac{n_{TB(0)} - n_{TB(t)}}{n_{TB(0)}} \cdot 100 \qquad \textbf{Equation 2.19 a}$$

$$\text{Product selectivity / \%} = \frac{n_{MB(t)}}{n_{TB(0)} - n_{TB(t)}} \cdot \frac{1}{3} \cdot 100 \qquad \textbf{Equation 2.19 b}$$

where $n_{TB(0)}$ are the mmoles of tributyrin at time 0 while $n_{TB(t)}$, and $n_{MB(t)}$ are the moles of tributyrin and methyl butyrate at time ***t***, respectively.

The initial reaction rate of formation of compound MB ($\boldsymbol{r}°_{MB}$) was found from the slope of the curves of the number of compound MB ($\boldsymbol{n}_{MB}$) *versus* time, as shown in **Equation 4.1** [116].

$$\boldsymbol{r}°_{MB} / \text{ mol Kg}^{-1}\text{h}^{-1} = \frac{1}{m}\left(\frac{\text{d}\boldsymbol{n}_{\text{MB}}}{\text{d}\boldsymbol{t}}\right)_{\text{t=0}} \qquad \textbf{Equation 4.1}$$

where m is the mass of the dry catalyst.

Turnover frequency (***TOF***) is defined as the moles of product per moles of catalyst per unit time (s^{-1} or h^{-1}), as shown in **Equation 4.2** [116].

$$\text{TOF / h}^{-1} = \frac{\text{reaction rate, } \boldsymbol{r}}{\text{operating capacity}} \qquad \textbf{Equation 4.2}$$

where operating capacity is the concentration of the active sites.

4.3.2. Calibration curve for the catalytic tests

Prior to running the catalytic tests, gas chromatography (GC) calibration curves of six points were performed for tributyrin (TB) and methyl butyrate (MB). The calibration curves of TB and MB are shown in **Figures 4.6 a** and **b**, respectively.

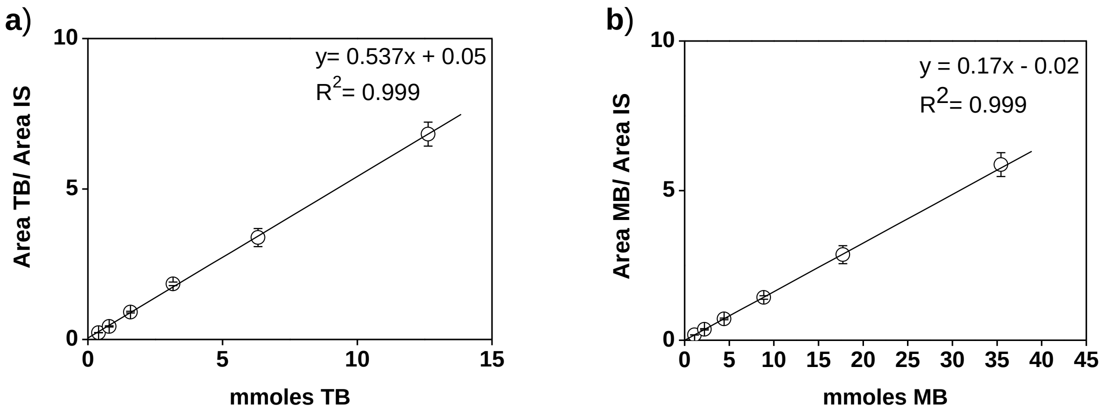

Figure 4.6. Calibration curves for (**a**) tributyrin (TB) and (**b**) methyl butyrate (MB). Error bars indicate standard deviation for replicated experiments.

These calibration curves were used for the conversion of the unknown peak area detected by the GC into TB and MB mmoles.

4.3.3. Catalyst pre-treatment

Use of strongly acidic cation and strong base anion resins in both H- and OH-form as catalysts for the transesterification reaction is commonly reported in the literature [84]. Catalytic properties of IERs are strictly related to their properties in the reaction medium [173]. On the one hand, ion exchange resins change their morphological properties depending on the medium used in the reaction [173]. The presence of polar solvents, such as alcohols or water, form non-permanent pores, enhancing the accessibility towards their active sites [173]. On the other hand, the interaction between water and the polystyrene matrix can show the opposite behaviour [173]. Water competes with the reacting species for the functional groups by adsorption by influencing the mechanism of the transesterification reaction and causing the hydrolysis of the ester and forming soap, which reduces the yield of the product [24, 173].

The reaction mechanism occurs following either a concerted or stepwise pathway [173]. In a concerted mechanism, all bonds are broken and formed in concert while a stepwise mechanism occurs over a number of distinct steps. As a result, the latter mechanism is slower. Transesterification catalysed by anionic or cationic resins occurs by two mechanisms [84, 192]. Several researchers have investigated a four-step mechanism for the transesterification reaction of oils with methanol over an anionic resin [84, 192]. The authors proposed, as a first step, the adsorption of methanol and the reaction of the alcohol with the active sites. This reaction forms water in a stoichiometric ratio of 1:1 [192]. This is the rate-determining step of the transesterification reaction [192]. The hydrolysis of esters with an excess of water can occur, forming soap [24]. This process is called saponification. It decreases the yield of the target fatty acid alkyl esters [24]. Then, if free fatty acids (FFA) are present, quaternary ammonium can absorb them by occupying functional sites, reducing ester yield. In our case, an oil with a high grade of 98 % was selected, so this step can be considered negligible [200]. Finally, methoxide (MeO^-) reacts with triglycerides to yield alkyl esters.

It is important to understand whether or not reaction water can affect the adsorption of MeOH and triglycerides over the ion exchange resins. Cren *et al.* have found that water has no effect on the adsorption of oleic acid over the 26OH resin [201]. Similarly, Jamal et al. have reported no water effect on the adsorption of soy oil over the same resin [192]. **Figure 4.7** illustrates the mechanism of the transesterification of tributyrin over a strong anion exchange resin.

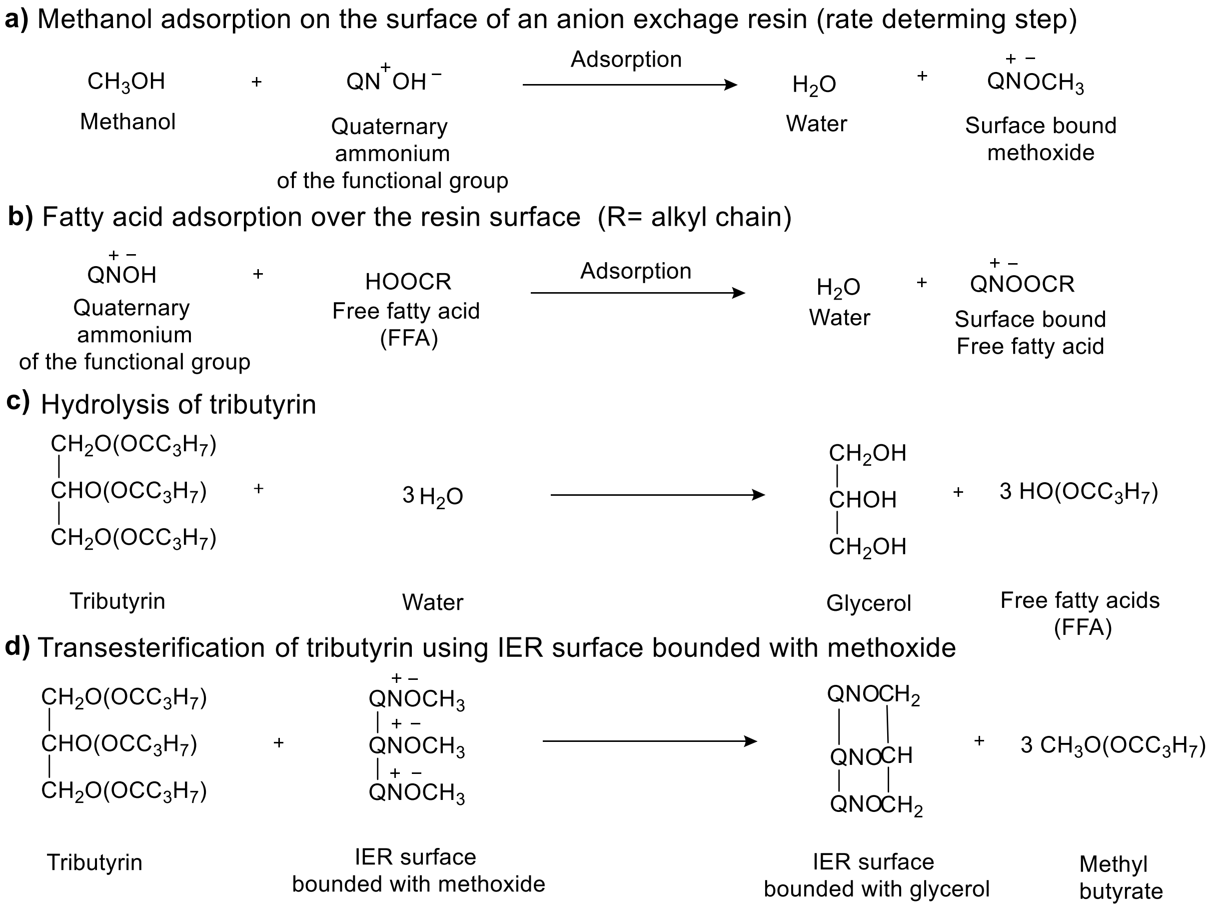

Figure 4.7. Reaction mechanism of transesterification of tributyrin over SBA resins occurs in four steps: (**a**) methanol adsorbs over the surface of the resin, forming water and methoxide; (**b**) adsorption of FFA over the surface of the SBA resin; (**c**) hydrolysis of the tributyrin in the presence of water and (**d**) transesterification of tributyrin catalysed by methoxide formed in the first step to yield methyl ester (biodiesel) (Reproduced from [192]).

Similarly, in the reaction mechanism of the transesterification reaction over an acid cation exchange resin, water is formed. In general, the active sites of the sulfonic groups are considered as protons H^+. In the presence of FFAs, these acids are adsorbed onto active sites to form carbocations. Then, the carbocations react with methanol to form esters and water. Since the grade of oil used was 98 %, FFA content can be considered negligible [200]. Tributyrin is adsorbed onto the active sites and reacts with them, forming a carbocation. Then, this carbocation reacts with methanol to yield methyl butyrate. The mechanism for the transterification over cation exchange resins is depicted in **Figure 4.8**.

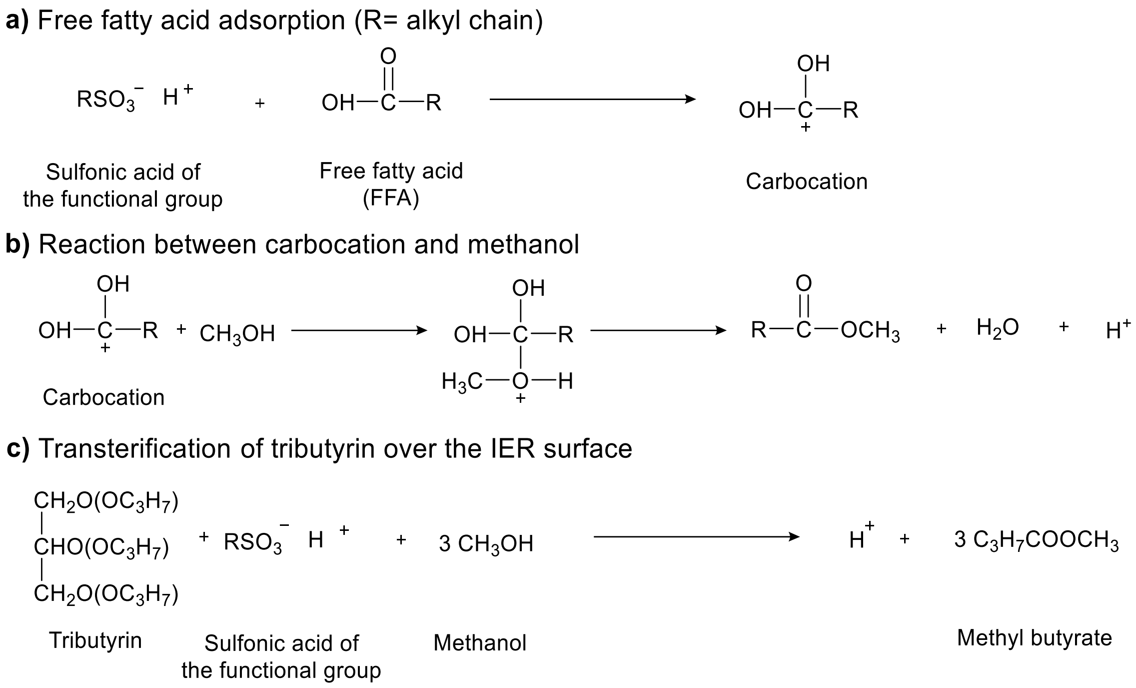

Figure 4.8. Reaction mechanism of transesterification of tributyrin over SCA exchange resins occurs in three steps: (**a**) free fatty acids adsorption over the resin to form carbocations; (**b**) carbocations react with methanol to form ester and water and (**c**) tributyrin reacts with acidic groups onto the resin to yield methyl butyrate (biodiesel) (Reproduced from [31]).

Both mechanisms of the transesterification reaction illustrate how different chemical species in the reaction mixture compete to adsorb on the active sites of IERs [202]. Water and alcohol exhibit very strong affinity for absorption onto resin groups [202]. Thus, to prevent the hydrolysis of the triglyceride and the water-alcohol competition in the transesterification reaction, Jamal and colleagues highly recommended water removal from IERs [192].

This study describes the role of the water on the catalytic performance of the resins. It was conducted by carrying out the transesterification reaction of tributyrin with methanol using 26OH as representative for all investigated resins. The water content was assayed using a gravimetric method.

4.3.3.1. Effect of water content on the catalytic performance of ion exchange resins

Ion exchange resins can store a remarkable amount of polar liquids, such as water and alcohol [132]. Since the tested IERs were supplied with a water content detected by TGA analysis of *ca.* 50 % for each resin, an appropriate pre-treatment of those IERs has been highly recommended to remove excess liquid that could affect their catalytic activity [132, 133, 203]. The study of the pre-treatment effect on the tested IERs was conducted using the macroreticular resin 26OH which was selected as representative of the IERs studied in this research work. The catalyst 26OH studied in this work was used as received, and labelled as native, while the term “pre-treated” was used for those IERs dried at 313 K for 12 h. The water content within the resin post-treatment has also been quantified by weighing the resin before and after drying in an atmospheric oven using **Equation 2.13 c** that was introduced in **Chapter 2** [128]. However, to aid the reader here is reported again:

$$\text{water / \%} = \frac{\text{mass of native IER} - \text{mass of dried IER}}{\text{mass of native IER}} \cdot 100 \qquad \textbf{Equation 2.13c}$$

The catalytic tests were conducted at a constant temperature of 333 K, stirring rate of 500 rpm, catalyst loading of 50 mg and, tributyrin and methanol molar ratio of 1:30. The selection of these reaction parameters is discussed in **Section 4.4**. The evolutions of tributyrin conversion for both the pre-treated and the native resins against time are reported in **Appendix B**.
Table 4.4 shows the amount of water released after pre-treatment into the atmospheric oven and, TB conversion and MB selectivity within 3 h reaction time for the resin 26OH.

Table 4.4. Comparison of the catalytic performance of native and pre-treated resin 26OH with the water content (%). Reaction conditions: stirring rate of 500 rpm, tributyrin: methanol molar ratio of 1:30 and 50 mg of catalyst, 333 K.

Pre-treatment	**% water content**	**Conversion** / %	**Selectivity** / %
Native	100	82	81
Pre-treated into the oven at 313 K for 12h	50	88 ± 9	86 ± 2

As can be seen in **Table 4.4**, the % water content within the tested resin decreased with increased exposure time of pre-treatment. Conversion and selectivity increased from 82 % and 81 % to 88 % and 86 %, respectively. It can be assumed that water present in native resin slightly hampered the accessibility of the reacting molecules to the functional groups.
Some of the IER samples in their ionic forms were dried at 313 K overnight. These IERs were 15H, 120H, 26OH and 402OH*. 15H and 120H are strong acidic cation exchange resins based on styrene-divinylbenzene copolymer functionalized with sulfonic groups. 26OH and 402OH* are strong base anion exchange resins based on styrene-divinylbenzene copolymer functionalized with quaternary ammonium hydroxide.
In parallel, IER samples of Cl ionic form were dried at 313 K overnight and then activated as described earlier in **Section 4.2.1**. No further pre-treatment was carried out on homemade

activate resins because of their brittle porosity. The homemade activate IERs consist of three gel-type IERs, 410Cl, 402Cl and 458Cl, and one acrylic macroreticular IER, 958Cl. These resins are prone to structure collapse due to long pre-treatment [27]. All resins were dried or activated and kept in a sealed vial inside a desiccator for at least 12 h until needed for the catalytic tests.

The catalyst pre-treatment of the IERs was summarized in **Figure 2.17** reported in **Chapter 2**. To aid the reader, the diagram is shown here.

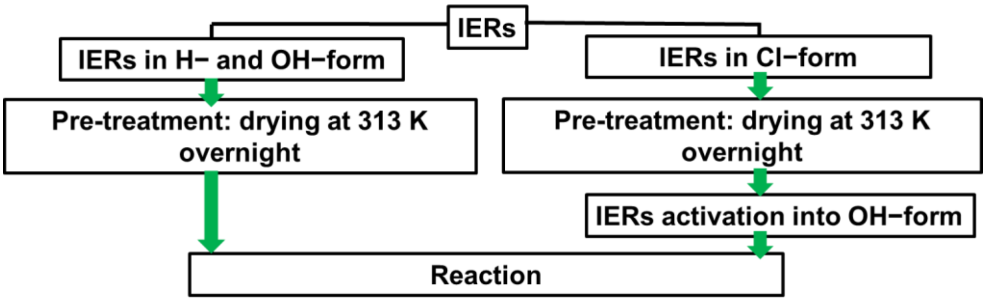

Figure 2.17. Flow diagram of IER activation and pre-treatment.

In this research work, the effect of the remaining water on adsorption of tributyrin over the anion exchange resin 26OH was also investigated. The resin was pre-treated at 313 K for 12 h. The test was performed by measuring the mmoles of tributyrin using the same methodology used for the catalytic tests but weighing only tributyrin and the internal standard, mesitylene. The withdrawn sample was taken within 60 minutes of reaction and diluted with the GC solvent, DCM. The results are shown in **Table 4.5**.

Table 4.5. Adsorption test of tributyrin over the anion exchange resin 26OH. Reaction conditions: 10 mmol of tributyrin, 50 mg of catalyst, 500 rpm of stirring rate, a constant temperature of 333 K.

Time / min	**mmoles of tributyrin in 5mL DCM** / mmol
0	8.4 ± 0.6
60	8.2 ± 0.6

The results show that there was no adsorption of tributyrin over the resin within 60 minutes. This is in line with Cren's work [201]. It was assumed that during the reaction experiments there was no adsorption of tributyrin over the resins, therefore, the mechanisms depicted in **Figure 4.7** and **Figure 4.8** can be applied in this work.

4.4. Catalyst screening test

Several screening tests on the IERs were conducted for selecting the most promising catalysts for transesterification of tributyrin with methanol. This selection was based on its outstanding catalytic activity and product selectivity.

Conversion of TB and selectivity of MB were performed at constant temperature of either 333 K or 313 K. A temperature of 313 K was selected because of the temperature limit of several resins such as the gel-type (Type II) 410OH and the acrylic resins (Type I), 458OH and 958OH, shown in **Table 4.1**. Functional groups of Type II resins have lower thermal stability than that of Type I IERs [204]. A temperature of 333 K was selected for the Type I SBA and SCA resins based on ST-DVB matrix because of the temperature limit of the remaining IERs, and it is very close to the boiling point of methanol, which is 337 K. Niu and colleagues have conducted the transesterification reaction under similar batch conditions. They have found that the use of temperatures above the methanol boiling point can give rise to evaporation of the alcohol, making the reaction difficult to control [205]. Chakrabarti and Sharma reported that external mass transfer controls the rate of a resin-catalyzed process when the viscosity of the reaction mixture is elevated, or the stirring speed is very low [206]. Therefore, the preliminary experiments of all IERs were conducted with a stirring rate of 500 rpm. The catalyst amount was fixed at *ca.* 1.6 wt% of oil (50 mg) to assure enough active sites were present to promote the transesterification reaction while a molar ratio of 1:30 was also used to drive the reaction to the alkyl esters, promoting the conversion of tributyrin [205].

Table 4.6 and **Table 4.7** reports tributyrin conversion and methyl butyrate selectivity within 180 min for the transterification reaction performed at 333 K and 313 K, respectively.

Table 4.6. Conversion and selectivity towards methyl butyrate after 180 min. Reaction conditions: 10 mmol of tributyrin, 300 mmol of MeOH, 50 mg of catalyst, 500 rpm of stirring rate, a constant temperature of 333 K.

Catalyst	Catalyst loading / %wt	Conversion / %	Selectivity / %
26OH	1.6	88 ± 9	87 ± 2
458OH	1.6	20	47
958OH	1.6	11	50
410OH	1.6	52	60
402OH	1.6	55	66
402OH*	1.6	82	72
15H	1.6	9	8
120H	1.6	7	10

Table 4.7. Conversion and selectivity towards methyl butyrate after 180 min. Reaction conditions: 10 mmol of tributyrin, 300 mmol of MeOH, 50 mg of catalyst, 500 rpm of stirring rate, a constant temperature of 313 K.

Catalyst	Catalyst loading / %wt	Conversion / %	Selectivity / %
26OH	1.6	84 ± 3	86 ± 7
458OH	1.6	0.6 ± 0.9	18 ± 10
958OH	1.6	1 ± 1	9 ± 12
410OH	1.6	3.7 ± 0.4	42.6 ± 0.2
402OH	1.6	6	13
402OH*	1.6	40	64
15H	1.6	0	0
120H	1.6	0.1	53

Figure 4.9 illustrates the catalytic profiles of the tested IERs at 333 K and 313 K. For some catalysts, two replicates for several experiments were conducted. Error bars indicate the standard deviation for the replicated measurements.

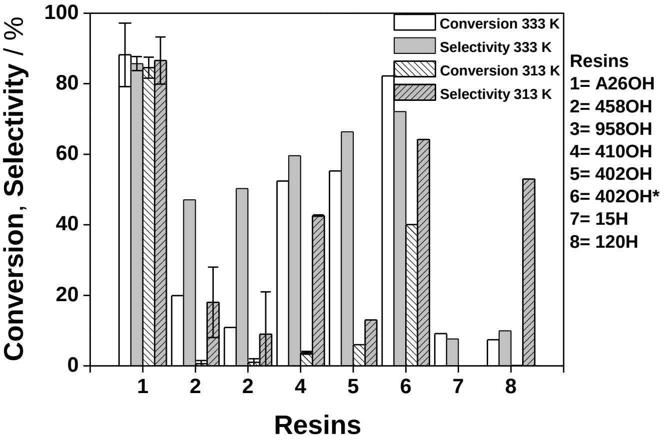

Figure 4.9. Transesterification reaction between tributyrin and methanol profile for the tested IERs: conversion (%) and product selectivity (%). Reaction conditions: 10 mmol of tributyrin, 300 mmol of MeOH, 50 mg of catalyst, 500 rpm of stirring rate, 333 K and 313 K. Error bars indicate the standard error for two replicated measurements. Some replications could not be repeated due to time constraints.

On average, all anionic resins are catalytically more active than their acidic counterparts. The anionic IERs 26OH and 402OH* have successufully catalyzed the transterification and yield methyl ester with high conversions at 333 K. The cationic resins have achieved poor conversion and product selectivity of *ca.*10 %. The results herein agree with the previous findings in the literature. These had outlined that the acidic catalysts had outstanding activity at much higher temperatures than the alcohol boiling point [88]. Also, these resins need an high alcohol: oil molar ratio to yield the ester [92]. The poor activity of the acidic IERs in the transesterification reaction was in agreement with the literature [84, 92]. This is due to the reaction mechanism. In the mechanism involving anionic resins, the adsorption of the alcohol is much stronger than that of tributyrin onto the active sites, giving rise to higher activity [60, 84]. Moreover, the transesterification reaction catalyzed by acidic resins needs to use much higher molar ratio of oil to alcohol than that used for basic catalysis [207, 208].

The effect of temperature on the reaction was studied by monitoring catalytic activity at a constant temperature of 333 K and 313 K. The results have shown the same pattern for both temperatures. Higher temperatures allow more frequent collisions between molecules of methanol and tributyrin, accelerating the transesterification reaction [205]. At higher temperatures, anion exchange resins are catalytically more active. 26OH and 402OH* reached conversions of *ca.* 88 % and 82 %, respectively with selectively greater than 80 % for both resins. The home-activated SBA resins afforded less than 55 % conversion and product selectivity greater than 50 %. The home-activated SBA resins displayed this pattern towards the reaction: 402OH > 410OH > 458OH > 958OH. The activity decay of the home-activate 402OH and the commercial activate 402OH* resins has been observed at 313 K, where the conversion of 26OH decreased slightly to 84 %.

Among the tested resins, 26OH exhibited the best catalytic performance for the transesterification reaction. This result is in good agreement with the literature [92, 192]. Both papers have reported outstanding conversion and selectivity for the transesterification of soy oil over the macroreticular 26OH [92, 192].

Physical and chemical properties of IERs can explain the differences in catalytic activity. Among the tested IERs, several have similar capacity but different polymer matrices and pore morphology. For instance, 402OH* and 26OH, both have an operating capacity of *ca.* 2 meq g^{-1} but different pore morphologies and both of them achieved excellent conversion. This suggests that other factors, such as operating capacity and swelling degree, should be included in any investigation of the resins as catalysts. The correlation of IER activity with their morphological properties, in both dry state and swollen state, has also been studied in this chapter. Dependence of the resin catalytic activity with their morphology in the dry state was investigated in terms of initial reaction rate, as illustrated in **Figure 4.10 a** and **b**.

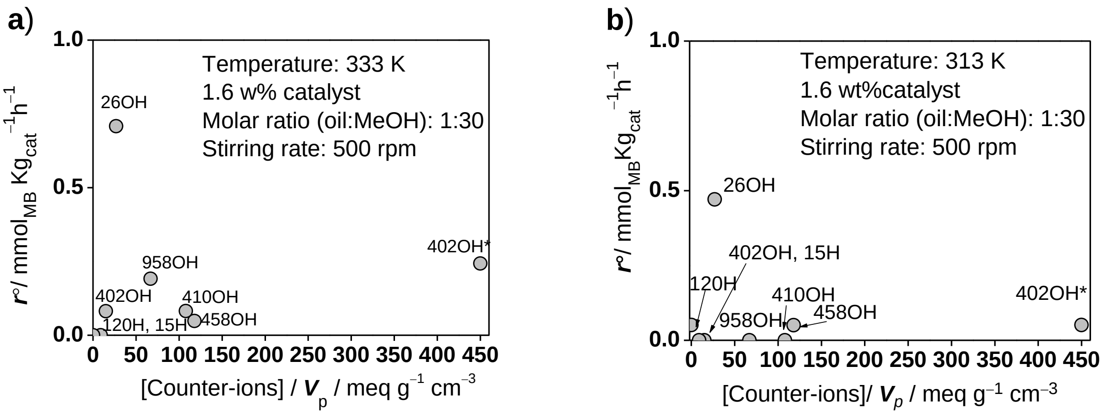

Figure 4.10. Dependence of the initial MB reaction rate, ***r***°on the density of the counter-ions (H$^+$ or OH$^-$) in the dry phase volume (V_p). Reaction condition: 500 rpm, molar ratio 1:30 (oil: methanol), 50 mg of catalyst, and 333 K (**a**) and 313 K (**b**).

As shown in **Figure 4.10 a** and **b**, the macroreticular 26OH has a noticeably higher initial reaction rate than the other resins. Its initial rate, ***r***° was about three-fold higher than that of 402OH*. The gel-type resins, 402OH, 410OH, 458OH and 120H, and the macroreticular 958OH and 15H all exhibit low initial reaction rates. There is no significant dependence between the initial reaction rate, ***r***°, and the ratio between the operating capacity and morphology in the dry resinous beads. This observation is in a good agreement to that previously reported in the literature [37, 134].

IERs swell in a polar medium, modifying their morphology. The swollen state of IERs more accurately represent the accessibility of the reacting molecules towards the active sites [37]. Thus, study of IERs in the dry state cannot give a valid representation of their morphological properties [204]. A representative description of IER morphology in the swollen state is needed to properly correlate with their catalytic activity [134]. Swelling degree is related to DVB content or cross-linking degree and nature of the functional groups [37]. In the literature, the cross-linking degree of the majority of tested IERs was not available, only that of the acidic IERs 15H and 120H and the SBA gel-type resin 458Cl was reported. It was found that gel-type resins 458Cl and 120H exhibit a cross-linking of *ca.* 8 % while macroreticular 15H has 20 %, as shown in **Table 4.1**.

An accurate picture of the IER swollen state was obtained from the swelling tests in **Chapter 3**. **Figures 4.11 a** and **b** depict the dependence of the conversion of TB on the swelling degree of the resinous beads in the reaction medium, at molar ratio of TB to MeOH of 1:30.

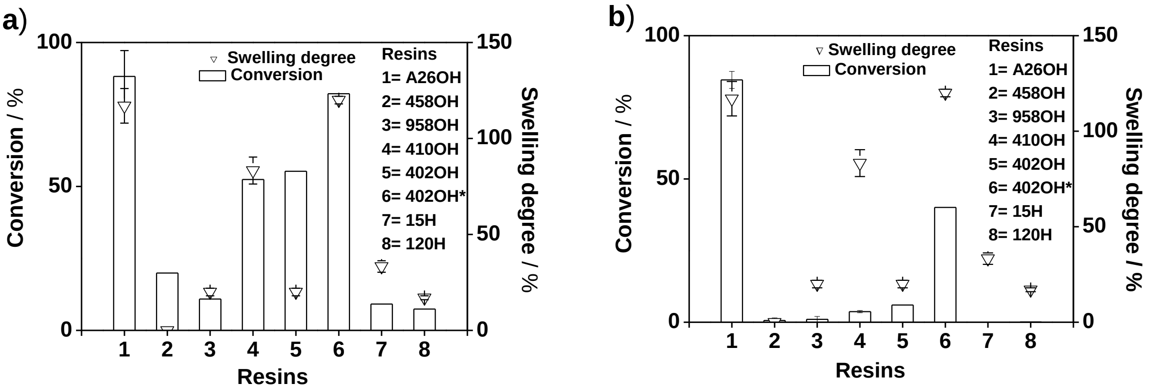

Figure 4.11. Dependence of the conversion of tributyrin on the swollen degree of the tested resins using a solution of molar ratio tributyrin to methanol 1:30. The bars indicate the conversion of each resins using the reaction condition: stirring rate of 500 rpm, molar ratio of tributyrin to methanol 1:30, 50 mg of catalyst, and a temperature of (**a**) 333 K and (**b**) 313 K. The triangles represent the swelling degree of each resin in the reaction mixture tributyrin to methanol 1:30. Error bars represent standard error for replicated catalytic experiments and swelling tests.

As can be seen, no major dependence for the SBA home-active resins 402OH, 458OH and 958OH, and the SCA resins on the conversion was observed. These resins exhibited no swelling and poor conversion. The swelling was significant only for the commercial activates 26OH and 402OH* and the home-active 410OH which achieved good conversion at both 313 K and 333 K. Permanent pores and resin swelling allow the access of reacting species into the inner part of the resin where the majority of active sites reside [92]. However, the remaining IERs showed only a limited-swelling in the reaction medium. It appeared that swelling is a crucial factor for accessibility. The excess of methanol used in the reaction increased IER swelling, promoting the accessibility of reacting species towards the gel phase of the resins [37]. 402OH* swelled more than 26OH because of the flexibility of the gel matrix, allowing the resin to achieve catalytic performances comparable to those of the macroreticular 26OH. Although, methyl methacrylic IERs exhibited a good capacity of *ca.* 1.3 meq g^{-1}, their catalytic performance was not as good as those resins with similar operating capacity because of their hydrophilic matrix. This matrix has a poor affinity with the reagents so that the concentration of the reagents inside the gel particles of the IERs is lower than that of the free solution, hindering accessibility to the active sites [144]. In addition, acidic resins showed a high capacity but only limited swelling degree. The poor swelling degree of 15H was due to its entangled polymeric structure [92]. This suggests that only the sulfonic groups attached to the external IER surface can react with reagents, affecting catalytic performance. This shows that high capacity and swelling degree are important parameters to assure good catalytic activity.

Another method to assess catalytic performance of resin catalysts based on active site accessibility is the turnover of frequency (TOF). TOF is calculated as the ratio between overall reaction rate and acidic/ basic capacity, assuming that all sites are accessible [134]. The activity level of the tested IERs can be compared in terms of TOF to better understand the relationship between acidic/basic activities of IERs per group [134]. This assumption is valid if IERs are in polar media and TOF can be used as a tool for describing the efficacy of the active sites for each resin, and also the accessibility of the active sites [134]. Since IERs have functional groups of the same nature, quaternary ammonium or sulfonic acid, it can be supposed that the tested resins will have comparable TOFs [209]. TOFs of the tested IERs determined at 1 h reaction time are shown in **Figure 4.12**.

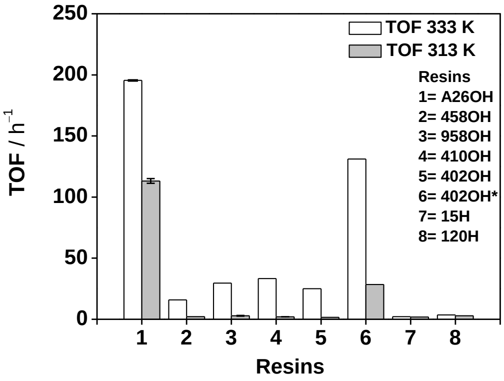

Figure 4.12. Turnover frequency (TOF) determined at 1 h reaction time for the transesterification reaction of tributyrin with methanol over the ion exchange resins tested in this research project.

As can be seen in **Figure 4.12**, TOFs of the IERs were recorded in the range of 2.1-196 h^{-1} and 1.6-133 h^{-1} at 333 K and 313 K, respectively. The TOF of 26OH was the highest and reached 195.5 h^{-1} at 333 K, achieving a tributyrin conversion of 88 %. The efficacy order of the catalysts at 333 K was 26OH > 402OH* > 410OH > 958OH > 402OH > 458OH >15H>120H. This order indicates that the local density of active sites enhances the transesterification rates. Both the rigid matrix of 26OH and the flexible matrix of 402OH* showed elevated basic capacity with high affinity for the transesterification reaction. The homemade active IERs were less active towards the transesterification reaction than the active commercial resins. It is worth noting that the TOF of IER 402OH showed a TOF equal to that of 958OH, whose the basic capacity of 402OH is almost double that of 958OH. Since all active sites have comparable nature, the discrepancy can be assumed to be either an insufficient contribution of the active sites to the reaction or diffusion issues of the reacting species [209].

It was also observed that the percentage of the non-exchanged chloride presented in the IERs affects the catalytic performances of the IERs [80]. Thus, a comparison of chloride content and catalytic activity at 333 K and 313 K was reported in **Table 4.8**. Chloride content for each tested IER was measured by ESEM-EDX. The obtained result for each resin is the averaged value of minimum six measurements.

Table 4.8. Comparison of the behaviour of chloride ion percentage within the tested IERs on the conversion of tributyrin at 333 K and 313 K.

IERs	**[Cl$^-$]**[a] / %wt	**Conversion** (333 K) / %	**Conversion** (313 K) / %
26OH	1.4 ± 0.2	88 ± 9	84 ± 3
458OH	0.57 ± 0.01	20	0.6 ± 0.9
958OH	0.75 ± 0.01	11	1 ± 1
410OH	0.88 ± 0.01	52	3.7 ± 0.4
402OH	3.43 ± 0.02	55	6
402OH*	n.d.	82	40
15H	n.d.	9	0
120H	n.d.	7	0.1

[a] SEM-EDX analysis; averaged value of minimum 6 beads. n.d. = not determined.

As can be seen in **Table 4.8**, no dependence of the residual chloride on conversion was observed. Although the home-activate 26OH has achieved a percentage of Cl of 1.36, it has achieved higher catalytic performances. While the homemade active, 402OH, with 3.43 % of chloride ions remaining in the polymer, had a conversion comparable with the other homemade activate IERs, such as 958OH.

All further experiments were carried out using the macroreticular 26OH as a catalyst since it has been revealed as the most promising catalyst among the tested IERs.

4.5. Analysis of the transesterification reaction variables

Design of experiment (DoE) is a statistical approach to reactants for screening the reaction variables simultaneously and optimazing the reaction conditions. The reaction variables were studied using experimental design, which is a less time-consuming and laborious approach than studying single variables at a time. The experimental design performed was a 2^4 factorial design. This design was selected because of the number of parameters studied; temperature, molar ratio tributyrin to methanol, catalyst load, and stirring rate and the number of experiments to be performed. This involves two discrete values or levels assumed by these four experimental variables or factors, therefore the design becomes a combination of 2^4 runs. In this case, the total number of experiments is 16. The two levels of the factorial design are coded as +1 for the highest level, −1 for the lowest level. The levels for the four factors are summarized in **Table 2.3**. To aid the reader, that table is shown here. A, B, C and D represent temperature (T), stirring rate (rpm), molar ratio and catalyst loading (mg).

Table 2.3. Level 1 and level 2 of four factors for the DoE.

Factor	Code	Temperature A / K	Stirring rate B / rpm	Molar ratio C	Catalyst loading D / mg
Level 1	−1	313	100	1/4	10
Level 2	+1	333	500	1/30	50

The experiments were performed using the high-performing catalyst 26OH. After conducting the experiments, all outcomes were randomly performed on Excel to ensure unwanted systematic effects were not introduced into the design of the experiment. The measured values of the results from experiments are called responses. In this work, the responses were conversion and product selectivity.

A caveat concerning the application of the experimental design to the data is the requirement of more data points to provide an accurate depiction of the resin performance and systematic variation within the data. It would be desirable to highlight the need to perform follow-up experiments to obtain a representative population in the experimental design.

An interaction model equation was selected by the Minitab 14 software to fit the experimental results. The model reflects the selected variables and their interactions on the responses, conversion and product selectivity. The general form of the model was shown in **Equation 2.20** [136].

$$\mathbf{Y} = \boldsymbol{b_0} + \sum_{i=1}^{k} \boldsymbol{b_i} x_i + \sum\sum_{i<j} \boldsymbol{b_{ij}} x_i x_j + \text{residual} \qquad \textbf{Equation 2.20}$$

$\boldsymbol{Y}$ is the response, $\boldsymbol{b_0}$ is a model constant; $\boldsymbol{b_i}$ are linear coefficients; $\boldsymbol{b_{ij}}$ are cross product coefficients and residual is the experimental error.

The statistical investigationof the data set is based on a hyphothesis test. This test involves two hyphothesis: the null hypothesis, $\boldsymbol{H_0}$ that is a statement to be tested and the alternative hyphothesis, $\boldsymbol{H_A}$, is an alternative statement to $\boldsymbol{H_0}$. $\boldsymbol{H_0}$ presumes no relationship between the variables. The method to reject $\boldsymbol{H_0}$ is called test statistic which uses two statistical methods, such as p-value and critical value. For the p-value method, p-value is an index to measure evidences against $\boldsymbol{H_0}$ and is compared with the significance level, alpha (α) [138]. Alpha is arbitrary and it was set at 0.05 and relates how likely the significant effects are due to chance. P-value < 0.05 points out no evidence of $\boldsymbol{H_0}$ and, the result is statistically significant [139]. While p-value > 0.05 indicates evidence of $\boldsymbol{H_0}$ and, the result is not statistically significant [139].

The p-values are calculated by the software and reported in the tables of the estimated coefficients for the interaction model equation.

The critical value is calculated based on the selected significance level, α and the probability distribution model and the test statistic is compared with the critical value [138]. The critical value is represented by a line in a Pareto chart. This chart is a graphical representation of the tables of the main effects. It consists of a histogram plot where the bars represent the effect magnitude of each factor in descending order.

Minitab 14 statistical software was used to evaluate the model validity of the coded matrix reported in **Table 4.9**. To aid the reader, the table is shown here. A, B, C and D represent temperature (T), stirring rate (rpm), molar ratio and catalyst loading (mg).

Table 4.9. Design matrix and the results of the four-factor full factorial design using the codes +1 and −1 for the appropriate levels.

Order of runs	**A**	**B**	**C**	**D**	**TB Conversion** / %	**MB Selectivity** / %
3	−1	−1	+1	−1	1	100
2	−1	+1	+1	+1	75	76
4	−1	−1	−1	−1	0	0
3	−1	+1	−1	−1	0	0
4	+1	−1	+1	+1	89	82
2	−1	+1	+1	−1	2	31
6	+1	−1	−1	+1	16	44
7	+1	+1	−1	+1	14	57
5	+1	+1	+1	+1	94	87
4	+1	−1	+1	−1	24	73
2	−1	+1	−1	+1	6	13
1	−1	−1	+1	+1	49	82
4	+1	+1	−1	−1	0	0
5	+1	+1	+1	−1	73	80
5	+1	−1	−1	−1	0	0
2	−1	−1	−1	+1	14	54

The results of the experiment are expressed in terms of the following regression models as function of the four variables: temperature (A), stirring rate (B), molar ratio (C) and catalyst loding (D).

Y(conversion) = 28.563 + 10.187A + 4.437B + 22.313C + 16.062D + 2.062AB+ 8.938AC − 1.562AD + 5.688BC − 1.812BD + 9.813CD

Y(selectivity) = + 48.688 + 4.187A − 5.688B + 27.688C + 13.187D + 8.813AB − 0.063AC + 1.437AD − 2.188BC + 2.063BD − 7.813CD

The factorial fit estimated the magnitude of the effects and coefficients for conversion and selectivity. Estimated effects and coefficients for conversion and selectivity are reported in **Table 4.10** and **Table 4.11**, respectively. The asterisk indicates the p-value < 0.05.

Table 4.10. Estimated effects and coefficients for conversion generated by Minitab 1.4.

Term	Effect	Coefficient	P-value
Constant		28.563	0.000(*)
Temperature (A)	20.375	10.187	0.021(*)
Stirring rate (B)	8.875	4.437	0.209
Molar ratio (C)	44.625	22.313	0.001(*)
Catalyst loading (D)	32.125	16.062	0.003(*)
Temperature×stirring rate (A×B)	4.125	2.062	0.533
Temperature×molar ratio (A×C)	17.875	8.938	0.034(*)
Temperature×catalyst loading (A×D)	−3.125	−1.562	0.633
Stirring rate×molar ratio (B×C)	11.375	5.688	0.124
Stirring rate×catalyst loading (B×D)	−3.625	−1.812	0.582
Molar ratio×catalyst loading (C×D)	19.625	9.813	0.024(*)

(*) indicates the significant factors with p-value < 0.05

Table 4.11. Estimated effects and coefficients for selectivity generated by Minitab 1.4.

Term	Effect	Coefficient	P-value
Constant		48.688	0.000(*)
Temperature (A)	8.375	4.187	0.390
Stirring rate (B)	−11.375	−5.688	0.257
Molar ratio (C)	55.375	27.688	0.002(*)
Catalyst loading (D)	26.375	13.187	0.031(*)
Temperature×stirring rate (A×B)	17.625	8.813	0.104
Temperature×molar ratio (A×C)	−0.125	−0.063	0.989
Temperature×catalyst loading (A×D)	2.875	1.437	0.760
Stirring rate×molar ratio (B×C)	−4.375	−2.188	0.644
Stirring rate×catalyst loading (B×D)	4.125	2.063	0.662
Molar ratio×catalyst loading (C×D)	−15.625	−7.813	0.139

(*) indicates the significant factors with p-value < 0.05.

The interpretations of the size of main effects for conversion and selectivity are provided in **Table 4.12** and **Table 4.13**, respectively.

Table 4.12. Size of the effects of each significant factor and their interpretation for conversion.

Main effects for conversion		
Factor	**Size of the effect**	**Interpretation**
Catalyst loading	+32.125	Using 50 mg of catalyst reached higher conversion than 10 mg did.
Molar ratio	+44.625	A molar ratio of 1:30 achieved higher conversion than 1:4.
Temperature	+20.375	Runs at 333 K had improved the conversion than runs at 313 K.

Table 4.13. Size of the effects of each significant factor and their interpretation for selectivity.

Main effects for selectivity		
Factor	**Size of the effect**	**Interpretation**
Catalyst loading	+26.375	50 mg of catalyst achieved better selectivity than 10 mg.
Molar ratio	+55.375	A molar ratio 1:30 had higher selectivity than 1:40.

The experimental results can be also graphically represented by Pareto plots, which highlight the most significant variables and the relationships between them [139].

Figures 4.13 a and **b** show the Pareto plots displaying bars which represent the main variables A, B, C and D and their interactions (i.e. A×B). This chart depicts the magnitude of the effect, ordered from the largest to the smallest one. Also, this plot shows a critical value line which indicates where the factors are statically important at the 0.05 alpha level. Any effects reaching beyond the critical value line are significant. In our case, this line is displayed in the Pareto charts at 2.57.

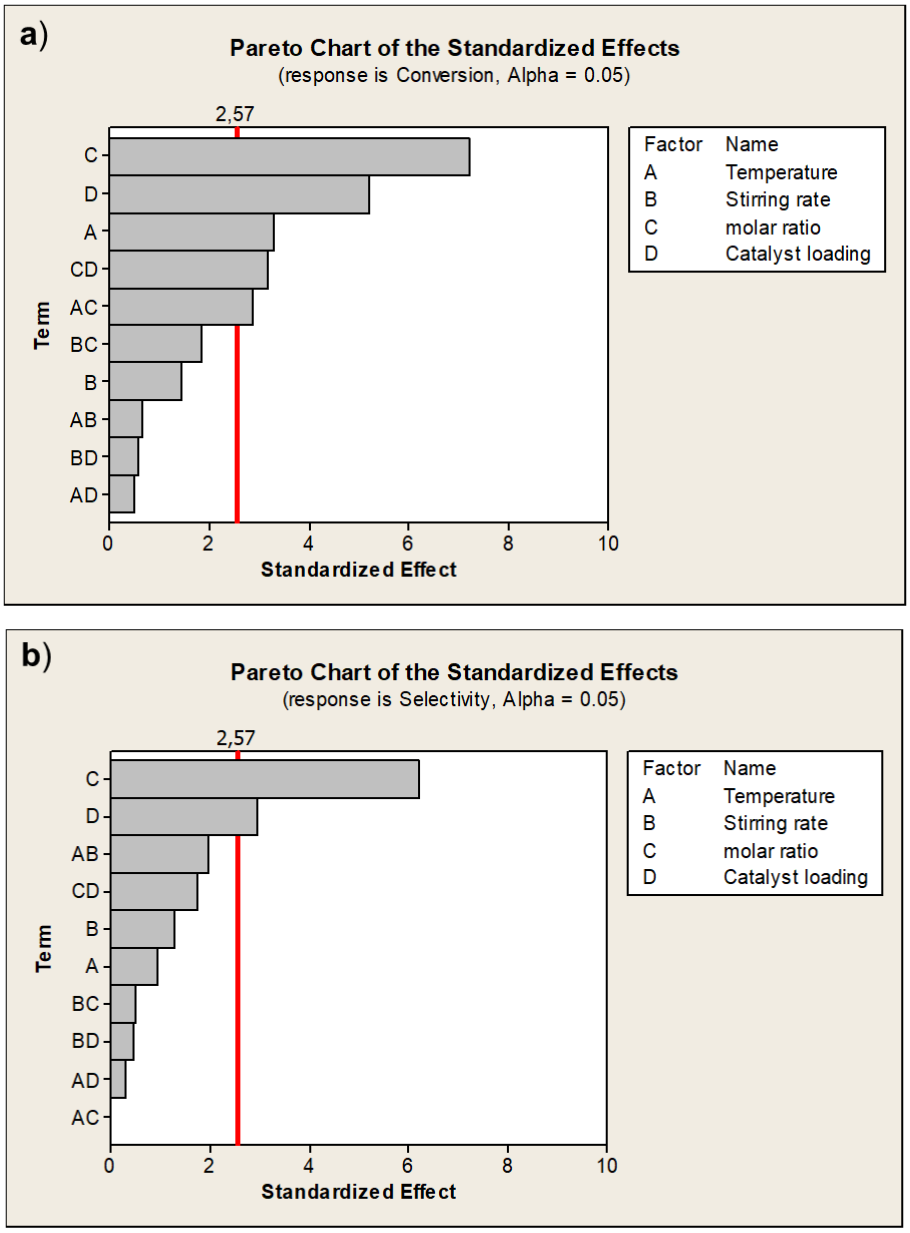

Figure 4.13. Illustration showing the Pareto charts of the magnitude of effects on (**a**) the TB conversion (%) and (**b**) the response MB selectivity (%).

Figures 4.13 a and **b** show that molar ratio and catalyst loading have a significant effect on both responses, while the stirring rate has no marked effect on either response. Moreover, the combined effects of the factors can be observed from the Pareto chart. For conversion, molar ratio, catalyst loading, temperature and two interactions, catalyst loading-molar ratio and temperature-molar ratio have been recognized to be significant. The response selectivity has shown that only two variables, molar ratio and catalyst loading, were statistically significant.

The interpretation of the interactions makes a clear picture of the system, giving, in our case, only positive contributions for conversion. **Figures 4.14 a** and **b** show surface plots of the conversion against molar ratio and catalyst loading and, temperature and molar ratio, respectively.

Figure 4.14 a shows the effect of molar ratio-catalyst loading on conversion and the maximum conversion obtained with the following reaction conditions: 333 K, 500 rpm, 50 mg of catalyst and a tributyrin to methanol molar ratio of 1:30. The low and high values of the studied factors are coded −1 and +1. It is observed that the conversion increases with increase in molar ratio and catalyst loading concomitantly. The difference in conversion between the runs using a molar ratio of 1:30 and 10 or 50 mg of catalyst is much more significant than using a molar ratio of 1:4. This trend can be explained by Le Chatelier's principle that shifts the equilibrium towards the products. The conversion improved with some methanol added up to 1:30. Similarly, **Figure 4.14 b** depicts the effect of temperature-molar ratio on conversion. From the surface plot, it can be seen that the conversion rises as the value of both temperature and molar ratio increases. The minimum conversion is achieved when the experiment is run at 313 K using a molar ratio of 1/4. Conversely, the maximum conversion occurs at 333 K with a molar ratio of 1/30. This result is due to the positive temperature-molar ratio interaction increases the production of biodiesel.

Table 4.12 reports that the effect of molar ratio is more significant than single effects of catalyst loading and temperature. However, both interaction effects, molar ratio-catalyst loading and temperature-molar ratio, have less effect on the conversion.

Due to time constraints and limited access to the equipment, we could not run replicates. Further experiments should be run to examine the trend found. A design with replicates enable to investigate sources of variability, such as change of equipment between experiments or other experimental factors which can vary over time.

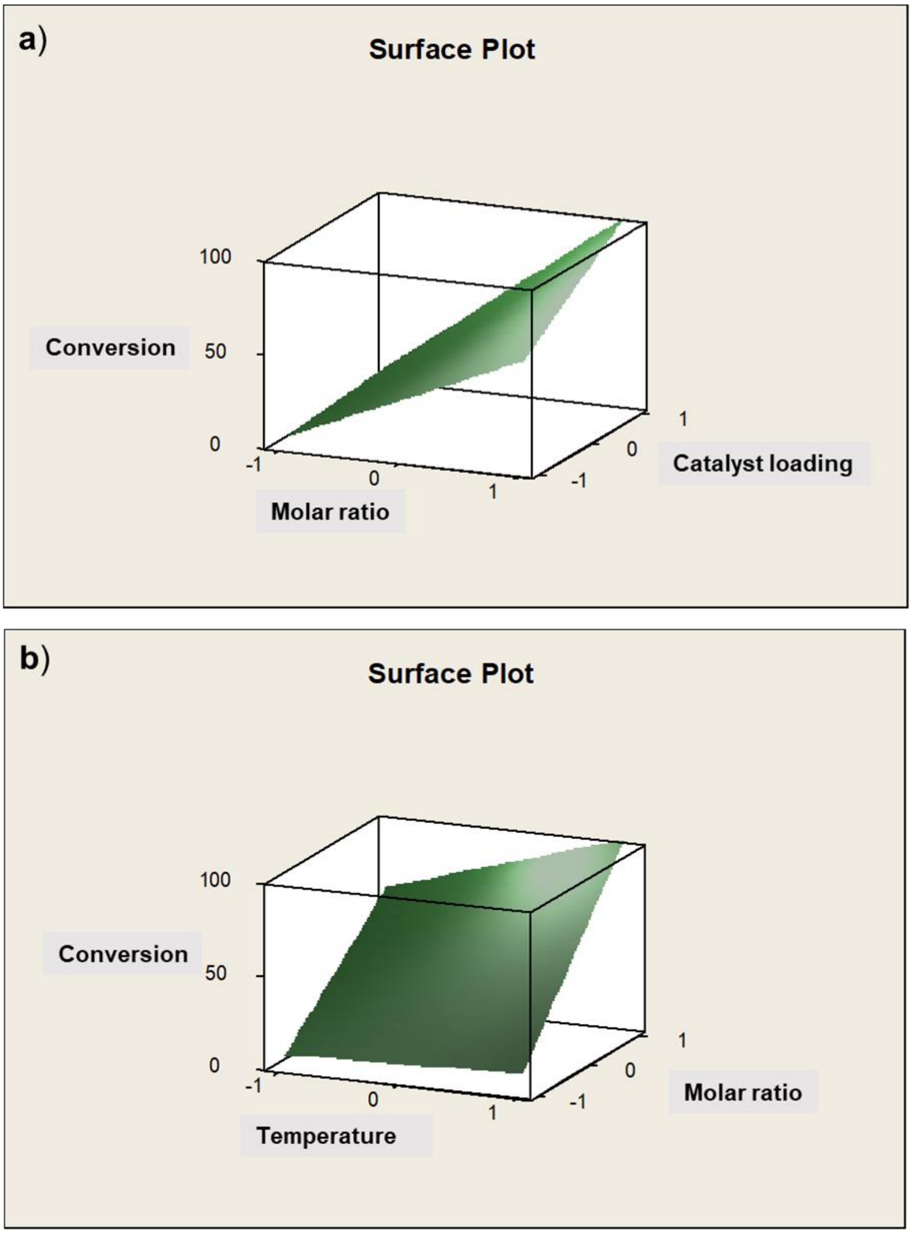

Figure 4.14. Response surface plot for of conversion against (**a**) molar ratio and catalyst loading and, (**b**) temperature and molar ratio. The low and high values of the studied factors are coded −1 and +1.

In conclusion, the experimental design methodology shows its advantages over the one-variable-at-a-time design to study the variable interactions using a limited number of experiments. In this section, we have explored the main effects on the methyl butyrate production using the anion exchange resins 26OH. The most significant factors were temperature, molar ratio and catalyst loading. Stirring rate does not show any significant effect on the TB conversion, validating the external mass transfer study conducted by Chakrabarti and Sharma [206]. It was also found that molar ratio and catalyst loading have a remarkable effect on MB selectivity. However, these resins have experienced internal mass transfer in their gel-phase [173]. Since the evaluation of the internal mass transfer is more complex to determine, this is studied in more detail in **Chapter 5**.

4.6. Conclusion

Chapter 4 reports the transesterification of tributyrin with methanol using various ion exchange resins as heterogeneous catalysts to to fill gaps concerning the catalytic performances of the anionic exchange resins studied.

Prior to running the catalytic tests, the Cl-resins were pre-treated and activated by converting counter-ions into hydroxyl ions using the appropriate NaOH solution to maximize the number of functional groups present in the resins. Resins provided in OH- and H-form were pre-treated to reduce water within their polymeric networks, also making the internal active sites more available for the transesterification reaction. A pre-treatment methodology for the resins was also investigated using the macroreticular IER 26OH as representative of the tested resins. The catalytic effectiveness of the resins was slightly reduced by the water content present in the resin. A slight increase in conversion and selectivity was found with the pre-treatment duration.

The catalyst screening of the eight IERs was conducted to select the most promising catalyst for the transesterification reaction by evaluating conversion and selectivity. Anionic resins are more active than acidic ones for the conversion of tributyrin with methanol. The results obtained were in agreement with the reaction mechanisms reported in the literature. Among the tested anion resins, 26OH was proved to be the highest performing catalyst. The conversion of tributyrin was 88 % when using 50 mg of 26OH, alcohol: oil molar ratio 1:30, stirring rate of 500 rpm, a constant temperature of 333 K and reaction time of 3 h. For this set of resins, catalytic performance correlated with their physical-chemical properties of the resins. The catalytic studies revealed that the gel-type resin 402OH* could achieve catalytic performance comparable with the macroreticular counterpart 26OH. The catalytic performance of these resins reflect the highest operating capacity of *ca.* 2 meq g^{-1} and ability to swell in the reaction medium.

The effects of the reaction parameters of the transesterification reaction over the anionic resin 26OH were studied with a DoE methodology. The DoE has contributed to our understanding of the resin behaviour in the reaction environment. It was found that the most important impact factors were temperature, molar ratio and catalyst loading. However, the external mass transfer was also investigated by varying the stirring rate between 100 and 500 rpm. The external mass transfer does not bear on the success of the resin catalysts. It was also observed that the stirring rate does not affect conversion as much as selectivity. The negligible impact of the stirring rate on catalytic performance of 26OH could suggest the use of a different reactor such as fixed bed reactor to reduce, therefore, the grounding of polymer beads and allowing their recovery from the reaction medium.

This work highlights some limitations, such as the lack of repetition of some experiments due to time constraints. Follow-up experiments and confirmation tests should be conducted to validate the results obtained.

Chapter 4 led to an improvement in the catalytic activity of the IERs. This chapter has filled the research gaps, which implies the lack of studies on these anionic resins in catalytic fields. To the author’s best knowledge, this is the first work that dealt with the activation of the resins in other ionic forms and IER pre-treatment study. The tested resins were used, for the first time, as catalysts for the transesterification reaction of a small triglyceride, tributyrin.

Our work has some limitations, such as the lack of replications for the screening tests and DoE experiment. Further experiments are needed to enhance both reproducibility and replicability of our results. Despite this, this work should prove to be a springboard for further research on IERs as catalysts for same reaction-type and add a growing body literature on IERs in the transesterification reaction.

The next chapter attempts to unravel the diffusion of reagents and products of the transesterification of tributyrin with methanol within the polymeric network and to discuss the challenges faced with the resinous beads.

Chapter 5

NMR diffusion studies: liquid confined in a porous material

5.1. Introduction

Porous materials, such as functionalised polymers and ordered mesoporous silica have found application in heterogeneous catalysis [27, 210, 211]. Functionalised polymers, ion exchange resins, and ordered mesoporous silica, such as SBA (Santa Barbara amorphous)-15 have shown potential as heterogeneous catalysts towards the production of biodiesel [27, 210, 211]. This chapter concerns the measurements of diffusion within pores. Any liquid confined within a porous material is expected to show different diffusion properties from the free bulk liquid because of the interactions present, both liquid-liquid and liquid-catalyst surface [212].

As a reaction occurs in micropores and mesopores, where the functional groups are immobilized, the motion of the molecules (diffusion) and residence time inside the pore are crucial steps for determining the overall reaction rate [27]. The pore connectivity of a porous material, which is estimated by a parameter called tortuosity, can generate diffusion limitations such as limited-access of bulky molecules will diminish the effectiveness of these materials and decrease the overall reaction rate [213].

D'Agostino and co-workers outlined the importance of the tortuosity in the porous network for three different supports, TiO_2, γ-Al_2O_3 and SiO_2 [212]. Recent work by Rottreau *et al.* reported the study on the tortuosity of two silica supports, SBA-15 and KIT-6, commonly used for the biodiesel production [210]. The diffusion coefficients of several carboxylic acids within the SBA-15 and KIT-6 pores were studied, showing a reduction in their measured diffusion coefficients for all the acids constrained in silica [210]. The tortuosity of both silica materials increase with the acid chain length [210]. D'Agostino *et al.* also investigated the behaviour of polyalcohols, such as 1,3-propanediol and glycerol, in a confined system [212]. An enhancement in the diffusion coefficients was observed due to the disruption of the hydrogen-bonding network of the bulk by the pore system in the solid [212, 214].

Nuclear magnetic resonance (NMR) relaxometry and diffusometry are both promising tools for the investigation of liquids confined in porous media [214]. NMR relaxometry studies the adsorption phenomena in porous material at liquid-solid interface by measuring the longitudinal, T_1, and transversal, T_2, relaxation time [215]. The ratio of these relaxation times T_1/T_2 measures the liquid-surface interaction [215]. Diffusion ordered NMR spectroscopy (DOSY) is a powerful NMR method for the investigation of molecular translation in various systems by estimating the diffusion coefficients of individual resonances observed in an NMR spectrum [215, 216].

DOSY has been used to reveal the motion of molecules through heterogeneous catalysts, explaining the pore structure and, for studying the interaction, the catalyst surface-molecules [212, 217].

In this chapter, DOSY NMR has been used to characterise both the silica support SBA-15 and two of the previously characterized ion exchange resins by measuring the diffusion coefficients of reagents and products related to the transesterification of tributyrin with methanol within their porous network. As indicated in **Chapter 4**, 26OH and 402OH*, which are based on styrene copolymers and functionalized with quaternary ammonium but different porosity, exhibited very different initial reaction rates, $\boldsymbol{r}^{\circ}$, plotted against the ratio between the operating capacity and pore volume of the tested resins. The macroreticular 26OH reached an initial reaction rate that was about three-fold higher than that of gel-type resin 402OH*. The motion of molecules within pores depends on the resin porosity.

This chapter is divided into eight sections. In the first section is a brief overview of the NMR principles. The second, third and fourth sections describe NMR diffusion principles for routine applications, the equipment used in this work and the sample preparation, respectively. The fifth section compares the diffusion results between the resins and SBA-15 and the reader's attention is drawn to the most relevant results and the challenges of these experiments.

5.2. Introduction to Nuclear Magnetic Resonance

Nuclear magnetic resonance (NMR) spectroscopy is a physical method to observe the magnetic properties of the various isotopes of elements in the periodic table [218] [218]. The nuclei studied have either an uneven mass number or even mass number with an odd atomic number [218]. These nuclei have a total orbital angular momentum, $\boldsymbol{I}$, which defines the magnitude of the momentum vector [103].

$$\boldsymbol{I}^{2} = \hbar^{2}\boldsymbol{I}(\boldsymbol{I} + 1) \qquad \textbf{Equation 5.1}$$

The projection of the orbital angular quantum number, $\boldsymbol{I}$, on the z-axis is

$$\boldsymbol{I}_{z} = \boldsymbol{m_I}\hbar \qquad \textbf{Equation 5.2}$$

where $\boldsymbol{m_I}$ represents the quantization of $\boldsymbol{I}$ and $\boldsymbol{I} = -\boldsymbol{I}, -\boldsymbol{I} + 1, -\boldsymbol{I} + 2, \ldots, +\boldsymbol{I}$ and $\hbar = \mathrm{h}/2\pi$ with $\mathrm{h} = 6.63 \times 10^{-34}\ \mathrm{m^2\ kg\ s^{-1}}$, Planck's constant.

For the nuclei characterised by uneven mass, the nuclear spin quantum number ***I*** is a half-integer while for those with an even mass number but odd atomic number ***I*** is integer value [103]. The proton with $\boldsymbol{I} = \frac{1}{2}$ is characterised by nuclear magnetic moment, $\boldsymbol{\mu}$, that gives rise to a magnetic field [103].

The proton is characterized by an electron spin angular momentum, ***S*** and a nuclear spin quantum number, $\boldsymbol{m}_s$ [103].

$$\boldsymbol{S}^2 = \hbar^2 \boldsymbol{s}(\boldsymbol{s} + 1) \qquad \textbf{Equation 5.3}$$

where ***s*** is the electron spin quantum number. In case of the proton, ***s*** is equal to 1/2.(unpaired electron) [103]. The projection of ***S*** on the z-axis gives rise to [103]

$$\boldsymbol{S}_z = \boldsymbol{m}_s \hbar \qquad \textbf{Equation 5.4}$$

The spin eigenstates of $\boldsymbol{m}_s$ are characterized by $\boldsymbol{m}_s = +1/2$ (spin up, *α*) and $\boldsymbol{m}_s = -1/2$ (spin down, *β*). **Figure 5.1** represents a schematic illustration of the nuclear spin quantum numbers.

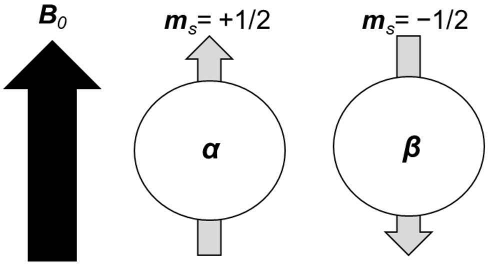

Figure 5.1. Schematic illustration of the nuclear magnetic spins in the spin-up (*α*) and spin-down (*β*) state, interacting with an external magnetic field $\boldsymbol{B}_0$ (Reproduced from [219]).

Electrons and nucleous as charged particles with an angular momentum can generate a magnetic momentum, $\boldsymbol{\mu}$. This magnetic momentum is described in **Equation 5.5** and **Equation 5.6** [103].

For electron $$\boldsymbol{\mu}_z = -\gamma_e \boldsymbol{S}_z \qquad \textbf{Equation 5.5}$$

For nucleous $$\boldsymbol{\mu}_z = \gamma_N \boldsymbol{I}_z \qquad \textbf{Equation 5.6}$$

where $\boldsymbol{\gamma}_e$ is the magnetogyric ratio of the electron and $\boldsymbol{\gamma}_e$= 1.76 × $10^{11}$$s^{-1}$$T^{-1}$ [103]. While $\boldsymbol{\gamma}_N$ is the magnetogyric ratio, and it is a constant characteristic of the nucleus. For this work, where only protons were studied, so $\boldsymbol{\gamma}_H$ = 2.68×10^8 rad s^{-1} T^{-1}.

When a hydrogen nucleus is placed into a magnetic field $\boldsymbol{B_0}$; the energy associated with the magnetic dipole is [103]

$$\boldsymbol{E} = -\boldsymbol{\mu}_z\boldsymbol{B_0} \qquad \textbf{Equation 5.7}$$

By replacing **Equation 5.5** and **Equation 5.6** in **Equation 5.7**, we have [103]

For electron $$\boldsymbol{E} = \boldsymbol{\gamma}_e\boldsymbol{\hbar m_s B_0} \qquad \textbf{Equation 5.8}$$

For nucleous $$\boldsymbol{E} = -\boldsymbol{\gamma}_N\boldsymbol{\hbar m_I B_0} \qquad \textbf{Equation 5.9}$$

where $\boldsymbol{m}_s$= ±1/2 and $\boldsymbol{m}_I$= ±1/2.

Figure 5.2 illustrates that the increase of the magnetic field, $\boldsymbol{B_0}$, generates the split of the energy level. Thus, the spins aligned to the field $\boldsymbol{B_0}$ with $\boldsymbol{m}_s$= +1/2 and $\boldsymbol{m}_I$ = −1/2, it is associated with a ground energy level ($\boldsymbol{E}$= −1/2$\boldsymbol{\gamma\hbar B_0}$). However, if the spin is oppositive to the field with $\boldsymbol{m}_s$= −1/2 and $\boldsymbol{m}_I$= +1/2. It is characterized by a high energy level ($\boldsymbol{E}$= +1/2$\boldsymbol{\gamma\hbar B_0}$).

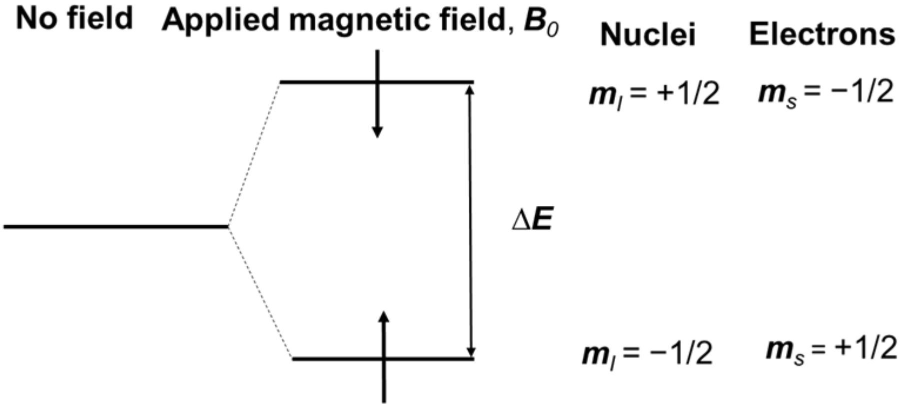

Figure 5.2. Splitting of the energy levels of the proton nucleus after a magnetic field, $\boldsymbol{B_0}$*,* is applied (Reproduced from [217]).

The distribution of the spins is given by the Boltzmann equation, **Equation 5.10** [103].

$$\frac{N_{upper}}{N_{lower}} = e^{-\frac{\Delta E}{k_B T}} \qquad \textbf{Equation 5.10}$$

where ΔE is the energy splitting, k_B is the Boltzmann constant (1.38×10^{-23} J K^{-1}), and T is the temperature (K).

The energy splitting is known as the Zeeman effect, and it is expressed as[103]

$$\Delta E = \frac{hv}{2\pi} = \frac{\gamma h B_0}{2\pi} \qquad \textbf{Equation 5.11}$$

The difference in energy levels, ΔE is proportional to the strength of the field B_0. At the equilibrium, the majority of nuclei would be on the ground level. However, when the nuclei are subject to an external field, they can absorb photons of energy, allowing them to move from the ground level to the high level.
The resonant frequency, also called Larmor frequency v_0 is given in the form [103]

$$v_0 = \frac{\gamma B_0}{2\pi} \qquad \textbf{Equation 5.12}$$

where v_0 is the Larmor frequency (Hz), γ is the gyromagnetic ratio (rad s^{-1} T^{-1}), and B_0 is the magnetic field (T).

or Larmor angular frequency ω_0 [103].

$$\omega_0 = \gamma B_0 \qquad \textbf{Equation 5.13}$$

ω_0 is expressed in rad s^{-1}.

NMR spectrometers are typically classified according to their observed proton frequencies. When a magnetic field with a strength of 7.05 T is applied, the protons resonate at 300 MHz. If the direction of the external magnetic field is parallel to the *z*-axis; it is termed as net or bulk magnetization M, and it represents a vector along the *z*-axis as illustrated in **Figure 5.3**.

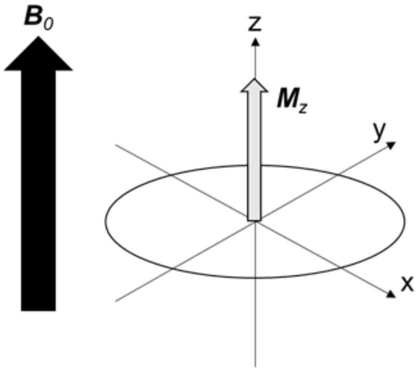

Figure 5.3. The net magnetisation (M_z) is aligned along z-axis when a magnetic field, B_0, is applied (Reproduced from [217]).

The application of a second magnetic field B_1 with a radio frequency (R.F.) pulse orthogonal to B_0, tilts the magnetization M of 90° on the *xy*-plane to give rise to the resonance phenomenon. It generates the net magnetization M in the *xy*-plane goes through a detector coil to produce a free induction decay (FID). After the R.F. pulse, it oscillates and decades to zero according to longitudinal relaxation, T_1 and transversal relaxation, T_2 [220]. These mechanisms of relaxation were investigated by Bloch and are described in **Section 5.2.3**.
The most critical parameters in a NMR spectrum are the chemical shift, scalar coupling (*J*-coupling), and longitudinal and transversal relaxation.

5.2.1. Chemical shift

^{1}H nuclei within a molecule do not resonate at the same frequencies. The differences in resonance frequency, also called chemical shifts, rely on the chemical environment in which the proton resides [221]. The chemical shift, δ is described by **Equation 5.14** [222].

$$\boldsymbol{\delta} / \text{ppm} = \frac{\boldsymbol{v} - \boldsymbol{v_0}}{\boldsymbol{v_0}} \qquad \textbf{Equation 5.14}$$

where v_0 is the resonance frequency of the reference while v is the resonance frequency of the compound. It is expressed in parts per million (ppm).

Chemical shifts give information on the local chemical environment such as chemical bonding. The resonance frequency of a nucleus is not related to the external magnetic field, B_0, but the local field, B_{loc}, experienced by the nucleus at the atomic level. The chemical shift is a result of magnetic susceptibility [223]. This susceptibility is the response of matter at atomic and molecular levels due to the application of an external magnetic field.

Electrons move around the nucleus (electron cloud), producing an induced magnetic field, $\boldsymbol{B}_{ind}$ that is opposed to $\boldsymbol{B}_0$, as illustrated in **Figure 5.4**.

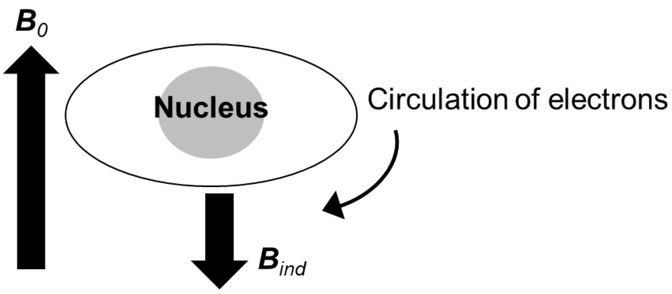

Figure 5.4. The motion of electrons generates the induced magnetic field, $\boldsymbol{B}_{ind}$ to respond to the applied field $\boldsymbol{B}_0$. $\boldsymbol{B}_{ind}$ opposes $\boldsymbol{B}_0$ and reduce the effect of $\boldsymbol{B}_0$ on the nucleus from $\boldsymbol{B}_0$ (Reproduced from [224]).

The electron cloud performs as a shield, protecting the nucleus from the external magnetic field $\boldsymbol{B}_0$ [221]. The local magnetic field, $\boldsymbol{B}_{loc}$ experienced by the nucleus is expressed as [221]

$$\boldsymbol{B}_{loc} = \boldsymbol{B}_0 - \boldsymbol{B}_{\mathrm{ind}} = \boldsymbol{B}_0(1 - \boldsymbol{\sigma}) \qquad \textbf{Equation 5.15}$$

where $\boldsymbol{\sigma}$ is the shielding parameter.

The frequency of a spin relies on the chemical and electronic neighbouring of the nucleus under investigation. Considering methane, CH_4, its protons have a chemical shift of 0.23 ppm. The chemical shift value changes measurably as one of the protons in CH_4 is replaced with a fluorine atom, CH_3F. Its protons resonate at 4.26 ppm. Therefore, nuclei associated with high electron density are shielded from the magnetic field $\boldsymbol{B}_0$ and the signal appears low chemical shifts while nuclei attached to electronegative atoms are de-shielded, and the signal appears at higher chemical shifts [218].

5.2.2. *J*-coupling: spin-spin interactions

J-coupling is a through bond-interaction in which the nuclear spins polarize the spins of the neighbouring nuclei, causing splitting in the NMR spectra. *J*-coupling is measured in Hz, and is field-dependent [218]. A detailed description of *J*-coupling is beyond the scope of this chapter.

5.2.3. Relaxation

NMR relaxometry concerns how the motion of molecules can affect the duration of magnetization by recording transverse T_2 and longitudinal T_1 components of magnetization as a function of time with several experiments. From there, relation time constants can be determined. This technique can evaluate the interactions of confined liquids with the pore walls and internal field gradients. In 1946, Bloch explained the relaxation processes with the assumption that the magnetisation, $\boldsymbol{M}$, could be resolved into three components as a function of the time ($\boldsymbol{M}_x(\boldsymbol{t})$, $\boldsymbol{M}_y(\boldsymbol{t})$ and $\boldsymbol{M}_z(\boldsymbol{t})$) [225]. $\boldsymbol{M}_x(\boldsymbol{t})$ and $\boldsymbol{M}_y(\boldsymbol{t})$ are the transverse components, while $\boldsymbol{M}_z(\boldsymbol{t})$ is their longitudinal counterpart.

5.2.3.1. Longitudinal relaxation-T_1

The spin-lattice relaxation time, or T_1 relaxation time, indicates how quickly the magnetisation recovers to the ground state. When the excited nuclear spins return from a high state to low state, they relax and release energy to reach equilibrium by dissipating excess energy to an environment-lattice. This process is called spin-lattice relaxation or longitudinal relaxation. Equilibrium is a state in which the Boltzmann equation describes the distribution of spins, and no transversal magnetisation is present. At the equilibrium, the magnetisation can be described as [220].

$$\boldsymbol{M}_z \propto \left(\boldsymbol{N}_\alpha - \boldsymbol{N}_\beta\right) \qquad \textbf{Equation 5.16}$$

where $\boldsymbol{N}_\alpha$ and $\boldsymbol{N}_\beta$ are the spin population in the ground (α) and the excited level (β), respectively.

The longitudinal relaxation, T_1 involves the energy exchange between the spins and the surrounding lattice, re-establishing the normal Gaussian population of spins in α and β spin states (thermal equilibrium) [219].

The net magnetisation, $\boldsymbol{M}_z$, is represented along the z-axis in the equilibrium state. When a 90° R.F. pulse is applied, $\boldsymbol{M}_z$ is reduced to zero. Then, the vector gradually moves backs to the initial position with a rate governed by the time constant, T_1, if no further R.F. pulse is applied [226]. The recovery of the net magnetisation, $\boldsymbol{M}_z$, follows an exponential curve (**Equation 5.17**) [218].

$$\boldsymbol{M}_z(\boldsymbol{t}) = \boldsymbol{M}_0(1 - \mathrm{e}^{-\boldsymbol{t}/\boldsymbol{T}_1}) \qquad \textbf{Equation 5.17}$$

where $\boldsymbol{M_z}$ is the magnetization along the *z*-axis, $\boldsymbol{M_0}$ is the initial maximum magnetization along the *z*-axis, ***t*** is the time, and T_1 is time-constant of the spin-lattice relaxation. **Figure 5.5** provides a graphical representation of the longitudinal relaxation T_1.

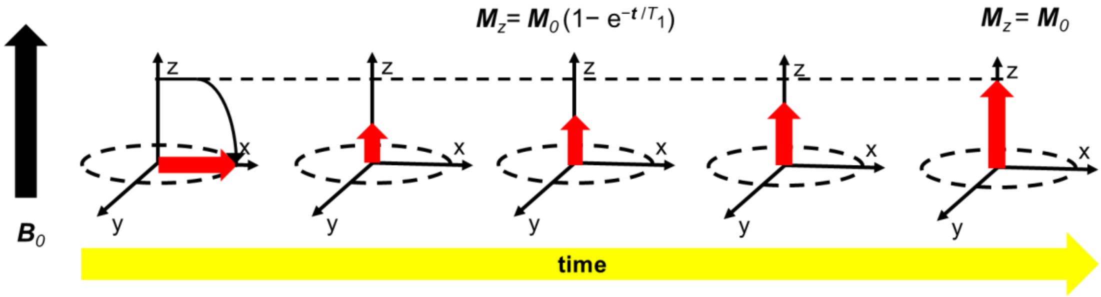

Figure 5.5. T_1 relaxation is a process in which the magnetization $\boldsymbol{M_z}$ turns back to its original maximum value $\boldsymbol{M_0}$ (Reproduced from [227]).

The relaxation $\boldsymbol{T_1}$ depends on the nuclei, molecular weight, temperature and magnitude of the magnetic field [218]. The precession occurs according to the Larmor frequenc, $\boldsymbol{\omega_0}$ (**Equation 5.18**). The spin-lattice relaxation is measured by applying a 180° pulse (inversion recovery method) [220].

For porous media T_1 is expressed as [218]

$$\frac{1}{T_1} = \frac{1}{T_{1,\,Bulk}} + \frac{1}{T_{1,\,Surface}} \qquad \textbf{Equation 5.18}$$

$T_{1,\,Bulk}$ is the relaxation time of the bulk liquid (s) and $T_{1,\,Surface}$ is the relaxation time in the porous material caused by the interactions between the liquid molecules and the material wall [228].

$$\frac{1}{T_{1,\,Surface}} = \boldsymbol{\rho_1}\frac{\boldsymbol{S}}{\boldsymbol{V}} \qquad \textbf{Equation 5.19}$$

where ***S*** is the pore surface area, ***V*** is the volume and $\boldsymbol{\rho_1}$ is the surface relaxivity.

Let us consider a surface layer of thickness, $\boldsymbol{\delta}$ of the liquid subjected to surface relaxation over a relaxation time, $\boldsymbol{T_s}$ [229].The surface relaxivity is described as

$$\boldsymbol{\rho} = \frac{\boldsymbol{\delta}}{\boldsymbol{T_s}} \qquad \textbf{Equation 5.20}$$

Combining **Equation 5.18** with **Equation 5.19** [228].

$$\frac{1}{T_1} = \frac{1}{T_{1,\,Bulk}} + \rho_1 \frac{S}{V}$$ **Equation 5.21**

where T_1 is the measured value of time-constant T_1, ρ_1 is the surface relaxivity which, indicates the interaction between the wall of the porous material and the molecules [228]. Thus, T_1 measured relies on the pore size and its distribution [228].

5.2.3.2. Transverse relaxation-T_2

Occurring simultaneously with the longitudinal relaxation, the transverse relaxation (spin-spin relaxation) T_2 occurs on the *xy*-plane due to the mechanism concerns why the spins wobble at different rates and thus the net magnetisation M_z is lost, as depicted in **Figure 5.6** [230].

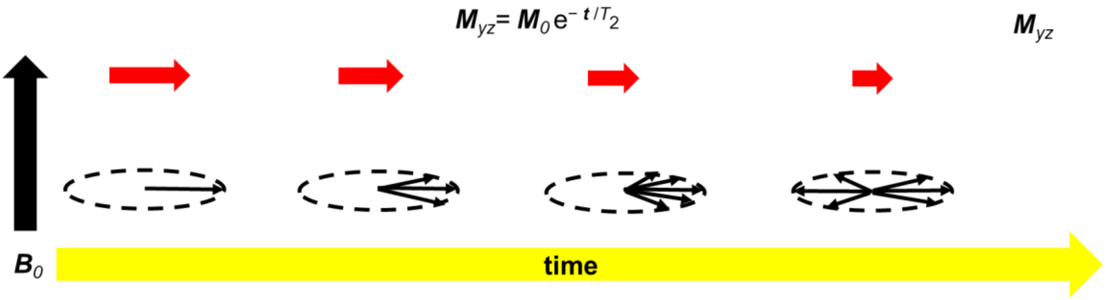

Figure 5.6. T_2 relaxation is a process due to loss of coherence of the spins. (Reproduced from [230]).

When an R.F. pulse is applied, the pulse rotates the magnetisation into the *xy*-plane. Thus, the spins dephase and they are characterised by their own Larmor frequency [220]. The transverse magnetization M_{xy} returns to the equilibrium according to T_2 [220].

$$M_{xy} = M_{xy0}\, e^{-t/T_2}$$ **Equation 5.22**

The net magnetization in the *xy*-plane reaches zero, and then it grows along *z* until it reaches the magnitude M_0 (equilibrium) ($T_2 \leq T_1$). The spins dephasing can arise from either the inhomogeneity of the magnetic field B_0 or the interactions between nuclei spins of the neighbouring atoms [220]. The combination of these factors is described by the constant T_2^* [220].

$$\frac{1}{T_2^*} = \frac{1}{T_2} + \frac{1}{T_{2,\,inhomogenous}} \qquad \textbf{Equation 5.23}$$

where T_2 is the time constant of the transverse relaxation while $T_{2,\ inhomogenous}$ is the time constant related to the imperfections of the magnetic field applied $\boldsymbol{B_0}$.

In porous media, the dephasing of the spin relies on the spin-spin interactions and the inhomogeneities of the external magnetic field, $\boldsymbol{B_0}$ [228]. It is associated with a time-constant T_2***** which is expressed as

$$\frac{1}{T_2^*} = \frac{1}{T_{2,\,Bulk}} + \frac{1}{T_{2,\,Inhomo}} + \frac{1}{T_{2,\,Surface}} + \frac{1}{T_{2,\,Diffusion}} \qquad \textbf{Equation 5.24}$$

where $T_{2,\ \mathrm{Bulk}}$ is the time constant of the bulk liquid, $T_{2,\ Inhomo}$ is the time-constant associated with the spin dephasing due to the interaction of $\boldsymbol{M_{xy}}$ with the inhomogeneities of $\boldsymbol{B_0}$. The effect of $T_{2,\ Inhomo}$ can be compensated by applying a spin-echo sequence [228]. $T_{2,\ Diffusion}$ is characterised by the differences in susceptibility between the solid and liquid phase, and its contribution can be reduced by applying short echo times [228]. $T_{2,\ Surface}$ consists of the relaxation effects between the walls and the molecules [228].
Likewise $T_{1,\ Surface}$**,** $T_{2,\ Surface}$ relies on the pore size and its distribution as shown in **Equation 5.25** [228].

$$\frac{1}{T_{2,\,Surface}} = \boldsymbol{\rho}_2\frac{\boldsymbol{S}}{\boldsymbol{V}} \qquad \textbf{Equation 5.25}$$

where $\boldsymbol{S}$ is the pore surface area, $\boldsymbol{V}$ is the volume and $\boldsymbol{\rho}_2$ is the surface relaxivity, which indicates the interaction between the wall of the porous material and the molecules.

Combining **Equation 5.24** with **Equation 5.25** [228].

$$\frac{1}{T_2^*} = \frac{1}{T_{2,\,Bulk}} + \frac{1}{T_{2,\,inhomo}} + \boldsymbol{\rho}_2\frac{\boldsymbol{S}}{\boldsymbol{V}} + \frac{1}{T_{2,\,Diffusion}} \qquad \textbf{Equation 5.26}$$

5.3. Diffusion theory

The term diffusion is used to describe both mutual and translational diffusion induced by the random thermal motion of molecules within porous materials [231]. Both diffusions are expressed in the unit m^2 s^{-1}. Their differences arise from a physical origin [231]. Mutual diffusion occurs when there are concentration gradients while translational diffusion is a random thermal motion of molecules or ions in a solution as the molecules constantly collide with other [231]. The latter is called Brownian motion [231]. This model explains the diffusion of a fluid at thermal equilibrium at a given temperature. At thermal equilibrium, the total energy is distributed equally among translational, rotational and vibrational motions. This is called equipartition theorem. When molecules travel in a solution, they experience the effect of friction force due to the neighbouring molecules. The frictional force, $\boldsymbol{F}$ is proportional to the frictional coefficient, $\boldsymbol{f}$ and the velocity, $\boldsymbol{v}$. This relationship is known as the Stokes' law [231].

$$\boldsymbol{F} = -\boldsymbol{fv} \qquad \textbf{Equation 5.27}$$

Einstein developed a statistical mechanics theory to connect the diffusion coefficient of Brownian movement of an individual particle with thermal energy and the friction coefficient (**Equation 5.28**) [232].

$$\boldsymbol{D} = \frac{\boldsymbol{k_B T}}{\boldsymbol{f}} \qquad \textbf{Equation 5.28}$$

where $\boldsymbol{k_B}$ is the Boltzmann constant (1.38×10^{-23} m^2 Kg s^{-2} K^{-1}), $\boldsymbol{T}$ is the temperature and, $\boldsymbol{f}$ is the frictional coefficient.

Equation 5.29 relates the friction coefficient, $\boldsymbol{f}$ with the solvent viscosity, $\boldsymbol{\eta}$.[233]. The frictional coefficient, $\boldsymbol{f}$ for spherical particles is [233]

$$\boldsymbol{f} = 6\pi\boldsymbol{\eta R} \qquad \textbf{Equation 5.29}$$

where $\boldsymbol{R}$ is the radius of the particles.

By combining **Equation 5.28** with **Equation 5.29**, the Stokes-Einstein equation is obtained [231].

$$\boldsymbol{D} = \frac{\boldsymbol{k_B T}}{6\pi\boldsymbol{\eta R}} \qquad \textbf{Equation 5.30}$$

$\boldsymbol{D}$ is the diffusion coefficient and it is expressed in m^{2}s^{-1}.

In isotropic media, such as most liquids and cubic crystals, the diffusion is a scalar factor and, physical and chemical properties are independent of direction [234]. The distribution of molecules in the solution is crucial, and it is described by Fick's first and second laws.

The first law can be applied to a steady state system, such as bulk liquids, where the concentration is constant, while the second law deals with non-steady state systems, such as liquids confined within porous material and, the concentration changes with time [234]. The first law relates the connection between the concentration gradient of molecules or atoms of an isotropic medium across the plane $(\partial \boldsymbol{C}/\partial \boldsymbol{x})$ and diffusion coefficient ***D*** of a given species in a specific solvent [234].

$$\boldsymbol{J} = -\boldsymbol{D}\frac{\partial \boldsymbol{C}}{\partial \boldsymbol{x}} \qquad \textbf{Equation 5.31}$$

where ***J*** is the flux.

However, the second law postulates that the change in concentration over time ***t*** is equal to the change in diffusion as [234]

$$\frac{\partial \boldsymbol{C}}{\partial \boldsymbol{t}} = -\frac{\partial \boldsymbol{J}}{\partial \boldsymbol{x}} \qquad \textbf{Equation 5.32}$$

Combining **Equation 5.31** and **Equation 5.33** [234][234].

$$\frac{\partial \boldsymbol{C}}{\partial \boldsymbol{t}} = -\frac{\partial \boldsymbol{C}}{\partial \boldsymbol{x}^2} \qquad \textbf{Equation 5.33}$$

Considering an isotropic system in three dimensions without thermal and concentration gradients, the average molecular distribution, ***r,*** is null in the three directions, but the mean square displacement, $<\boldsymbol{r}^2>$ moved along the *x*-axis in an interval of time ***t*** is [217]

$$<\boldsymbol{r}^2> = 6\boldsymbol{Dt} \qquad \textbf{Equation 5.34}$$

For isotropic materials, diffusion is the same in each direction and it is associated with a single diffusion coefficient, ***D***.

Anisotropic media exhibit different diffusion properties in different directions. Anisotropy influences the direction of the correlation between diffusion and gradient coefficients. In anisotropic materials, diffusion cannot be expressed by a single diffusion coefficient but a diffusion tensor. This is a symmetrical matrix [3×3] in which the subscript indices the direction of diffusion, **Equation 5.35** [235].

$$D = \begin{bmatrix} D_{xx} & D_{xy} & D_{xz} \\ D_{yx} & D_{yy} & D_{yz} \\ D_{zx} & D_{zy} & D_{zz} \end{bmatrix} \qquad \textbf{Equation 5.35}$$

The three diagonal coefficients represent the coefficients measured along *x*-, *y*- and *z*-directions while the six-off diagonal coefficients correspond to the random walk of molecules in the main directions. The diffusion coefficients can be measured employing an appropriate NMR pulse sequence with Diffusion Ordered Spectroscopy (DOSY). These pulse sequences consist of radiofrequency pulse, pulsed magnetic field gradients and delays. During the diffusion experiment, molecules undergo translational motion between two gradient pulses. The first pulse dephases the magnetization and the second pulse refocuses it by a delay $\boldsymbol{\Delta}$. The spatial discrimination of the nuclei is achieved using a spatially magnetic field gradient $\boldsymbol{g}(z)$ [236]. The gradient causes a linear variation of the magnetic field $\boldsymbol{B_0}$ as [236].

$$\boldsymbol{B} = (\boldsymbol{B_0} + \boldsymbol{g}(z)) \qquad \textbf{Equation 5.36}$$

Due to the spatially gradient, the precession of the spins depends on the position [236].

$$\boldsymbol{\omega}_{total} = -\boldsymbol{\gamma}(\boldsymbol{B_0} + \boldsymbol{g}(z)) = \boldsymbol{\omega_0} - \boldsymbol{\gamma g}(z) \qquad \textbf{Equation 5.37}$$

This equation highlights the dependence of the nucleus precession on the position *z*, allowing a phase shift of the spins. In a pulse sequence, the gradient pulse applied for a short time $\boldsymbol{\delta}$ (s) produces a precession in the frame of angular frequency $\boldsymbol{\omega_0}$ of $-\boldsymbol{\gamma g}(z)\boldsymbol{\delta}$ [236]. Thus, the gradient generates a helical pattern of magnetisation vectors within the sample with a vertical distance between two consecutive turns, with a pitch of [236].

$$\Lambda = \frac{2\pi}{\boldsymbol{\gamma g}(z)\boldsymbol{\delta}} \qquad \textbf{Equation 5.38}$$

This event occurs when the spin re-occupies the same position after the application of the gradient and there is no loss of signal [236]. However, if the spin moves into another position, i.e as a result of molecular diffusion, there will not be a complete re-focusing [236]. A free induction decay (FID) is detected from a receiver coil employing Faraday induction and converted into a frequency domain signal (NMR spectrum) by Fourier transform [236]. Thus, the molecular diffusion produces a reduction of the intensity signal that is proportional to the applied gradient intensity ($\boldsymbol{g}$) and the duration ($\boldsymbol{\delta}$) [236].

The attenuation of signal is expressed by the Stejskal-Tanner equation, **Equation 5.39** [217].

$$\frac{\boldsymbol{S}}{\boldsymbol{S_0}} = e^{\left(-\boldsymbol{\gamma}^2\boldsymbol{g}^2\boldsymbol{D}\boldsymbol{\delta}^2\left(\Delta - \frac{\boldsymbol{\delta}}{3}\right)\right)} = e^{(-\boldsymbol{bD})} \qquad \textbf{Equation 5.39}$$

where $\boldsymbol{S}$ and $\boldsymbol{S_0}$ are the signal intensity obtained in presence and in absence of applied field gradient, respectively, $\boldsymbol{q}$ is the gradient pulse area ($\boldsymbol{\gamma g \delta}$), $\boldsymbol{\gamma}$ is the magnetogyric ratio of hydrogen atoms (2.676×10^8 rad^{-1}s^{-1}T^{-1}), $\boldsymbol{g}$ is the gradient amplitude along z axis, $\boldsymbol{\delta}$ is the width of the gradient pulse, and $\boldsymbol{\Delta}$ is the diffusion time [217].

Equation 5.39 presumes a Gaussian distribution of the diffusing spins. This is usually applied for free diffusion, such as bulk liquids [237]. However, this equation can be applied for systems in quasi-homogeneous behaviour, such as porous media [237]. The Stejskal-Tanner equation is used to fit the measured attenuation and obtain the diffusion coefficient.

In isotropic systems, $\boldsymbol{D}$ is independent of the diffusion time, thus, the mean square displacement $\langle \boldsymbol{r}^2 \rangle$ [238].

A completely different scenario occurs when the diffusing molecules are confined within boundaries, $\boldsymbol{D}$ is diffusion time dependent [238]. The diffusive transport of a liquid confined within porous media is subject to restrictions due to morphological structure of pores. For short $\boldsymbol{\Delta}$, a free diffusion profile is obtained and the mean square displacement increases with $\boldsymbol{\Delta}^{1/2}$, because only few diffusing molecules interact with the pore walls [238]. For longer $\boldsymbol{\Delta}$**,** more diffusing molecules can interact with the pore walls, giving important information on pore size, structure and architecture [238]. The application of DOSY measurements gives an effective diffusion coefficient, $\boldsymbol{D_{eff}}$, which depends on the pore medium structure and on the diffusion time used [214]. Another important parameter is tortuosity, which defines the pore connectivity of the pores within the material. Tortuosity is defined as dimensionless parameter, $\boldsymbol{\xi}$. and it is the ratio of the free bulk liquid diffusivity, $\boldsymbol{D_0}$ to the effective diffusion coefficient, $\boldsymbol{D_{eff}}$ of the liquid within the pores, **Equation 5.40** [210].

$$\boldsymbol{\xi} = \frac{\boldsymbol{D_0}}{\boldsymbol{D_{eff}}} \qquad \textbf{Equation 5.40}$$

5.4. NMR hardware

The NMR spectrometer utilizes a superconducting magnet so that a low temperature its resistivity reaches zero [220]. The magnet consists of a coil of wire in which the current travels, producing a magnetic field, $\boldsymbol{B_0}$. The advantage of this magnet is that it is very stable, and once the current pass through the wire, it generates a magnetic field and no further electrical power is required [220]. To operate in the superconducting conditions, this magnet needs to be immersed in a bath of liquid helium. This bath is surrounded by another bath of liquid nitrogen at 77 K that minimizes the helium boiling-off [220]. The superconducting magnet and the two baths consist of a whole part in which a vertical tube (bore tube) is located in the centre of the magnet, and the magnetic field has the same direction of the tube [220].

In general, good resolution data require a high field homogeneity (> 1 in 10^7) [239]. Thus, the superconducting magnet cannot provide such a perfect homogeneous field, $\boldsymbol{B_0}$. As a result of this, the shim coils are used to produce tiny magnetic fields, adjusting the current passing through their wires until the magnetic field reaches homogeneity [220]. The assessment of its homogeneity is achieved by recording the spectrum. However, to improve homogeneity, a shimming process is required in which the shims can be either manually modified or uploaded from a shim set for an appropriate probe (i.e. ^{1}H) [220]. These shims are labelled using algebraic terms like x, y and z. Additional components such as their quadratic ones (i.e. z^2) and their combinations (i.e. xy) are also available.

The probe is a cylindrical metal tube located in the bore probe. It consists of a coil that can excite and record the NMR signal. Another additional adjustment is the maximization of the power between the probe and the receiver and transmitter [220]. The transmitter system allows to set up an R.F. pulse and gradient pulses, producing a sine wave characterised by the desired frequency. The PC controls the R.F. source. The system generates the magnetic field $\boldsymbol{B_1}$ that allows spins to tilt by 90° or 180° and records the signal. In addition, the probe contains gradient coils that generate a magnetic field along the x-, y- and z-axes [226]. The pulse programmer creates gradient pulses, which can vary in their amplitude and shape [240]. A synthesizer is used as an R.F. source. Its signal passes through a gate to produce an R.F. pulse of the desired energy (a gating output). The timing and amplitude of the output are customized by the computer [220]. The NMR signal coming from the probe has small magnitude, and it is amplified using an amplifier. The coil in the probe is used to excite the spins and to record the signal. To separate the receiver and the transmitter has used a diplexer [220]. Thus, when the pulse is on the R.F. pulse is directed towards the probe while the receiver is disconnected.

Conversely, when the pulse is off, the receiver is connected, and the transmitter is disconnected [220]. The voltage is, then, converted to a binary number by an analogue to digital converter (ADC) [220]. Finally, the signal is sampled at regular intervals by the ADC, using the collected data points for the FID representation [222]. The output is based on the total number of bit that ADC uses [220] A schematic illustration of a NMR spectrometer is depicted in **Figure 5.7**.

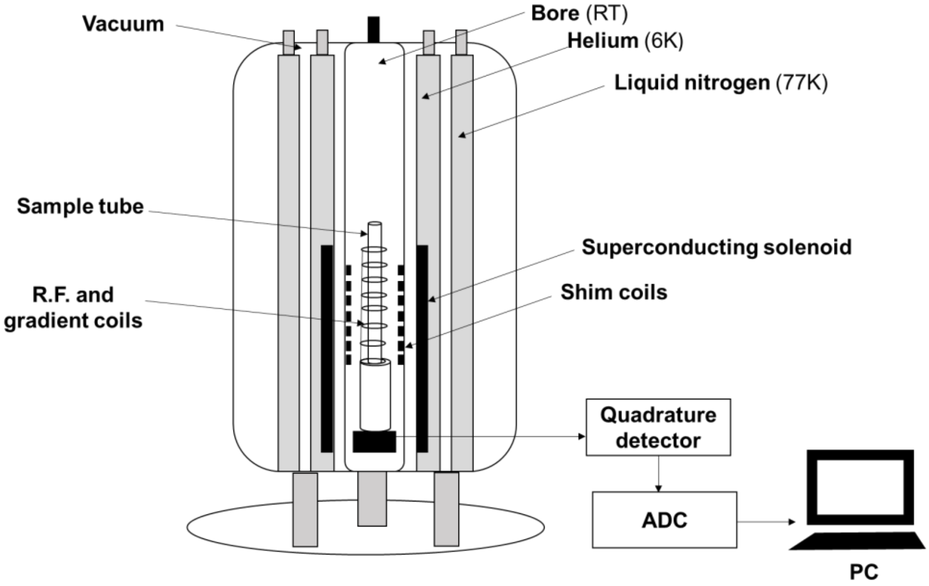

Figure 5.7. Schematic diagram detailing the main components of a modern nuclear magnetic resonance (NMR) spectrometer (Reproduced from [217]).

5.5. Calibration of the instrument

The experiments were carried out on a Bruker Avance spectrometer with a frequency of 300 MHz and operating at a magnetic field strength of 7.05 T. This instrument was calibrated by former PhD student, Dr Taylor J. Rottreau. The detailed calibration is reported in his PhD thesis [217]. Three parameters were calibrated to ensure that pulsed field gradients have not been affected by errors in gradient applications, temperature fluctuations and convection.

The gradient calibration was performed by comparing the diffusion coefficients of three samples, 1% H_2O in D_2O, dimethyl sulfoxide (DMSO) and cyclohexane, with their literature values to check the nominal value of gradient strength installed in the NMR spectrometer [217]. The nominal value of the gradient was 5.35 G cm^{-1} [219]. A systematic error in the diffusion coefficients of the species analysed was found. Thus, the value of the gradient constant was replaced by the measured value, 5.64 G cm^{-1}, and the diffusion coefficients matched the literature values [217]. The experiments were conducted using the new value of gradient strength.

Temperature is another parameter that can affect the measurement. As the temperature sensor is located below the sample probe in the spectrometer, it will experience a different temperature than that of the sample [217]. The exact temperature of the sample was measured using deuterated methanol that has a temperature-dependent chemical shift, which acted as NMR thermometer by using the methodology developed by Findeisen *et al.* [241] .
Convection has also been found to affect significantly the accuracy of diffusion data. The effect of convection was evaluated using the methodology described by Morris and co-workers [242-244]. It was found that the use of a compensated pulse sequence with bipolar pulse gradient, DSTEBPGP_3S, was successful in reducing the convection on diffusion data [217]. This bipolar pulse gradient is illustrated in **Figure 5.8**.

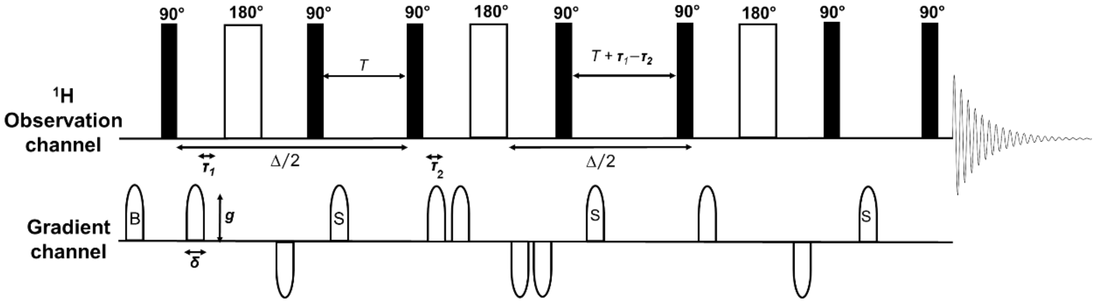

Figure 5.8. The double stimulated echo bipolar pulse pair sequence (DSTEBPGP_3S) used in this work (Reproduced from [210]).

The diffusion delay, ***Δ***, is split into two parts, and two sets of bipolar pulse pairs to assure that the only 180° pulse can re-phase the net magnetisation [210]. The sequence incorporates spoiler gradients (marked as S) to remove any unwanted signal in the *xy*-plane [210]. These gradients are counterbalanced by the gradient pulse marked as B [210].This sequence was used for the diffusion experiments performed in this project. The attenuated signal, S/S_0, is written in the following form showed in **Equation 5.41** [210].

$$\frac{S}{S_0} = e^{-D\gamma^2\delta^2\sigma^2 g^2\left[\Delta + \left[\frac{(2\kappa - 2\lambda - \delta)}{2}\right] - \left[\frac{(\tau_1 + \tau_2)}{2}\right]\right]} \qquad \textbf{Equation 5.41}$$

where S_0 is the signal before a gradient was applied, D is the diffusion coefficient, γ is the gyromagnetic ratio of a proton, δ is the gradient length (0.001 s), g is the gradient strength, τ_1 and τ_2 are inter-gradient delays within the bipolar gradient pulses. σ, k and λ are all parameters associated with shaped gradient pulse. σ represents the efficiency of the gradient pulse, and it is equal to 2/π. k and λ are equal to 1/2 and 3/8, respectively for half-sine gradients pulses.

The delay time, ***Δ***, has a value of 0.3 s. For all experiments summarised here, ten magnetic field gradient amplitudes from 7.19×10^{-3} to 2.87×10^{-2} T m^{-1} were used and incremented in equal steps of gradient squared.

All these calibrations ensure reproducible and accurate instrument performance.

5.6. Materials

Commercial polymeric resins and silica powders such as SBA-15 have been used as catalysts and catalyst support, respectively [27, 109]. The commercial resins, 26OH and 402OH*, were supplied in their catalytic form ready to be used while the silica powder SBA-15 was prepared by Dr Christopher M. A. Parlett using the method of Stucky [245]. SBA-15 exhibits highly ordered 2D hexagonal symmetry (*p6mm*) with an average pore size of 6.3 nm [246]. The detailed characterisation of this silica has been reported elsewhere [246].

5.7. Sample preparation

20 mM of tributyrin, methyl butyrate and glycerol were prepared with deuterated methanol. Prior to being used, 26OH and 402OH* were dried in the oven at 313 K while the silica support, SBA-15, at 378 K for 24 h. Then, the samples were placed in the desiccator for further 24 h. The solutions were pipetted onto each solid, and the catalyst allowed to swell for at least 12 h. The catalyst was dried using a pre-soaked filter paper to remove the excess of liquid and finally transferred into a 5 mm diameter NMR tube. The tube was sealed with parafilm and centrifuged at 1000 rpm for 1 h to enhance liquid diffusion into the pores and homogenize the sample. Prior to running the experiment, the tube was placed into the spectrometer and allowed it to reach the thermal equilibrium for 20 min. The NMR measurements were acquired at 294.0 K.

5.8. NMR experiment

Experiments were carried out on a Bruker Avance spectrometer with a frequency of 300 MHz and operating at a magnetic field strength of 7.05 T. For the diffusion measurements, a 5 mm PABBO BB-1H Z-GRD probe head was used with a maximum gradient of 2.9×10^{-2} m^{-1} T. A sequence of bipolar gradients and a longitudinal eddy current delay (LED) is used to reduce the eddy current artefacts, reducing the distortions due to the application of the gradient. The magnitude of the LED depends on the quality of the probe and how it is shielded [248]. In this work, a double stimulated echo bipolar pulse pair sequence (DSTEBPGP_3S) was used for removing any convection effect from the diffusion measurement [210].

5.8.1. Diffusion study

Prior to NMR experiments, all the catalysts were characterised by NLDFT analysis. The pore size of these solid was found to be of the order of ten nanometers, as shown in **Table 5.1**.

Table 5.1. NLDFT characterisation of the catalysts investigated in this study.

Catalyst	Pore size / nm
26OH	27.4
402OH*	4.1
SBA-15	6.3

The tortuosity of these catalysts by using the dimensionless parameter ξ, which was introduced in **Equation 5.40** in **Section 5.3** [210]. To aid the reader, the equation is reported here.

$$\xi = \frac{D_0}{D_{eff}} \qquad \textbf{Equation 5.42}$$

where D_{eff} is the diffusion coefficient of species travelling in a porous media while D_0 is the diffusion coefficient of the bulk solution.

The diffusion NMR data were processed using the DOSY Toolbox software package [247]. The data processing provides a DOSY spectrum. This is a 2-dimensional spectrum indicating both the NMR chemical shifts and the diffusion coefficients associated with them.

5.8.2. Results and discussion

Figure 5.9, **Figure 5.11** and **Figure 5.13** show the chemical structures of tributyrin, methyl butyrate and glycerol while their NMR spectral assignments are shown in **Table 5.2**, **Table 5.3** and **Table 5.4**, respectively. It also exhibits DOSY spectra for tributyrin, methyl butyrate and glycerol in bulk methanolic solution and within two distinct materials, the resins 26OH and 402OH* with mean mesopore diameter of 27.4 and 4.1 nm, respectively, and the silica support SBA-15 with an average diameter of 6.3 nm [246]. All the diffusion experiments were acquired using tetramethylsilane (TMS) as internal chemical shift reference and deuterated methanol (CD_3OD) as solvent. The chemical shift of TMS is set at 0 ppm while that of CD_3OD falls at 3.3 ppm. The water content of the samples contributes with the singlet at 4.8 ppm.

- **Tributyrin**

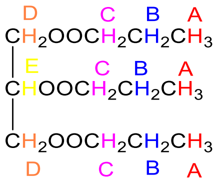

Figure 5.9. Chemical structure of tributyrin (TB).

Table 5.2. ^{1}H NMR data for tributyrin (TB) in methanolic solution.

Assignment	Shift / ppm	Multiplet structure
A	0.99	Triplet
B	1.7	Sextet
C	2.3	Triplet
D	4.1	Duplet of duplet
E	5.7	Quintet

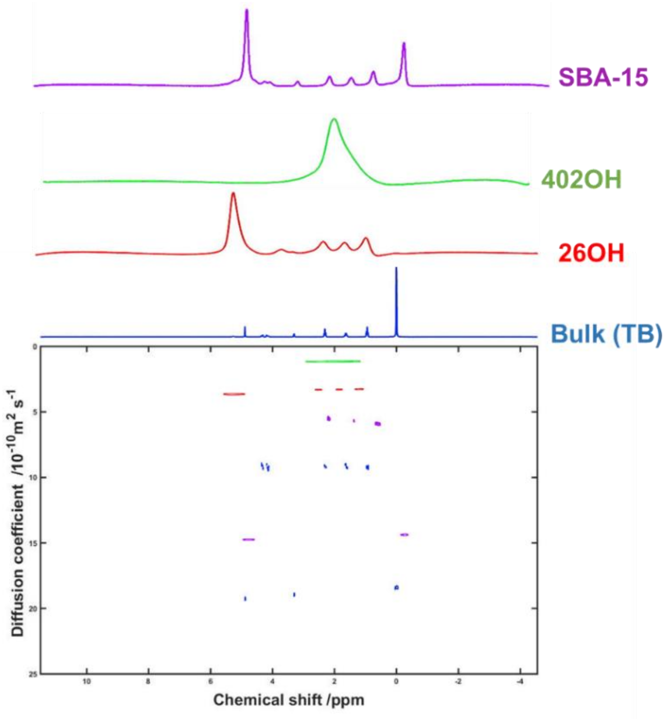

Figure 5.10. DOSY spectra for tributyrin (TB) in methanol-d4 in bulk solution (blue), 26OH (red), 402OH* (green) and SBA-15 (purple).

- **Methyl butyrate**

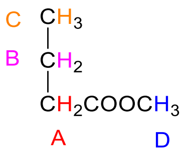
$CH_3CH_2CH_2COOCH_3$

Figure 5.11. Chemical structure of methyl butyrate (MB).

Table 5.3. ^{1}H NMR data for methyl butyrate (MB) in methanolic solution.

Assignment	Shift / ppm	Multiplet structure
A	0.9	Triplet
B	2.5	Sextet
C	3.1	Triplet
D	4.5	Singlet

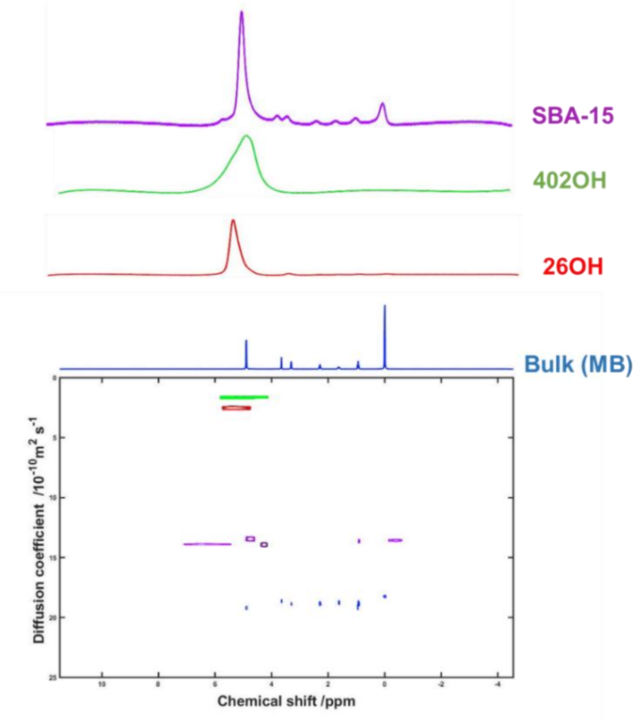

Figure 5.12. DOSY spectra for methyl butyrate (MB) in methanol-d4 in bulk solution (blue), 26OH (red), 402OH* (green) and SBA-15 (purple).

- **Glycerol**

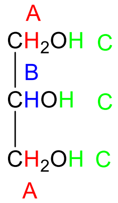

Figure 5.13. Chemical structure of glycerol (GLY).

Table 5.4. ^{1}H NMR data for glycerol (GLY) in methanolic solution.

Assignment	Shift / ppm	Multiplet structure
A	3.5	Multiplet
B	3.6	Multiplet
C	4.8	Singlet

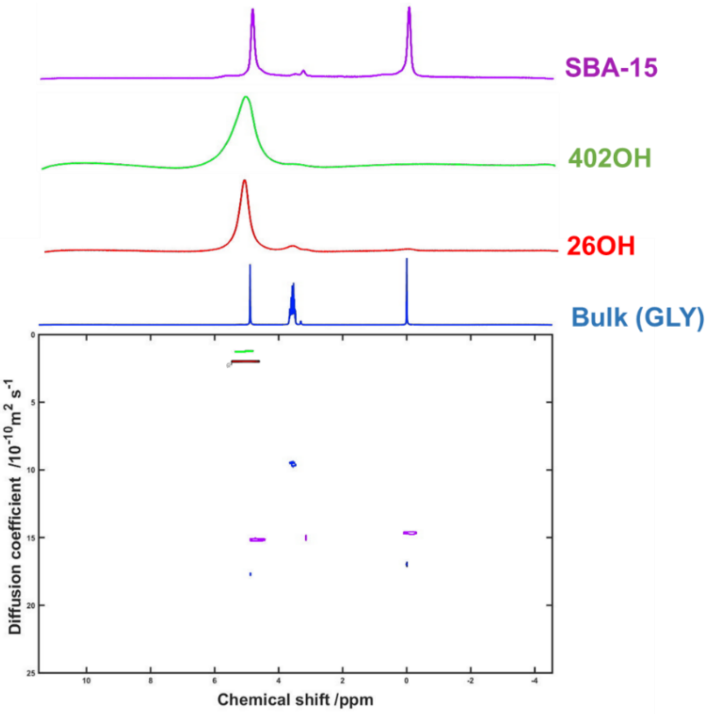

Figure 5.14. DOSY spectra for glycerol (GLY) in methanol-d4 in bulk solution (blue), 26OH (red), 402OH* (green) and SBA-15 (purple).

As can be seen, samples imbibed into the resins all exhibited severely distorted spectra, a result of the high inhomogeneity of the resins and the poor shimming. The DOSY spectra of the resins exhibit unconventionally broadened water peaks, concealing the neighbouring peaks due to the radiation damping effects and generating its own R.F. signal, which affects the water nuclei [248]. In addition, these peaks are consequences of the heterogeneity of sample preparation and bubbles presented in the NMR tube, broadening the Lorentzian line of the peaks, as illustrated in **Figure 5.10**, **Figure 5.12** and **Figure 5.14** [248]. Also, the failure of locking the sample leads to the shifting of peaks. This behaviour was observed for the gel resin 402OH*, as shown in **Figure 5.10**. Conversely, the SBA-15 was an easy-to-pack material. The versatility of this silica powder resides in the ability to provide a more homogeneous sample in term of length scale of the individual grains than that of the resins in the NMR tube, as illustrated in **Figure 5.15**.

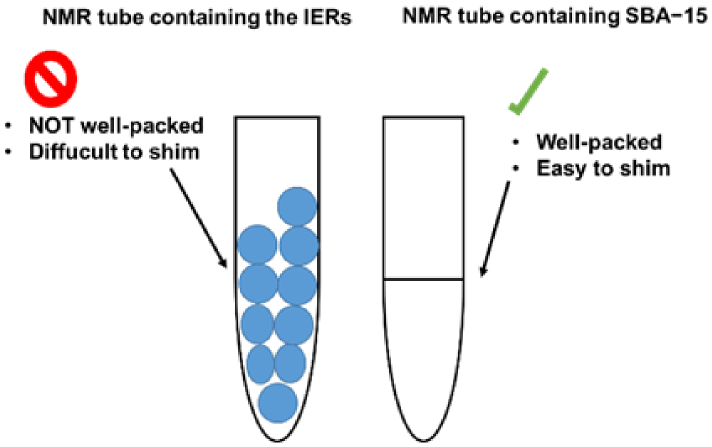

Figure 5.15. Illustration showing the heterogeneity in the sample of the resins.

The SBA-15 showed ^{1}H NMR spectrum easier to lock and shim, therefore allowing for successful acquisition of diffusion NMR experiments. When confined in a pore, the diffusion coefficients are lower for the species measured in the bulk solution. The diffusion coefficients measured are in the order bulk > SBA-15. The further reduction in the diffusion coefficient for the methanolic solutions within SBA-15 is due to the motion of the liquid subjected to restrictions. Considering that the NMR diffusion experiments, the diffusion delay time used, ***Δ*** exceeds the pore size of the material [210].

$$\Delta \gg \frac{<\boldsymbol{r}^2>}{6\boldsymbol{D}} \qquad \textbf{Equation 5.43}$$

where ***Δ*** is the diffusion delay time, ***r*** is the mean squared displacement and ***D*** is the diffusion coefficient.

As the diffusion delay is long enough, the species in solutions undergo collisions with the walls of the solid material [210]. Thus, the reduction of the diffusion coefficients describes the tortuosity of the solid [210]. The diffusivity data of the bulk liquids and the liquids into the mesoporous silica SBA-15 are reported in **Table 5.5**.

Table 5.5. Diffusion coefficients, ***D*** and tortuosity, ***ξ*** of tributyrin, methyl butyrate and glycerol confined in SBA-15, 26OH and 402OH.

Compound	**Experimental D_0** $/\times10^{-10}$ m^{2}s^{-1}	**Experimental D_{eff} in SBA-15** (6.3 nm) $/\times10^{-10}$ m^{2}s^{-1}	**Experimental D_{eff} in 26OH** (27.3 nm) $/\times10^{-10}$ m^{2}s^{-1}	**Experimental D_{eff} in 402OH** (5.2 nm) $/\times10^{-10}$ m^{2}s^{-1}	***ξ*** **SBA-15**
TB	9.31 ± 0.02	6.78 ± 0.03	9.12 ± 0.07	n.d.	1.4
MB	19.25 ± 0.08	14.1 ± 0.4	n.d.	n.d.	1.4
GLY	9.80 ± 0.07	15.0 ± 0.1	n.d.	n.d.	0.6

n.d. = not determined

As can seen from **Table 5.5**, the molecules have undergone a decrease in diffusion coefficients within the pores. It is worth noticing that the diffusion coefficient ***D*** of glycerol appears to be higher in SBA-15 than in the bulk liquid; 15.0×10^{-10} m^{2}s^{-1} in SBA-15 against 9.80×10^{-10} m^{2}s^{-1} as the free bulk liquid. This behaviour of polyalcohols has been previously observed by D'Agostino *et al.* [212]. The polyalcohols appear to diffuse faster in pores than expected, and sometimes faster than in the bulk liquid. This behaviour is caused by the hydrogen bonding disruption of the organic molecules with multiple hydroxyl groups by pores, which takes place in silica supports such as SBA-15.

Further experiments need to be run to validate the true tortuosity in SBA-15 and support this theory.

5.9. Conclusions

NMR diffusion was used to investigate the organic molecules involved in the reaction (tributyrin, methyl butyrate and glycerol) within the pores of the polymeric resins. By comparing the results obtained from the resins with those from the ordered mesoporous silica SBA-15, it was noticed that the measurements on the resins failed due to high inhomogeneity of the samples. This, in turn, leads to poor shimming of the swollen resin samples. The peaks in the spectra are broader. Poor shimming is likely generated by the sample heterogeneity (beads) and the presence of water, which covers part of the resonance region of interest.

The ratio between the diffusion coefficients of the free bulk liquid and that of the confined liquid gives an estimation of the tortuosity of SBA-15. More accurate data can be collected using a non-interacting species as a probe, such as n-heptane. Among the organic molecules studied, the polyalcohol exhibits unusual behaviour: an enhancement in diffusivity of glycerol within SBA-15 is higher than that of the bulk due to the disruption of the hydrogen network by the pores.

The result shows that the NMR technique is an effective tool for the characterisation of porous media to gain a more in-depth insight into the liquid-phase dynamics in the pores. It would be interesting in the future to investigate diffusivity for a serie of polyalcohols, such as glycerol, ethylene glycol and propylene glycol, to verify the enhancement in diffusivity observed and study the interactions alcohol-catalyst by using a non interacting specie, such as n-heptane.

It would be interesting in the future to conduct NMR relaxation experiment to measure the strength of surface interactions of various organic molecules in porous catalysts studied. It would be shed light on the adsorption of the organic molecules and, therefore, validate the different mechanism of reactions for cationic and anionic IERs described by several researchers in **Chapter 4**.

Chapter 6

Conclusions and future work

6.1. Limitations of this work

Due to the nature of research and limited access to equipment, **Chapter 4** was based on a restricted number of experiments. The results did not provide, in some cases, statistically significant outcomes because of the lack of repeated experiments. The performance of additional experiments would be needed to pave the way for future research. Moreover, the lack of equipment to study the resins do not allow to study the IERs in a working state altogether. Thus, the behaviour of IERs in the swollen state needs to be investigated. These limitations are topics to be addressed in future work.

6.2. Future work

The research work reported herein makes significant progress from the past literature, which contributes to further understanding of the behaviour of the resins in reactions. Studying the behaviour of the resins acting in transesterification reactions can be exploited in similar reactions such as esterification or aldol condensation. However, room for further improvements remain.

6.2.1. Complementary techniques for characterisation of the ion exchange resins

This work introduces the use of standard techniques of characterisation and the challenges faced. However, other techniques may be useful to investigate the resins.

Firstly, the morphology of the IERs was described using N_2 adsorption-desorption and thermoporometry to estimate the pore morphology of the resins in the dry and swollen state, respectively. Unfortunately, the thermoporometry failed at describing the IER morphology. There is potential research into new techniques to describe the swollen state of the IERs in various media. This can be achieved with reliable techniques such as Inverse Steric Exclusion Chromatography (ISEC) and NMR cryoporometry. ISEC is a chromatographic technique for measurament of the pore size distribution of porous media. Numerous papers have been published on the use of ISEC for the pore measurements of soft materials in the swollen state [147]. In this case, it would be possible to have a representative pore size and volume using the reaction solvent as a probe, obtaining, therefore, more representative data for the IER morphology. NMR cryoporometry is a method to determine PSDs through the depression melting point of confined liquids within porous materials. This technique was successfully used to measure the PSD of the macroreticular resin 26OH [187].

Secondly, the assessment of the strength and the number of acidic and basic sites of the IERs can be performed by using isothermal titration calorimetry [249]. Knowing the strength of the IERs could help to understand the resin behaviour in the reaction medium and to classify the resins as catalysts for reaction type.

6.4.2. Further improvements of the catalytic performances of ion exchange resins

To improve the efficiency of these polymers in operating conditions, both pre-treatment and activation have been shown to enhance IER activity. Water removal from the polymer using long heat pre-treatment or freeze-drying improves the accessibility of the functional groups by drying off more water from the polymer, maximizing, therefore, the operating capacity. Also, the catalytic tests of the factorial design need to be repeated with more data points to provide a more accurate representation of the performances of the IERs in a batch reactor. Recent work reported that the IERs lost their capacity when they are used in a batch reactor while the resins, in a fixed bed reactor, preserve their physical appearance [250]. Therefore, it would be useful to test the resins in a fixed bed reactor to check if any loss of operating capacity is observed.

Two further potential avenues would be interesting to pursue; the reusability of the tested resins and their catalytic performance for the transesterification of an oil. It would be interesting to run reusability tests to check IER catalytic activity for multiple cycles at 313 K and 333 K with no catalyst regeneration. Moreover, testing the IERs for the transesterification of oil would assess the applicability of the resins as catalysts for the biodiesel production in the industrial market. In this case, it is highly recommended that an economic analysis of the use of IERs for biodiesel production in order to find out if the resins could replace homogeneous catalysts.

6.2.3. Continuation of NMR diffusion work on SBA-15

Diffusion of liquids confined within the pores of mesoporous silica has been well-documented. However, the behaviour of polyalcohols within the pore of highly ordered silica SBA-15 has not yet been reported. The diffusion experiments within the pores of SBA-15 were successfully conducted, demonstrating the silica was easily characterized. The diffusion coefficients within SBA-15 were easily acquired for all three compounds, tributyrin, methyl butyrate and glycerol. When tributyrin and methyl butyrate are confined within pores, their acquired diffusion coefficients are reduced while glycerol exhibited a slight enhancement in diffusion coefficient. Further NMR diffusion and relaxation experiments will help to validate this theory. It would be beneficial to investigate the behaviour of a class of alcohols with varied chain lengths within pores and how much these species could interact with the porous structural material, explaining the reaction mechanisms involving alcohols and SBA-15 as a catalyst. The interaction can be measured by using a non-interacting species.

This thesis has demonstrated an improvement in the characterisation of these resins, demonstrating that IER characterisation is useful in the selection of the resins for the catalysis of transesterification reaction. In addition, the optimization of the performance of these commercial anionic exchange resins by both pre-treatment and activation study has been useful for applications in the catalytic field. These findings provide new insights into heterogeneous catalysis concerning ion exchange resins and, combined with IER characterisation in the wet state will give a more detailed picture of the catalytic reactions over IERs.

References

[1] Stead, C.; Wadud, Z.; Nash, C.; Li, H. Introduction of Biodiesel to Rail Transport: Lessons from the Road Sector. *Sustainability*. **2019**, *11*, 904.

[2] Bailey, R. The Trouble with Biofuels: Costs and Consequences of Expanding Biofuel Use in the United Kingdom; Chatham House; **2013**.

[3] International Energy Agency. World Energy Outlook 2015; IEA PUBLICATIONS. **2015**.

[4] Babu, A.K.; Devaradjane, G. Vegetable oils and their derivatives as fuels for CI engines: an overview. *Journal of Fuels and Lubricant*. **2003**, *112*, 406-419.

[5] Huber, G.W.; Iborra, S.; Corma, A. Synthesis of transportation fuels from biomass: chemistry, catalysts, and engineering. *Chem. Rev*. **2006**, *106*, 4044-4098.

[6] Hanaki, K.; Portugal-Pereira, J. The effect of biofuel production on greenhouse gas emission reductions. *Biofuels and Sustainability*. Springer. **2018**.

[7] European Biofuel Portal. European experts appeal for prohibition of the biodiesel use in cars and trucks in Europe. 2020. Available from: http://eufuel.de/news-european-experts-appeal-for-prohibition-of-the-bio-6.html [Accessed 18 Nov 2020].

[8] Naik, S.N.; Goud, V.V.; Rout, P.K.; Dalai, A.K. Production of first and second generation biofuels: A comprehensive review. *Renewable and Sustainable Energy Reviews*. **2010**, *14*, 578-597.

[9] Lee, A.F.; Bennett, J.A.; Manayil, J.C.; Wilson, K. Heterogeneous catalysis for sustainable biodiesel production *via* esterification and transesterification. *Chem. Soc. Rev*. **2014**, 7887-7916.

[10] Srivastava, A.; Prasad, R. Triglycerides-based diesel fuels. *Renewable and Sustainable Energy Reviews*. **2000**, *4*, 111-133.

[11] Meher, L.C.; Sagar, D.V.; Naik, S. Technical aspects of biodiesel production by transesterification-a review. *Renewable and Sustainable Energy Reviews*. **2006**, *10*, 248-268.

[12] Hanh, H.D.; Dong, N.T.; Okitsu, K.; Nishimura, R.; Maeda, Y. Biodiesel production through transesterification of triolein with various alcohols in an ultrasonic field. *Renewable Energy*. **2009**, *34* 766-768.

[13] Ren, Y.; He, B.; Yan, F.; H. Wang, H.; Cheng, Y.; Lin, L.; Feng, Y.; Li, J. Continuous biodiesel production in a fixed bed reactor packed with anion-exchange resin as heterogeneous catalyst, *Bioresource Technology*. **2012**, *113*, 19-22.

[14] Ma, F.; Hanna, M.A. Biodiesel production: a review. *Bioresource Technology*. **1999**, *70*, 1-15.

[15] Freedman, B.; Butterfield, R.; Pryde, E. Transesterification kinetics of soybean oil. *J Am Oil Chem Soc*. **1985**, *63*, 1375-1380.

[16] Bhandari, V.M.; Sorokhaibam, L.G.; Ranade, V.V. Ion exchange resin catalyzed reactions-an overview. *Industrial Catalytic Processes for Fine and Specialty Chemicals*; Elsevier **2016**, 393-426.

[17] Dicks, A.P.; Hent, *A. Green chemistry metrics: a guide to determining and evaluating process greenness*; Springer. **2014**.

[18] Harmer, M.A.; Sun, Q. Solid acid catalysis using ion-exchange resins. *Applied Catalysis A: General*. **2001**, *221*, 45-62.

[19] Qiu, F.; Li, Y.; Yang, D.; Li, X.; Sun, P. Heterogeneous solid base nanocatalyst: preparation, characterisation and application in biodiesel production. *Bioresource technology*. **2011**, *102*, 4150-4156.

[20] Martínez, A.; Mijangos, G.E.; Romero-Ibarra, I.C.; Hernández-Altamirano, R.; Mena-Cervantes, V.Y.*In-situ* transesterification of *Jatropha curcas* L. seeds using homogeneous and heterogeneous basic catalysts. *Fuel*. **2019**, *235*, 277-287.

[21] Rosan, A.M. Green Chemistry: An Introductory Text (Mike Lancaster). *J. Chem. Educ.* **2003**, *80*, 1141-1142.

[22] Wheeler, A. *Reaction rates and selectivity in catalyst pores*. Advances in Catalysis; Elsevier. **1951**.

[23] Leofanti, G.; Padovan, M.; Tozzola, G.; Venturelli, B. Surface area and pore texture of catalysts. *Catalysis Today*. **1998**, *41*, 207-219.
[24] Schuchardt, U.; Sercheli, R; Vargas, R.M. Transesterification of vegetable oils: a review. *J. Braz. Chem. Soc.* **1998**, *9*, 199-210.
[25] Pinzi, S.; Garcia, I.; Lopez-Gimenez, F.; Luque de Castro, M.; Dorado, G.; Dorado, M. The ideal vegetable oil-based biodiesel composition: a review of social, economical and technical implications. *Energy Fuels*. **2009**, *23*, 2325-2341.
[26] Ciriminna, R.; Pina, C.D.; Rossi, M.; Pagliaro, M. Understanding the glycerol market. *Eur. J. Lipid Sci. Technol.* **2014**, *116*, 1432-1439.
[27] Joshi, S.S.; Ranade, V.V. *Industrial catalytic processes for fine and specialty chemicals*; Elsevier. **2016**.
[28] Barbaro, P.; Liguori, F. Ion exchange resins: catalyst recovery and recycle. *Chemical reviews*. **2009**, *109*, 515-529.
[29] Hanif, M.A.; Nisar, S.; Rashid, U. Supported solid and heteropoly acid catalysts for production of biodiesel. *Catalysis Reviews*. **2017**, *59*, 165-188.
[30] Boey, P.-L.; Maniam, G.P.; Hamid, S.A. Performance of calcium oxide as a heterogeneous catalyst in biodiesel production: a review. *Chemical Engineering Journal*. **2011**, *168*, 15-22.
[31] Li, J.; Fu, Y.-J.; Qu, X.-J.; Wang, W.; Luo, M.; Zhao, C.-J.; Zu, Y.-G. Biodiesel production from yellow horn (*Xanthoceras sorbifolia* Bunge) seed oil using ion exchange resin as heterogeneous catalyst. *Bioresource technology*. **2012**, *108*, 112-118.
[32] Dorfner, K. *Ion exchangers*, Walter de Gruyter. **2011**.
[33] Wheaton, R.; Lefevre, L. *Fundamentals of Ion Exchange*, The Dow chemical Company. **2000**.
[34] Helfferich, F.G. *Ion Exchange*; Courier Corporation.**1995**.
[35] Kumar, S.; Jain, S. History, introduction, and kinetics of ion exchange materials. J. Chem. **2013**.
[36] Kammerer, J.; Carle, R.; Kammerer, D.R. *Adsorption and ion exchange: basic principles and their application in food processing*. *J. Agric. Food Chem*. **2010**, *59*, 22-42.
[37] Van de Steene, E.; De Clercq, J.; Thybaut, J.W. Ion-exchange resin catalyzed transesterification of ethyl acetate with methanol: Gel versus macroporous resins. *Chemical Engineering Journal*. **2014**, *242*, 170-179.
[38] Cooper, A. *Porous Polymers*, Wiley-VCH. **2012**.
[39] Ousalem, M.; Zhu, X.X.; Hradil, J. Evaluation of the porous structures of new polymer packing materials by inverse size-exclusion chromatography. *Journal of Chromatography A*. **2000**, *903*, 13-19.
[40] Brunauer, S.; Emmett, P.H.; Teller, E. Adsorption of gases in multimolecular layers. *J. Am. Chem*. **1938**, *60*, 309-319.
[41] Hanková, L.; Holub, L.; Jeřábek, K. Formation of porous polymer morphology by microsyneresis during divinylbenzene polymerization. *J. Polym. Sci., Part B: Polym. Phys*. **2015**, *53*, 774-781.
[42] Howdle, S.M.; Jerabek, K.; V. Leocorbo, V.; Marr, P.C.; Sherrington, D.C. Reversibly collapsible macroporous poly (styrene-divinylbenzene) resins. *Polymer*. **2000**, *41*, 7273-7277.
[43] Rottreau, T.J.; Parlett, C.M.; Lee, A.F.; Evans, R. Extending the range of liquids available for NMR cryoporometry studies of porous materials. *Microporous and Mesoporous Materials*, **2019**, *274*, 198-202.
[44] Widdecke, H. Polystyrene-supported acid catalysis. *British polymer journal*. **1984**, *16*,188-192.
[45] Srikanth, M.; Sunil, S.A.; Rao, N.S.; Uhumwangho, M.U.; Ramana Murthy, K.V. Ion-exchange resins as controlled drug delivery carriers. *Journal of Scientific Research*. **2010**, *2*, 597.
[46] Lenntech. *Ion Exchange for Dummies*, Rohm and Haas. **2008**.
[47] Harland, C.E. *Ion exchange: theory and practice*, Royal society of Chemistry.**1994**.
[48] Ezzeldin, H.A.; Apblett, A.; Foutch, G.L. Synthesis and properties of anion exchangers derived from chloromethyl styrene codivinylbenzene and their use in water treatment.

International Journal of Polymer Science, **2010.** Available from: https://doi.org/10.1155/2010/684051 [Accessed 18 Nov 2020].

[49] HM Government, The Carcinogenic Substances Regulations 1967, Legislation.gov.uk.**1967**. Available from: https://www.legislation.gov.uk/uksi/1967/879/made [Accessed 18 Nov 2020].

[50] Pepper, K; Paisley, H.; Young, M. Properties of ion-exchange resins in relation to their structure. Part VI. Anion-exchange resins derived from styrene-divinyl-benzene copolymers. *J. Chem. Soc.,* **1953**, 4097-4105.

[51] De Dardel, F. Ion Exchange. **2010**. Available from: http://dardel.info/IX/index.html [Accessed 22 Jan 2020]

[52] DuPont. *Ion Exchange Resins-Conversion to a Different Form* Available from: https://water.custhelp.com/app/answers/detail/a_id/469 [Accessed 14 Dec 2019].

[53] Di Girolamo, M; Marchionna, M. Acidic and basic ion exchange resins for industrial applications. *Journal of molecular catalysis A: chemical*. **2001**, 177, 33-40.

[54] DuPont. *Ion Exchange Resins-Decomposition Mechanisms [online]*. Available from: https://water.custhelp.com/app/answer/detail/a_id/153/~/ion-exchange-resins-decomposition-mechanisms [Accessed 02 Mar 2020].

[55] Tomoi, M.; Yamaguchi, K.; Ando, R.; Kantake, Y.; Aosaki Y.; Kubota, H. Synthesis and thermal stability of novel anion exchange resins with spacer chains. *Journal of Applied Polymer Science*. **1997**, *64*, 1161-1167.

[56] Cope, A.C.; Mehta, A.S. Mechanism of the Hofmann elimination reaction: an ylide intermediate in the pyrolysis of a highly branched quaternary hydroxide. *J. Am. Chem. Soc.* **1963**, *85* ,1949-1952.

[57] Ege, S.N. *Organic chemistry: Structure and reactivity;* 4th ed.; Massachusetts; Cengage Learning.**1998**

[58] Volkov, A.G. *Interfacial catalysis*, CRC Press. **2002**.

[59] Hubicki, Z.; Gęca, M.; Kołodyńska, D. Sorption of heavy metal metatartrate complexes on polystyrene anion exchangers. *Environmental technology*. **2011**, *32*, 569-582.

[60] Hart, M.; Fuller, G.; Brown, D.R.; Dale, J.; Plant, S. Sulfonated poly (styrene-co-divinylbenzene) ion-exchange resins: acidities and catalytic activities in aqueous reactions. *Journal of molecular catalysis A: chemical*. **2002**, *182* , 439-445.

[61] Mazzotti, M.; Neri, B.; Gelosa, D.; Kruglov, A.; Morbidelli, M. Kinetics of liquid-phase esterification catalyzed by acidic resins. *Ind. Eng. Chem. Res.* **1997**, *36* ,3-10.

[62] Liu, P.; Chen, G.-F. *Porous materials: processing and applications*, Elsevier. **2014**.

[63] Zdravkov, B.D.; Čermák, J.J.; Šefara, M.; Janků, J. Pore classification in the characterisation of porous materials: A perspective. *Central European journal of chemistry*. **2007**, 5, 385-395.

[64] Kaneko, K. Determination of pore size and pore size distribution: 1. Adsorbents and catalysts, *Journal of membrane science*.**1994**, *96*, 59-89.

[65] Hu, Y.; Foster, J.; Boyer, T.H Selectivity of bicarbonate-form anion exchange for drinking water contaminants: influence of resin properties. *Separation and Purification Technology*. **2016**, *163*, 128-139.

[66] Sanz, M.T.; Murga, R.; Beltran, S.; Cabezas, J.L.; Coca, J. Autocatalyzed and ion-exchange-resin-catalyzed esterification kinetics of lactic acid with methanol. *Ind. Eng. Chem. Res*. **2002**, *41*, 512-517.

[67] Hollenbeck, G.R.; Jiang, X. Aqueous sustained-release drug delivery system for highly water-soluble electrolytic drugs.U.S. Patent Application 11/198,937. **2006**.

[68] McDermott, J.J.; Hollenbeck, G.R.; Attikson, C.L. Compositions comprising an antihistamine, antitussive and decongestant in extended release formulations. U.S. Patent Application 12/770,486. **2010**.

[69] Otterbeck, N.; Gruber, P. Pellet formulation for the treatment of the intestinal tract. U.S. Patent 8,911,778. **2014**.

[70] Rohm and Haas. Amberlite^{TM} IRP69: Pharmaceutical Grade Cation Exchange Resin (Sodium Polystyrene Sulfonate USP). Rohm and Haas. **2006**.

[71] World Bank Group’s mining department. *Mining and development*. **2002**.

[72] Hilson, G.; Monhemius, A.J. Alternatives to cyanide in the gold mining industry: what prospects for the future?. *Journal of Cleaner production*. **2006**, *14*, 1158-1167.

[73] Dobrosz-Gómez, I.; García, B.D.R.; GilPavas, E.; García, M.Á.G. Kinetic study on HCN volatilization in gold leaching tailing ponds. *Minerals Engineering*. **2017**, *110*, 185-194.

[74] Environmental Protection Agency. Laws and Executive Orders. Available from: https://www.epa.gov/laws-regulations/laws-and-executive-orders [Accessed 22 Sept 2019].

[75] Sole, K.C.; Mooiman, M.B.; Hardwick, E. Present and future applications of ion exchange in hydrometallurgy: an overview. *International Ion Exchange Conference IEx,* p. 2016*.* At Cambridge (UK), **2016**.

[76] Khawassek, Y.M.; Eliwa, A.A.; El Sayed, A.H.; Omar, S.A.; Abdel-Wahab, S.M. Adsorption of rare earth elements by strong acid cation exchange resin thermodynamics, characteristics and kinetics, *SN Applied Sciences*. **2019**, *1*, 51.

[77] Fitch, F.T.; Russell, D.S. The separation of the rare earths by ion-exchange procedures. *Canadian journal of chemistry*. **1951**, *29*, 363-371.

[78] Council of Europe. *Resolution AP (2004) 3 on ion exchange resins and adsorbent resins in processing of foodstuffs*, **2004**.

[79] DuPont. Ion Exchange and Adsorbent Solutions for the Nutrition Market: Food matters, DuPont makes it better. DuPont. **2020**.

[80] Gelbard, G. Organic synthesis by catalysis with ion-exchange resins. *Ind. Eng. Chem. Res.* **2005**, *44*, 8468-8498.

[81] López, D.E.; Goodwin Jr, J.G.; Bruce, D.A. Transesterification of triacetin with methanol on Nafion® acid resins. Journal of Catalysis. **2007**, *245*, 381-391.

[82] Otera, J. Transesterification. *Chemical reviews*. **1993**, *93*, 1449-1470.

[83] Gray, C.; Narang, J.; Barker, S. Immobilization of lipase from *Candida cylindraceae* and its use in the synthesis of menthol esters by transesterification. *Enzyme and Microbial Technology*. **1990**, *12*, 800-807.

[84] Shibasaki-Kitakawa, N.; Honda, H.; Kuribayashi, H.; Toda, T.; Fukumura, T.; Yonemoto, T. Biodiesel production using anionic ion-exchange resin as heterogeneous catalyst. *Bioresource Technology*. **2007**, *98*, 416-421.

[85] Vicente, G.; Coteron, A.; Martinez, M.; Aracil, J. Application of the factorial design of experiments and response surface methodology to optimize biodiesel production. *Industrial crops and products*. **1998**, *8*, 29-35.

[86] A. Rabee, A.; Manayil, J.; Isaacs, M.; Parlett, C.; Durndell, L; Zaki, M.; Lee, A.; Wilson, K. On the Impact of the Preparation Method on the Surface Basicity of Mg-Zr Mixed Oxide Catalysts for Tributyrin Transesterification. *Catalysts*. **2018**, 8, 228.

[87] Oi, L.E.¸ Choo, M.-Y; Lee, H.V.; Rahman, N.A.; Juan, J.C. Mesoporous and other types of catalysts for conversion of non-edible oil to biogasoline via deoxygenation. *Sustainable Bioenergy*. **2019**, 257-281.

[88] Wang, C.; Yuan, F.; Liu, L.; Niu, X.; Zhu, Y. Transesterification of tributyrin and dehydration of fructose over a carbon-based solid acid prepared by carbonization and sulfonation of glucose. *ChemPlusChem*. **2015**, *80*, 1657-1665.

[89] Xi, Y.; Davis, R.J. Influence of textural properties and trace water on the reactivity and deactivation of reconstructed layered hydroxide catalysts for transesterification of tributyrin with methanol. *Journal of Catalysis*. **2009**, *268*, 307-317.

[90] Montero, J.M.; Wilson, K.; Lee, A.F. Cs promoted triglyceride transesterification over MgO nanocatalysts. *Topics in Catalysis*. **2010**, *53*, 737-745.

[91] Jiang, W.; Niu, X.; Yuan, F.; Zhu, Y.; Fu, H. Preparation of KF-$La_2O_2CO_3$ solid base catalysts and their excellent catalytic activities for transesterification of tributyrin with methanol. Catalysis Science & Technology. **2014**, *4*, 2957-2968.

[92] Oliveira, E.V.; Costa, L.C.; Thomaz, D.M.; Costa, M.A.; Santa Maria, L.C.; Transesterification of soybean oil to biodiesel by anionic and cationic ion exchange resins. *Revista Virtual de Quimica*. **2015**, *7*, 2314-2333.

[93] Öchsner, A.; Altenbach, H. *Properties and Characterisation of Modern Materials*. Springer, **2017**.

[94] Fanconi, B.; Wang, F.; Houston, D.; Mopsik, F. Materials Characterisation for Systems Performance and Reliability. JW McCauley and V. Weiss. **1986.**

[95] The Dow Chemical Company. *Ambelyst^{TM} A26 OH: Industrial Grade Strongly Basic Polymeric Resin*. The Dow Chemical Company, **2001**.

[96] Rohm and Haas*. Amberlite^{TM}IRA458 Cl Ion Exchange Resin; Acrylic Strong Base Anion Exchanger*. Rohm and Haas*,* **2019**.

[97] Rohm and Haas. *Amberlite^{TM} IRA958 Cl: Industrial Grade Strong Base Anion Exchanger*. Rohm and Haas, **2008**

[98] DuPont. *AmberLite^{TM} IRA410Cl Ion Exchange Resin: Gaussian, Gel, Strong Base Anion (Type II) Exchange Resin for Industrial Demineralization Applications.* DuPont. **2019**.

[99] DuPont. *AmberLite^{TM} IRA402 Cl Ion Exchange Resin: Gaussian, Gel, Strong Base Anion Exchange Resin for Industrial Demineralization Applications*. DuPont, **2019**.

[100] Rohm and Haas. Amberlite IRA402OH: Strong Base Anion Exchanger. Rohm and Haas, **1999**.

[101] The Dow Chemical Company. *Amberlyst^{TM} 15WET Industrial Grade Strongly Acidic Catalyst*. The Dow Chemical Company, **2006**.

[102] DuPont. *Amberlite^{TM} IRC120 H Ion Exchange Resin: Gaussian, Gel, Strong Acid Cation Exchange Resin for Industrial Demineralization Applications*. DuPont, **2019**.

[103] Atkins, P.W.; De Paula, J.; Keeler, J. *Atkins's physical chemistry*, Simple Mixtures. **2018**.

[104] Westermarck, S. Use of mercury porosimetry and nitrogen adsorption in characterisation of the pore structure of mannitol and microcrystalline cellulose powders, granules and tablets. Academic dissertation. Helsinki: University of Helsinki. **2000**.

[105] Particle Technology Labs, Mesopore Measurement. Available from: https://www.particletechlabs.com/analytical-testing/gas-adsorptionandporosimetry/mesopore-measurement [Accessed 22 Jan 2019].

[106] Sing, K. The use of nitrogen adsorption for the characterisation of porous materials. *Colloids and Surfaces A: Physicochemical and Engineering Aspects*. **2001**, *187*, 3-9.

[107] Trunschke, A. *Moder method in heterogeneous catalysis research: surface area and pore size determination*. Max Planck Gesellschaft. **2013**.

[108] Sing, K.S.W.; Everett, D.H.; Haul, R.A.W.; Moscou, L.; Pierotti, R.A.; Rouquérol, J; Siemieniewska, T. Reporting physisorption data for gas/solid systems with special reference to the determination of surface area and porosity (Recommendations 1984). *Pure and Appl. Chem.* **1985**, *57*, 603-619.

[109] Salis, A.; Meloni, A. D.; Ligas, S.; Casula, M.F.; Monduzzi, M.; Solinas, V; Dumitriu, E. Physical and chemical adsorption of *Mucor javanicus* lipase on SBA-15 mesoporous silica. Synthesis, structural characterisation, and activity performance. *Langmuir*. **2005**, *21*, 5511-5516.

[110] Casula, M.F.; Corrias, A.; Paschina, G. FeCo–SiO_2 nanocomposite aerogels by high temperature supercritical drying. *J. Mat. Chem*. **2002**, *12*, 1505-1510.

[111] Labani, M.M.; Rezaee, R.; Saeedi, A.; Al Hinai, A. Evaluation of pore size spectrum of gas shale reservoirs using low pressure nitrogen adsorption, gas expansion and mercury porosimetry: A case study from the Perth and Canning Basins, Western Australia. Journal of Petroleum Science and Engineering. **2013**, *112*, 7-16.

[112] Sing, K.S.W.; Williams, R.T. Physisorption hysteresis loops and the characterisation of nanoporous materials. *Adsorption Science & Technology*. **2004**, *22*, 773-782.

[113] Cychosz, K.A.; Thommes, M. Progress in the physisorption characterisation of nanoporous gas storage material. *Engineering*. **2018**, *4*, 559-566.

[114] Landers, J.; Gor, G.Y.; Neimark, A.V. Density functional theory methods for characterisation of porous materials. Colloids and Surfaces A: Physicochemical and Engineering Aspects. **2013**, *437*, 3-32.

[115] Kupgan, G.; Liyana-Arachchi, T.P.; Colina, C.M. NLDFT pore size distribution in amorphous microporous materials. *Langmuir*. **2017**, *33*, 11138-11145.

[116] Badia, J.H.; Fité, C.; R. Bringué, R.; Ramírez, E.; Iborra, M. Relevant properties for catalytic activity of sulfonic ion-exchange resins in etherification of isobutene with linear primary alcohols. *J. Ind. Eng. Chem.* **2016**, *42*, 36-45.

[117] Landry, M.R. Thermoporometry by differential scanning calorimetry: experimental considerations and applications. *Thermochimica acta*. **2005**, *433*, 27-50.

[118] Majda, D.; Makowski, W.; Mańko, M. Pore size distribution of micelle-templated silicas studied by thermoporosimetry using water and n-heptane. *Journal of thermal analysis and calorimetry*. **2012**, *109*, 663-669.

[119] Majda, D.; Bhattarai, A.; Riikonen, J.; Napruszewska, B.D.; Zimowska, M.; Michalik-Zym, A.; Töyräs, J.; Lehto, V.-P. New approach for determining cartilage pore size distribution: NaCl-thermoporometry. *Microporous and Mesoporous Materials*. **2017**, *241*, 238-245.

[120] Iza, M.; Woerly, S.; Danumah, C.; Kaliaguine, S.; Bousmina, M. Determination of pore size distribution for mesoporous materials and polymeric gels by means of DSC measurements: thermoporometry. Polymer. **2000**, *41*, 5885-5893.

[121] Brun, M.; Lallemand, A.; Quinson, J.-F.; Eyraud, C. A new method for the simultaneous determination of the size and shape of pores: the thermoporometry, *Thermochimica acta*. 21, **1977**, 59-88.

[122] Friel, J.J.; Lyman, C.E. Tutorial review: X-ray mapping in electron-beam instruments. *Microscopy and Microanalysis*. **2006**, *12*, 2-25.

[123] Newbury, D.E.; Ritchie, N.W. Is scanning electron microscopy/energy dispersive X-ray spectrometry (SEM/EDS) quantitative? *Scanning*. **2013**, *35*, 141-168.

[124] Tanaka, N. *Scanning transmission electron microscopy of nanomaterials*. London: Imperial College Press, **2015**.

[125] Giazzi, *G. Characterisation of Polymers and Plastics Using an Elemental Analyzer*. Available from: https://www.thermofisher.com/blog/materials/characterisation-of-polymers-and-plastics-using-an-elemental-analyzer/ [Accessed 07 Dec 2019].

[126] Instrumental Criteria Subcommittee. *Amc technical briefs: CHNS Elemental Analyser*. The Royal Society of Chemistry. **2008**.

[127] Skoog, D.A.; West, D.M.; Holler, F.J.; Crouch, S.R. *Fundamentals of analytical chemistry*. Nelson Education, **2013**.

[128] Fisher, S.; Kunin, R. Routine exchange capacity determinations of ion exchange resins. *Anal. Chem.* **1955**, *27*, 1191-1194.

[129] Inczédy, J. *Analytical applications of ion exchangers*. Elsevier, **2016**.

[130] Patel, V.C. *The behaviour of ion-exchange resins with basic solvents*. Doctoral thesis, Surrey: University of Surrey, **1963**.

[131] Heinemann, H. Catalyst performance testing. *Catalysis today*, **1994**, *22*, 281-293.

[132] Bejarano-Alva, I.J.; Hirata, G.A.M.; Sampaio, K.A.; Batista, E.A.C.; Meirelles, A.J.A. High Conversion of Palm Olein to Ethyl Esters Using a Strong Anion Exchange Resin: Study of the Operational Parameters. J. Braz. Chem. Soc., **2020**, *31*, 1401-1412.

[133] Deboni, T.M.; Hirata, G.A.M.; Shimamoto, G.G.; Tubino, M.; de Almeida Meirelles, A.J. Deacidification and ethyl biodiesel production from acid soybean oil using a strong anion exchange resin, *Chemical Engineering Journal*. **2018**, *333*, 686-696.

[134] Badia, J.H.; Fité, C.; Bringué, R.; Ramírez, E.; Tejero, J. Simultaneous etherification of isobutene with ethanol and 1-butanol over ion-exchange resins. *Applied Catalysis A: General*. **2017**, *541*, 141-150.

[135] Einax, J.W. *Chemometrics in analytical chemistry*. *Analytical and Bioanalytical Chemistry*. **2008**, *390*, 1225-1226.

[136] Lundstedt, T; Seifert, E.; Abramo, L.; Thelin, B.; Nyström, Å.¸ Pettersen, J. Bergman, R. Experimental design and optimization. *Chemometrics and intelligent laboratory systems.* **1998**, 42, 3-40.

[137] Minitab 18 Support. What is a hypothesis test ?. Available from: https://support.minitab.com/en-us/minitab/18/help-and-how-to/statistics/basic-statistics/supporting-topics/basics/what-is-a-hypothesis-test/. [Accessed 10 Nov 2020]

[138] Hartmann, K.; Krois, J.; Waske, B. E-Learning Project SOGA: Statistics and Geospatial Data Analysis. Department of Earth Sciences, Freie Universitaet Berlin. Available form: https://www.geo.fu-berlin.de/en/v/soga/Basics-of-statistics/Hypothesis-Tests/Introduction-to-Hypothesis-Testing/Critical-Value-and-the-p-Value-Approach/index.html. [Accessed 17 Dec 2020].

[139] Minitab 18 Support. Statistical and pratical significance. Available from: https://support.minitab.com/en-us/minitab/18/help-and-how-to/statistics/basic-statistics/supporting-topics/basics/statistical-and-practical-significance/. [Accessed 10 Nov 2020]

[140] Bramston-Cook, R. *Primer on Flame Ionization Detectors*. Lotus Flower, Inc, **2011**.

[141] Natarajan, V.; Cramer, S. A methodology for the characterisation of ion-exchange resins. *Separation Science and Technology*, **2000**, 35, 1719-1742.

[142] Badia, J.H.; Fité, C.; Bringué, R.; Iborra, M.; Cunill, F. Catalytic activity and accessibility of acidic ion-exchange resins in liquid phase etherification reactions. *Topics in Catalysis*. **2015**, 58, 919-932.

[143] Soto, R.; Fité, C.; Ramírez, E.; Iborra, M.; Tejero, J. Catalytic activity dependence on morphological properties of acidic ion-exchange resins for the simultaneous ETBE and TAEE liquid-phase synthesis. *Reaction Chemistry & Engineering*. **2018**, *3*, 195-205.

[144] Corain, B.; Zecca, M.; Jeràbek, K. Catalysis and polymer networks: the role of morphology and molecular accessibility. *Journal of molecular catalysis. A, Chemical*. **2001**, *177*, 3-20.

[145] Khokhlov, A.R. Swelling and collapse of polymer networks. *Polymer*. **1980**, *21*, 376-380.

[146] Ramírez, E.; Bringué, R.; Fité, C.; Iborra, M.; Tejero, J.; Cunill, F. Role of ion-exchange resins as catalyst in the reaction-network of transformation of biomass into biofuels. *Journal of Chemical Technology & Biotechnology*. **2017**, *92*, 2775-2786.

[147] Jeřábek, K. Ion exchanger catalysts. *Kemija u industriji: Časopis kemičara i kemijskih inženjera Hrvatske*. **2013**, *62*, 171-176.

[148] Brown, R. *Prof Robert Brown highlights focus on ion-exchange catalysts for IEX 2016.* Availble from: https://www.soci.org/news/separation-science/catalytic-applications-of-ion exchange-materials [Accessed 07 Mar 2020].

[149] Ahn, J.-H.; Ihm, S.-K.; Park, K.S. The effects of the local concentration and distribution of sulfonic acid groups on 1-butene isomerization catalyzed by macroporous ion-exchange resin catalysts. *Journal of Catalysis*. **1988**, *113*, 434-443.

[150] Sterchele, S.; Centomo, P.; Zecca, M.; Hanková, L.; Jeřábek, K. Dry-and swollen-state morphology of novel high surface area polymers. *Microporous and mesoporous materials*. **2014**, *185,* 26-29.

[151] Grinham, R.; Chew, A. A Review of Outgassing and Methods for its Reduction. *Applied Science and Convergence Technology*. **2017**, *26*, 95-109.

[152] Olson, E. The importance of the sample preparation when measuring specific surface area, *Journal of GXP Compliance*. **2012**, *16*, 52-62.

[153] Omnexus. *Glass transition temperature.* Available from: https://omnexus.specialchem.com/polymer-properties/properties/glass-transition-temperature [Accessed 10 Mar 2020].

[154] Minelli, M.; Paul, D.R.; Sarti, G.C. On the interpretation of cryogenic sorption isotherms in glassy polymers. *Journal of Membrane Science*. **2017**, *540*, 229-242.

[155] Condon, J.B. Surface Area and Porosity Determinations by Physisorption: Measurement. *Classical Theories and Quantum Theory*. Elsevier, **2019**.

[156] Zhihuan, W. Nova@ 2000e Models 25 and 26 Nova win Gas sorption system operating manual, **2015**.

[157] Lapham, D.P.; Lapham, J.L. Gas adsorption on commercial magnesium stearate: effects of degassing conditions on nitrogen BET surface area and isotherm characteristics. International journal of pharmaceutics. **2017**, *530*, 364-376.

[158] Silvestre-Albero, A.M.; Juárez-Galán, J.M ; Silvestre-Albero, J.; Rodríguez-Reinoso, F. Low-pressure hysteresis in adsorption: an artifact?. *The Journal of Physical Chemistry C*. **2012**, *116*, 16652-16655.

[159] Jeromenok, J.; Weber, J. Restricted access: on the nature of adsorption/desorption hysteresis in amorphous, microporous polymeric materials. *Langmuir*. **2013**, *29* ,12982-12989.

[160] Basiuk, V.A.; Basiuk, E.V. *Green processes for nanotechnology*. Springer, **2015**.
[161] Lubensky, T.C. Soft condensed matter physics. *Solid State Communications*. **1997**, *102*, 187-197.
[162] Bertier, P.; Schweinar, K.; Stanjek, H.; Ghanizadeh, A.; Clarkson, C.R.; Busch, A.; N. Kampman, N.; Prinz, D.; Amann-Hildenbrand, A.; Krooss, B.M. On the use and abuse of N_2 physisorption for the characterisation of the pore structure of shales. In the clay minerals society workshop lectures series. **2016**.
[163] Gregg, S.J. The surface chemistry of solids. *Chapman & Hall*, **1961**.
[164] Reichenauer, G.; Scherer, G.W. Nitrogen sorption in aerogels. *Journal of non-crystalline solids*. **2001**, *285*, 167-174.
[165] Hart, K.E.; Springmeier, J.M.; McKeown, N.B.; Colina, C.M. Simulated swelling during low-temperature N_2 adsorption in polymers of intrinsic microporosity. *Physical Chemistry Chemical Physics*. **2013**, *15*, 20161-20169.
[166] Weber, J.; Antonietti, M.; Thomas, A. Microporous networks of high-performance polymers: Elastic deformations and gas sorption properties. *Macromolecules*. **2008**, *41*, 2880-2885.
[167] Tsujita, Y. Gas sorption and permeation of glassy polymers with microvoids. *Progress in polymer science*. **2003**, *28*, 1377-1401.
[168] Heuchel, M.; Fritsch, D.; Budd, P.M.; McKeown, N.B.; Hofmann, D. Atomistic packing model and free volume distribution of a polymer with intrinsic microporosity (PIM-1). *Journal of Membrane Science*. **2008**, *318*, 84-99.
[169] Thommes, M.; Kaneko, K.; Neimark, A.V.; Olivier, J.P.; Rodriguez-Reinoso, F.; Rouquérol, J.; Sing, K.S. Physisorption of gases, with special reference to the evaluation of surface area and pore size distribution (IUPAC Technical Report). *Pure and Appl. Chem*. **2015**, *87*, 1051-1069.
[170] Zárybnická, L., Stránská, E., Machotová, J., Černošková, E.; Melánová, K. Characterisation of ion-exchange resins under thermal loading. *Membr. Membr. Technol*. **2016**, *1*, 35-41
[171] Singare, P.U.; Lokhande, R.S.; Madyal, R.S. Thermal degradation studies of some strongly acidic cation exchange resins. *Open Journal of Physical Chemistry*. **2011**, *1*, 45.
[172] Hatch, M.J.; Lloyd, W.D. Preparation and properties of a neophyl type anion exchange resin, *Journal of Applied Polymer Science*. **1964**, *8*, 1659-1666.
[173] Guilera, J.; Ramírez, E.; Fité, C.; Iborra, M.; Tejero, J. Thermal stability and water effect on ion-exchange resins in ethyl octyl ether production at high temperature. *Applied Catalysis A: General*. **2013**, *467*, 301-309.
[174] Ping, Z.; Nguyen, Q.; Chen, S.; Zhou, J.; Ding, Y. States of water in different hydrophilic polymers-DSC and FTIR studies. *Polymer*. **2001**, *42*, 8461-8467.
[175] El-Sayed, S.A.; Mostafa, M.E. Thermal pyrolysis and kinetic parameter determination of mango leaves using common and new proposed parallel kinetic models. *RSC Adv.* **2020,** *10*, 18160-18179.
[176] Gill, S.K.; Roohpour, N.; An, Y.; Gautrot, J.E.; Topham, P.D.; Tighe, B.J. Hydrophobic and hydrophilic effects on water structuring and adhesion in denture adhesives. *Journal of Biomedical Materials Research Part A*. **2018**, *106*, 1355-1362.
[177] Liu, W.G.; De Yao, K. What causes the unfrozen water in polymers: hydrogen bonds between water and polymer chains? *Polymer*. **2001**, *42*, 3943-3947.
[178] Tiihonen, J.; Markkanen, I.; Laatikainen, M.; Paatero, E. Elasticity of ion-exchange resin beads in solvent mixtures. *Journal of applied polymer science.* **2001**, *82*, 1256-1264.
[179] Smith, L.S.A.; Schmitz, V. The effect of water on the glass transition temperature of poly (methyl methacrylate). *Polymer.* ***1988,*** *29*, 1871-1878.
[180] Rouquerol, J.; Rouquerol, F.; Triaca, M.; Cerclier, O. The use of thermal analysis to select the standard outgassing conditions of a set of reference adsorbents. *Thermochimica Acta*. 1985, *85,* 311-314.
[181] Qian, Q.; Machida, M.; Tatsumoto, H. Preparation of activated carbons from cattle-manure compost by zinc chloride activation. *Bioresource Technology*. **2007**, *98*, 353-360.

[182] Marras, C.; Loche, Carta, D; Casula, M.F.; Schirru, M.; Cutrufello, M.G.; Corrias, A. Copper-based catalysts supported on highly porous silica for the water gas shift reaction. *ChemPlusChem*. **2016**, *81*, 421-432.

[183] Kyriakou, G; Theocharis, C.R. The anomalous sorptive behaviour of ZSM-5 and silicalite-I: Observation of low-pressure hysteresis in nitrogen adsorption. *Studies in Surface Science and Catalysis*. Elsevier, **2002**.

[184] Amidon, G.L.; Lee, P.I.; Topp, E.M. *Transport processes in pharmaceutical systems*. CRC Press, **1999**.

[185] Zhu, Q. *Hypercrosslinked polymer supported sulfonic acids for esterification of carboxylic acids*, Academic thesis. Huddersfield: University of Huddersfield, **2013**.

[186] Boz, N.; Degirmenbasi, N.; Kalyon, D.M. Esterification and transesterification of waste cooking oil over Amberlyst 15 and modified Amberlyst 15 catalysts. *Applied Catalysis B*: *Environmental*. **2015**, *165*, 723-730.

[187] Elabd, A.A.; Zidan, W.I.; Abo-Aly, M.M.; Bakier, E.; Attia, M. Uranyl ions adsorption by novel metal hydroxides loaded Amberlite IR120. *Journal of environmental radioactivity*. **2014**, *134*, 99-108.

[188] Rottreau, T.J.; Parkes, G.E.; Schirru, M.; Harries, J.L.; Mesa, M.G.; Topham, P.D.; Evans, R. NMR cryoporometry of polymers: cross-linking, porosity and the importance of probe liquid. *Colloids and Surfaces A: Physicochemical and Engineering Aspects*. **2019**, *575*, 256-263.

[189] Booth, S.F. *Precision Measurement and Calibration*. US Department of Commerce. National Bureau of Standards,**1961**.

[190] Okada, T.; Harada, M.; Hydration of halide anions in ion-exchange resin and their dissociation from cationic groups. *Analytical chemistry*. 2004, *76*, 4564-4571.

[191] Sienkiewicz, A.; Krasucka, P.; Charmas, B.; Stefaniak, W.; Goworek, J. Swelling effects in cross-linked polymers by thermogravimetry. *Journal of Thermal Analysis and Calorimetry*. **2017**, *130*, 85-93.

[192] Jamal, Y.; Rabie, A.; B.O. Boulanger, B.O. Determination of methanolysis rate constants for low and high fatty acid oils using heterogeneous surface reaction kinetic models. *Reaction Kinetics, Mechanisms and Catalysis*. **2015**, *114*, 63-74.

[193] Ho, R.; Nievergelt, A.¸ Pires, C.S.; Cuendet, M. Histone deacetylases as cancer chemoprevention targets for natural products. Studies in Natural Products Chemistry. **2012**, 247-267.

[194] Kozlowski, J.T.; Aronson, M.T.; Davis, R.J. Transesterification of tributyrin with methanol over basic Mg: Zr mixed oxide catalysts. *Applied Catalysis B*: *Environmental*. **2010**, 96, 508-515.

[195] Liberti, L.; Passino, R.; Petruzzelli, D. Chloride/sulphate exchange on anion resins. kinetic investigation, viii. influence of some physico-chemical properties of the resins. *Desalination*. **1982**, *41*, 199-207.

[196] Iborra, M.; Tejero, J.; Cunill, F.; Izquierdo, J.F.; Fité, C. Drying of Acidic Macroporous Styrene-Divinylbenzene resins with 12-20 cross-Linking degree. *Ind. Eng. Chem. Res*. **2000**, *39*, 1416-1422.

[197] Sigma-Aldrich. Amberlite®IR120 Na^+ form. Available from: https://www.sigmaaldrich.com/catalog/-product/aldrich/224359?lang=it&region=IT [Accessed 23 Jul 2020].

[198] DuPont. *Properties, Impurities and Concentrations of Regenerant Chemicals*, DuPont, **2019**. Available from: https://www.dupont.com/content/dam/dupont/amer/us/en/water-solutions/public/documents/en/45-D01105-en.pdf [Accessed 29 Jul 2021].

[199] Lokhande, R.S.; Singare, P.U.; Kolte, A.R. Ion exchange equilibrium for some uni-univalent and uni-divalent reaction systems using strongly basic anion exchange resin Duolite A-102 D. *Bull. Chem. Soc. Ethiop.* **2008**, *22*, 107-114.

[200] Knothe, G.; Krahl, J.; Van Gerpen, J. *The biodiesel handbook*, Elsevier, **2015**.

[201] Cren, É.C.; Meirelles, A.J.A. Adsorption isotherms for oleic acid removal from ethanol+ water solutions using the strong anion-exchange resin Amberlyst A26 OH. *J. Chem. Eng. Data*. **2005**, *50* 1529-1534.

[202] Bamunusingha, B.A.N.N.; De Silva, E.C.L.; Gunasekera, M.Y. Performance of ion exchange resin as solid catalyst for the esterification of acetic acid with ethanol. *J. Natn. Sci.Foundation Sri Lanka.* **2016**, *44*, 83-93.

[203] Bianchi, C.L.; D.C. Boffito, D.C; Pirola, C.; Ragaini, V. Low temperature de-acidification process of animal fat as a pre-step to biodiesel production. *Catalysis letters*. **2010**, *134*, 179-183.

[204] Mitsubishi Chemical Corporation. *Ion exchange resins: Strongly Basic Anion Exchange Resins*. Available from: https://www.diaion.com/en/products/ion_exchange_resins/strongly_basic_anion/--Index.html [Accessed 20 Nov 2020]

[205] Niu, X.; Xing, C.; Jiang, W.; Dong, Y.; Yuan, F.; Zhu, Y. Activity and stability of solid base KF/La_2O_3 catalysts for transesterification of tributyrin with methanol. *Reaction Kinetics, Mechanisms and Catalysis*, **2013**,*109*, 167-179.

[206] Chakrabarti, A.; Sharma, M.M. Cationic ion exchange resins as catalyst. *Reactive Polymers*. **1993**, *20*, 1-45.

[207] Hart, K.E.; Abbott, L.J.; Colina, C.M. Analysis of force fields and BET theory for polymers of intrinsic microporosity. *Molecular Simulation*. **2013**, *39*, 397-404.

[208] de Rezende, S.M.; de Castro Reis, M.; Reid, M.G.; Silva Jr, P.L.; Coutinho, F.M.B.; San Gil, R.A.d.S; Lachter, E.R. Transesterification of vegetable oils promoted by poly (styrene-divinylbenzene) and poly (divinylbenzene). *Applied catalysis A: General*. **2008**, *349*, 198-203.

[209] Vlasenko, N.V.; Kochkin, Y.N.; Serebrii, T.G.; Strizhak, P.E. Physicochemical Properties and Catalytic Performance of Sulphonic Resins of Various Morphological Types in Ethyl t-Butyl Ether Synthesis. *Adsorption Science & Technology*. **2015**, *33*, 545-551.

[210] Rottreau, T.J.; Parlett, C.M.A.; Lee, A.F.; Evans, R. Diffusion NMR characterisation of catalytic silica supports: a tortuous path. *J. Phys. Chem. C*. **2017**, *121*, 16250-16256.

[211] Lee, A.F.; Wilson, K. Sol–gel sulfonic acid silicas as catalysts. *Handbook of Green Chemistry*: Online. **2010**, 37-57.

[212] D'Agostino, C.; Mitchell, J.; Gladden, L.F.; Mantle, M.D. Hydrogen bonding network disruption in mesoporous catalyst supports probed by PFG-NMR diffusometry and NMR relaxometry. *J. Phys. Chem. C*. **2012**, *116*, 8975-8982.

[213] Pirez, C.; Caderon, J.-M.; Dacquin, J.-P.; A.F. Lee, A.F.; Wilson, K. Tunable KIT-6 mesoporous sulfonic acid catalysts for fatty acid esterification. *ACS catalysis*. **2012**, *2*, 1607-1614.

[214] Robinson, N.; D'Agostino, C. NMR investigation into the influence of surface interactions on liquid diffusion in a mesoporous catalyst support. *Top Catal*. **2020**, *63*, 319-327.

[215] Johnson Jr, C.S. Diffusion ordered nuclear magnetic resonance spectroscopy: principles and applications. *Progress in Nuclear Magnetic Resonance Spectroscopy*. **1999**, *34*, 203-256.

[216] Tanner, J.E.; Stejskal, E.O. Restricted self-diffusion of protons in colloidal systems by the pulsed-gradient, spin-echo method. *J. Chem. Phys*. **1968**, *49*,1768-1777.

[217] Rottreau, T. J. *Application of the liquid state nuclear magnetic resonance techniques for the study of porous materials*. Doctoral thesis. Birmingham: Aston University, **2018**.

[218] Hatzakis, E. Nuclear magnetic resonance (NMR) spectroscopy in food science: A comprehensive review. *Comprehensive Reviews in Food Science and Food Safety*. **2019**, *18*, 189-220.

[219] Brown, J.L. *Vapour-Liquid Equilibria within Nanoporous Media*. Doctoral thesis. Cambridge: University of Cambridge, **2018**.

[220] Keeler, J. *Understanding NMR spectroscopy*. John Wiley & Sons, **2011**.

[221] Elster, D.A. *What is meant by chemical shift?* Available from: http://www.mri-q.com/chemical-shift.html [Accessed 20/05/2020].

[222] Harris, R.K.; Becker, E.D.; De Menezes, S.M.C.; Goodfellow, R.; Granger, P. NMR nomenclature. Nuclear spin properties and conventions for chemical shifts (IUPAC Recommendations 2001). *Pure Appl. Chem.* **2001**, *73*, 1795-1818.

[223] Ross, A.; Schlotterbeck, G.; Dieterle, F.; H. Senn, H. "NMR spectroscopy techniques for application to metabonomics". *The handbook of metabonomics and metabolomics*. London: Elsevier. **2007**.

[224] University of Colorado. *Spin states, magnetic fields, and electromagnetic radiation*. Available from: https://orgchemboulder.com/Spectroscopy/nmrtheory/nmrtheory.shtml [Accessed 02 Oct 2020].
[225] Bloch, F. Nuclear induction, *Phys. rev.*, **1946**, *70*, 460.
[226] Hornak, J.P. *The basics of NMR.* Available from: https://www.cis.rit.edu/htbooks/nmr/inside.htm [Accessed 18 May 2020]
[227] Elster, D.A. *T_1 Relaxation: Definition*. Available from: http://www.mriquestions.com/what-is-t1.html [Accessed 02 Oct 2020].
[228] Anderson, S.H. *Soil-water-root processes: advances in tomography and imaging*. John Wiley & Sons, **2020**.
[229] Song, Y.-Q. Magnetic resonance of porous media (MRPM): A perspective. Journal of Magnetic Resonance. **2013**, *229,* 12-24.
[230] Elster, A.D. *T2 Relaxation: Definition*. Available from: http://mri-q.com/what-is-t2.html [Accessed 02 Oct 2020].
[231] Willis, S.A.; Stait-Gardner, T.; Torres, A.M.; Price, W.S. Fundamentals of Diffusion Measurements using NMR. *Diffusion NMR of Confined Systems.* **2016**.
[232] Einstein, A. On the theory of the Brownian movement. *Ann. Phys*. **1906**, *19*, 371-381.
[233] Stokes, G.G. On the effect of the internal friction of fluids. *Trans. Camb. Phil. Soc*. **1856**, *9* 24.
[234] Mehrer, H. *Diffusion in solids: fundamentals methods, materials, diffusion-controlled processes*. Springer Science & Business Media. **2007**.
[235] Elster, D.A. Isotropic vs Anisotropic. What is the difference between isotropic and anisotropic diffusion? Available from: http://mriquestions.com/iso-anisotropic-diffusion.html [Accessed 13 Aug 2021].
[236] Pagès, G.; Gilard, V.; Martino, R.; Malet-Martino, M. Pulsed-field gradient nuclear magnetic resonance measurements (PFG NMR) for diffusion ordered spectroscopy (DOSY) mapping. *Analyst*. **2017**, *142*, 3771-3796.
[237] Harmon, J.; Coffman, C.; Villarrial, S.; Chabolla, S.; Heisel, K.A.; Krishnan, V.V. Determination of molecular self-diffusion coefficients using pulsed-field-gradient NMR: An experiment for undergraduate physical chemistry laboratory. *Journal of Chemical Education*. **2012**, *89*, 780-783.
[238] Shemesh, N.; Özarslan, E.; Bar-Shir, A.; Basser, P.J.; Cohen, Y. Observation of restricted diffusion in the presence of a free diffusion compartment: single-and double-PFG experiments. *Journal of Magnetic Resonance.* **2009**, *200*, 214-225.
[239] Padley, F.B.; Harwood, J.L.; Gunstone, F.D. *The lipid handbook*. (Eds: Gunstone F.D.; Harwood J.L.; Padley, F.D.). Chapman & Hall, London, **1986**.
[240] Sinnaeve, D. The Stejskal-Tanner equation generalized for any gradient shape-an overview of most pulse sequences measuring free diffusion. *Concepts in Magnetic Resonance Part A*. **2012**, *40*, 39-65.
[241] Findeisen, M.; Brand, T.; Berger, S. A 1H-NMR thermometer suitable for cryoprobes. *Magnetic Resonance in Chemistry*. **2007**, *45*, 175-178.
[242] Pelta, M.D.; Morris, G.A.; Stchedroff, M.J.; Hammond, S.J. A one-shot sequence for high-resolution diffusion-ordered spectroscopy. *Magnetic Resonance in Chemistry*. **2002**, *40*, S147-S152.
[243] Swan, I.; Reid, M.; Howe, P.W.A.; Connell, M.A.; M. Nilsson, M.; Moore, M.A.; Morris, G.A. Sample convection in liquid-state NMR: why it is always with us, and what we can do about it. *Journal of magnetic resonance*. **2015**, *252*, 120-129.
[244] Barbosa, T.M.; Rittner, R.; Tormena, C.F.; Morris, G.A.; Nilsson, M. Convection in liquid-state NMR: expect the unexpected. *RSC adv.* **2016**, *6*, 95173-95176.
[245] Zhao, D.; Feng, J.; Huo, Q.; Melosh, N.; Fredrickson, G.H.; Chmelka, B.F.; Stucky, G.D. Triblock copolymer syntheses of mesoporous silica with periodic 50 to 300 angstrom pores. *Science*. **1998**, *279*, 548-552.
[246] Rottreau, T.J.; Parlett, C.M.A.; Lee, A.F.; Evans, R. NMR cryoporometric measurements of porous silica: A method for the determination of melting point depression parameters of probe liquids. *Microporous and Mesoporous Materials*. **2018**, *264*, 265-271.

[247] Manchester NMR Methodology Group. *DOSY toolbox.* Available from: https://nmr.chemistry.manchester.ac.uk/?q=node/8 [Accessed 07 Nov 2019].
[248] Torres, A.M.; Price, W.S. Common problems and artifacts encountered in solution-state NMR experiments. *Concepts in Magnetic Resonance Part A*. **2016**, *45*, e21387.
[249] Ambroz, F.; Macdonald, T.J.; Martis, V.; Parkin, I.P. Evaluation of the BET Theory for the Characterisation of Meso and Microporous MOFs. *Small Methods*. **2018**, *2,* 1800173.
[250] Abidin, S.Z. *Production of biodiesel from used cooking oil (UCO) using ion exchange resins as catalysts*. Doctoral thesis. Loughborough: Loughborough University. **2012**.

APPENDICES

Appendix A-Supporting information for Chapter 3

Measuring thermal stability-Thermogravimetric analysis

Figures A1.1 a-f contain the analogous graphs to **Figure 3.5 a** and **b**, Chapter 3, for the remaining resins. TGA (black line) and DTG (blue line) curves for the IERs under nitrogen performed in the temperature range 298 K–878 K with a flow rate of 20 cm^3 min^{-1} and heating rate of 10 K: **a**) 458Cl; **b**) 958Cl; **c**) 410Cl; **d**) 402Cl; **e**) 15H and **f**) 120H.

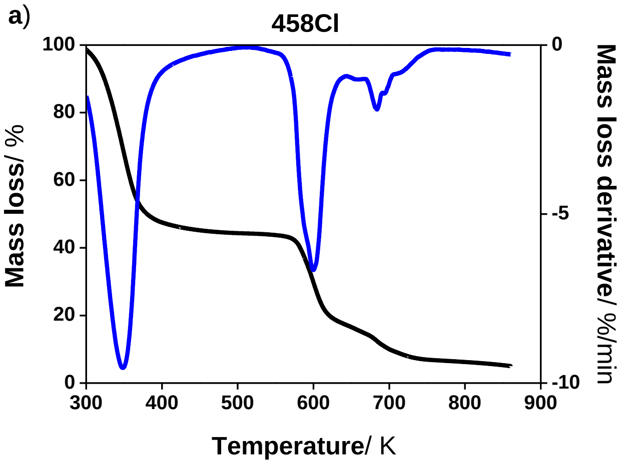

Figure A1.1 a. TGA (black line) and DTG (blue line) curves for the IER 458Cl under nitrogen performed in the temperature range 298 K–878 K with a flow rate of 20 cm^3 min^{-1} and heating rate of 10 K.

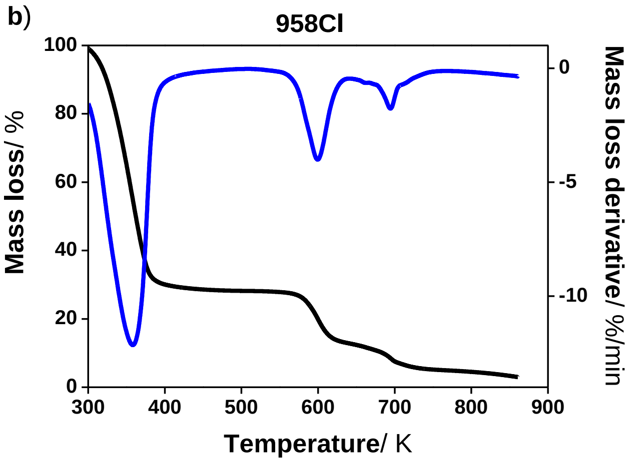

Figure A1.1 b. TGA (black line) and DTG (blue line) curves for the IER 958Cl under nitrogen performed in the temperature range 298 K–878 K with a flow rate of 20 cm^3 min^{-1} and heating rate of 10 K.

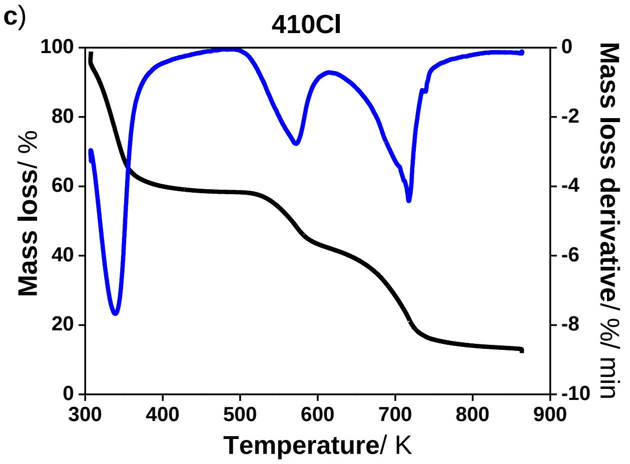

Figure A1.1 c. TGA (black line) and DTG (blue line) curves for the IER 410Cl under nitrogen performed in the temperature range 298 K–878 K with a flow rate of 20 cm^3 min^{-1} and heating rate of 10 K.

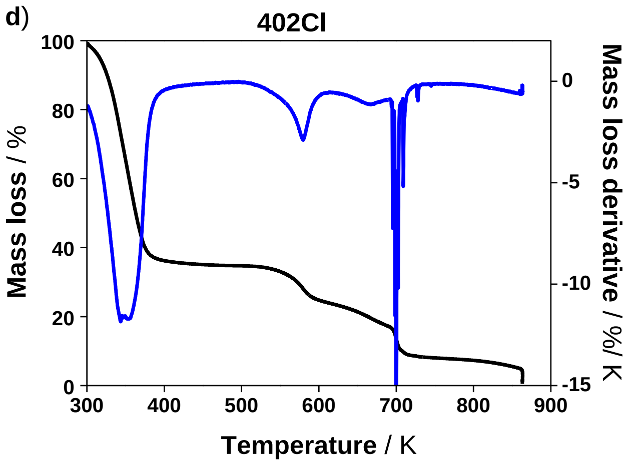

Figure A1.1 d. TGA (black line) and DTG (blue line) curves for the IER 402Cl under nitrogen performed in the temperature range 298 K–878 K with a flow rate of 20 cm^3 min^{-1} and heating rate of 10 K.

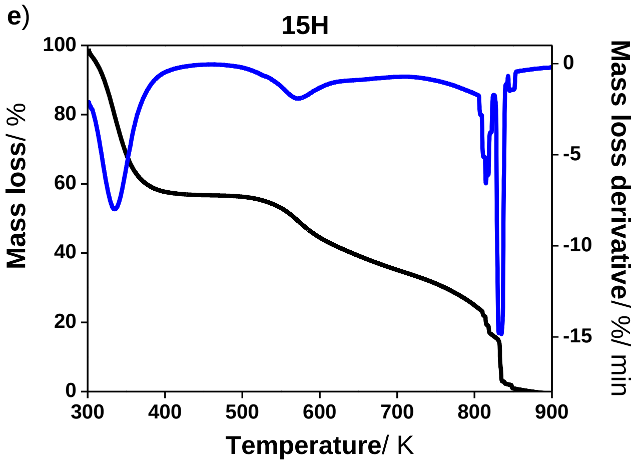

Figure A1.1 e. TGA (black line) and DTG (blue line) curves for the IER 15H under nitrogen performed in the temperature range 298 K–878 K with a flow rate of 20 cm^3 min^{-1} and heating rate of 10 K.

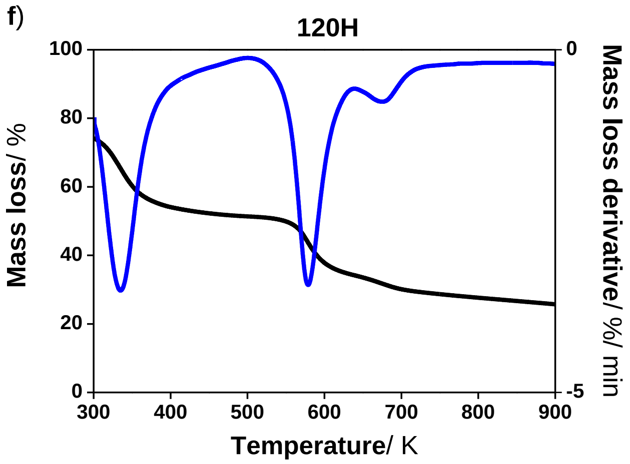

Figure A1.1 f. TGA (black line) and DTG (blue line) curves for the IER 120H under nitrogen performed in the temperature range 298 K–878 K with a flow rate of 20 cm^3 min^{-1} and heating rate of 10 K.

Recording the thermal event-Differential scanning calorimetry analysis

Figures A1.2 a-f display the analogous graphs to **Figure 3.6 a** and **b**, **Chapter 3**, for the remaining resins. DSC thermograms performed under nitrogen with a flow rate of 50 cm^3 min^{-1} of **a**) **458Cl**; **b**) **958Cl**; **c**) **410Cl**; **d**) **402Cl**; **e**) **15H** and **f**) **120H**. These thermograms showed intermediate water, glass transition point and the endo- and exothermic events.

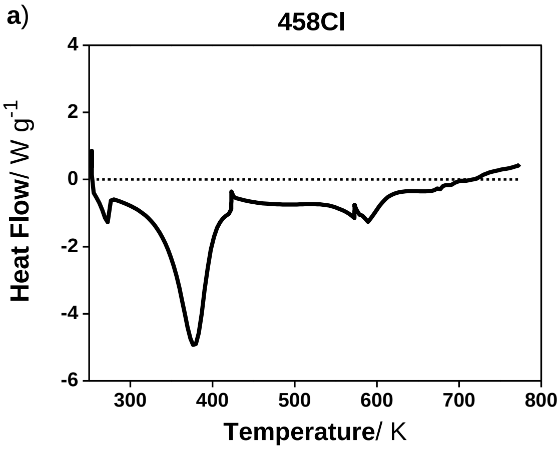

Figure A1.2 a. DSC thermograms of the gel resin 458Cl under nitrogen (50 cm^3 min^{-1}).

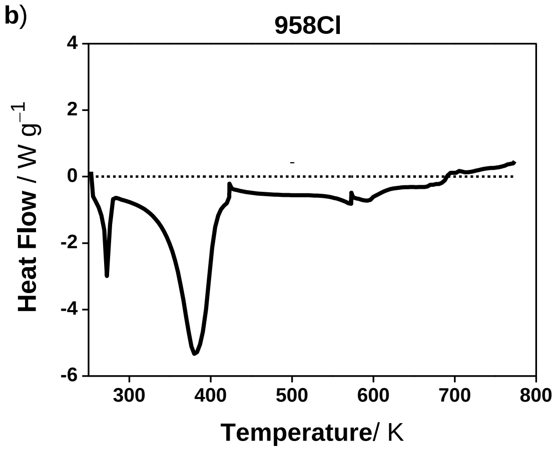

Figure A1.2 b. DSC thermograms of the macroreticular resin 958Cl under nitrogen (50 cm^3 min^{-1}).

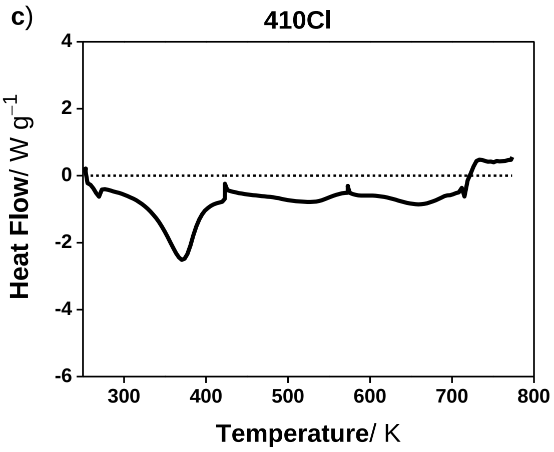

Figure A1.2 c. DSC thermograms of gel resin 410Cl under nitrogen (50 cm^3 min^{-1}).

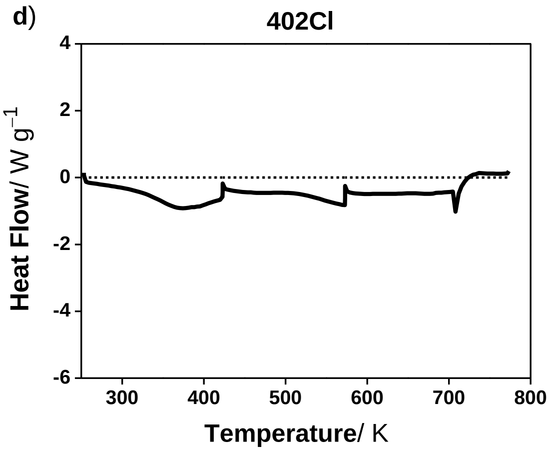

Figure A1.2 d. DSC thermograms of gel resin 402Cl under nitrogen (50 cm^3 min^{-1}).

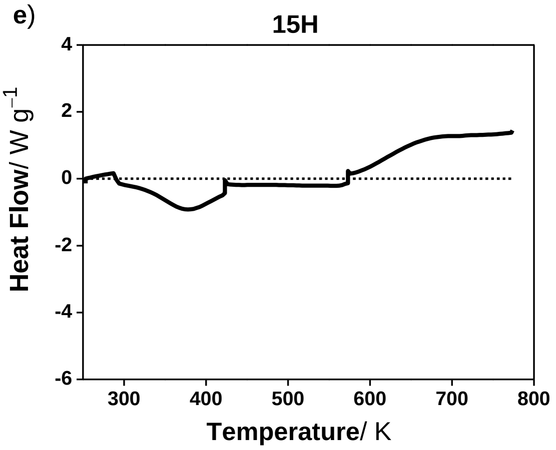

Figure A1.2 e. DSC thermograms of the macroreticular 15H under nitrogen (50 cm^3 min^{-1}).

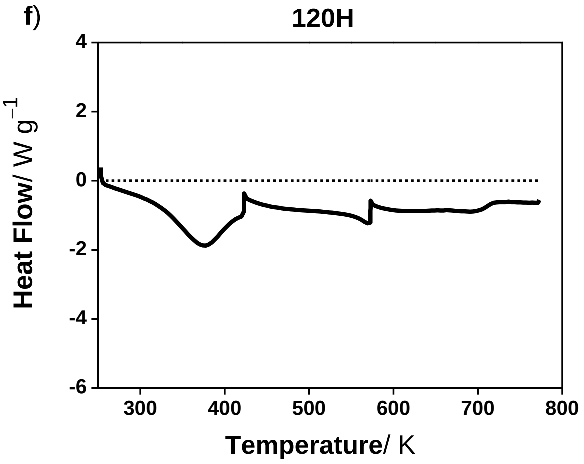

Figure A1.2 f. DSC thermograms of the gel resin 120H under nitrogen (50 cm^3 min^{-1}).

Isotherms-N_2 adsorption-desorption

Figures A1.3 a-f show the analogous graphs to **Figure 3.7 a** and **b**, **Chapter 3**, for the remaining resins. The different outgassing conditions were carried out on the resins: 313 K for 3 h on native, 313 K for 12 h on native and 313 K for 3 h on pre-treated at 313 K for 12 h. These are represented by black, grey and white circles. All the isotherms were characterized by low-hysteresis pressure. The lack of some analyses is due to materiality handling.

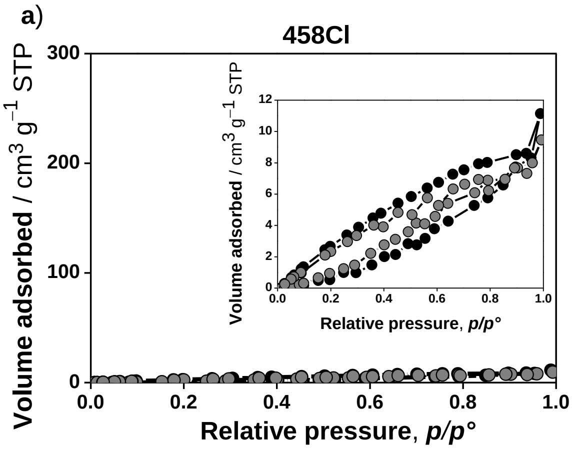

Figures A1.3 a. N_2 adsorption-desorption isotherm at 77 K on 458Cl using different outgassing conditions (black circle) 313 K for 3 h on native; (grey circle) 313 K for 12 h on native; (white circle) 313 K for 3 h on pre-treated at 313 K for 12 h.

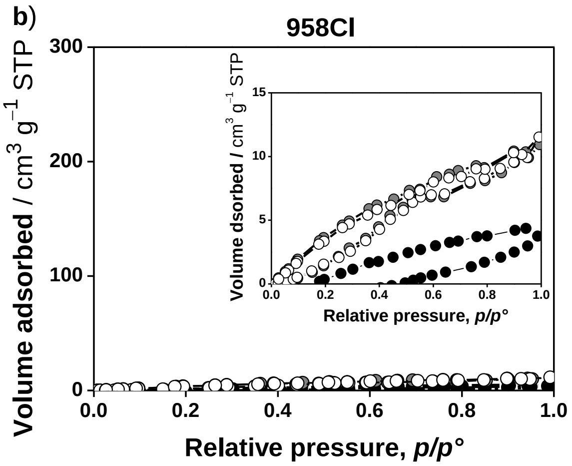

Figures A1.3 b. N_2 adsorption-desorption isotherm at 77 K on 958Cl using different outgassing conditions (black circle) 313 K for 3 h on native; (grey circle) 313 K for 12 h on native; (white circle) 313 K for 3 h on pre-treated at 313 K for 12 h.

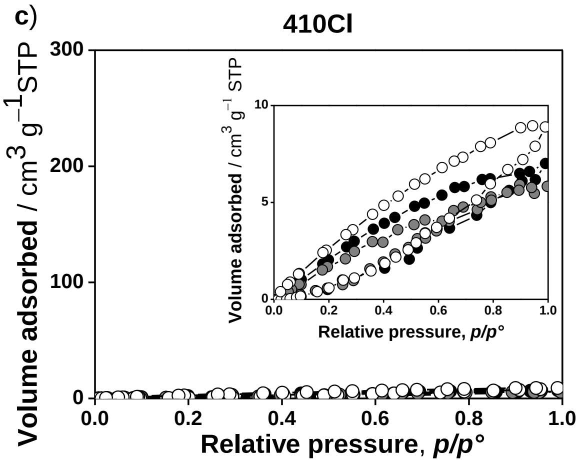

Figures A1.3 c. N_2 adsorption-desorption isotherm at 77 K on 410Cl using different outgassing conditions (black circle) 313 K for 3 h on native; (grey circle) 313 K for 12 h on native; (white circle) 313 K for 3 h on pre-treated at 313 K for 12 h.

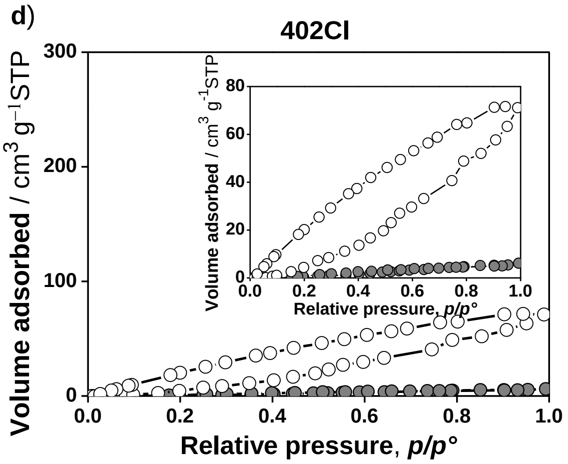

Figures A1.3 d. N_2 adsorption-desorption isotherm at 77 K on 402Cl using different outgassing conditions (grey circle) 313 K for 12 h on native; (white circle) 313 K for 3 h on pre-treated at 313 K for 12 h.

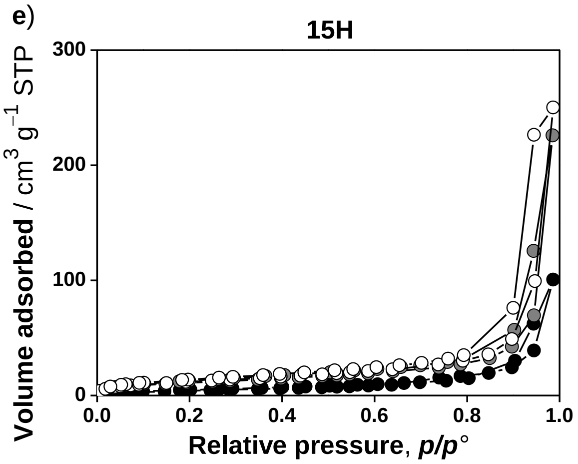

Figures A1.3 e. N_2 adsorption-desorption isotherm at 77 K on 15H using different outgassing conditions (black circle) 313 K for 3 h on native; (grey circle) 313 K for 12 h on native; (white circle) 313 K for 3 h on pre-treated at 313 K for 12 h.

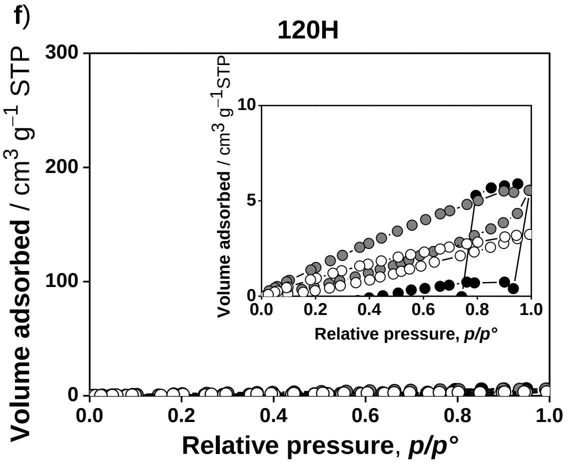

Figures A1.3 f. N_2 adsorption-desorption isotherm at 77 K on 120H using different outgassing conditions (black circle) 313 K for 3 h on native; (grey circle) 313 K for 12 h on native; (white circle) 313 K for 3 h on pre-treated at 313 K for 12 h.

Measuring the pore size distribution of the IERs-N_2 adsorption-desorption

Figures A1.4. **a-q** contain the analogous graphs representing the pore size distribution (PSD) to **Figures 3.8 a** and **b**, **Chapter 3**, for the remaining resins. Three different outgassing procedures were carried out on each IER. The PSDs were obtained by applying the BJH model, the NLDFT-adsorption and NLDFT-desorption models that are representing by black, grey and white circles. Each resin exhibited a broader and unsymmetrical pore size distribution for NLDFT-adsorption model than those obtained for other two models, BJH and NLDFT-desorption models.

Gel-type 458Cl
Outgassed at 313 K for 3h on native

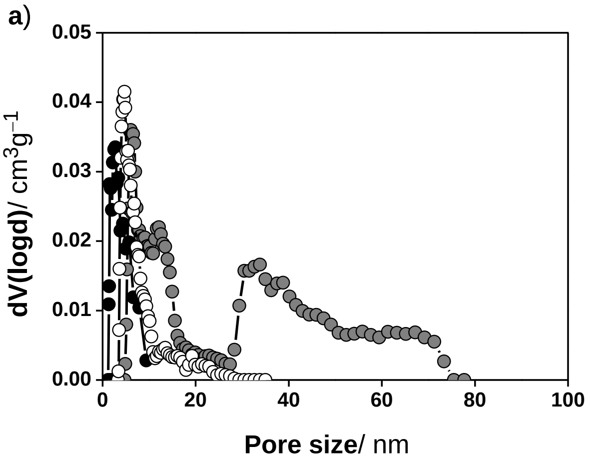

Figures A1.4 a. pore size distributions (PSDs) of the gel-type resin 458Cl based on (black circle) the BJH method; (grey circle) the NLDFT (adsorption) method; (white circle) NLDFT (desorption) method. The outgassing conditions were 313 K for 3 h on native.

Outgassed at 313 K for 12 h on native

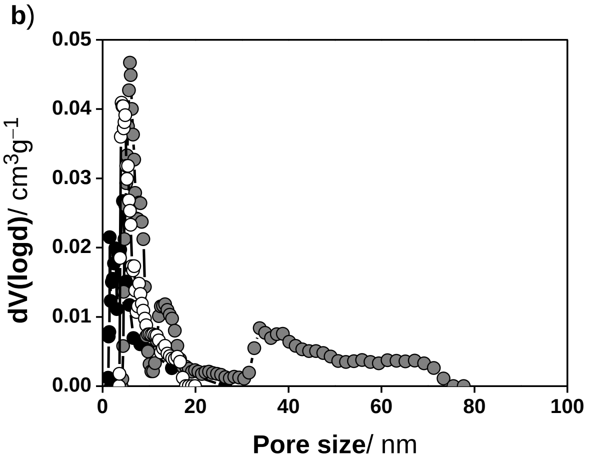

Figures A1.4 b. Pore size distributions (PSDs) of the gel-type resin 458Cl based on (black circle) the BJH method; (grey circle) the NLDFT (adsorption) method; (white circle) NLDFT (desorption) method. The outgassing conditions were 313 K for 12 h on native.

Macroreticular 958Cl
Outgassed at 313 K for 3 h on native

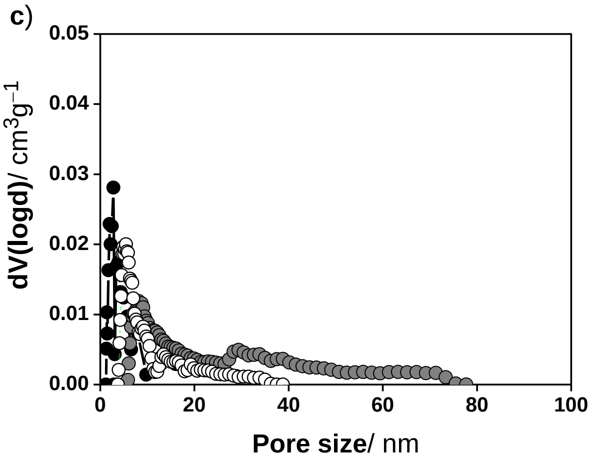

Figures A1.4 c. Pore size distributions (PSDs) of the macroreticular resin 958Cl based on (black circle) the BJH method; (grey circle) the NLDFT (adsorption) method; (white circle) NLDFT (desorption) method. The outgassing conditions were 313 K for 3 h on native.

Outgassed at 313 K for 12h on native

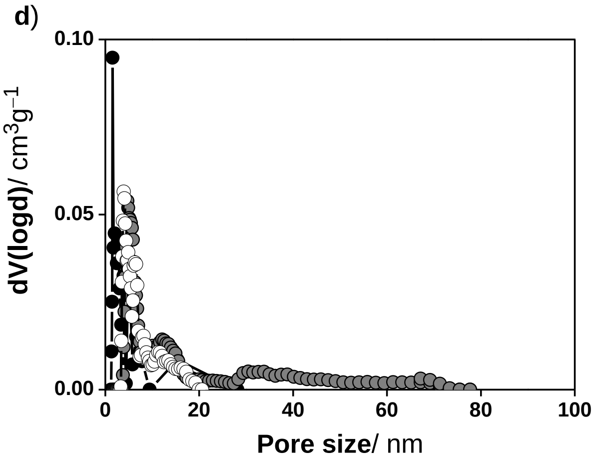

Figures A1.4 d. Pore size distributions (PSDs) of the macroreticular resin 958Cl based on (black circle) the BJH method; (grey circle) the NLDFT (adsorption) method; (white circle) NLDFT (desorption) method. The outgassing conditions were 313 K for 12 h on native.

Outgassed at 313 K for 3h on pre-treated IER

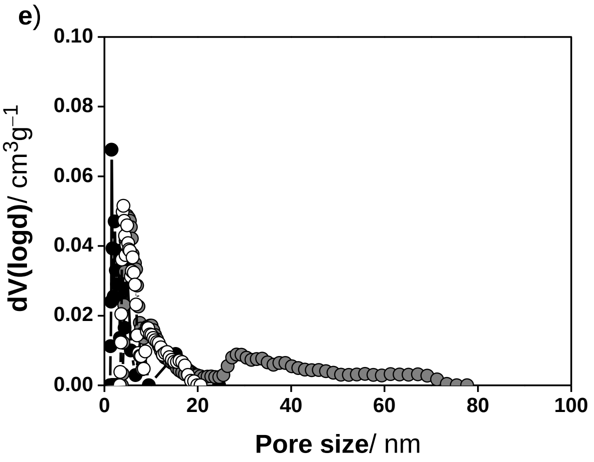

Figures A1.4 e. Pore size distributions (PSDs) of the macroreticular resin 958Cl based on (black circle) the BJH method; (grey circle) the NLDFT (adsorption) method; (white circle) NLDFT (desorption) method. The outgassing conditions were 313 K for 3 h on native.

Gel-type 410Cl
Outgassed at 313 K for 3h on native

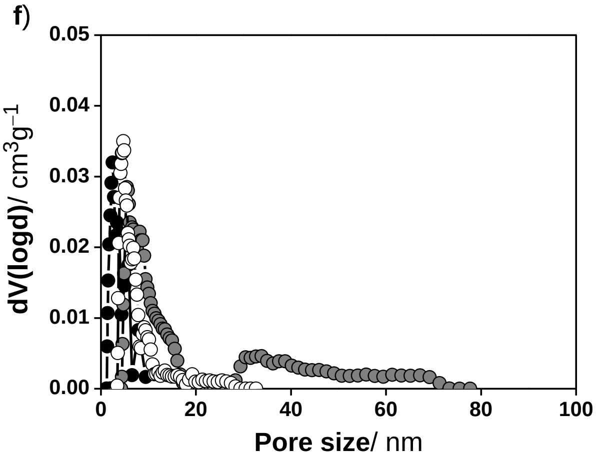

Figures A1.4 f. Pore size distributions (PSDs) of the gel-type resin 410Cl based on (black circle) the BJH method; (grey circle) the NLDFT (adsorption) method; (white circle) NLDFT (desorption) method. The outgassing conditions were 313 K for 3 h on native.

Outgassed at 313 K for 12 h on native IER

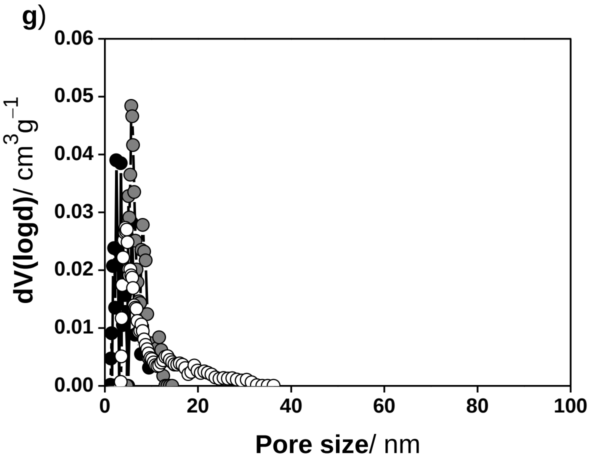

Figures A1.4 g. Pore size distributions (PSDs) of the gel-type resin 410Cl based on (black circle) the BJH method; (grey circle) the NLDFT (adsorption) method; (white circle) NLDFT (desorption) method. The outgassing conditions were 313 K for 3 h on pre-treated IER.

Outgassed at 313 K for 3 h on pre-treated IER

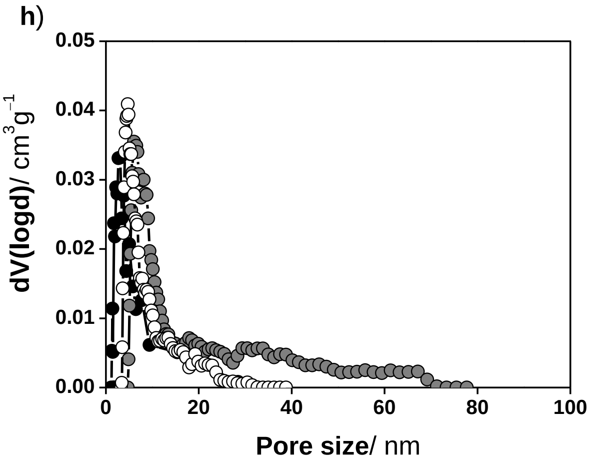

Figures A1.4 h. Pore size distributions (PSDs) of the gel-type resin 410Cl based on (black circle) the BJH method; (grey circle) the NLDFT (adsorption) method; (white circle) NLDFT (desorption) method. The outgassing conditions were 313 K for 3 h on pre-treated IER.

Gel-type 402Cl
Outgassed at 313 K for 12h on native

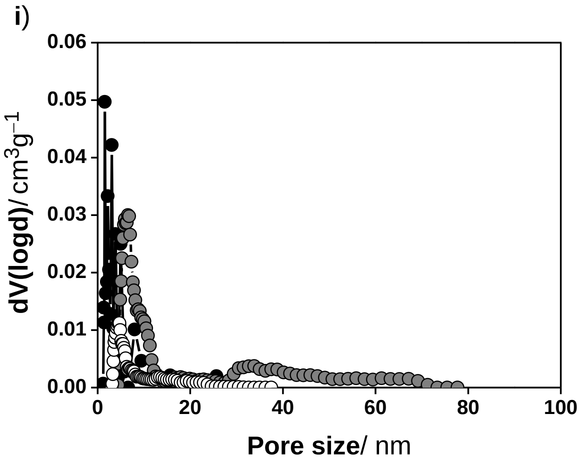

Figures A1.4 i. Pore size distributions (PSDs) of the gel-type resin 402Cl based on (black circle) the BJH method; (grey circle) the NLDFT (adsorption) method; (white circle) NLDFT (desorption) method. The outgassing conditions were 313 K for 12 h on native.

Outgassed at 313 K for 3h on pre-treated IER

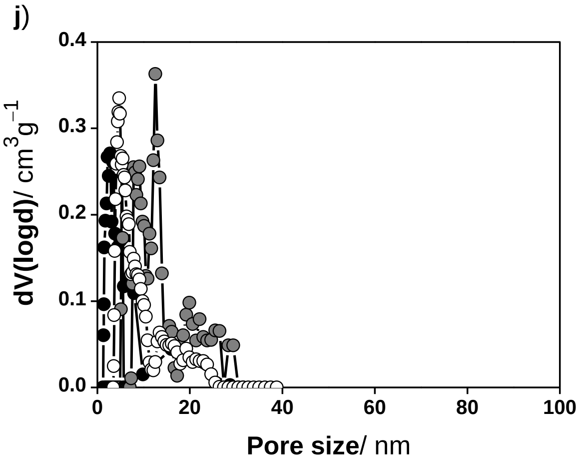

Figures A1.4 j. Pore size distributions (PSDs) of the gel-type resin 402Cl based on (black circle) the BJH method; (grey circle) the NLDFT (adsorption) method; (white circle) NLDFT (desorption) method. The outgassing conditions were 313 K for 3 h on pre-treated IER.

Macroreticular 15H
Outgassed at 313 K for 3h on native

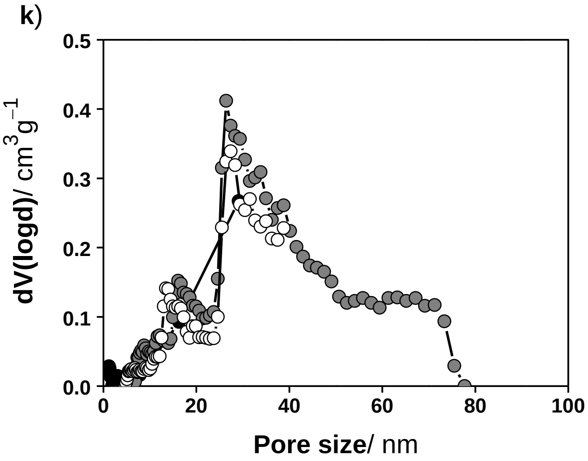

Figures A1.4 k. Pore size distributions (PSDs) of the macroreticular resin 15H based on (black circle) the BJH method; (grey circle) the NLDFT (adsorption) method; (white circle) NLDFT (desorption) method. The outgassing conditions were 313 K for 3 h on native.

Outgassed at 313 K for 12h on native

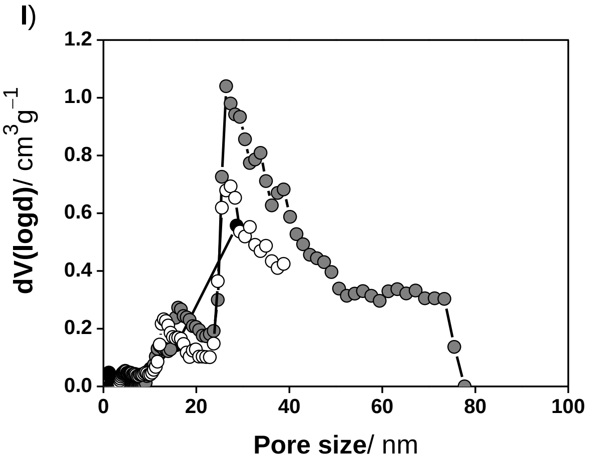

Figures A1.4 l. Pore size distributions (PSDs) of the macroreticular resin 15H based on (black circle) the BJH method; (grey circle) the NLDFT (adsorption) method; (white circle) NLDFT (desorption) method. The outgassing conditions were 313 K for 12 h on native.

Outgassed at 313 K for 3h on pre-treated IER

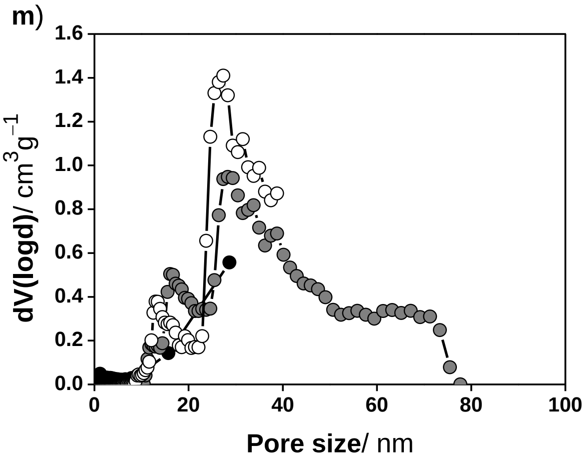

Figures A1.4 m. Pore size distributions (PSDs) of the macroreticular resin 15H based on (black circle) the BJH method; (grey circle) the NLDFT (adsorption) method; (white circle) NLDFT (desorption) method. The outgassing conditions were 313 K for 3 h on pre-treated IER.

Gel-type 120H

Outgassed at 313 K for 3h on native

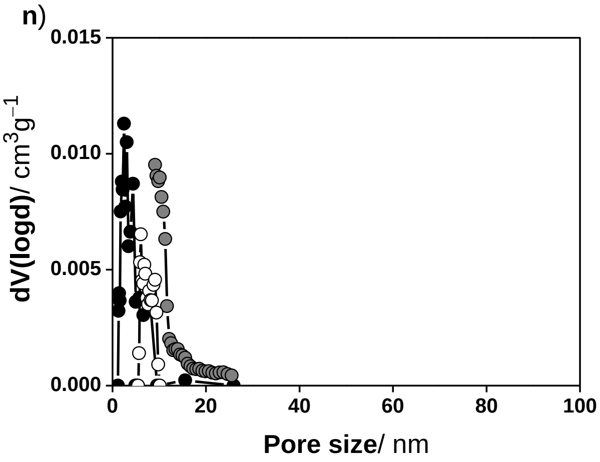

Figures A1.4 n. Pore size distributions (PSDs) of the gel-type resin 120H based on (black circle) the BJH method; (grey circle) the NLDFT (adsorption) method; (white circle) NLDFT (desorption) method. The outgassing conditions were 313 K for 3 h on pre-treated IER.

Outgassed at 313 K for 12h on native

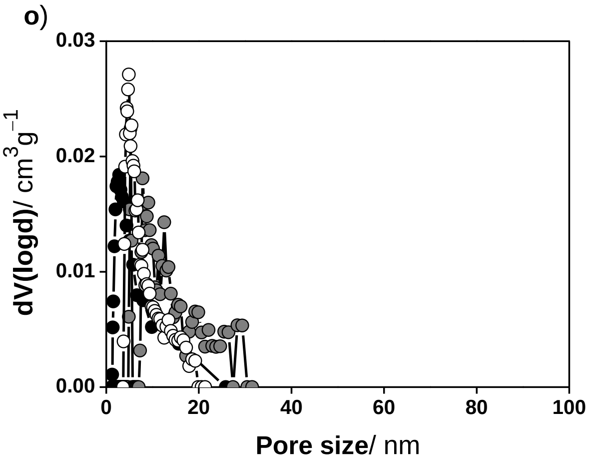

Figures A1.4 o. Pore size distributions (PSDs) of the gel-type resin 120H based on (black circle) the BJH method; (grey circle) the NLDFT (adsorption) method; (white circle) NLDFT (desorption) method. The outgassing conditions were 313 K for 12 h on native.

Outgassed at 313 K for 3h on pre-treated IER

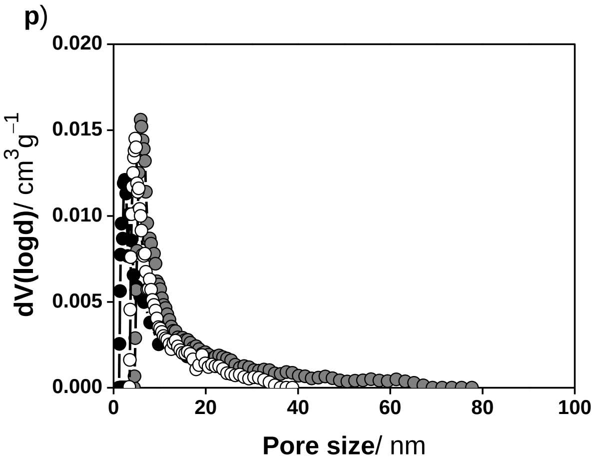

Figures A1.4 p. Pore size distributions (PSDs) of the gel-type resin 120H based on (black circle) the BJH method; (grey circle) the NLDFT (adsorption) method; (white circle) NLDFT (desorption) method. The outgassing conditions were 313 K for 3 h on pre-treated IER.

Finding the linear BET range-N$_2$ adsorption-desorption

Figures A1.5 a-v show the BET plots of each resin, and correlation coefficients, R^2. To calculate the specific surface area, a linear range was selected within the ***p/p***° range 0.05-0.2, and the ***C*** constant must be greater than zero [107] [107]. Due to the material nature and resource-constrained related to the access to the porosimeter, several graphs are missing.

Macroreticular 26OH
Outgassed at 313 K for 3h on native

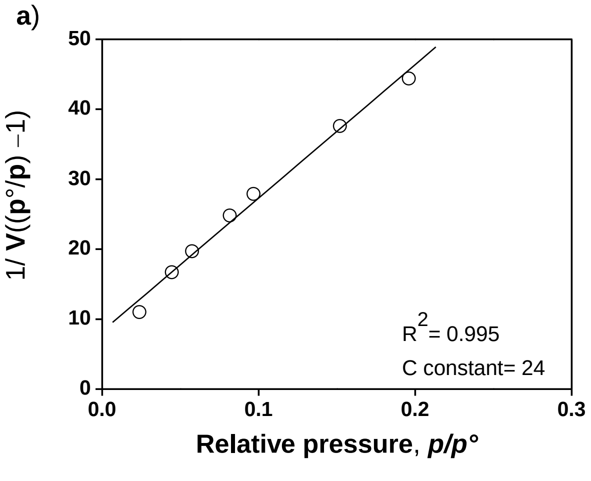

Figures A1.5 a. BET surface area plot of the native macroreticular 26OH outgassed at 313 K for 3h. The C constant was obtained from BET equation.

Outgassed at 313 K for 12h on native

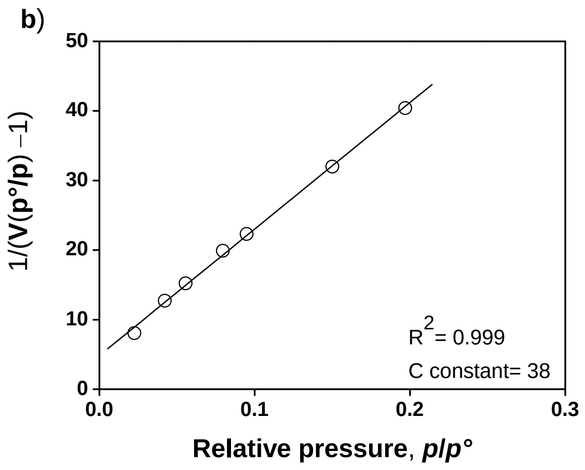

Figures A1.5 b. BET surface area plot of the native macroreticular 26OH outgassed at 313 K for 12h. The C constant was obtained from BET equation.

Outgassed at 313 K for 3h on pre-treated IER

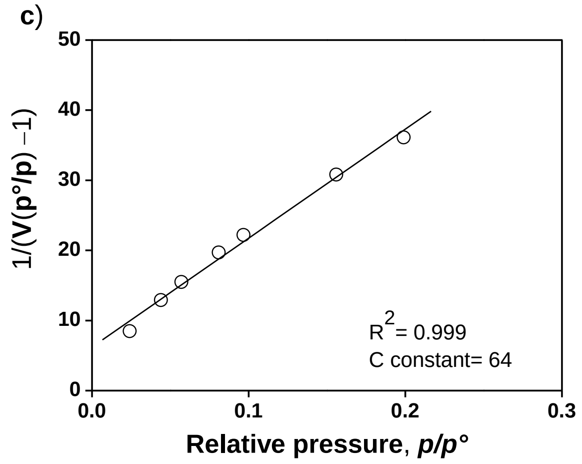

Figures A1.5 c. BET surface area plot of the pre-treated macroreticular 26OH outgassed at 313 K for 3h. The C constant was obtained from BET equation.

Gel-type 458Cl

Outgassed at 313 K for 3h on native

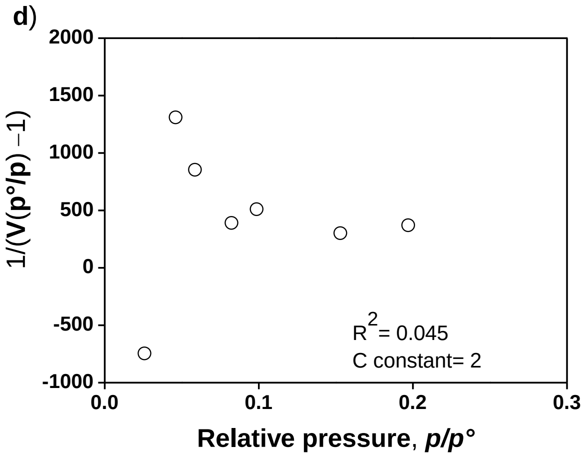

Figures A1.5 d. BET surface area plot of the native gel-type 458Cl outgassed at 313 K for 3h. The C constant was obtained from BET equation.

Outgassed at 313 K for 12 h on native

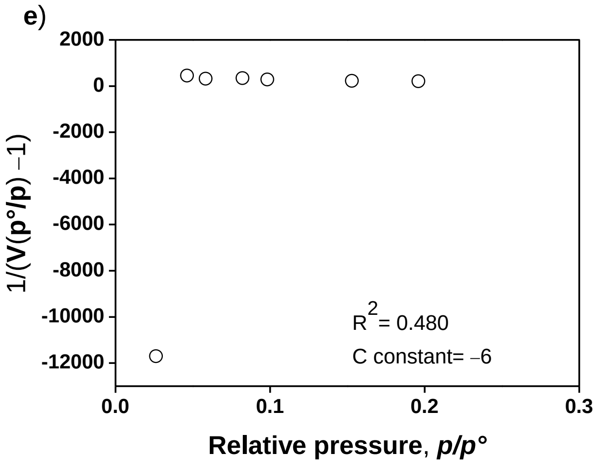

Figures A1.5 e. BET surface area plot of the native gel-type 458Cl outgassed at 313 K for 12h. The C constant was obtained from BET equation.

Gel-type 958Cl
Outgassed at 313 K for 3h on native

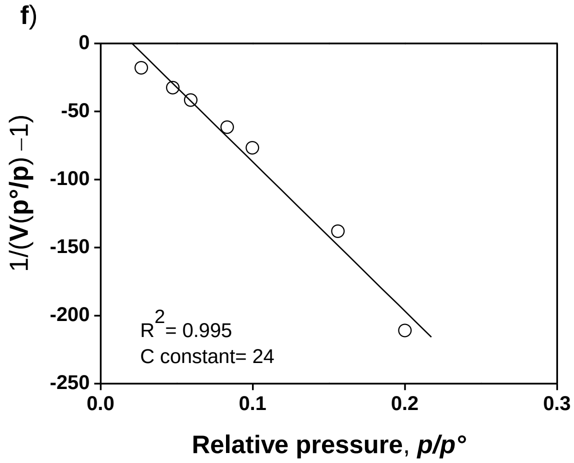

Figures A1.5 f. BET surface area plot of the native gel-type 958Cl outgassed at 313 K for 3h. The C constant was obtained from BET equation.

Outgassed at 313 K for 12 h on native

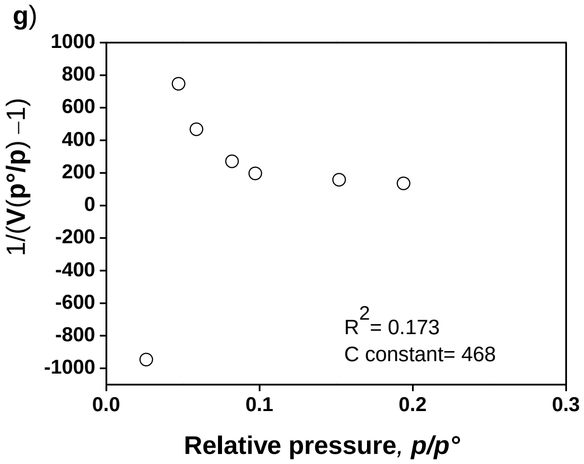

Figures A1.5 g. BET surface area plot of the native gel-type 958Cl outgassed at 313 K for 12h. The C constant was obtained from BET equation.

Outgassed at 313 K for 3h on pre-treated IER

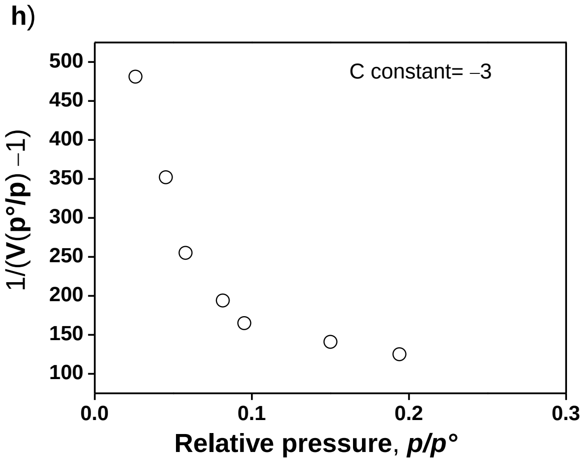

Figures A1.5 h. BET surface area plot of the pre-treated gel-type 958Cl outgassed at 313 K for 3h. The C constant was obtained from BET equation.

Gel-type 410Cl

Outgassed at 313 K for 3h on native

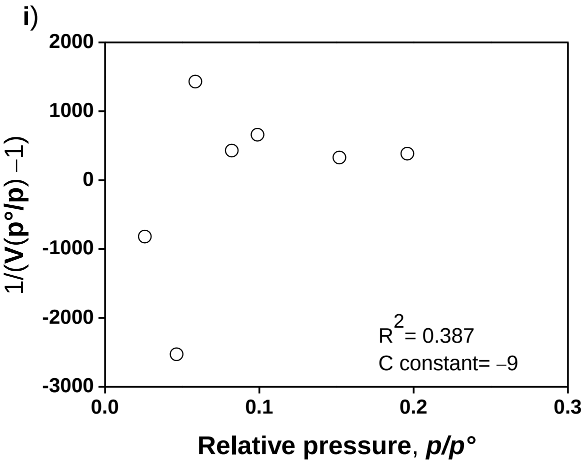

Figures A1.5 i. BET surface area plot of the native gel-type 410Cl outgassed at 313 K for 3h. The C constant was obtained from BET equation.

Outgassed at 313 K for 12 h on native

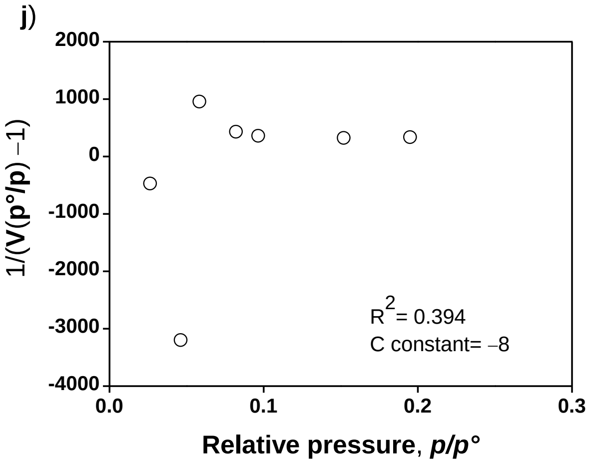

Figures A1.5 j. BET surface area plot of the native gel-type 410Cl outgassed at 313 K for 3h. The C constant was obtained from BET equation.

Outgassed at 313 K for 3h on pre-treated IER

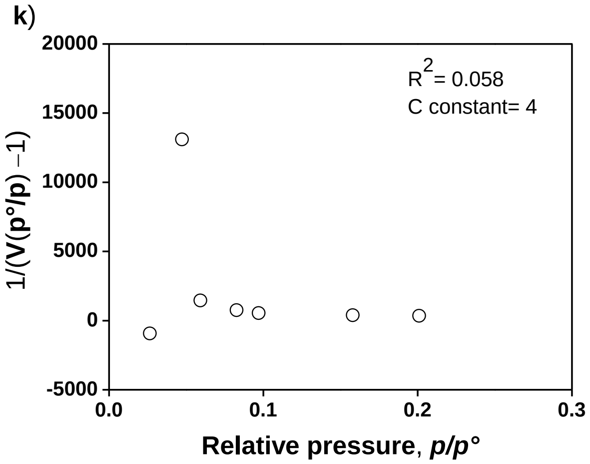

Figures A1.5 k. BET surface area plot of the pre-treated gel-type 410Cl outgassed at 313 K for 3h. The C constant was obtained from BET equation.

Gel-type 402Cl

Outgassed at 313 K for 12 h on native

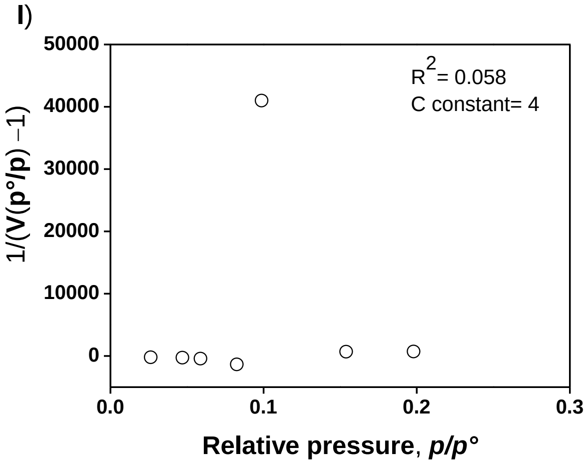

Figures A1.5 l. BET surface area plot of the native gel-type 402Cl outgassed at 313 K for 12h. The C constant was obtained from BET equation.

Outgassed at 313 K for 3h on pre-treated IER

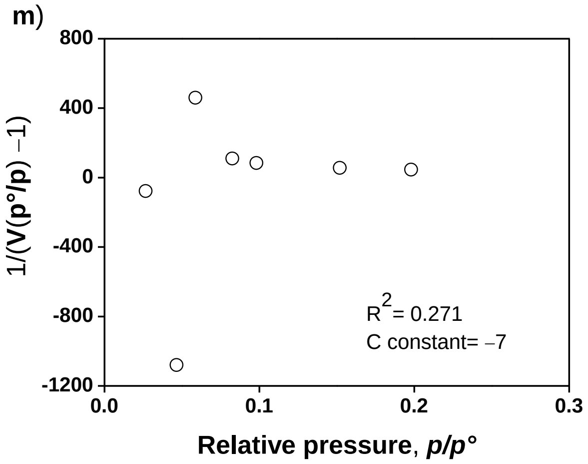

Figures A1.5 m. BET surface area plot of the pre-treated gel-type 402Cl outgassed at 313 K for 3h. The C constant was obtained from BET equation.

Gel-type 402OH
Outgassed at 313 K for 3 h on native

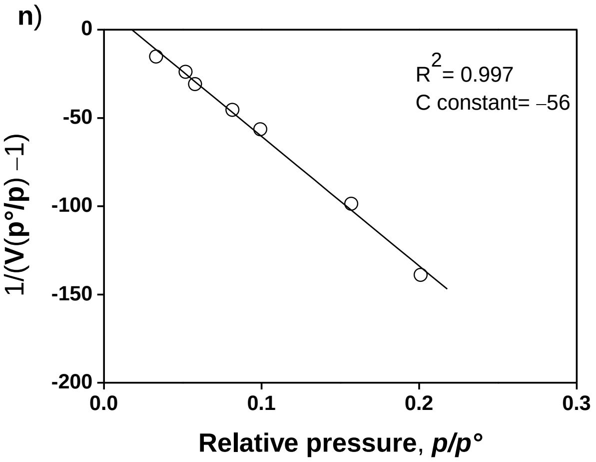

Figures A1.5 n. BET surface area plot of the native gel-type 402OH outgassed at 313 K for 3h. The C constant was obtained from BET equation.

Outgassed at 313 K for 12 h on native

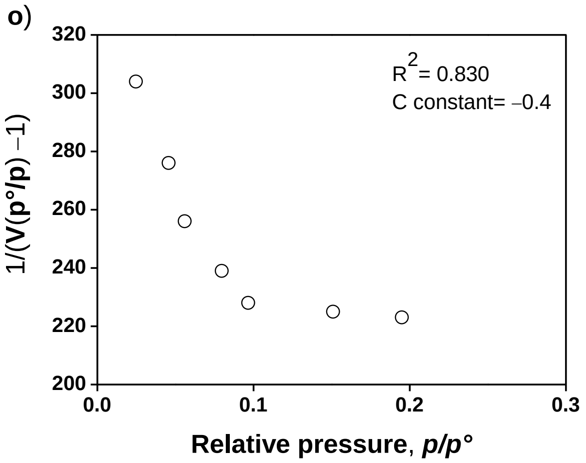

Figures A1.5 o. BET surface area plot of the native gel-type 402OH outgassed at 313 K for 12 h. The C constant was obtained from BET equation.

Outgassed at 313 K for 3h on pre-treated IER

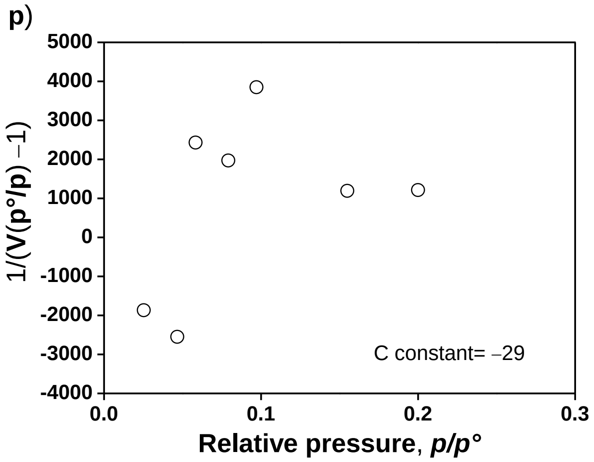

Figures A1.5 p. BET surface area plot of the pre-treated gel-type 402OH outgassed at 313 K for 3h. The C constant was obtained from BET equation.

Macroreticular 15H
Outgassed at 313 K for 3 h on native

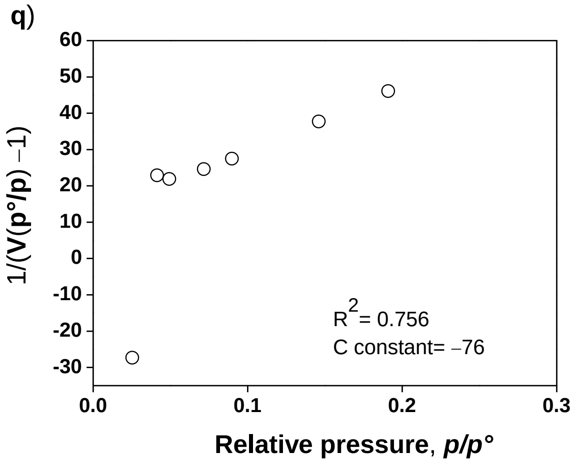

Figures A1.5 q. BET surface area plot of the native macroreticular 15H outgassed at 313 K for 3h. The C constant was obtained from BET equation.

Outgassed at 313 K for 12 h on native

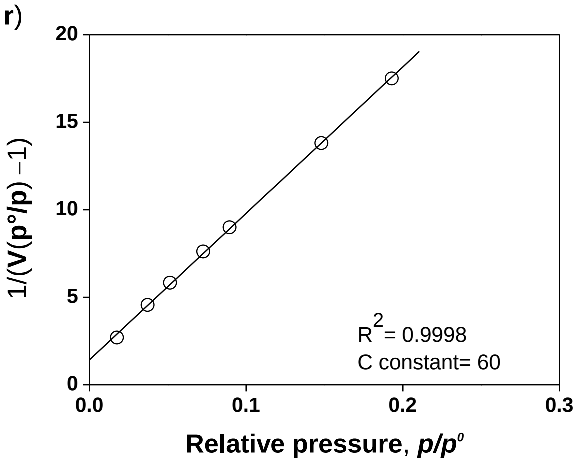

Figures A1.5 r. BET surface area plot of the native macroreticular 15H outgassed at 313 K for 12h. The C constant was obtained from BET equation.

Outgassed at 313 K for 3h on pre-treated IER

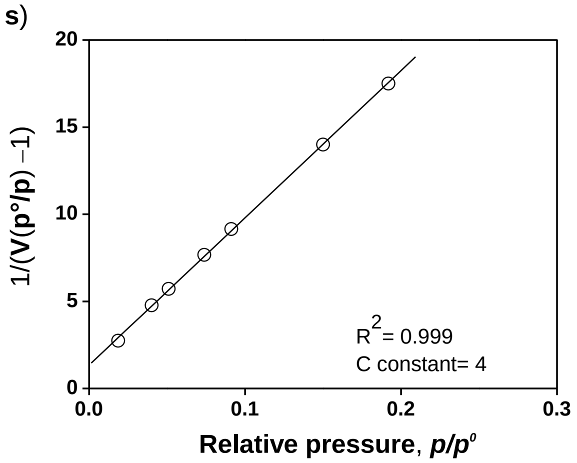

Figures A1.5 s. BET surface area plot of the pre-treated macroreticular 15H outgassed at 313 K for 3h. The C constant was obtained from BET equation.

Gel-type 120H
Outgassed at 313 K for 3 h on native

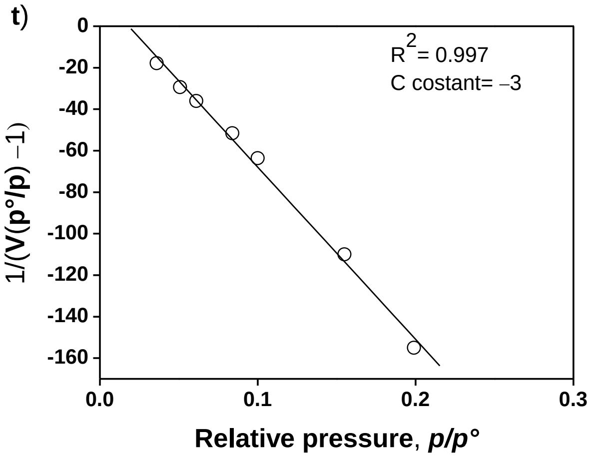

Figures A1.5 t. BET surface area plot of the native gel-type 120H outgassed at 313 K for 3h. The C constant was obtained from BET equation.

Outgassed at 313 K for 12 h on native

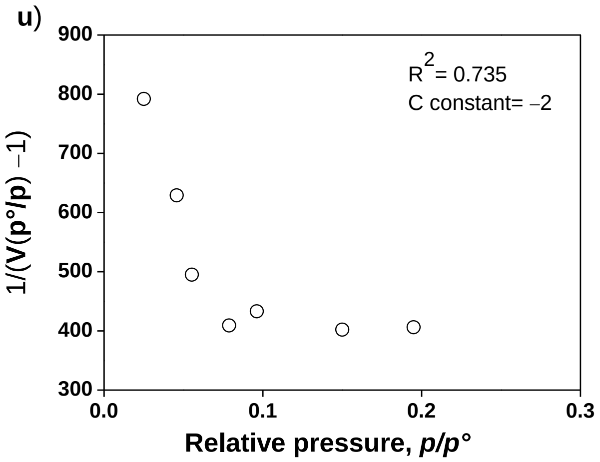

Figure A1.5 u. BET surface area plot of the native gel-type 120H outgassed at 313 K for 12h. The C constant was obtained from BET equation.

Outgassed at 313 K for 3h on pre-treated IER

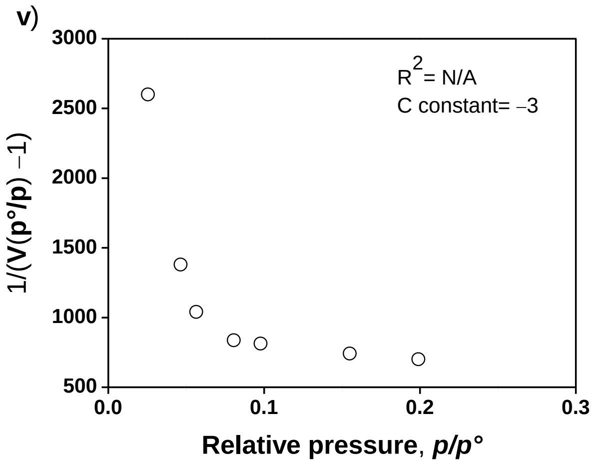

Figure A1.5 v. BET surface area plot of the pre-treated gel-type 120H outgassed at 313 K for 3h. The C constant was obtained from BET equation.

Measuring the pore diameter-Differential scanning calorimetry analysis

Figures A1.6 a-h display the melting point of the water confined in the resins using the DSC method discussed in **Chapter 2**. **Figures A1.5 a** and **g** clearly showed the melting peak of confined water at about 270 K and the melting peak of bulk water at 273 K. However, **Figures A1.6 b**, **c**, **d**, **e**, **f** and **h** display only the melting peak of the bulk water at a temperature of 273 K.

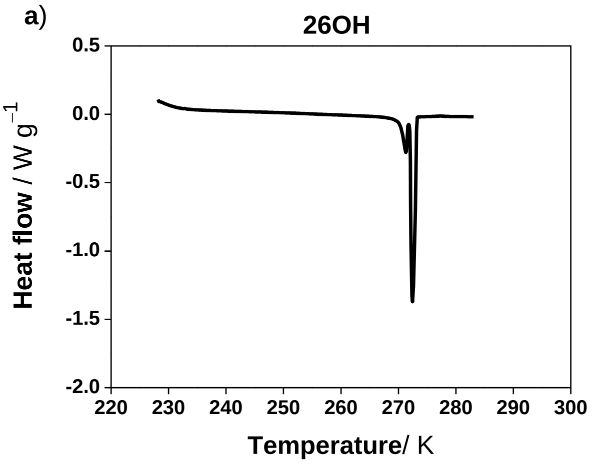

Figures A1.6 a. Melting thermogram of water in the porous network of the macroreticular resin 26OH using a heating rate of 0.5 K min^{-1}.

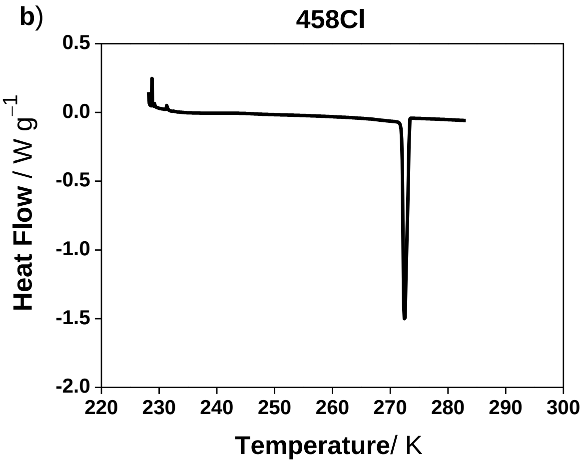

Figures A1.6 b. Melting thermogram of water in the porous network of the gel resin 458Cl using a heating rate of 0.5 K min^{-1}.

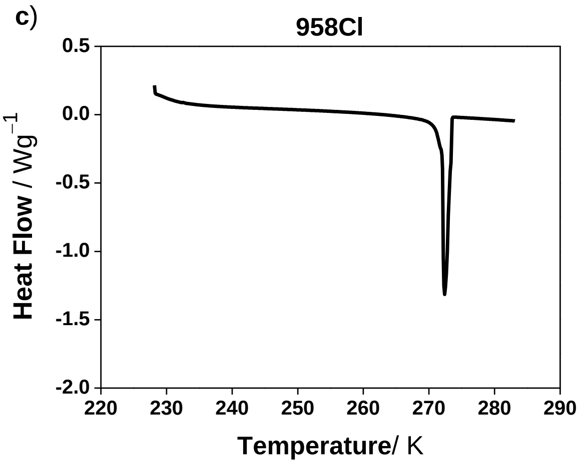

Figures A1.6 c. Melting thermogram of water in the porous network of the gel resin 958Cl using a heating rate of 0.5 K min^{-1}.

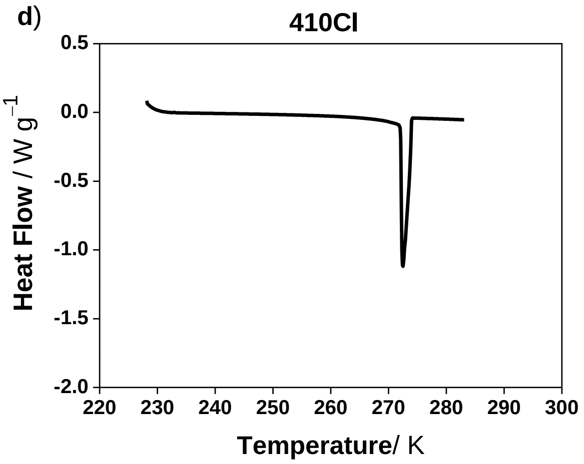

Figures A1.6 d. Melting thermogram of water in the porous network of the gel resin 410Cl using a heating rate of 0.5 K min^{-1}.

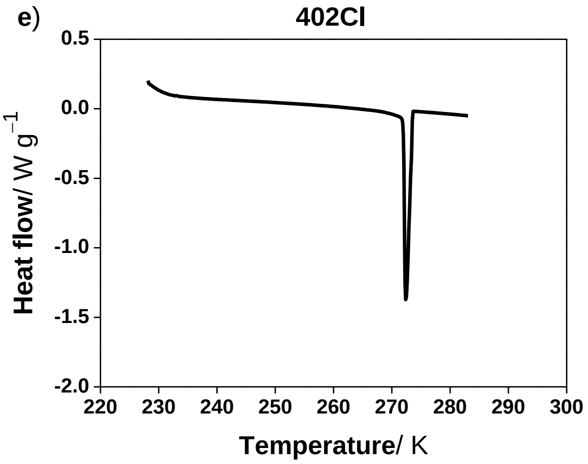

Figures A1.6 e. Melting thermogram of water in the porous network of the gel resin 402Cl using a heating rate of 0.5 K min^{-1}.

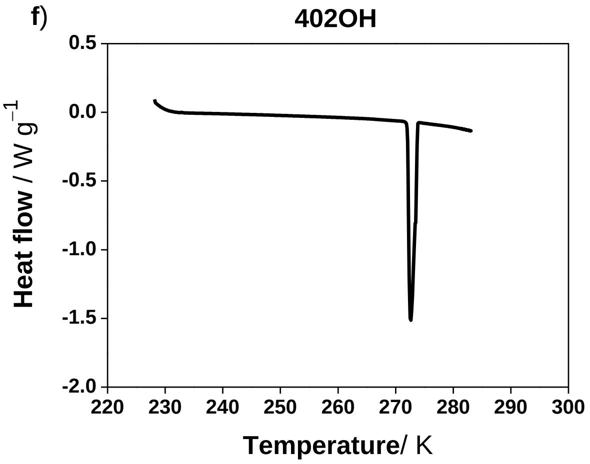

Figures A1.6 f. Melting thermogram of water in the porous network of the gel resin 402OH using a heating rate of 0.5 K min^{-1}.

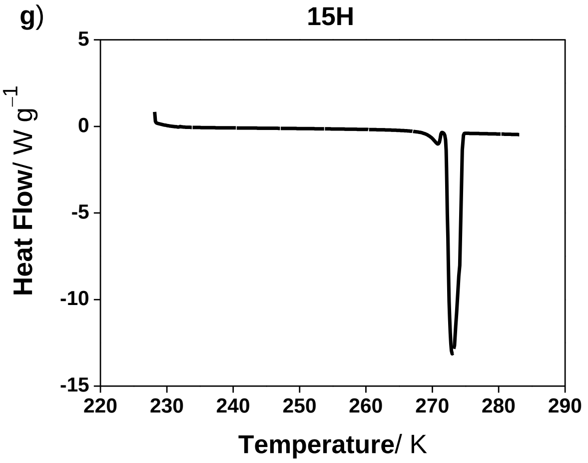

Figures A1.6 g. Melting thermogram of water in the porous network of the macroreticular resin 15H using a heating rate of 0.5 K min^{-1}.

h)

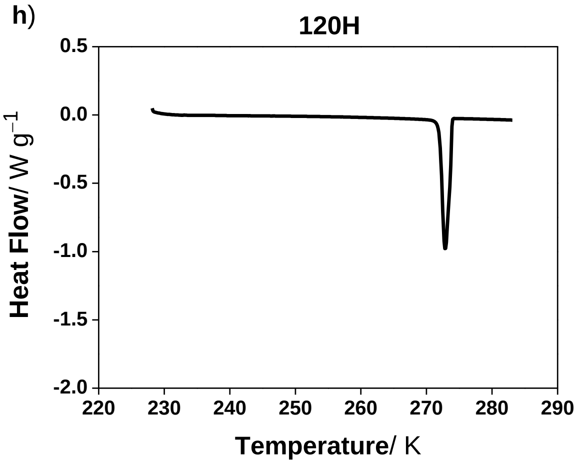

Figures A1.6 h. Melting thermogram of water in the porous network of the gel resin 120H using a heating rate of 0.5 K/min.

Total capacity of ion exchange resins-Elemental analysis CHN

The complete elemental analysis of the resins is reported in **Table A1.2**. Among the IERs, the anionic resins based on an acrylic matrix and acid resins showed the highest density of functional groups. Prior to running the IERs, acetanilide was used as a calibration standard. The elemental analysis of the standard is shown in **Table A1.1**. The results of the acidic IERs 15H and 120H were obtained from the literature. Due to resource-constrained related to the access to the elemental analyzer, the CHN analysis of 26OH is missing.

Table A1.1. Elemental analysis of acetanilide as a calibration standard.

Acetanilide	C%	H%	N%
Theorical values	71.09	6.71	10.36
Experimental values	70.91	6.88	10.38

Table A1.2. Complete elemental analysis of the resins studied in this work.

IERs	**Carbon / %**	**Hydrogen / %**	**Nitrogen / %**	**Sulphur / %**	**Oxygen / %**
26OH	n.d.	n.d.	n.d.	n.d.	n.d.
458Cl	45.43	10.91	11.24	n.d.	n.d.
958Cl	47.70	10.79	10.83	n.d.	n.d.
410Cl	57.47	9.71	5.06	n.d.	n.d.
402Cl	58.47	9.95	5.36	n.d.	n.d.
402OH	58.83	9.79	4.93	n.d.	n.d.
15H [195]	53.14	6.12	0.05	16.17	24.52
120H [196]	51.64	4.73	n.d.	18.38	n.d.

n.d. = not determined

Total capacity of ion exchange resins-Calibration curve

Figure A1.7 depicts the calibration curve (logarithm scale) for the determination of chloride ions released by the Cl-resins (458Cl, 958Cl, 402Cl and 410Cl), which were converted from the chloride ionic form into the sulphate ionic form to measure their total capacity. The calibration curve was built using seven standard solutions of 1, 2, 4, 6, 10,100 and 1000 ppm Cl^-. The ion selective electrode measured the potential (***P***) for each standard solution, and plotted against their concentration.

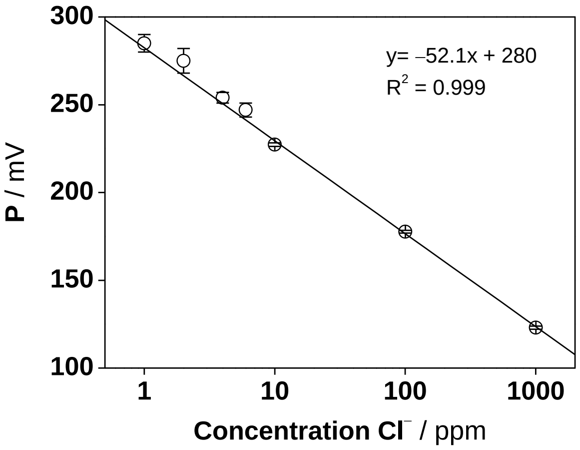

Figure A1.7. Calibration curve (logarithm scale) for the determination of total capacity of the Cl-resins (458Cl, 958Cl, 402Cl and 410Cl). Error bars represent the standard deviation for two repeated experiments.

Appendix B-Supporting information for Chapter 4

Activation of the Cl-resins-Calibration curves

Figures B1.1. a-c depict the calibration curves for 958Cl and 402Cl exchanged in 1 M and 0.1 M NaOH solution and, their equations for the determination of chloride ions released by the resins converted from the Cl-form into the OH-form to select the most promising activation process. The calibration curves were built using seven standard solutions of 1, 2, 4, 6, 10,100 and 1000 ppm Cl^-. The ion selective electrode measured the potential (***P***) for each standard solution, and plotted against their concentration.

Calibration curve for the resin 958Cl in 1M NaOH solution

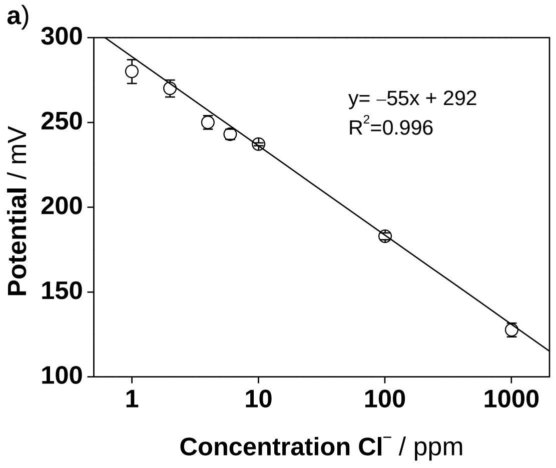

Figure B1.1 a. Calibration curve of the macroreticular resin 958Cl in 1M NaOH solution. Error bars represent the standard deviation for two repeated experiments.

Calibration curve for the resin 402Cl in 1M NaOH solution

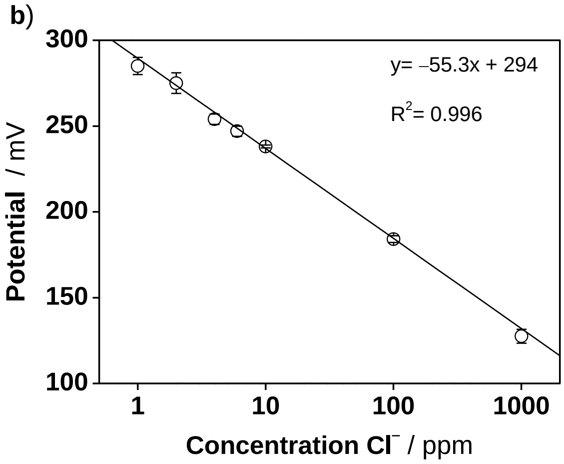

Figure B1.1 b. Calibration curve of the gel resin 402Cl in 1M NaOH solution. Error bars represent the standard deviation for two repeated experiments.

Calibration curve for the resins 458Cl, 958Cl, 410Cl and 402Cl in 0.1M NaOH solution

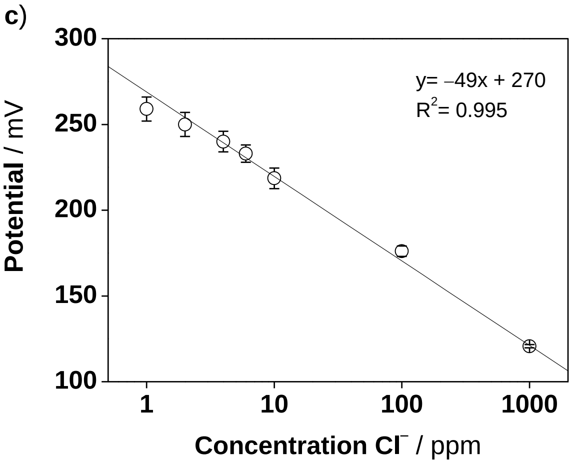

Figure B1.1 c. Calibration curve of the resins 458Cl, 958Cl, 410Cl and 402Cl in 0.1M NaOH solution. Error bars represent the standard deviation for two repeated experiments.

Pre-treatment of the resins for the catalytic conversion of tributyrin

Figure B1.2. Catalytic performance on native (black circle) and pre-treated (white circle) for the macroreticular 26OH. The reactions were performed with a stirring rate of 500 rpm, molar ratio oil: methanol of 1:30, 50 mg of catalyst, and 333 K. Error bars represent the standard deviation for two repeated experiments

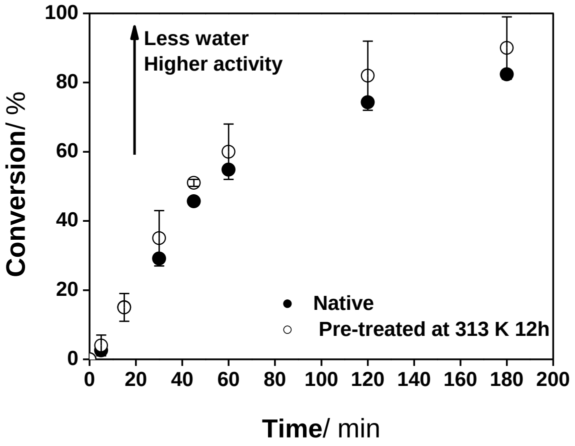

Figure B1.2. Catalytic performance on native and pre-treated 26OH. Reaction conditions: 10 mmol of tributyrin, 300 mmol of methanol, 500 rpm, 50 mg of catalyst, 333 K. Error bars represent the standard deviation for two repeated experiments.